Intelligent Scatter Radio, RF Harvesting Analysis, and Resource Allocation for Ultra-Low-Power Internet-of-Things

BY

PANOS N. ALEVIZOS

A DISSERTATION

SUBMITTED IN PARTIAL FULFILLMENT OF THE

REQUIREMENTS FOR THE DEGREE OF

DOCTOR OF PHILOSOPHY

IN

TECHNICAL UNIVERSITY OF CRETE

SCHOOL OF ELECTRICAL AND COMPUTER ENGINEERING

COMMITTEE IN CHARGE:

ASSOCIATE PROFESSOR AGGELOS BLETSAS (SUPERVISOR)

ASSOCIATE PROFESSOR GEORGE N. KARYSTINOS

ASSOCIATE PROFESSOR ANTONIOS DELIGIANNAKIS

DECEMBER 2017

Abstract

Ubiquitous sensing anywhere and anytime is envisioned under the general umbrella of Internet-of-Things (IoT). The objective of this dissertation is to contribute ultra-low-power IoT technology, exploiting novel concepts in wireless communications and networking.

The first part of this work studies far field radio frequency (RF) energy harvesting, taking into account non-linearity, sensitivity, and saturation effects of existing rectenna circuits. The proposed methodology offers the statistics of the harvested power for any given rectenna model, under mild assumptions. It is also demonstrated that currently-used linear RF harvesting models in the literature deviate from reality. In the second part, scatter radio technology, i.e., communication via means of reflection, is studied in order to enable ultra-low-power radio communication with single-transistor front-ends. The thesis proposes low-complexity detection schemes as well as decoding techniques for short block-length channel codes, tailored to coherent, as well as noncoherent reception of scatter radio. The goal was to target resource-constrained, i.e., hardware-"thin", scatter radio tags and simple, low-latency receivers. The developed detection and decoding algorithms are based on composite hypothesis testing framework. Interestingly, it is demonstrated that the bit error rate (BER) performance gap between coherent and noncoherent reception depends on the kind of channel codes employed, the fading conditions, as well as the utilized coding interleaving depth. The third part of this work proposes a multistatic scatter radio network architecture, based on orthogonal signaling, contrasted to existing architectures for dyadic Nakagami fading. Orthogonal signaling allows for collision free multi-user access for low-bitrate tags. It is shown that the proposed scatter radio architecture offers better diversity order, more reliable reception, as well as better field coverage, while demonstrating smaller sensitivity to the topology of the scatter radio tags, compared to existing monostatic architecture. Finally, the last part of the dissertation studies resource allocation in multi-cell backscatter sensor networks (BSNs). The average long-term signal-to interference-plus-noise ratio (SINR) of linear detectors is explored for multi-cell BSNs, and subsequently harnessed to allocate frequency sub-channels at tags. The proposed resource allocation algorithm is based on the Max-Sum inference algorithm and its convergence-complexity trade-off is quantified. Experimental studies in an outdoor scatter radio testbed corroborate the theoretical findings of this work. Hopefully, this thesis will establish the viability of scatter radio for ultra-low-power communications, enabling critical current and future IoT applications.

Acknowledgements

I would like to take some time to thank the people that were supporting me during my Ph.D studies; this dissertation would have not been possible without them.

First of all, I would like to wholeheartedly thank my supervisor, Aggelos Bletsas, for his guidance and his support during my studies at TUC, his integrity, his persistence on conducting high-quality research, and for believing on my skills. His advice and suggestions all these years undoubtedly improved the quality of my work. I would also like to thank all the guys from our research group for all the wonderful time we had together during the last 6 years.

I am very grateful for having the chance to collaborate with Prof. Sidiropoulos at the University of Minnesota. Except an excellent researcher, advisor, and teacher, his attitude towards life, in general, is a paradigm to be followed.

I am very grateful to Prof. Liavas who offered a gamut of important subjects that improved our engineering and mathematical skills and I am now able to understand difficult mathematical concepts encountering in my research. His passion for studying advanced mathematical topics and his patience on explaining difficult mathematical proofs to his students deserve a very big thanks!

I would like to thank Prof. Karystinos for the collaboration we had the last 3 years. I always learned from him. His suggestions are always to the point and help me to improve the quality of my work.

I would also like to thank Profs. Deligiannakis, Paterakis, and Lagoudakis for agreeing to serve as my committee.

I am very grateful to Prof. Manousakis for conveying advanced, general mathematical concepts to my head.

Big thanks to Prof. M. Petrakis. I admire his personality, his love about mathematics, and his perspective on many aspects of real life.

Dear adorable friends, I would like to say that I really appreciate your company, your true friendship, your love, and your support in many difficult situations all these years! Thank you!!

I would like to thank my parents and my family for their unconditional love. The words: support, encouragement, and patience obtain a different meaning when I am speaking about you.

Last, I would like to express my sincerest thanks to Georgia for her love and for helping me to be a better and integrated person. I really appreciate everything she has done for me all these years. She is one of the most valuable persons in my life.

To Georgia and my family

Contents

Chapter 1

Introduction

1.1 An Overview on the Internet-of-Things

The continuous evolution of radio frequency identification (RFID) systems, smart sensors, communication technologies, and Internet protocols flourished the concept of Internet-of-things (IoT). IoT is a disruptive technology that will play a leading role in ubiquitous sensing applications and existing industrial systems. In particular, IoT can be considered as a global network infrastructure composed by a variety of things (or objects or devices) around us (such as RFID tags, sensors, actuators, mobile phones) which are able to interact with each other through the Internet in order to reach common goals [1]. The IoT framework enables these objects to: think, hear, cooperatively execute jobs, share information, and coordinate decisions by harnessing the underlying IoT technologies, such as ubiquitous and pervasive computing, wireless communication technologies, sensor and actuator networks, Internet protocols and applications. IoT devices are required to fit to customer demands in terms of availability anywhere and anytime.

The IoT framework offers a vast number of opportunities, encapsulating a wide range of applications that (a) improve the quality of our lives, (b) provide important information regarding our environment, (c) grow the world's economy. Some of the most prominent application examples are mentioned below [1–3]:

- transportation and smart vehicles: assisted driving, smart cars, congestion control, automatic road tolling, mobile ticketing, augmented maps,

- logistics: supply chain monitoring and item identification,

- industry: manufacturing, inventory and production management,
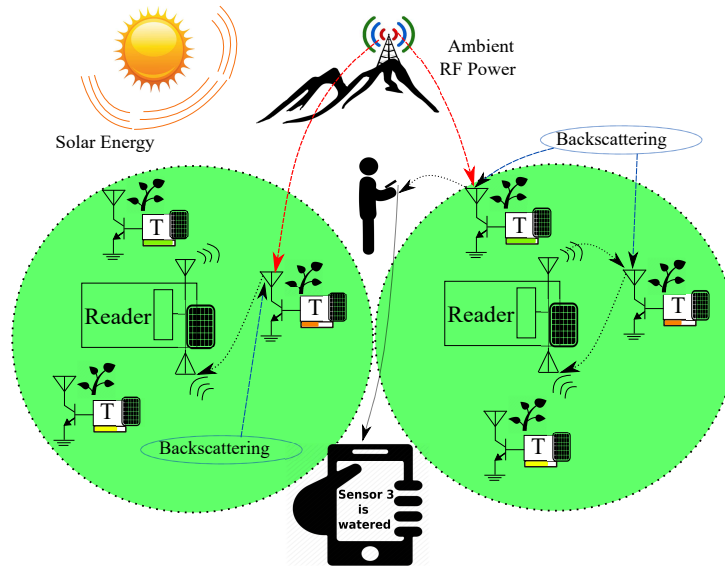
Figure 1.1: Precision agriculture: 80-85% of total water is consumed for agriculture purposes, thus, intelligent plant irrigation that could save even a small amount of water, e.g., 30%, would offer significant socioeconomic impact.

- healthcare: patient identification and authentication, patient tracking, and patient data collection,

- building management systems: smart homes, smart museums and gyms,

- environmental sensing: precision agriculture, smart farming, environmental monitoring, and environmental variables data collection,

- personal and social: social networking, thefts, losses, and historical queries.

Fig. 1.1 discusses the socioeconomic impact of precision agriculture that belongs to the class of environmental sensing applications.

Each application has specific requirements in terms of: latency, throughput, communication range, energy, scalability, and security. Depending on the intended application, designers may have to make a trade-off among these requirements to achieve a good balance in terms of cost versus benefits.

To attain full functionality and deliver high-quality services to IoT customers, IoT integrates six key elements.

- Identification: name and match services according to their demand.

- Sensing: data gathering from related objects/sensors within the network along with the transmission of the collected information to a data warehouse, database, or cloud.

- Communication: connectivity establishment between heterogeneous objects to deliver specific services. IoT devices should be low-power and offer resiliency against communication errors.

- Computation: Processing units (e.g., micro-controllers, microprocessors), software and cloud platforms, and software applications constitute the computational resources of IoT.

- Services: IoT services depend on the IoT application.

- Semantics: the ability (a) to discover and use resources and modeling information and (b) to recognize and analyze data for efficient decision making, in order to provide the required services.

To this end, it is worth noting that by the end of 2020, 212 billion IoT smart objects are expected to be deployed globally [4]. Furthermore, the whole annual economic impact caused by the IoT is estimated to be in the range of 2.7 trillion to 6.2 trillion dollars by 2025 [5].

1.2 Background and Motivation

It is apparent that RFID systems lie at the heart of IoT—the majority of low-power IoT devices in many applications are RFID tags [1–3]. RFID tags emit information wirelessly through the *backscatter principle* (or simply scatter principle) [6]: A carrier wave (CW) illuminator emits a radio frequency (RF) continuous CW signal, which in turn impinges on the antenna of an RF tag. The tag terminates its antenna load according to the data to be transmitted in order to modulate the information on top of the impinged signal. The incident signal is modulated and scattered back towards a reader (interrogator) for decoding and processing. Fig. 1.2 illustrates the concept of backscatter principle.

First, basic scatter radio principles are revisited from electromagnetic theory to obtain a basic idea of how scatter radios work and what their main characteristics are. The backscattered electric field values of a tag alternating its antenna termination between M loads $\{Z_i\}_{i=0}^{M-1}$ can be expressed as [7]:

$$\vec{E}_m = \vec{E}_0 \left(A_s - \Gamma_{m-1} \right), \quad m = 1, 2, \ldots, M, \tag{1.1}$$

where $\vec{E}_0$ is the load-independent backscattered field, A_s is the antenna structural mode term, Γ_{m-1}, $m = 1, 2, \ldots, M$, are the reflection coefficients corresponding to the M an-
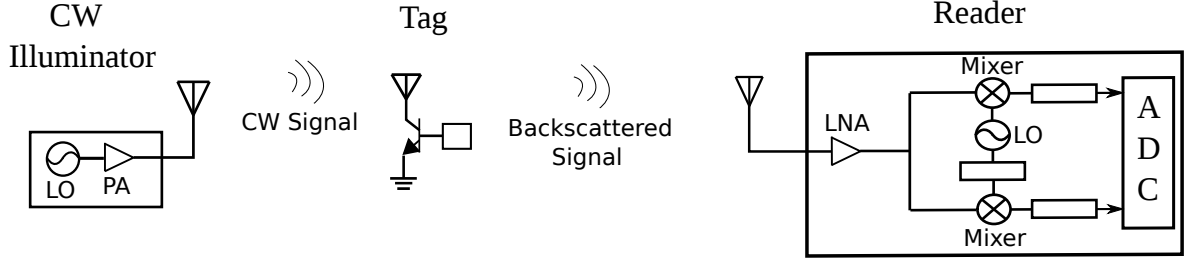
Figure 1.2: The principle of scatter radio: CW illuminator may be co-located with the reader or dislocated from the reader. Abbreviations LO, PA, LNA, and ADC, stand for local oscillator, power amplifier, low-noise amplifier, and analog-to-digital converter, respectively.

tenna loads and can be expressed as

$$\Gamma_i = \frac{\mathsf{Z}_i - \mathsf{Z}_\mathrm{a}^*}{\mathsf{Z}_i + \mathsf{Z}_\mathrm{a}}, \quad i = 0, 1, \ldots, M - 1, \tag{1.2}$$

where Z_a is the antenna impedance. The most common choice in scatter radio is $M = 2$ load values, but extension to more than 2 loads can be found in [8, 9].

Since backscatter radios reflect the incident signal without actively radiating, the energy cost for scattering operation needs to be carefully evaluated. The energy cost required for backscattering is due to the termination of the antenna between load values, i.e., backscattering can be realized by the alternation of a simple RF transistor switch. In addition, a very simple logic unit is embedded at the tags, in order to decide the modulation type and the transmitted bit sequence according to the sensed data. Overall, due to the absence of active signal conditioning components, scatter radio communication demands ultra-low power consumption, in the order of 10 μWatt [10], and at the same time requires low monetary cost.

Depending on the modulation, tags alter their antenna load accordingly. For instance, for amplitude-shift keying (ASK), the tag terminates its antenna at load Z_0 or Z_1 depending on the transmitted bit "0" or "1" over a bit duration T [11]. Whereas, for frequency-shift keying (FSK), the tag alternates the antenna load between Z_0 and Z_1 over a bit duration T with rate f_0 for bit "0" and rate f_1 for bit "1" [12]. More sophisticated continuous-phase modulations at tags, such as minimum shift-keying, are designed in [13].

Reflection coefficients Γ_0 and Γ_1 highly affect the performance of scatter radio systems in terms of both bit error rate (BER) as well as in terms of RF harvested energy, explained subsequently. Particularly, increasing the absolute difference of Γ_0 and Γ_1, i.e., the quantity $|\Gamma_0 - \Gamma_1|$, the amplitude of the backscattered signal is magnified and thus, the corresponding received signal-to-noise ratio (SNR) is increased (equivalently the BER

is decreased) [14]. On the other hand, the larger the quantity $|\Gamma_0 - \Gamma_1|$ is, the smaller the amount of power available to the tag from the CW incident signal becomes , because the power transfer efficiency from the antenna to the RF harvesting circuit decreases [15]. Thus, an interesting trade-off arises on how the designer should choose parameters Γ_0 and Γ_1 [7], and this clearly depends on the studied scatter radio application.

On the other side, Marconi radios (e.g., our cellphones) consist of signal conditioning RF components, such as amplifiers, mixers or active filters, and thus the total energy consumption and monetary cost becomes much larger compared to scatter radio communication.

While many RFID applications have already been established in practice, the potential of scatter radio technology envisions even more applications requiring ultra-low-power IoT devices with few meters communication ranges, e.g., healthcare [1, 3], smart buildings [16], and environmental sensing [17–19], as well as many others. Target applications include scenarios where traditional Marconi radios cannot achieve the desired communication ranges and meet the minimum power consumption constraints within the desired weight/size requirements [20]. The aforementioned class of applications incorporates two aspects: (a) prolonged sensor battery lifetime with almost fully autonomous sensor operation and (b) high reliability and several meters tag-to-reader communication range. Unfortunately, the provided performance of current RFID technology is still limited compared to the demands for large tag-to-reader ranges and high reliability.

The dissertation is motivated by the fact that the status quo of current ultra-low-power IoT technology can be significantly empowered by the following points of view:

- **Semi-Passive Tags**

  RFID systems utilize *passive tags*, i.e., tags powered by the illuminating RF field. The main drawback of current RFID technology is the limited tag-to-reader range, currently on the order of a few meters [21, 22]. The principal reasons of such poor communication ranges are: (a) the limited passive tag sensitivity due to stringent power limitations [15] and (b) the fact that the illuminating signal from the reader is used for both powering and communication of the tag.

  On the other hand, *semi-passive tags*, i.e., tags powered from external power or ambient sources, are more suitable for increased scatter radio communication ranges [13]. As the modulation at tags requires only the termination of the tag/sensor antenna at different loads, ultra-low power is required for (uplink) communication purposes. Such small amount of power can be available from a battery or a supercapacitor [17] or an ambient source, such as solar, RF or their combination [23].
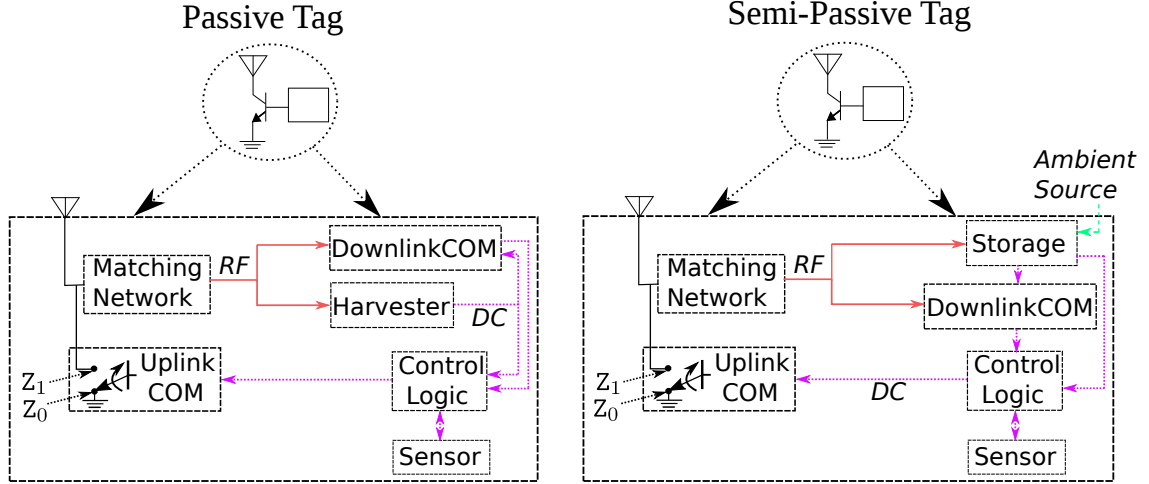
Figure 1.3: Passive versus semi-passive tag. The first is powered only through the RF harvested energy scavenged from incident CW signal, while the second is powered through an ambient source or through a storage unit that may be a battery or super-capacitor.

Fig. 1.3 illustrates the circuit components of passive and semi-passive tags. The matching network is responsible for reducing the transmission loss from the antenna, while the control logic is the "brain" of the tag, determining the tag's communication operations through software or hardware resources. Note that the storage unit may contain a harvesting circuit responsible for charging a battery or a super-capacitor, or alternatively, the powering can be accomplished by an external ambient source.

- **Realistic Signal and Wireless Channel Scatter Radio Model**

  The vast majority of the works conducting physical layer research on scatter radio assumes Rayleigh fading for CW illuminator-to-tag and tag-to-reader links [24–26]. Small-scale fading channel models with line-of-sight LoS component, such as Nakagami or Rician fading [27], are more appropriate for fading modeling in scatter radio. That assumption is made because wireless scatter radio links are usually subject to strong LoS signal, due to the relatively small distance involved. Hence, a major goal of this dissertation is to incorporate realistic small-scale fading channel models in scatter radio wireless model.

  In practice, path-loss is a major source of signal attenuation in scatter radio links, e.g., CW illuminator-to-tag-to-reader compound link is in practice extremely power-limited due to strong power loss. Thus, it becomes imperative to incorporate path-loss-related parameters in scatter radio wireless model, especially for systems operating with multiple tags, because, in practice, the power level of signals backscattered from multiple tags is highly different, e.g., it may differ by several dBs. Existing

works in scatter radio neglect the impact of different path-losses across different tags in their analysis and, for that reason, this dissertation will attempt to evaluate multi-tag performance metrics by embodying the impact of path-loss in wireless scatter radio models.

For scatter radio systems with passive tags, e.g., RFID systems, the energy outage events at tags have to be accounted on the signal model. An energy outage event occurs if the incident RF illuminating power at the tag is below its sensitivity power threshold, i.e., the minimum power level for the tag to harvest adequate power to operate. Note from Fig. 1.3-Left, that if the RF power at the output of matching network is below the RF harvester's sensitivity, then the passive tag is not able to backscatter. State-of-the-art passive RFID tags exhibit sensitivities around only -22 dBm [28]. The dissertation aims to seek the parameters affecting the energy outage in passive tags scenarios trying to provide an in-depth analysis.

- **Impact of Nonlinear RF Harvesting Efficiency**

Passive (and energy-assisted) IoT devices power their electronics (charge their storage units) by collecting the incident RF power over a specific time period. RF harvesting significantly determines the overall performance of passive devices in many aspects—without adequate energy to power their electronics, IoT devices cannot operate. Even for energy-assisted devices exploiting RF energy harvesting to charge their batteries, one would like to assess the expected charging time of the battery to the minimum level for proper operation. A variety of circuits in the microwave literature [29–31] has demonstrated three operation input RF power regimes, stemming directly from the presence of diodes in the rectifier circuits of RF harvester. First, for input power below the sensitivity of the harvester (i.e., the minimum required power for the harvester to operate), the harvested power is zero. Second, for input power between sensitivity and saturation threshold (the power level above which the output harvesting power saturates), the harvested power is a continuous, nonlinear, increasing function of input RF power, with response dependent on the operating frequency and the circuit components of the rectifier. Lastly, for input power above saturation, the output power of harvester is saturated, i.e., it is constant. Until the writing of this dissertation, prior art in communication theory studying RF energy harvesting, was completely neglecting the above three operation regimes and the harvested power was modeled as a linear function of input power. Any analysis involving such non-accurate modeling may offer results that probably deviate from reality. Hence, accurate modeling of RF harvested power as well as the extent of
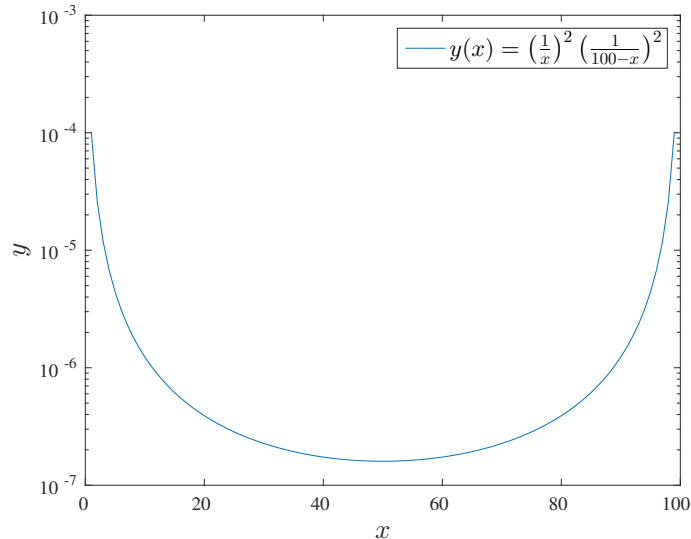
Figure 1.4: The asymmetries in scatter radio links can mitigate the large path-loss atten-
uation in scatter radio communications.

the mismatch between prior art and industry-level RF harvesting models deserves
further investigation.

- **Venture of Alternative Scatter Radio Network Architecture**

  Let us first present the following toy example: consider a scatter radio point-to-
  point scenario with a CW illuminator or carrier emitter (CE), a tag, and a reader
  placed co-linearly, i.e., CE and reader are dislocated. CE-to-reader range is 100
  meters and the tag is placed somewhere on the line segment formed by the CE
  and the reader. Suppose that x is the CE-to-tag distance. Then, for free-space
  propagation loss, the quantity $y(x) = \left(\frac{1}{x}\right)^2 \left(\frac{1}{100-x}\right)^2$ is proportional to the path-loss
  at the reader under backscattering operation, for $x \in (0, 100)$. Fig. 1.4 shows that
  function y is minimized at $x = 50$, while as x moves either towards 0 or 100, function
  y tends to increase. This simple example discloses that strong asymmetries in
  scatter radio link—even for free-space model—can offer 2 orders of magnitude larger
  path-loss compared to fully symmetric case of $x = 50$. The fully symmetric case
  corresponds also to the case where CE and reader are co-located, i.e., they belong
  to the same device. As a result, in order to realize ultra-low power and massive
  wireless connectivity in IoT without compromising on communication ranges, the
  scatter radio architecture needs to be redesigned.

  There are two different architectures for scatter radio systems, namely the monos-
  tatic and the bistatic architectures. In the monostatic architecture [32], the reader
  consists of both the CW illuminator and the receiver of signals reflected back from

the tags. In the bistatic architecture [33], the CW illuminator and the receiver of the reflected (backscattered) signals are distinct units, located at different positions, offering flexible network topologies with asymmetric scatter radio links. At the network level, the extension of bistatic architecture is the multi-bistatic (or simply multistatic) architecture with several low-cost CEs available, two orders of magnitude cheaper than the reader. Simple intuition as well as the observation from Fig. 1.4 indicate that due to the morphology of the multistatic architecture, each tag can be close to a CE with high probability, offering two desired implications: (a) the tag-to-reader coverage is increased with high probability and (b) using passive tags that harvest RF energy from the illuminating emitters, the probability of energy outage during the energy harvesting phase can be decreased. A detailed comparison among these two scatter radio architectures will be the subject of a chapter in this dissertation.

- **Resource Allocation in Backscatter Sensor Networks**

  Wireless sensor networks (WSNs) have been emerged as a notorious framework to support any environmental sensing application. The key components of low-power, large-scale WSNs are: (a) the ultra-low-power devices (sensors) that sense and send the data and (b) the fusion centers (cores) that gather the measured data and cooperate with each other for data extraction, state estimation, or smart decision making. To achieve the ultimate goal of WSNs, i.e., extended coverage, high-scalability, and complete energy autonomy, any type of resource allocation at the cores or the sensors is prerequisite.

  Current research trend [13, 31, 34–36] advocates backscatter radio as a candidate, key-enabling technology for future ultra-low-power, large-scale WSNs. Exploiting the aspects discussed in the previous paragraphs, a sequel of recent works in scatter radio, targeting directly on WSN applications, has experimentally demonstrated more than one hundred meters tag-to-reader communication ranges [37–39]. As the scatter radio is capable to confront the issue of limited range, scatter radio tags could replace the conventional ultra-low-power sensors, leading to the notion of multi-cell backscatter sensor networks (BSNs), where each core forms a backscatter cell and decodes the signals from the tags within its cell. Any resource allocation algorithm executed at the cores of BSNs should respect the peculiarities of the scatter radio wireless and signal model.

  However, as multi-cell BSNs are completely unexplored topic up to this time, capitalizing upon point-to-point scatter radio prior art and designing signal reception

algorithms as well as resource allocation algorithms that both account the idiosyncrasies of multi-cell BSNs would be an interesting research avenue.

1.3 Objectives

In order to offer a tangible improvement of IoT technology under the prism of wireless communications and networking, the objectives of this dissertation are:

1. Accurate RF energy harvesting analytical tools for ultra-low-power IoT devices equipped with any rectifier circuit.

2. Enhanced scatter radio receiver designs for extended tag-to-reader communication ranges, which could be harnessed with ultra-low complexity at current and future ultra-low-power IoT devices.

3. New scatter radio network architecture with extended coverage and reliability that could potentially leverage the adoption of scatter radios in network-based, ultra-low-power IoT applications.

4. Resource allocation for multi-cell backscatter sensor networks that will reduce installation cost and extend network coverage of future environmental sensing applications.

For each of the above topics a unique chapter is devoted.

1.4 Contributions and Organization

The contributions of each chapter can be summarized as follows:

- **Chapter 2** offers nonlinear far field RF energy harvesting in wireless communications. A linear RF harvesting model is commonly assumed in recent simultaneous wireless information and power transfer (SWIPT) research, i.e., RF harvested power is assumed to be a scaled version of the input (received) power. However, rectifiers typically used in the microwave and RFID industry are nonlinear devices; thus, RF harvesting efficiency is not constant, but depends on the input power. To approximate the real energy harvesting model, a piece-wise linear approximation is proposed, amenable to closed-form and tuning-free modeling. Three example scenarios are considered, including duty-cycled (non-continuous), as well as continuous SWIPT, comparing linear with industry-level non-linear RF harvesting. It is

demonstrated that the proposed methodology, even though simple, offers exact performance for all studied metrics. On the other hand, linear RF harvesting models offer results that deviate from reality, and in some cases are off by one order of magnitude.

- **Chapter 3** proposes physical layer receiver designs for scatter radio point-to-point systems. We provide a detailed exposition of a scatter radio signal model that accounts for all microwave, tag-related, and wireless channel parameters of FSK modulation at tags. The latter is ideal for the power-limited regime, which in turn is the operating regime of ultra-low-power IoT devices. Coherent and noncoherent detection and decoding algorithms tailored to the scatter radio FSK signal model are designed. For fixed energy budget per packet, noncoherent schemes do not sacrifice energy per information bit as the requirement for training bits of coherent schemes (for channel estimation) at the packet preamble is eliminated. Noncoherent symbol-by-symbol and sequence detectors based on hybrid composite hypothesis test (HCHT) and generalized likelihood-ratio test (GLRT), for the uncoded case and noncoherent decoders based on HCHT, for small block-length channel codes, are derived. Small block-length reduces significantly the processing delay at the reader when multiple tags need to be processed simultaneously. Diversity order analysis under a fully interleaved coherent coded system reveals that the offered diversity order of maximum-likelihood (ML) decoder for scatter radio FSK is the same with ML text-book decoders of Marconi radios. BER performance comparison under Rician, Rayleigh or no fading, taking into account fixed energy budget per packet is presented. It is shown that the performance gap between coherent and noncoherent reception depends on what channel codes are employed, the fading conditions (e.g., Rayleigh vs Rician vs no fading), as well as the utilized coding interleaving depth; the choice of one coding scheme over another depends on the wireless fading parameters and the design choice for extra diversity vs extra power gain. Finally, experimental outdoor results at 13 dBm transmission power corroborate the practicality of the proposed detection and decoding techniques for extended range scatter radios.

- **Chapter 4** compares two scatter radio network architectures. Specifically, monostatic and multistatic scatter radio network architectures are evaluated and contrasted in terms of several multi-tag performance metrics. The dyadic Nakagami fading model is employed to model the small-scale fading in scatter radio links and the path-loss is also incorporated in the power of fading random variables, filling a gap in the literature. Maximum-likelihood coherent and noncoherent BER, diversity

order, average information and energy outage probability comparison is performed, under the dyadic Nakagami fading. The proposed closed-form expressions for average energy and information outage probability are evaluated over an ensemble of square grid topologies, offering a topology-independent performance assessment. Judicious simulation study over realistic small-scale fading and path-loss models reveals that not only the BER decay is doubled in a multistatic architecture compared to a monostatic one, but also, energy and information outage events are less frequent in multistatic systems due to the flexible morphology of the multistatic architecture. It is shown that the multistatic architecture can offer very low BER in fully asymmetric scatter radio network topologies where monostatic architecture cannot be defined. As a contribution of [40], a proof-of-concept digital multistatic, scatter radio WSN with a single receiver, four low-cost emitters and multiple ambiently-powered, low-bitrate tags, is experimentally demonstrated (at 13 dBm transmission power), covering an area of 3500 m^2.

- **Chapter 5** focuses on multi-cell backscatter sensor networks (BSNs), consisting of few cores that employ conventional Marconi radio technology and act as fusion centers, as well as scatter radio sensors that are responsible for measuring environmental quantities and transmission of the sensed information towards the cores. A complete multi-cell scatter radio signal and wireless model is offered incorporating path-losses, tag- and microwave-related parameters over a dyadic Rician fading channel. A new multi-tag channel estimation closed-form solution is proposed based on a linear minimum mean-squared error (LMMSE) estimator. The average long-term signal-to-interference-plus-noise ratio (SINR) of maximum-ratio combining (MRC) and zero-forcing (ZF) linear detectors is found and subsequently harnessed to allocate frequency sub-channels at tags. The proposed resource allocation algorithm is based on the Max-Sum algorithm, obtained from the inference literature, adhering to simple message-passing update rules. The algorithm is very lightweight and converges to the optimal solution within very few iteration steps. Detailed simulation results reveal that the ZF detector is more suitable for large-scale BSNs when multiple receiver antennas can be exploited at the receiver side, capable to cancel out the intra-cell interference. It is found that the proposed Max-Sum algorithm offers remarkable convergence-complexity trade-off as it is very lightweight and converges to the desired optimal solution very quickly.

Finally, **chapter 6** contains the dissertation's concluding remarks and examines future research directions.

Chapter 2

Nonlinear Far Field RF Energy Harvesting Analysis

This chapter focuses on far field RF energy harvesting in contemporary wireless communications systems. In contrast to the vast majority of wireless communications RF harvesting prior art which neglects the nonlinearities imposed by the presence of the diodes in rectifier circuits, we model the RF harvested power as an arbitrary nonlinear, continuous, and non-decreasing function of received power, taking into account sensitivity and saturation effects. To approximate the real energy harvesting model, a piece-wise linear approximation is proposed, amenable to closed-form and tuning-free modeling. Three performance metrics are examined, comparing how close to real industry-level nonlinear RF harvesting is the proposed piece-wise linear approximation versus the linear baseline RF harvesting models from prior art. It is demonstrated that the proposed methodology, even though simple, offers exact performance for all studied metrics. On the other hand, linear RF harvesting modeling results deviate from reality, and in some cases the gap is more than an order of magnitude. The material of this chapter is filling a gap in recent wireless communications RF harvesting literature, opening new research avenues for practical RF harvesting in Internet-of-Things.

Related Work

Simultaneous wireless information and power transfer (SWIPT) literature within the wireless communications theory research community has mainly studied protocol architecture problems as well as fundamental performance metrics. Protocols that split time or power among RF energy harvesting and information transfer modules within a radio terminal are studied in [41], so that specific communication tasks are performed, while the radio ter-
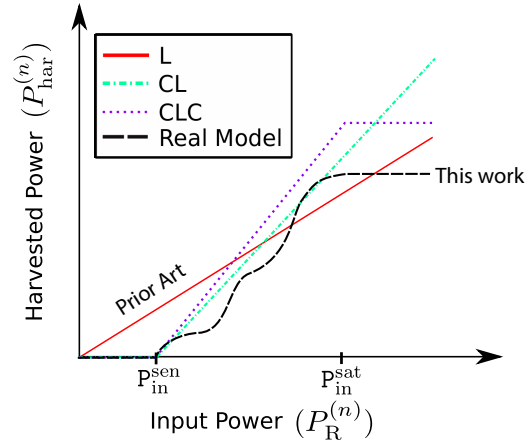
Figure 2.1: Harvested power versus input power for the baseline models. Also an arbitrary harvesting model is depicted where harvested power is an increasing function of input power.

minal is solely powered by the receiving RF signal. The aspect of wireless power transfer in wireless communication imposes additional energy harvesting constraints [42]. Multi-user orthogonal frequency-division multiplexing (OFDM) systems with SWIPT-based resource allocation algorithms have been proposed in [43, 44]. The objective in [45] is to maximize the total harvested power at the energy harvesting receiver under minimum required signal-to-interference-plus-noise ratio (SINR) constraints, whereas the authors in [46] study the minimization of total transmit power under energy harvesting and minimum required signal-to-interference-plus-noise constraints. Both [45, 46] formulated the underlying optimization problems as semidefinite programs and solved them with standard convex optimization algorithms. The above works are a small sample of existing RF harvesting literature in wireless communications, which is vastly evolving. Recent reviews such as in [47–51], offer the current perspective of the wireless communications theory community in RF harvesting.

RF energy harvesting suffers from limited available density issues, typically in the regime of sub-microWatt incident RF power, e.g., work in [52] reports 0.1μWatt/cm^2 from cellular GSM base stations. In sharp contrast, other ambient energy sources like sun, motion or electrochemistry can offer high density power.[1] Such limited RF density in RF energy harvesting can power only ultra low-power devices in continuous (non-duty-cycled) operation or low-power devices, such as low-power wireless sensors in delay-limited, duty-cycled operation, since sufficient RF energy must be scavenged before operation. That

---

[1]For example, sun can offer 35mW/cm^2 using a low-cost 5.4 cm × 4.3 cm polycrystalline blue solar cell [53], while electric potential across the stem of a 60 cm-tall avocado plant can offer 1.15μWatt at noon time [18].

is due to the fact that far field wireless power decreases very fast with distance, e.g., with the second power of distance in free space, while RF harvesting circuits have limited sensitivity as well as efficiency (explained in more detail subsequently).

The most critical component of far field RF harvesting circuits is the rectenna, i.e., the antenna and the rectifier that converts the input RF signal to DC voltage. The rectifier circuit usually consists of one or multiple diodes, imposing strong nonlinearity on the conversion of power. It has been noticed that the rectifier circuit operates in three input RF power regimes, stemming directly from the presence of diodes. First, for input power below the *sensitivity* of the harvester (i.e., the minimum power for harvesting operation), the harvested power is zero. Second, for input power between sensitivity and saturation threshold (the power level above which the output harvesting power saturates), the harvested power is a continuous, nonlinear, increasing function of input RF power, with response depending on the operating frequency and the circuit components of the rectifier. Lastly, for input power above saturation, the output power of harvester is saturated, i.e., it is constant. The above three characteristic regimes are depicted in Fig. 2.1, with the black-dashed line curve, which adhere to a variety of circuits in the microwave literature [29–31]. The nonlinearity of harvested power as a function of input power is also verified by the fact that conversion *efficiency* in the microwave circuits literature is always referenced to specific level of input power. Unfortunately, the vast majority of recent communications theory SWIPT papers, for simplification purposes, adopts linear input-output models for harvested power as a function of input RF power, also depicted with red-solid curve in Fig. 2.1.

A diode-based rectifier and broadband rectenna are designed in [54] for energy harvesting from ambient RF signals, while work in [55] designed monopole dual-band antenna for RF energy harvesting. The authors in [29] study far field powering issues for low-power and low-duty cycle wireless sensors with low incident power density; rectenna designs are also proposed. Work in [56] demonstrated conversion efficiencies on the order of 85% operating at 40 dBm input power. Such input power values are very infrequent in practical far field RF energy harvesting, because input power usually cannot exceed 0 to 10 dBm. Work in [57] has demonstrated efficiencies on the order of 10% at −10 dBm input power, while rectenna designs for batteryless backscatter sensor networks offering efficiency 28% at −20 dBm input power can be found in [31].

Contributions

This chapter contributes to far field RF energy harvesting in the following aspects:

- For the first time in the wireless communications literature, harvested power can be modeled as an arbitrary nonlinear, continuous, and non-decreasing function of input RF power, accounting for: (*i*) the nonlinear efficiency of realistic rectenna and RF harvesting circuits, (*ii*) the zero response of energy harvesting circuit for input power below sensitivity, and (*iii*) the saturation effect of harvested power. Two conversion efficiency models from prior art circuits are used as examples and compared to linear (baseline) models.

- A piece-wise linear approximation of the actual harvested power is harnessed to calculate/approximate harvested power probability density function (PDF) and cumulative distribution function (CDF) statistics; harvested power is the product of the nonlinear harvesting efficiency and the input power. It is found that for choosing the data points in the utilized approximation uniformly, to achieve approximation accuracy at least ϵ, at most $\mathcal{O}(\sqrt{1/\epsilon})$ number of data points is required.

- Three performance metrics are studied: (i) expected harvested energy at the receiver, (ii) expected charging time at the receiver (time-switching scenario), and (iii) successful reception at interrogator for passive RFID tags (power-splitting scenario). What can be attributed as the most important contribution of this chapter is the demonstration that the proposed methodology offers *exact performance* with the real, arbitrary nonlinear energy harvesting model for all studied metrics, without requiring tuning of any parameter. On the contrary, linear RF harvesting modeling results deviate from reality, and in some cases they deviate from the real model by one order of magnitude.

Organization and Notation

The rest of this chapter is organized as follows. Section 2.1 introduces the channel model, Section 2.2 presents fundamentals of far field RF energy harvesting, explaining the inherent nonlinearity in real energy harvesting models. Section 2.3 presents the proposed approximation methodology, while Section 2.4 compares baseline, linear harvesting models used in prior art with the nonlinear harvesting model, under three performance metrics.

The set of natural and real numbers is denoted as $\mathbb{N}$ and $\mathbb{R}$, respectively. For natural number $N \in \mathbb{N}$, set $\{1, 2, \ldots, N\}$ is denoted as $[N] \triangleq \{1, 2, \ldots, N\}$. Symbol $\odot$ stands for the component-wise (Hadamard) product and $(\cdot)^\top$ denotes the transpose of a vector. Notation $\mathcal{CN}(0, \sigma^2)$ stands for circularly-symmetric complex Gaussian distribution of variance σ^2. For a continuous random variable (RV) x, supported over interval set $\mathcal{X}$, the corresponding PDF and CDF is denoted as $\mathsf{f}_x(\cdot)$ and $\mathsf{F}_x(x_0) = \int_{y \in \mathcal{X}: y \leq x_0} \mathsf{f}_x(y) \mathsf{d}y$,

respectively. The expectation and variance of $\mathsf{g}(x)$ is denoted as $\mathbb{E}[\mathsf{g}(x)]$ and $\mathsf{var}[\mathsf{g}(x)] \triangleq \mathbb{E}[(\mathsf{g}(x) - \mathbb{E}[\mathsf{g}(x)])^2]$, respectively. The Dirac delta function is denoted as $\Delta(\cdot)$. The probability of event $\mathcal{A}$ is denoted as $\mathbb{P}(\mathcal{A})$. For a function g, **domg** denotes its domain.

2.1 Wireless System Model

A source of radio frequency (RF) signals illuminates with wireless power an information and far field RF energy harvesting (IEH) terminal. A dedicated power source is assumed for the source of RF signals, while the far field IEH terminal harvests RF energy from the incident signals on its antenna and can operate as information transmitter or receiver.

Narrowband transmissions are considered over a quasi-static flat fading channel. The downlink received signal at the output of matched filter at IEH terminal for a single channel use is given by:

$$y = \sqrt{P_\mathrm{T}\, T_\mathrm{s}\, \mathsf{L}(d)}\, h\, s + w, \tag{2.1}$$

where s is the transmitted symbol, with $\mathbb{E}[s] = 0$ and $\mathbb{E}\left[|s|^2\right] = 1$, P_T is the average transmit power of RF source, T_s is the symbol duration, h is the complex baseband channel response, $\mathsf{L}(d)$ is the path-loss coefficient at distance d, and $w \sim \mathcal{CN}(0, \sigma_\mathrm{d}^2)$ is the additive white complex Gaussian noise at the IEH receiver.

A block fading model is considered and the channel response changes independently every coherence block of T_c seconds. Symbol $h^{(n)}$ denotes the complex baseband channel response at the n-th coherence block. Every coherence block, RF source transmits a packet whose duration spans T_p seconds, which in turn spans several symbols, with $T_\mathrm{p} \leq T_\mathrm{c}$. During the n-th coherence time block, the received RF input power (simply abbreviated as *input power*) at the IEH terminal is given by:

$$P_\mathrm{R}^{(n)} = \mathbb{E}\left[|s|^2\right] P_\mathrm{T}\, \mathsf{L}(d)\, \left|h^{(n)}\right|^2 = \mathsf{P}(d)\gamma^{(n)}, \tag{2.2}$$

where $\mathsf{P}(d) \triangleq P_\mathrm{T}\, \mathsf{L}(d)$ and $\gamma^{(n)} \triangleq \left|h^{(n)}\right|^2$. Note that $P_\mathrm{R}^{(n)}$ is a function of $\gamma^{(n)}$, i.e., $P_\mathrm{R}^{(n)} \equiv P_\mathrm{R}^{(n)}(\gamma^{(n)})$. Due to the definition of channel coherence time block, RVs $\left\{h^{(n)}\right\}$, across different values of n, are independent and identically distributed (IID). It is also assumed that RVs $\gamma^{(n)}$ are drawn from a continuous distribution, denoted as $\mathsf{f}_{\gamma^{(n)}}(\cdot)$, supported over the non-negative reals, $\mathbb{R}_+$. Hence, the corresponding distribution of $P_\mathrm{R}^{(n)}$ has a continuous density in $\mathbb{R}_+$. For exposition purposes, for any natural number N, the vector of input power coefficients up to coherence block N is defined as $\mathbf{p}_N \triangleq \left[P_\mathrm{R}^{(1)}\ P_\mathrm{R}^{(2)}\ \ldots P_\mathrm{R}^{(N)}\right]^\top$.

The results for the PDF and the CDF of harvested power will be offered without having in mind a specific type of fading distribution. For specific numerical results, Nakagami

fading will be considered, as it can describe small-scale wireless fading under both line-of-sight (LoS) or non-line-of-sight (NLoS) scenarios. Under Nakagami fading, the PDF of $\gamma^{(n)}$ follows Gamma distribution with shape parameters $\left(\mathtt{m}, \frac{\Omega}{\mathtt{m}}\right)$, i.e.,

$$\mathsf{f}_{\gamma^{(n)}}(x) = \left(\frac{\mathtt{m}}{\Omega}\right)^{\mathtt{m}} \frac{x^{\mathtt{m}-1}}{\Gamma(\mathtt{m})} \mathsf{e}^{-\frac{\mathtt{m}}{\Omega}x}, \quad x \geq 0, \tag{2.3}$$

where $\Gamma(x) = \int_0^\infty t^{x-1} \mathsf{e}^{-t} \mathsf{d}t$ denotes the Gamma function, while Nakagami parameter $\mathtt{m}$ has to satisfy $\mathtt{m} \geq \frac{1}{2}$. Fading power parameter Ω satisfies $\Omega = \mathbb{E}\left[\left|h^{(n)}\right|^2\right] = \mathbb{E}\left[\gamma^{(n)}\right]$. For the special cases of $\mathtt{m} = 1$ and $\mathtt{m} = \infty$, Rayleigh and no-fading is obtained, respectively. For $\mathtt{m} = \frac{(\kappa+1)^2}{2\kappa+1}$ the distribution in Eq. (2.3) is approximated by Rice, with Rician parameter κ [27]. The corresponding CDF of $\gamma^{(n)}$ is given by:

$$\mathsf{F}_{\gamma^{(n)}}(x) = 1 - \int_x^\infty \mathsf{f}_{\gamma^{(n)}}(y) \mathsf{d}y = 1 - \frac{\Gamma\left(\mathtt{m}, \frac{\mathtt{m}}{\Omega}x\right)}{\Gamma(\mathtt{m})}, \quad x \geq 0, \tag{2.4}$$

where $\Gamma(\alpha, z) = \int_z^\infty t^{\alpha-1} \mathsf{e}^{-t} \mathsf{d}t$ is the upper incomplete gamma function. For exposition purposes, $\Omega = 1$ is assumed and thus, input power $P_\mathrm{R}^{(n)}$ in Eq. (2.2) follows Gamma distribution with shaping parameters $\left(\mathtt{m}, \frac{\mathsf{P}(d)}{\mathtt{m}}\right)$.

2.2   Fundamentals of Far Field RF Energy Harvesting

This section offers fundamentals in RF energy harvesting, filling a gap largely overlooked in recent wireless communications theory prior art. The principal component of the far field RF energy harvesting circuits is the *rectenna*, i.e., antenna and rectifier, that converts the incoming AC RF signal to DC under a completely nonlinear operation, commonly realized by one or more diodes. The efficiency is improved by increasing the number of diodes, but at the same time, the sensitivity of the harvester is reduced. Fig. 2.2 depicts typical examples of rectifier circuits found in the literature. Matching network is responsible for reducing the transmission loss from the antenna. A boost converter usually follows the rectifier, in order to amplify the required voltage and also offer maximum power point tracking (MPPT), exactly because the output of the rectifier is a nonlinear function of the rectifier input power $P_\mathrm{R}^{(n)}$. Accurately modeling the nonlinearities of the RF harvester becomes mandatory in information and wireless power transfer, and that motivates the work in chapter.
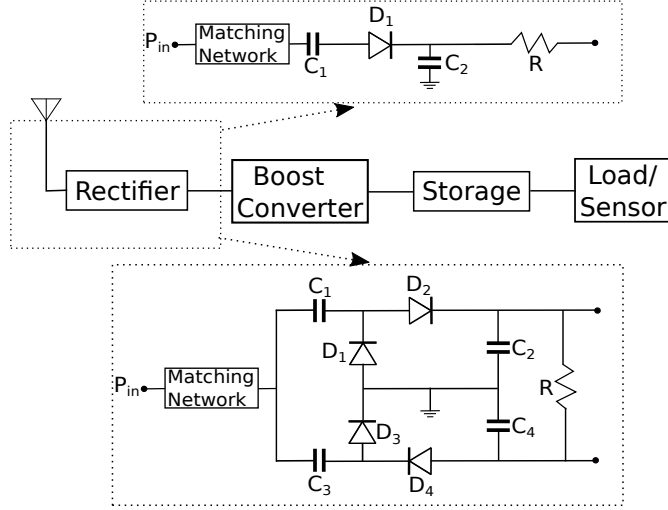
Figure 2.2: Architecture of far field RF energy harvesters. Typical rectifier circuits with a single diode [31] (upwards) or multiple diodes [58] (downwards) are also depicted, emphasizing the nonlinear relationship between harvested and input RF power.

2.2.1 Realistic Far Field RF Energy Harvesting Model

The harvested power at the output of the RF harvesting circuit is modeled as:

$$P_{\text{har}}^{(n)} \equiv P_{\text{har}}^{(n)}\left(P_{\text{R}}^{(n)}\right) = \mathsf{p}\left(P_{\text{R}}^{(n)}\right), \tag{2.5}$$

where

$$\mathsf{p}(x) \triangleq \begin{cases} 0, & x \in [0, \mathsf{P}_{\text{in}}^{\text{sen}}], \\ \eta(x) \cdot x, & x \in [\mathsf{P}_{\text{in}}^{\text{sen}}, \mathsf{P}_{\text{in}}^{\text{sat}}], \\ \eta(\mathsf{P}_{\text{in}}^{\text{sat}}) \cdot \mathsf{P}_{\text{in}}^{\text{sat}} & x \in [\mathsf{P}_{\text{in}}^{\text{sat}}, \infty). \end{cases} \tag{2.6}$$

Function $\eta\left(P_{\text{R}}^{(n)}\right)$ is the harvesting efficiency as a function of input power, defined over the interval $\mathcal{P}_{\text{in}} \triangleq [\mathsf{P}_{\text{in}}^{\text{sen}}, \mathsf{P}_{\text{in}}^{\text{sat}}]$. $\mathsf{P}_{\text{in}}^{\text{sen}}$ is the harvester's sensitivity and for any input power value smaller than the sensitivity the harvested power is zero, i.e., $\mathsf{p}(x) = 0$ for $x \leq \mathsf{P}_{\text{in}}^{\text{sen}}$. $\mathsf{P}_{\text{in}}^{\text{sat}}$ denotes the saturation power threshold of the harvester, after which the harvested power is constant.

The power harvesting function $\mathsf{p} : \mathbb{R}_+ \longrightarrow \mathbb{R}_+$ is assumed to be:

1. non-decreasing, i.e., $x < y \implies \mathsf{p}(x) \leq \mathsf{p}(y)$, and

2. continuous.

Note that the assumptions above, even though mild, are in full accordance with harvested power curves reported in the RF energy harvesting circuits prior art, e.g., [29–31, 59].
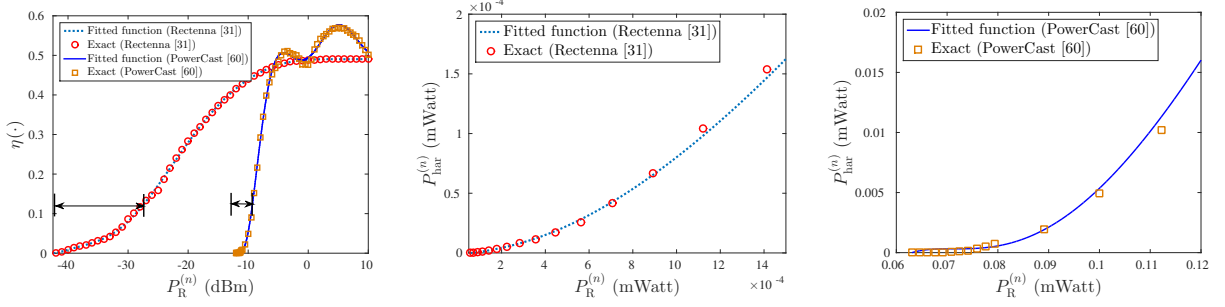
Figure 2.3: Left: Efficiency of RF harvesting circuit as a function of input power in dBm for (a) the rectenna proposed in [31], depicted with circles and (b) the PowerCast module [59] (at 868 Mhz), depicted with squares. Center (Right): Harvested power vs input power in mWatt for the range of input power values depicted with arrows in the left figure for the rectenna in [31] (module in [59]).

Fig. 2.3-Left shows two examples of RF harvesting efficiency as a function of input power in dBm (based on harvesting circuits in [31] and [59]), while Fig. 2.3-Center (Right) illustrates the harvested power as a function of input power in mWatt, for the rectenna in [31] (harvester in [59]) and the input power range marked with arrows in Fig. 2.3-Left. It can be clearly seen that output (harvested) power is a nonlinear function of the input power. The efficiency functions in Fig. 2.3 are represented as polynomials at the dBm domain, as follows:

$$\eta(x) = w_0 + \sum_{i=1}^{W} w_i (10\log_{10}(x))^i, \tag{2.7}$$

where x takes values in mWatt, W is the degree of the fitted polynomial in dBm, and $\{w_i\}_{i=0}^{W}$ are the coefficients of the polynomials. The degrees of the polynomials for the fitted functions are $W = 10$ and $W = 12$ for the models in [31] and in [59], respectively (depicted in Fig. 2.3 with dotted and solid curves, respectively). Moreover, input power intervals $\mathcal{P}_{\text{in}} = [10^{-4.25}, 10^{1.6}]$ and $\mathcal{P}_{\text{in}} = [10^{-1.2}, 10]$ (both in mWatt) are utilized for the efficiency models in [31] and [59], respectively.

2.2.2 Prior Art (Linear) RF Energy Harvesting Models

Three baseline models are considered for comparison:

Linear (L) Energy Harvesting Model

The first baseline model is the linear (L) model adopted by a gamut of information and wireless energy transfer prior art. For the linear baseline model, the harvested power (as

function of $P_{\mathrm{R}}^{(n)}$) is expressed as follows:

$$\widetilde{\mathsf{p}}_{\mathrm{L}}\left(P_{\mathrm{R}}^{(n)}\right) = \eta_{\mathrm{L}} \cdot P_{\mathrm{R}}^{(n)}, \ \forall P_{\mathrm{R}}^{(n)} \in \mathbb{R}_+, \tag{2.8}$$

with constant $\eta_{\mathrm{L}} \in [0,1)$. The functional form of harvested power in (2.8) is depicted in Fig. 2.1 with a red solid curve. This model ignores the dependence of RF harvesting efficiency on input power, the fact that the harvester cannot operate below the sensitivity threshold, and the fact that the harvested power saturates when input power level is above a power threshold.

Constant-Linear (CL) Energy Harvesting Model

The harvested power for the constant-linear (CL) baseline model is expressed as:

$$\widetilde{\mathsf{p}}_{\mathrm{CL}}\left(P_{\mathrm{R}}^{(n)}\right) \triangleq \begin{cases} 0, & P_{\mathrm{R}}^{(n)} \in [0, \mathsf{P}_{\mathrm{in}}^{\mathrm{sen}}], \\ \eta_{\mathrm{CL}} \cdot (P_{\mathrm{R}}^{(n)} - \mathsf{P}_{\mathrm{in}}^{\mathrm{sen}}), & P_{\mathrm{R}}^{(n)} \in [\mathsf{P}_{\mathrm{in}}^{\mathrm{sen}}, \infty), \end{cases} \tag{2.9}$$

with constant $\eta_{\mathrm{CL}} \in [0,1)$. The harvested power curve for the CL model is depicted with a dash-dotted line in Fig. 2.1. This model takes into account the fact that the RF harvester is not able to operate below sensitivity threshold $\mathsf{P}_{\mathrm{in}}^{\mathrm{sen}}$, but ignores that RF harvesting efficiency is a non-constant function of input power and that the harvested power saturates when the input power level is above $\mathsf{P}_{\mathrm{in}}^{\mathrm{sat}}$.

Constant-Linear-Constant (CLC) Energy Harvesting Model

For constant-linear-constant (CLC) baseline model, harvested power is expressed as function of input power $P_{\mathrm{R}}^{(n)}$ through the following expression:

$$\widetilde{\mathsf{p}}_{\mathrm{CLC}}\left(P_{\mathrm{R}}^{(n)}\right) \triangleq \begin{cases} 0, & P_{\mathrm{R}}^{(n)} \in [0, \mathsf{P}_{\mathrm{in}}^{\mathrm{sen}}], \\ \eta_{\mathrm{CLC}} \cdot (P_{\mathrm{R}}^{(n)} - \mathsf{P}_{\mathrm{in}}^{\mathrm{sen}}), & P_{\mathrm{R}}^{(n)} \in [\mathsf{P}_{\mathrm{in}}^{\mathrm{sen}}, \mathsf{P}_{\mathrm{in}}^{\mathrm{sat}}], \\ \eta_{\mathrm{CLC}} \cdot (\mathsf{P}_{\mathrm{in}}^{\mathrm{sat}} - \mathsf{P}_{\mathrm{in}}^{\mathrm{sen}}), & P_{\mathrm{R}}^{(n)} \in [\mathsf{P}_{\mathrm{in}}^{\mathrm{sat}}, \infty), \end{cases} \tag{2.10}$$

where constant $\eta_{\mathrm{CLC}} \in [0,1)$. The CLC model is depicted in Fig. 2.1 with a dotted curve and as can be noticed it ignores the nonlinear dependence of harvesting efficiency on input power.
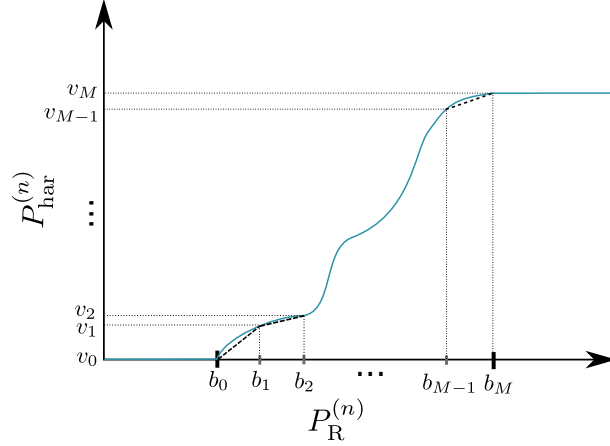
Figure 2.4: A graphical illustration of the proposed piece-wise linear approximation for an RF energy harvesting model, adhering to the mild assumptions of Section 2.2.1.

2.3   Statistics of Harvested Power

Consider the harvesting model in Eq. (2.6) where function $\mathsf{p}(\cdot)$ satisfies the assumptions of Section 2.2.1. A piece-wise linear approximation of function $\mathsf{p}(\cdot)$ over interval $\mathcal{P}_{\mathrm{in}}$ using a set of $M+1$ points is proposed.

Since harvested power $P_{\mathrm{har}}^{(n)}$ in (2.6) changes over the range of input power values $\mathcal{P}_{\mathrm{in}}$, a set of support points $\{b_m\}_{m=0}^M$ is defined, with $b_0 = \mathsf{P}_{\mathrm{in}}^{\mathrm{sen}}$, $b_{m-1} < b_m$, for $m \in [M]$, and $b_M = \mathsf{P}_{\mathrm{in}}^{\mathrm{sat}}$. The corresponding set of image points $\{v_m\}_{m=0}^M \triangleq \{\mathsf{p}(b_m)\}_{m=0}^M$ satisfy $v_{m-1} = \mathsf{p}(b_{m-1}) \leq \mathsf{p}(b_m) = v_m$, $m = 1, 2, \ldots, M$, with $v_0 = 0$ and $v_M = \mathsf{p}(\mathsf{P}_{\mathrm{in}}^{\mathrm{sat}})$. Without loss of generality, $0 = v_0 < v_1 < v_2 < \ldots < v_{M-1} < v_M = \mathsf{p}(\mathsf{P}_{\mathrm{in}}^{\mathrm{sat}})$ is assumed. A graphical illustration of the proposed methodology is provided in Fig. 2.4.

Given the $M+1$ points $\{b_m\}_{m=0}^M$ and $\{v_m\}_{m=0}^M$, slopes $l_m \triangleq \frac{v_m - v_{m-1}}{b_m - b_{m-1}}$, $m \in [M]$, are defined. The utilized methodology approximates function $P_{\mathrm{har}}^{(n)}$ in Eq. (2.6) through the following piece-wise linear function:

$$\widetilde{P}_{\mathrm{har}}^{(n)} = \widetilde{\mathsf{p}}\left(P_{\mathrm{R}}^{(n)}\right) \triangleq \begin{cases} 0 & P_{\mathrm{R}}^{(n)} \in [0, b_0], \\ l_m(P_{\mathrm{R}}^{(n)} - b_{m-1}) + v_{m-1}, & P_{\mathrm{R}}^{(n)} \in (b_{m-1}, b_m], \ \forall m \in [M], \\ v_M, & P_{\mathrm{R}}^{(n)} \in [b_M, \infty). \end{cases} \quad (2.11)$$

2.3.1   Statistics of $\widetilde{P}_{\mathrm{har}}^{(n)}$ and Approximation Error

This section offers the PDF and CDF of $\widetilde{P}_{\mathrm{har}}^{(n)}$. First, the following is defined:

$$\xi_m \triangleq \mathsf{F}_{P_{\mathrm{R}}^{(n)}}(b_m), \ m = 0, 1, \ldots, M, \quad (2.12)$$

where $\mathsf{F}_{P_{\mathrm{R}}^{(n)}}(\cdot)$ is the CDF of $P_{\mathrm{R}}^{(n)}$. In view of Eq. (2.11) it can be deduced that $\widetilde{P}_{\mathrm{har}}^{(n)} = 0$ with probability

$$\mathbb{P}\left(P_{\mathrm{R}}^{(n)} \leq b_0\right) = \int_0^{b_0} \mathsf{f}_{P_{\mathrm{R}}^{(n)}}(x)\mathrm{d}x = \mathsf{F}_{P_{\mathrm{R}}^{(n)}}(b_0) = \xi_0$$

$$\implies \mathsf{f}_{\widetilde{P}_{\mathrm{har}}^{(n)}}(x) = \xi_0\,\Delta(x), \ \ x = 0. \tag{2.13}$$

For any $m \in [M-1]$, when $P_{\mathrm{R}}^{(n)} \in (b_{m-1}, b_m]$, $\widetilde{P}_{\mathrm{har}}^{(n)} \in (v_{m-1}, v_m]$ holds. Thus, using the formula for linear transformations in [60] the following is obtained for any $m \in [M-1]$:

$$\mathsf{f}_{\widetilde{P}_{\mathrm{har}}^{(n)}}(x) = \frac{1}{l_m}\,\mathsf{f}_{P_{\mathrm{R}}^{(n)}}\!\left(\frac{x - v_{m-1} + l_m b_{m-1}}{l_m}\right), \ \ x \in (v_{m-1}, v_m]. \tag{2.14}$$

Note that the last interval $P_{\mathrm{R}}^{(n)} \in (b_{M-1}, b_M]$ requires special attention due to the fact that the inverse of function $\widetilde{\mathsf{p}}(\cdot)$ does not exist at point v_M. Restricting $P_{\mathrm{R}}^{(n)} \in (b_{M-1}, b_M)$, the following holds:

$$\mathsf{f}_{\widetilde{P}_{\mathrm{har}}^{(n)}}(x) = \frac{1}{l_M}\,\mathsf{f}_{P_{\mathrm{R}}^{(n)}}\!\left(\frac{x - v_{M-1} + l_M b_{M-1}}{l_M}\right), \ \ x \in (v_{M-1}, v_M). \tag{2.15}$$

Finally, in view of (2.11), $\widetilde{P}_{\mathrm{har}}^{(n)} = v_M$ with probability given by:

$$\mathbb{P}\left(P_{\mathrm{R}}^{(n)} \geq b_M\right) = 1 - \lim_{x \uparrow b_M} \mathsf{F}_{P_{\mathrm{R}}^{(n)}}(x) \overset{(a)}{=} 1 - \xi_M$$

$$\implies \mathsf{f}_{\widetilde{P}_{\mathrm{har}}^{(n)}}(x) = (1 - \xi_M)\,\Delta(x - v_M), \ \ x = v_M, \tag{2.16}$$

where (a) stems from the continuity of $\mathsf{F}_{P_{\mathrm{R}}^{(n)}}(\cdot)$ as an integral function of a continuous PDF [61], as well as the definition of ξ_M. The overall probabilistic description of $\widetilde{P}_{\mathrm{har}}^{(n)}$ is summarized through the following proposition.

Proposition 2.1. For any a given distribution of fading power $\gamma^{(n)}$, supported on $\mathbb{R}_+$, in view of Eq. (2.2), the corresponding distribution of input power, $P_{\mathrm{R}}^{(n)}$, is $\mathsf{f}_{P_{\mathrm{R}}^{(n)}}(x) = \frac{1}{\mathsf{P}(d)}\mathsf{f}_{\gamma^{(n)}}\!\left(\frac{x}{\mathsf{P}(d)}\right)$. The proposed approximation utilized for harvested power in Eq. (2.11) has PDF given by:

$$\mathsf{f}_{\widetilde{P}_{\mathrm{har}}^{(n)}}(x) = \begin{cases} \xi_0\,\Delta(x), & x = v_0 = 0, \\ \frac{1}{l_m}\,\mathsf{f}_{P_{\mathrm{R}}^{(n)}}\!\left(\frac{x - v_{m-1} + l_m b_{m-1}}{l_m}\right), & x \in (v_{m-1}, v_m]\backslash\{v_M\}, \ m \in [M], \\ (1 - \xi_M)\,\Delta(x - v_M), & x = v_M, \\ 0, & x \in \mathbb{R}\backslash[0, v_M]. \end{cases} \tag{2.17}$$

The corresponding CDF of $\widetilde{P}_{\mathrm{har}}^{(n)}$ is given by:

$$
\mathsf{F}_{\widetilde{P}_{\mathrm{har}}^{(n)}}(x) = \begin{cases} 0 & x < 0, \\ \mathsf{F}_{P_{\mathrm{R}}^{(n)}}\left(\frac{x - v_{m-1} + l_m b_{m-1}}{l_m}\right), & x \in [v_{m-1}, v_m] \backslash \{v_M\}, \ m \in [M], \\ 1, & x \geq v_M. \end{cases} \tag{2.18}
$$

Proof. The proof of Eq. (2.17) is immediate from Eqs. (2.13)–(2.16). The proof of Eq. (2.18) is given in Appendix 2.5. $\qquad\square$

As the next proposition asserts, the proposed approximation in Eq. (2.11) offers approximation error that decays quadratically with the number of utilized points, even for a uniform choice of points: $\{b_m\}$, i.e., $b_m = b_{m-1} + \delta_M$, $m \in [M]$, with uniform step size $\delta_M \triangleq \frac{\mathsf{P}_{\mathrm{in}}^{\mathrm{sat}} - \mathsf{P}_{\mathrm{in}}^{\mathrm{sen}}}{M}$.

Proposition 2.2 (Approximation Error with Uniform Point Selection)**.** Suppose that we choose $b_m = b_{m-1} + \delta_M$, $m \in [M]$, with δ_M defined as above. If function $\mathsf{p}(\cdot)$ is in addition continuously differentiable, then function $\widetilde{\mathsf{p}}(\cdot)$ in (2.11) restricted over $\mathcal{P}_{\mathrm{in}}$, approximates $\mathsf{p}(\cdot)$ in $\mathcal{P}_{\mathrm{in}}$ with absolute error that is bounded as:

$$
\int_{\mathcal{P}_{\mathrm{in}}} |\mathsf{p}(x) - \widetilde{\mathsf{p}}(x)| \, \mathsf{d}x \leq \frac{\mathsf{C}_{\mathsf{p}} \left(\mathsf{P}_{\mathrm{in}}^{\mathrm{sat}} - \mathsf{P}_{\mathrm{in}}^{\mathrm{sen}}\right)^3}{8 \, M^2}, \tag{2.19}
$$

where C_{p} is a constant independent of M.

Proof. The proof is provided in Appendix 2.5. $\qquad\square$

Thus, at most $\mathcal{O}\left(\sqrt{\frac{1}{\epsilon}}\right)$ support points are required to approximate function $\mathsf{p}(\cdot)$ with an accuracy of at least ϵ.

2.4 Evaluation

2.4.1 Baseline Comparison: Average Harvested Energy

For baseline comparison, the expected harvested energy is considered. Let $U_N \triangleq \sum_{n=1}^{N} P_{\mathrm{har}}^{(n)}$ be denoting the accumulated harvested power up to coherence block N, with which one can calculate the expected harvested energy over N coherence periods as:

$$
\mathbb{E}[T_{\mathrm{p}} U_N] = T_{\mathrm{p}} \mathbb{E}\left[\sum_{n=1}^{N} P_{\mathrm{har}}^{(n)}\right] = N \, T_{\mathrm{p}} \, \mathbb{E}\left[P_{\mathrm{har}}^{(n)}\right], \tag{2.20}
$$

for some $n \in [N]$. The last equality stems from the fact that $\{P_{\mathrm{har}}^{(n)}\}_{n\in[N]}$ are identically distributed, since $\{\gamma^{(n)}\}_{n\in[N]}$ are also identically distributed. Let us also denote $\overline{\mathsf{P}}_{\mathrm{L,har}}$, $\overline{\mathsf{P}}_{\mathrm{CL,har}}$, $\overline{\mathsf{P}}_{\mathrm{CLC,har}}$, and $\overline{\overline{\mathsf{P}}}_{\mathrm{har}}$ the expected harvested power over a single coherence block of the following models, respectively: linear in Eq. (2.8), constant-linear in Eq. (2.9), constant-linear-constant in Eq. (2.10), and proposed in Eq. (2.11).

Under Nakagami fading, the average harvested power for the baseline linear models can be expressed as:

$$\overline{\mathsf{P}}_{\mathrm{L,har}} = \eta_{\mathrm{L}}\,\mathsf{P}(d) \tag{2.21}$$

$$\overline{\mathsf{P}}_{\mathrm{CL,har}} = \int_0^\infty \tilde{\mathsf{p}}_{\mathrm{CL}}(x)\,\mathsf{f}_{P_{\mathrm{R}}^{(n)}}(x)\mathrm{d}x$$

$$= \eta_{\mathrm{CL}}\left(\mathsf{P}(d)\frac{\Gamma\left(\mathsf{m}+1, \frac{\mathsf{m}}{\mathsf{P}(d)}\mathsf{P}_{\mathrm{in}}^{\mathrm{sen}}\right)}{\Gamma(\mathsf{m}+1)} - \frac{\mathsf{P}_{\mathrm{in}}^{\mathrm{sen}}\,\Gamma\left(\mathsf{m}, \frac{\mathsf{m}}{\mathsf{P}(d)}\mathsf{P}_{\mathrm{in}}^{\mathrm{sen}}\right)}{\Gamma(\mathsf{m})}\right) \tag{2.22}$$

$$\overline{\mathsf{P}}_{\mathrm{CLC,har}} = \int_0^\infty \tilde{\mathsf{p}}_{\mathrm{CLC}}(x)\,\mathsf{f}_{P_{\mathrm{R}}^{(n)}}(x)\mathrm{d}x$$

$$= \left(\frac{\mathsf{P}(d)\left(\Gamma\left(\mathsf{m}+1, \frac{\mathsf{m}}{\mathsf{P}(d)}\mathsf{P}_{\mathrm{in}}^{\mathrm{sen}}\right) - \Gamma\left(\mathsf{m}+1, \frac{\mathsf{m}}{\mathsf{P}(d)}\mathsf{P}_{\mathrm{in}}^{\mathrm{sat}}\right)\right)}{\Gamma(\mathsf{m}+1)}\right.$$

$$\left. + \frac{\mathsf{P}_{\mathrm{in}}^{\mathrm{sat}}\,\Gamma\left(\mathsf{m}, \frac{\mathsf{m}}{\mathsf{P}(d)}\mathsf{P}_{\mathrm{in}}^{\mathrm{sat}}\right)}{\Gamma(\mathsf{m})} - \frac{\mathsf{P}_{\mathrm{in}}^{\mathrm{sen}}\,\Gamma\left(\mathsf{m}, \frac{\mathsf{m}}{\mathsf{P}(d)}\mathsf{P}_{\mathrm{in}}^{\mathrm{sen}}\right)}{\Gamma(\mathsf{m})}\right)\eta_{\mathrm{CLC}}, \tag{2.23}$$

where the expressions above rely on $\Gamma(\mathsf{m}+1) = \mathsf{m}\cdot\Gamma(\mathsf{m})$, as well as on the following formula from [62, Eq. (3.381.9)]:

$$\int_a^b x^i\,\mathsf{f}_{P_{\mathrm{R}}^{(n)}}(x)\mathrm{d}x = \left(\frac{\mathsf{P}(d)}{\mathsf{m}}\right)^i \frac{\Gamma\left(\mathsf{m}+i, \frac{\mathsf{m}}{\mathsf{P}(d)}a\right) - \Gamma\left(\mathsf{m}+i, \frac{\mathsf{m}}{\mathsf{P}(d)}b\right)}{\Gamma(\mathsf{m})},\ i \in \mathbb{N} \cup \{0\}. \tag{2.24}$$

Again with the aid of Eq. (2.24), the expected harvested power over a single coherence period for the proposed nonlinear model is given by:

$$\overline{\overline{\mathsf{P}}}_{\mathrm{har}} = \sum_{m=1}^M \int_{b_{m-1}}^{b_m} (l_m(x - b_{m-1}) + v_{m-1})\mathsf{f}_{P_{\mathrm{R}}^{(n)}}(x)\mathrm{d}x + \int_{b_M}^\infty v_M\mathsf{f}_{P_{\mathrm{R}}^{(n)}}(x)\mathrm{d}x$$

$$= \sum_{m=1}^M \left(\frac{l_m\,\mathsf{P}(d)\left(\Gamma\left(\mathsf{m}+1, \frac{\mathsf{m}\,b_{m-1}}{\mathsf{P}(d)}\right) - \Gamma\left(\mathsf{m}+1, \frac{\mathsf{m}\,b_m}{\mathsf{P}(d)}\right)\right)}{\Gamma(\mathsf{m}+1)}\right.$$

$$\left. + \frac{(v_{m-1} - l_m b_{m-1})\left(\Gamma\left(\mathsf{m}, \frac{\mathsf{m}\,b_{m-1}}{\mathsf{P}(d)}\right) - \Gamma\left(\mathsf{m}, \frac{\mathsf{m}\,b_m}{\mathsf{P}(d)}\right)\right)}{\Gamma(\mathsf{m})}\right) + \frac{v_M\,\Gamma\left(\mathsf{m}, \frac{\mathsf{m}}{\mathsf{P}(d)}\mathsf{P}_{\mathrm{in}}^{\mathrm{sat}}\right)}{\Gamma(\mathsf{m})}, \tag{2.25}$$
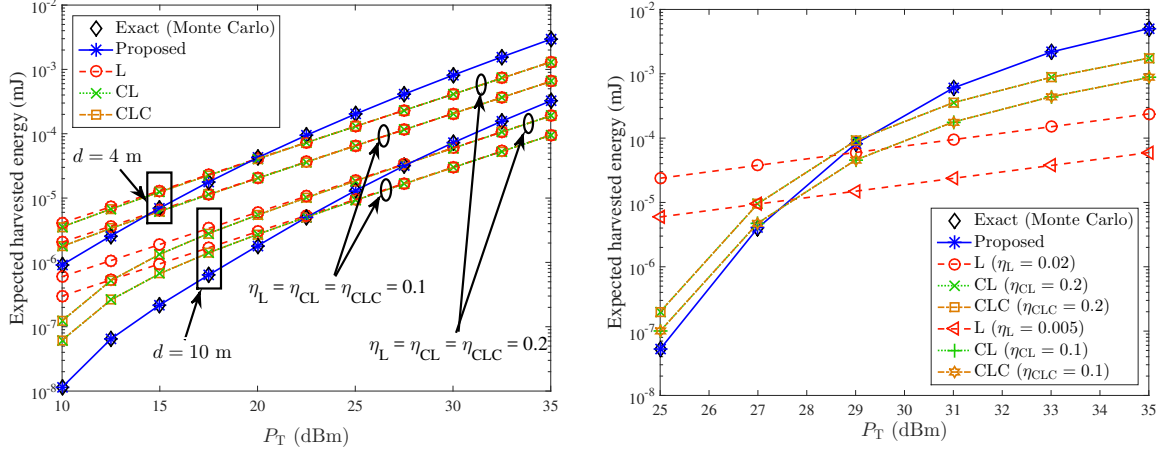
Figure 2.5: Left (Right): Expected harvested energy per coherence block ($N = 1$) vs transmission power P_{T} for the rectenna proposed in [31] (harvesting module in [59]).

Numerical Results

The expected harvested energy in Eq. (2.20) is calculated for the actual energy harvesting model in Eq. (2.6) (obtained through Monte Carlo experiments), as well as for the three linear baseline models and the proposed approximated nonlinear energy harvesting model. For the evaluation, the following path-loss model is adopted:

$$\mathsf{L}(d) = \left(\frac{\lambda}{d_0 \, 4 \, \pi} \right)^2 \left(\frac{d_0}{d} \right)^{\nu}, \tag{2.26}$$

with reference distance $d_0 = 1$, propagation wavelength $\lambda = 0.3456$ and path-loss exponent (PLE) ν.

Fig. 2.5 examines the impact of transmit power P_{T} on average harvested energy over $N = 1$ coherence period using $T_{\mathrm{p}} = 50$ msec packet duration. In Fig. 2.5-Left, PLE $\nu = 2.1$ and $\mathtt{m} = 5$ are set for the rectenna in [31]. It can be seen that the expected harvested energy performance of the proposed approximation in (2.11) with $M + 1 = 1171$ points is the same with the performance of the actual harvesting model for all studied distance scenarios of $d = 4$ and $d = 10$ meters; thus, it is deduced that the approximation with the specific number M of points is accurate. The slope of the expected harvested energy for the baseline (linear) schemes is different compared to the exact model, demonstrating their deviation from the real energy harvesting model.

In Fig. 2.5-Right, under the same small- and large-scale fading parameters as above, with $M + 1 = 2201$ approximation points and distance $d = 3$ m, it is shown that the linear model is highly inaccurate for the second harvesting circuit module; thus, the widely adopted linear model cannot capture realistic efficiency models. The performance

of the other two baseline linear models is closer to the actual harvesting model. However, the slopes are different and non-negligible mismatch still exists.

2.4.2   Time-Switching RF Energy Harvesting Scenario: Expected Charging Time

Another important metric is the expected time for the RF harvesting circuit to charge its storage unit at the minimum required level, before operation. This is graphically illustrated in Fig. 2.6, showing *time-switching* RF energy harvesting and communication protocols, where the terminal (e.g., a wireless sensor) first scavenges the necessary energy required for transmission and then communicates (e.g., work in [31]). This is a very common situation in many RF harvesting protocols, since the available power density in μWatt/cm^2 regime is limited and may not be able to retain the power requirements of the overall apparatus. As a result, a duty-cycled, non-continuous operation is imperative, as depicted in Fig. 2.6. Thus, the required time to harvest the necessary energy before operation should be carefully quantified.

An energy harvesting outage event after N coherence periods will occur if the harvested energy after N coherence periods is below a threshold. The latter is determined by the capacity of the energy storage unit (e.g., capacitor C) and the operating voltage V of the harvesting circuit. Thus, the outage event is given by:

$$
\begin{aligned}
\mathcal{O}_N &\triangleq \left\{ \mathbf{p}_N \in \mathbb{R}_+^N : T_{\mathrm{p}} \sum_{n=1}^{N} P_{\mathrm{har}}^{(n)}\left(P_{\mathrm{R}}^{(n)}\right) \leq \frac{1}{2}\,\mathsf{C}\,\mathsf{V}^2 \right\} \\
&= \left\{ \mathbf{p}_N \in \mathbb{R}_+^N : \sum_{n=1}^{N} P_{\mathrm{har}}^{(n)}\left(P_{\mathrm{R}}^{(n)}\right) \leq \theta_{\mathrm{harv}}^{\mathrm{th}} \right\},
\end{aligned}
\tag{2.27}
$$

where the power threshold is determined by the minimum required stored energy for operation, equal to $\frac{1}{2}\mathsf{C}\mathsf{V}^2$, as well as the transmission duration T_{p}, i.e., $\theta_{\mathrm{harv}}^{\mathrm{th}} \triangleq \frac{\mathsf{C}\mathsf{V}^2}{2T_{\mathrm{p}}}$. Note that the above event depends on the fading coefficients $\{\gamma^{(n)}\}_{n\in[N]}$.

RV $N^\star$ is defined as the first coherence time index when the accumulated harvested power is above threshold $\theta_{\mathrm{harv}}^{\mathrm{th}}$, given that there exist $N^\star - 1$ consecutive outage events;
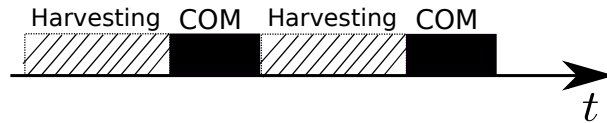

Figure 2.6: Time-switching operation. Necessary energy is harvested before communication, in duty-cycled, non-continuous applications (e.g., wireless sensors).

thus, the probability mass function (PMF) of RV $N^\star$ can be derived as:

$$\mathbb{P}(N^\star = N) \triangleq \mathbb{P}\left(\mho_{N-1} \cap \left\{\mathbf{p}_N \in \mathbb{R}_+^N : P_{\text{har}}^{(N)}\left(P_{\text{R}}^{(N)}\right) > \theta_{\text{harv}}^{\text{th}} - \sum_{n=1}^{N-1} P_{\text{har}}^{(n)}\left(P_{\text{R}}^{(n)}\right)\right\}\right)$$

$$= \mathbb{P}\left(\sum_{n=1}^{N-1} P_{\text{har}}^{(n)} \leq \theta_{\text{harv}}^{\text{th}} \cap P_{\text{har}}^{(N)} > \theta_{\text{harv}}^{\text{th}} - \sum_{n=1}^{N-1} P_{\text{har}}^{(n)}\right)$$

$$\overset{(a)}{=} \mathbb{P}\left(U_{N-1} \leq \theta_{\text{harv}}^{\text{th}} \cap U_{N-1} > \theta_{\text{harv}}^{\text{th}} - P_{\text{har}}^{(N)}\right)$$

$$\overset{(b)}{=} \int_{x \in \mathbf{dom} \mathsf{f}_{P_{\text{har}}}} \mathbb{P}\left(U_{N-1} \leq \theta_{\text{harv}}^{\text{th}} \cap U_{N-1} > \theta_{\text{harv}}^{\text{th}} - x\right) \mathsf{f}_{P_{\text{har}}^{(N)}}(x)\mathsf{d}x$$

$$\overset{(c)}{=} \mathsf{F}_{U_{N-1}}(\theta_{\text{harv}}^{\text{th}}) - \int_{x \in \mathbf{dom} \mathsf{f}_{P_{\text{har}}}} \mathsf{F}_{U_{N-1}}(\theta_{\text{harv}}^{\text{th}} - x) \mathsf{f}_{P_{\text{har}}^{(N)}}(x)\mathsf{d}x, \tag{2.28}$$

where step (a) used the definition of RV U_N, i.e., $U_{N-1} = \sum_{n=1}^{N-1} P_{\text{har}}^{(n)}$, step (b) exploited the law of iterated expectation and the fact that U_{N-1} and $P_{\text{har}}^{(N)}$ are independent, and step (c) employed the CDF definition. Note that the expression above requires the CDF of U_{N-1}, which will be offered subsequently, while PDF of $P_{\text{har}}^{(N)}$ can be given with the methodology of Section 2.3.1.

The expected value of discrete RV $N^\star$ is given by:

$$\overline{N^\star} = \sum_{N=1}^{\infty} N \cdot \mathbb{P}(N^\star = N). \tag{2.29}$$

$\overline{N^\star}$ can be interpreted as the average number of coherence periods, i.e., $\overline{N^\star} T_{\text{c}}$ seconds, required for charging, before communication. As the harvesting of adequate RF energy is necessary for any communication operation at the IEH terminal, the expected charging time $\overline{N^\star} T_{\text{c}}$ is a prerequisite time interval.

To calculate $\overline{N^\star}$ for the proposed model, Eq. (2.28) must be exploited using $\widetilde{U}_{N-1} \triangleq \sum_{n=1}^{N-1} \widetilde{P}_{\text{har}}^{(n)}$ and $\widetilde{P}_{\text{har}}^{(N)}$. However, only the PDF of each individual RV $\widetilde{P}_{\text{har}}^{(n)}$, $n \in [N]$, is available. To this end, a numerical methodology to calculate the CDF and the PDF of $\widetilde{U}_{N-1}$ is proposed, exploiting the fact that the latter can be written as a sum of independent RVs. The proposed methodology to evaluate Eq. (2.28), and thus $\overline{N^\star}$, is provided in Appendix 2.5. The PMF of RV $N^\star$ is calculated for the proposed model using Eq. (2.53) for any threshold $\theta_{\text{harv}}^{\text{th}}$.

Consider the rectenna model in [31], the path-loss model given in (2.26) with $\nu = 2.1$ and $d = 5$ m, transmission power $P_{\text{T}} = 1.5$ Watt, Nakagami parameter $\mathtt{m} = 5$, while the parameters for the power threshold are set to $\mathtt{V} = 1.8$ V, $\mathtt{C} = 10$ μF, $T_{\text{p}} = 50$ msec. Fig. 2.7 shows the histogram of actual U_N and the corresponding estimated PDF of RV
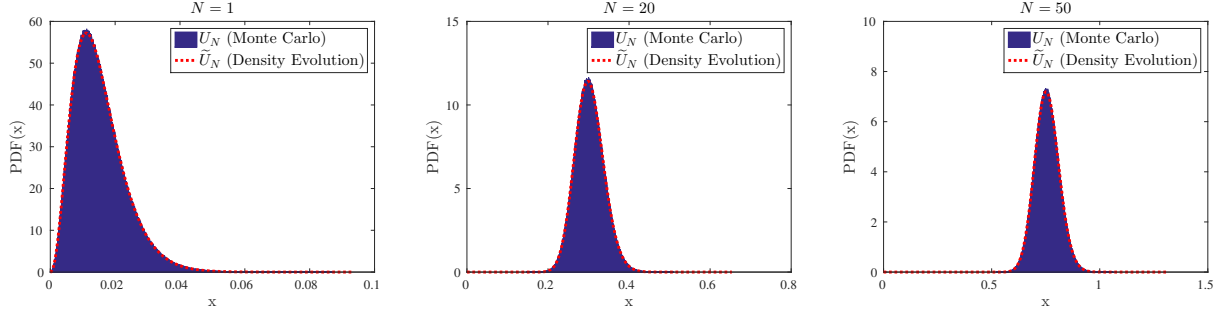
Figure 2.7: Histogram of actual U_N and the corresponding PDF vector $\mathbf{v_f}$ for $N = 1$, $N = 20$, and $N = 50$ for the energy harvesting model in [31].

$\widetilde{U}_N$, for $N = 1$, $N = 20$, and $N = 50$.[2] It can be seen that the red dotted curves of the the estimated PDFs perfectly match with the actual PDFs (i.e., the histogram obtained through Monte Carlo).
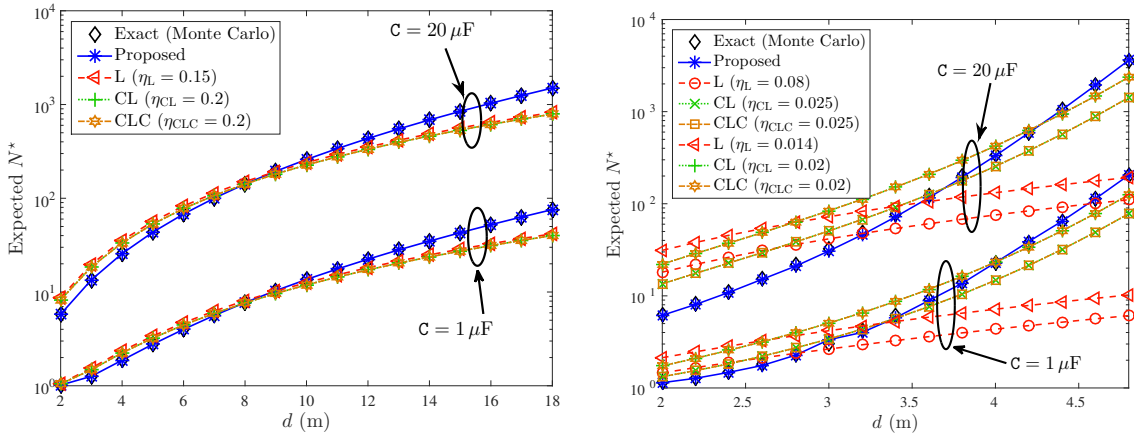
Figure 2.8: Left (Right): Expected number of coherence periods $N^\star$ necessary for charging vs distance for the rectenna proposed in [31] (PowerCast module [59]).

Numerical Results

Fig. 2.8 depicts the expected $N^\star$ for the realistic, proposed, and baseline models as a function of distance for different capacitor values for the two harvesting efficiency models in [31] (Left) and [59] (Right) using $\mathtt{V} = 1.8$ V and $T_{\mathrm{p}} = 50$ msec. The path-loss model in Eq. (2.26) is employed for the evaluation in conjunction with Nakagami fading. In Fig. 2.8-Left (Right) the utilized wireless channel parameters are $\nu = 2.1$, $\mathtt{m} = 5$, $P_{\mathrm{T}} = 1.5$ Watt, while for density evolution, the following parameters are employed: $H = 2^{17}$ and

---

[2]Appendix 2.5 parameters are $H = 2^{16}$, $S_{\mathrm{m}} = 0$, $S_{\mathrm{M}} = N\mathbb{E}\left[\widetilde{P}_{\mathrm{har}}^{(n)}\right] + 10\sqrt{N\,\mathsf{var}\left[\widetilde{P}_{\mathrm{har}}^{(n)}\right]}$, $\Delta = \frac{S_{\mathrm{M}} - S_{\mathrm{m}}}{H}$, and $J_{\mathrm{FFT}} = 2^{17}$.
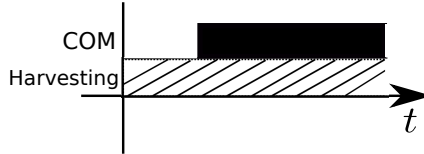
Figure 2.9: Power-splitting operation mode.

$J_{\mathrm{FFT}} = 2^{18}$ ($J_{\mathrm{FFT}} = 2^{19}$). The number of data points to approximate harvested power in Eq. (2.11) was $M + 1 = 1171$ and $M + 1 = 2201$ data points for efficiency models in [31] and [59], respectively.

For both harvesting efficiency models in [31] and [59] the expected charging time for the proposed approximation and the true harvested power model coincide, verifying the accuracy of a) the proposed approximation in Eq. (2.11) and b) the Appendix 2.5 framework.

For the baseline models, results are obtained through Monte Carlo. It is observed that although the best possible values for η_{L}, η_{CL}, and η_{CLC} are chosen for the baseline models, they fail to offer the same slope with the true energy harvesting model. Consequently, the obtained $N^{\star}$ for the linear models may deviate one order of magnitude from the true value, offering deviations from the true duty-cycle and the available resources for wireless communications. It is also noted that the presence of a boost converter at the rectifier output may also magnify the necessary time for charging, further amplifying charging time differences.

The proposed methodology with the nonlinear harvesting model is clearly able to offer accurate estimation of the charging time.

2.4.3 Power-Splitting RF Energy Harvesting Scenario: Passive RFID Tags

Next, a backscatter RFID scenario is considered where the EIH node is a passive RFID tag that splits input RF power for operation and wireless communication, simultaneously (see Fig. 2.9), as opposed to time-switching (duty-cycled) operation. Passive RFID tags typically use a simple RF switch (e.g., transistor) to communicate with an interrogator.

Fig. 2.10 illustrates a typical operating block diagram of a passive RFID tag. Suppose that tag's antenna is terminated between two load values Z_0 and Z_1. When the antenna is terminated at load Z_1, the tag reflects the incoming signal, i.e., backscatters information (uplink), provided that it has sufficient amount of energy. On the other hand, when the antenna is terminated at load Z_0, tag's antenna is matched to input load and the

tag absorbs the power from the incident signal. The duration of the overall round-trip communication between the interrogator and the tag is assumed to last a single coherence time period. Hence, to minimize the notation we focus on a single coherence time block, omitting the index n throughout.

The parameter τ_d is the fraction of time the antenna load is at Z_0 (absorbing state), while the rest $1 - \tau_d$ corresponds to the fraction of time at load Z_1 (reflection state). Assume that χ is the fraction of receiving input power (when tag's antenna load is at absorbing state) dedicated for RF energy harvesting operation; thus, a total of $\zeta_{har} = \chi \tau_d$ percentage of input power is dedicated for energy harvesting, with $\zeta_{har} \in (0, 1)$. The rest $(1 - \chi)\tau_d$ of the input signal power is utilized by the tag downlink communication circuitry. Furthermore, parameter ρ_u denotes the fraction of incident input power that is used for uplink (reflection) scatter radio operation. This number depends on the scattering efficiency and the fraction of time the tag antenna is terminated at load Z_1 (i.e., $\rho_u \leq 1 - \tau_d$). It is emphasized that scattering efficiency depends on reflection coefficients, which in turn are input power-independent. With monostatic architecture, the incident input power at the tag is $P_R = P_T \, \mathsf{L}(d) \, \gamma = \mathsf{P}(d)\gamma$. Since, only a fraction ρ_u of input power is backscattered (i.e., $\rho_u \, P_R$), the received power at the interrogator due to the round trip nature of the backscattering operation is given by:

$$P_{int}(P_R) = \rho_u \, P_R \, \mathsf{L}(d) \, \gamma = \rho_u \frac{(P_R)^2}{P_T}. \tag{2.30}$$
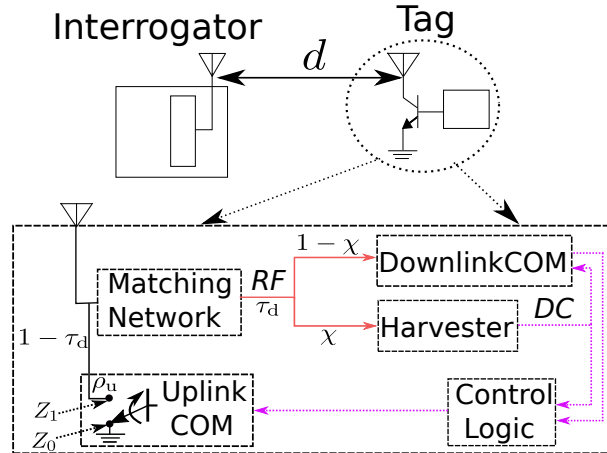
Figure 2.10: Monostatic backscatter architecture consisting of an interrogator and a passive RFID tag. The interrogator's antenna acts as transmitter of the illuminating signal, as well as receiver of reflected, i.e., backscattered (from the tag) information, hence the term *monostatic*.

The two following events are needed:

$$\mathcal{A} \triangleq \{\text{The BER at reader is below a threshold } \beta\}$$

$$= \left\{ P_R \in \mathbb{R}_+ : 2\,\mathsf{Q}\left(\frac{\sqrt{P_{\text{int}}(P_R)}}{\sigma_u}\right)\left(1 - \mathsf{Q}\left(\frac{\sqrt{P_{\text{int}}(P_R)}}{\sigma_u}\right)\right) < \beta \right\} \qquad (2.31)$$

and

$$\mathcal{B} \triangleq \{\text{The harvested power is larger than tags' power consumption } \mathsf{P_c}\}$$

$$= \{P_R \in \mathbb{R}_+ : P_{\text{har}}(\zeta_{\text{har}}\, P_R) > \mathsf{P_c}\}, \qquad (2.32)$$

where $\mathsf{Q}(x) \triangleq \frac{1}{\sqrt{2\pi}} \int_x^\infty \exp\left(-\frac{t^2}{2}\right) \mathrm{d}t$ is the Q-function and the expression in the last line of Eq. (2.31) is the probability of bit error under coherent maximum-likelihood detection with FM0 line coding [63], and threshold $\beta \in [0, \frac{1}{2}]$. Parameter σ_u^2 is the properly scaled variance of thermal AWGN noise at the receiving circuit of the interrogator. The expression in (2.31) can be further simplified with the aid of the following proposition:

Proposition 2.3. The function

$$y = \mathsf{R}(x) \triangleq 2\,\mathsf{Q}(x)\,(1 - \mathsf{Q}(x)), \ x \in \mathbb{R}_+, \qquad (2.33)$$

is monotone decreasing and invertible for $x \in \mathbb{R}_+$; the inverse function is given by

$$x = \mathsf{R}^{-1}(y) = \mathsf{Q}^{-1}\left(\frac{2 - \sqrt{4 - 8\,y}}{4}\right), \ y \in [0, 0.5], \qquad (2.34)$$

where function $\mathsf{Q}^{-1}(\cdot)$ denotes the inverse of Q-function (with respect to composition).

Proof. The proof is given in Appendix 2.5. $\qquad\qquad\qquad\qquad\qquad\qquad\qquad$ □

The event of successful interrogator reception is denoted by $\mathcal{S}$; the non-successful reception event at interrogator $\mathcal{S}^c$ occurs if a) the harvested power is below the tag's power consumption or (b) given that the harvested power is above the tag's power consumption $\mathsf{P_c}$, the BER at the interrogator is above the threshold β:

$$\mathbb{P}(\mathcal{S}^c) = \mathbb{P}(\mathcal{B}^c) + \mathbb{P}(\mathcal{A}^c|\mathcal{B})\mathbb{P}(\mathcal{B}) = 1 - \mathbb{P}(\mathcal{B}) + \mathbb{P}(\mathcal{A}^c|\mathcal{B})\mathbb{P}(\mathcal{B})$$

$$= 1 - \mathbb{P}(\mathcal{B})(1 - \mathbb{P}(\mathcal{A}^c|\mathcal{B})) = 1 - \mathbb{P}(\mathcal{B})\mathbb{P}(\mathcal{A}|\mathcal{B}) = 1 - \mathbb{P}(\mathcal{A} \cap \mathcal{B}) = 1 - \mathbb{P}(\mathcal{S}). \quad (2.35)$$

Thus, in view of Eq. (2.35), the probability of a successful event is expressed as:

$$\mathbb{P}(\mathcal{S}) = \mathbb{P}\left(\mathsf{R}\left(\frac{\sqrt{P_{\text{int}}(P_{\text{R}})}}{\sigma_{\text{u}}}\right) < \beta \cap P_{\text{har}}(\zeta_{\text{har}} P_{\text{R}}) > \mathsf{P}_{\text{c}}\right)$$
$$\overset{(a)}{=} \mathbb{P}\left(P_{\text{R}} > \frac{\sqrt{P_{\text{T}}} \, \mathsf{R}^{-1}(\beta)\sigma_{\text{u}}}{\sqrt{\rho_{\text{u}}}} \cap P_{\text{har}}(\zeta_{\text{har}} P_{\text{R}}) > \mathsf{P}_{\text{c}}\right). \tag{2.36}$$

where step (a) employed the fact that function R^{-1} is monotone decreasing and exploited Eq. (2.30).

The corresponding probability expressions can be derived for the baseline linear models and the proposed nonlinear harvesting model. The successful reception event at the interrogator for the baseline models is denoted as $\mathcal{S}_{\text{c}}$, $\text{c} \in \{\text{L}, \text{CL}, \text{CLC}\}$ and for the proposed model as $\widetilde{\mathcal{S}}$. The following proposition summarizes the results:

Proposition 2.4. Suppose that $\mathsf{P}_{\text{c}} > 0$ and consider Nakagami fading. Let us define threshold $\theta_{\mathcal{A}} \triangleq \frac{\sqrt{P_{\text{T}}} \, \mathsf{R}^{-1}(\beta)\sigma_{\text{u}}}{\sqrt{\rho_{\text{u}}}} > 0$. For the linear model, the probability of event $\mathcal{S}_{\text{L}}$ is given by:

$$\mathbb{P}(\mathcal{S}_{\text{L}}) = \frac{\Gamma\left(\mathsf{m}, \frac{\mathsf{m}}{\mathsf{P}(d)}\theta_{\max}^{\text{L}}\right)}{\Gamma(\mathsf{m})}, \tag{2.37}$$

where $\theta_{\max}^{\text{L}} \triangleq \max\{\theta_{\mathcal{A}}, \frac{\mathsf{P}_{\text{L}}^{-1}(\mathsf{P}_{\text{c}})}{\zeta_{\text{har}}}\}$.

For the constant-linear model, the probability of event $\mathcal{S}_{\text{CL}}$ is given by:

$$\mathbb{P}(\mathcal{S}_{\text{CL}}) = \frac{\Gamma\left(\mathsf{m}, \frac{\mathsf{m}}{\mathsf{P}(d)}\theta_{\max}^{\text{CL}}\right)}{\Gamma(\mathsf{m})}, \tag{2.38}$$

where $\theta_{\max}^{\text{CL}} \triangleq \max\{\theta_{\mathcal{A}}, \frac{\mathsf{P}_{\text{CL}}^{-1}(\mathsf{P}_{\text{c}})}{\zeta_{\text{har}}}\}$.

For the last baseline model (CLC), the probability of event $\mathcal{S}_{\text{CLC}}$ is expressed as follows:

$$\mathbb{P}(\mathcal{S}_{\text{CLC}}) = \begin{cases} \frac{\Gamma\left(\mathsf{m}, \frac{\mathsf{m}}{\mathsf{P}(d)}\theta_{\max}^{\text{CLC}}\right)}{\Gamma(\mathsf{m})}, & 0 < \mathsf{P}_{\text{c}} < \mathsf{p}_{\text{CLC}}(\mathsf{P}_{\text{in}}^{\text{sat}}), \\ 0, & \mathsf{P}_{\text{c}} \geq \mathsf{p}_{\text{CLC}}(\mathsf{P}_{\text{in}}^{\text{sat}}), \end{cases} \tag{2.39}$$

where $\theta_{\max}^{\text{CLC}} \triangleq \max\{\theta_{\mathcal{A}}, \frac{\mathsf{P}_{\text{CLC}}^{-1}(\mathsf{P}_{\text{c}})}{\zeta_{\text{har}}}\}$.

Finally, for the proposed nonlinear energy harvesting model, the probability of event $\widetilde{\mathcal{S}}$ is given by:

$$\mathbb{P}(\widetilde{\mathcal{S}}) = \begin{cases} \frac{\Gamma\left(\mathsf{m}, \frac{\mathsf{m}}{\mathsf{P}(d)}\widetilde{\theta}_{\max}\right)}{\Gamma(\mathsf{m})}, & 0 < \mathsf{P}_{\text{c}} < v_M, \\ 0, & \mathsf{P}_{\text{c}} \geq v_M, \end{cases} \tag{2.40}$$
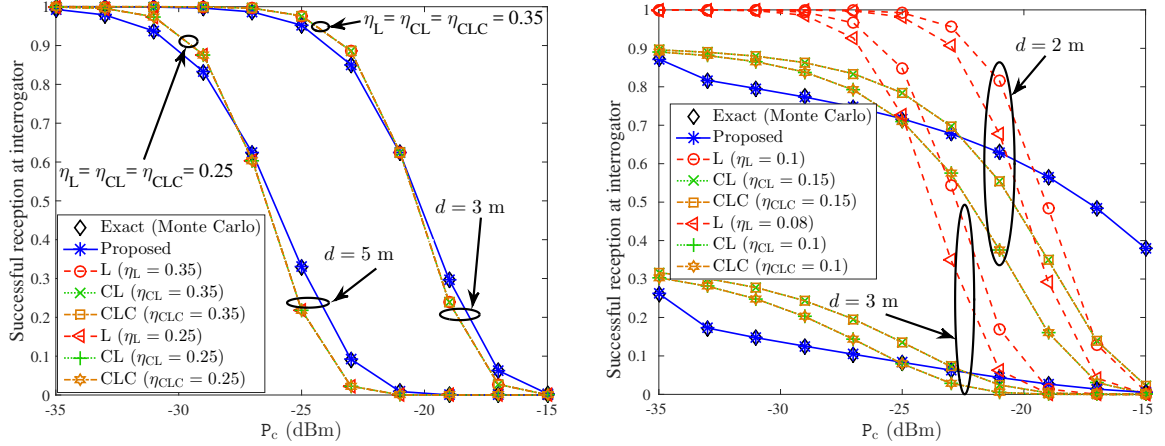
Figure 2.11: Left (Right): Probability of successful reception at the interrogator/RFID reader, as a function of the tags' power consumption P_c and the tag-reader distance, for the rectenna model in [31] (PowerCast module [59]).

where $\widetilde{\theta}_{\max} \triangleq \max\{\theta_{\mathcal{A}}, \frac{\widetilde{\mathsf{p}}^{-1}(\mathsf{P_c})}{\zeta_{\mathrm{har}}}\}$.

Proof. The proof can be found in Appendix 2.5. $\qquad\qquad\square$

Numerical Results

Fig. 2.11 offers the probability of successful reception at the interrogator/reader, as a function of the tag power consumption P_c and the tag-reader distance under the path-loss model in Eq. (2.26). The following parameters are utilized: $\tau_{\mathrm{d}} = 0.5$, $\chi = 0.5$, $\rho_{\mathrm{u}} = 0.01$, $\beta = 10^{-5}$, $\sigma_{\mathrm{u}}^2 = 10^{-11}$ mWatt. In Fig. 2.11-Left (Right) the rectenna model in [31] (harvesting module in [59]) is studied using parameters $\nu = 2.1$, $\mathtt{m} = 5$, and $P_{\mathrm{T}} = 1.5$ Watt ($P_{\mathrm{T}} = 3$ Watt) under two distance setups: $d = 5$ m and $d = 3$ m ($d = 3$ m and $d = 2$ m), and using $M + 1 = 1171$ ($M + 1 = 2201$) data points.

From both figures it can be seen that the performance of the proposed approximation in Eq. (2.11) is the same as the performance of the real model in Eq. (2.6). On the other hand, the baseline models deliver different slopes compared to the nonlinear model and fail to approach its performance; this holds for both harvesting circuits, even though deviations are more obvious for the harvester in [59]; it is also noted that the selected values of η_{L}, η_{CL}, and η_{CLC} were chosen so as to reduce the performance difference. It is also noted that the linear model's performance curve has completely different slope and curvature compared to the real harvesting model.

Again, it can be deduced that in sharp contrast to the linear harvesting models, the proposed harvesting model and the offered methodology provide accurate results.

2.5 Appendix: Proofs of Chapter 2

Proof of Proposition 2.1

Here the CDF expression in Eq. (2.18) is shown. Using the PDF of Eq. (2.17), for any $x \in [v_{m-1}, v_m] \setminus \{v_M\}$, $m \in [M]$:

$$
\begin{aligned}
\mathsf{F}_{\widetilde{P}_{\mathrm{har}}^{(n)}}(x) &= \int_0^x \mathsf{f}_{\widetilde{P}_{\mathrm{har}}^{(n)}}(y)\mathrm{d}y \\
&\overset{(a)}{=} \sum_{j=1}^{m-1} \int_{v_{j-1}}^{v_j} \frac{1}{l_j} \mathsf{f}_{P_{\mathrm{R}}^{(n)}}\left(\frac{y - v_{j-1} + l_j b_{j-1}}{l_j}\right) \mathrm{d}y + \int_{v_{m-1}}^x \frac{1}{l_m} \mathsf{f}_{P_{\mathrm{R}}^{(n)}}\left(\frac{y - v_{m-1} + l_m b_{m-1}}{l_m}\right) \mathrm{d}y \\
&\overset{(b)}{=} \sum_{j=1}^{m-1} \int_{b_{j-1}}^{b_j} \mathsf{f}_{P_{\mathrm{R}}^{(n)}}(y)\mathrm{d}y + \int_{b_{m-1}}^{\frac{x - v_{m-1} + l_m b_{m-1}}{l_m}} \mathsf{f}_{P_{\mathrm{R}}^{(n)}}(y)\mathrm{d}y \\
&= \int_0^{\frac{x - v_{m-1} + l_m b_{m-1}}{l_m}} \mathsf{f}_{P_{\mathrm{R}}^{(n)}}(y)\mathrm{d}y = \mathsf{F}_{P_{\mathrm{R}}^{(n)}}\left(\frac{x - v_{m-1} + l_m b_{m-1}}{l_m}\right),
\end{aligned} \tag{2.41}
$$

where in (a) the integral is divided in a sum of integrals associated with disjoint intervals and in (b) change of variables $y' = \frac{y - v_{j-1} + l_j b_{j-1}}{l_j}$ is performed for each individual integral. Note that due to the right-continuity of CDF [60], Eq. (2.41) covers the case of $x = v_0 = 0$ since $\mathsf{F}_{\widetilde{P}_{\mathrm{har}}^{(n)}}(0) = \mathsf{F}_{P_{\mathrm{R}}^{(n)}}\left(\frac{l_1 b_0}{l_1}\right) = \xi_0$.

For $x \geq v_M$ the following holds

$$
\mathsf{F}_{\widetilde{P}_{\mathrm{har}}^{(n)}}(x) \overset{(a)}{=} \int_0^{v_M^-} \mathsf{f}_{\widetilde{P}_{\mathrm{har}}^{(n)}}(y)\mathrm{d}y + \int_{v_M}^x \mathsf{f}_{\widetilde{P}_{\mathrm{har}}^{(n)}}(y)\mathrm{d}y \overset{(b)}{=} \xi_M + (1 - \xi_M) = 1, \tag{2.42}
$$

where in (a) the integral is divided over the disjoint intervals $[0, v_M)$ and $[v_M, x)$, while in (b), we plugged the definition of CDF found in Eq. (2.41) over interval $[0, v_M)$, and we used the definition of PDF in (2.17) for $x \geq v_M$. The above conclude the proof.

Proof of Proposition 2.2

The proof of this proposition relies on polynomial interpolation theorem [64, Th. 6.2]. For any continuously differentiable function $\mathsf{g}(\cdot)$ defined over an interval $[x_0, x_1]$ and a linear function $\widetilde{\mathsf{g}}(\cdot)$ that interpolates $\mathsf{g}(\cdot)$ on x_0 and x_1, for any $x \in [x_0, x_1]$ there exists $\phi \equiv \phi(x) \in (x_0, x_1)$ satisfying the following

$$
\mathsf{g}(x) - \widetilde{\mathsf{g}}(x) = \frac{(x - x_0)(x - x_1)}{2} \mathsf{g}''(\phi), \tag{2.43}
$$

where $g''(\cdot)$ denotes the second order derivative of function $g(\cdot)$. Using the above, the absolute error is upper bounded as

$$\int_{x_0}^{x_1} |g(x) - \widetilde{g}(x)| \, dx \leq \frac{1}{2} \max_{x \in [x_0, x_1]} |g''(x)| \int_{x_0}^{x_1} |(x - x_0)(x - x_1)| \, dx$$

$$= \frac{1}{2} C_g \int_{x_0}^{x_1} (x - x_0)(x_1 - x) dx, \tag{2.44}$$

where constant $C_g \equiv C_g(x_0, x_1) \triangleq \max_{x \in [x_0, x_1]} |g''(x)|$ depends on function $g(\cdot)$ as well as points x_0 and x_1. Combining the following identity

$$\max_{x \in [x_0, x_1]} (x - x_0)(x_1 - x) = \frac{(x_1 - x_0)^2}{4} \tag{2.45}$$

with Eq. (2.44), the absolute error can be upper bounded as

$$\int_{x_0}^{x_1} |g(x) - \widetilde{g}(x)| \, dx \leq \frac{C_g (x_1 - x_0)^3}{8}. \tag{2.46}$$

Next, the above framework is applied to the proposed piece-wise linear approximation function $\widetilde{p}(\cdot)$. Since $p(\cdot)$ is continuously differentiable in $\mathcal{P}_{\text{in}}$, using the fact that $p(b_m) = \widetilde{p}(b_m)$, for $m = 0, 1, \ldots, M$, applying the results above, the following is obtained

$$\int_{\mathcal{P}_{\text{in}}} |p(x) - \widetilde{p}(x)| \, dx = \sum_{m=1}^{M} \int_{b_{m-1}}^{b_m} |p(x) - \widetilde{p}(x)| \, dx \overset{(a)}{\leq} \frac{(\delta_M)^3}{8} \sum_{m=1}^{M} \max_{x \in [b_{m-1}, b_m]} |p''(x)|$$

$$\overset{(b)}{\leq} \frac{(\delta_M)^3}{8} M \max_{x \in \mathcal{P}_{\text{in}}} |p''(x)| = \frac{C_p \left(P_{\text{in}}^{\text{sat}} - P_{\text{in}}^{\text{sen}}\right)^3}{8 M^2}. \tag{2.47}$$

where in (a) $\delta_M = b_m - b_{m-1}$ is utilized, combined with the result in (2.46), while in (b), $\max_{x \in \mathcal{P}_{\text{in}}} |p''(x)| \geq \max_{x \in [b_{m-1}, b_m]} |p''(x)|$ for any $m \in [M]$ is employed. Constant $C_p \equiv C_p(\mathcal{P}_{\text{in}}) \triangleq \max_{x \in \mathcal{P}_{\text{in}}} |p''(x)|$ depends on set $\mathcal{P}_{\text{in}}$ and the given function $p(\cdot)$, and is independent of M.

Numerical Density Evolution Framework for the Sum of Independent RVs

Consider a RV x which can be expressed as $x = \sum_{n=1}^{N} x^{(n)}$, where $\{x^{(n)}\}_{n=1}^{N}$ are independent of each other, supported by sets $\mathcal{S}^{(n)}$, $n \in [N]$, respectively. It is assumed that the PDF of each individual RV $x^{(n)}$ is given, $f_{x^{(n)}}(\cdot)$, over the support $\mathcal{S}^{(n)}$, $n \in [N]$, and each $\mathcal{S}^{(n)}$ is bounded. In addition note that the support of RV x is $\mathcal{S} = \mathcal{S}^{(1)} + \mathcal{S}^{(2)} + \ldots + \mathcal{S}^{(N)}$ (set addition), due to the required convolution operation.

The idea of density evolution is to approximate numerically the PDF of RV x exploiting the fact that it can be written as the convolution of individual PDFs. To do so, consider the support set $[S_\mathrm{m}, S_\mathrm{M}]$ as an approximation of set $\bigcup_{n=1}^{N} \mathcal{S}^{(n)} \cup \mathcal{S}$. Note that set can be chosen so as $\int_{y \in [S_\mathrm{m}, S_\mathrm{M}]} \mathsf{f}_{x^{(n)}}(y)\mathsf{d}y \approx 1$, $\forall n \in [n]$ and $\int_{y \in [S_\mathrm{m}, S_\mathrm{M}]} \mathsf{f}_x(y)\mathsf{d}y \approx 1$. Support set $[S_\mathrm{m}, S_\mathrm{M}]$ is discretized using $H + 1$ grid points with uniform grid resolution $\Delta = \frac{S_\mathrm{M} - S_\mathrm{m}}{H}$, and the following discrete (support) set is formed

$$\mathcal{H}_\Delta = \{S_\mathrm{m} + h\,\Delta\}_{h=0}^{H}. \tag{2.48}$$

Set $\mathcal{H}_\Delta$ is a discrete approximation of support $[S_\mathrm{m}, S_\mathrm{M}]$ and can be also viewed as a vector with $H + 1$ elements, whose the j-th element is $\mathcal{H}_\Delta[j] = S_\mathrm{m} + (j - 1)\Delta$. Let us denote $\mathbf{v}_\mathsf{f}^{(1)}, \mathbf{v}_\mathsf{f}^{(2)}, \ldots, \mathbf{v}_\mathsf{f}^{(N)}$ the $H + 1$-dimensional PDF vectors of RVs $x^{(1)}, x^{(2)}, \ldots, x^{(N)}$, respectively, where each element of $\mathbf{v}_\mathsf{f}^{(n)}$ is given by

$$\mathbf{v}_\mathsf{f}^{(n)}[j] \triangleq \mathsf{f}_{x^{(n)}}(\mathcal{H}_\Delta[j]), \ j \in [H + 1]. \tag{2.49}$$

Note that with the above definition of PDF vector $\mathbf{v}_\mathsf{f}^{(n)}$, the following approximation holds: $1 = \int_{y \in \mathcal{S}^{(n)}} \mathsf{f}_{x^{(n)}}(y)\mathsf{d}y \approx \sum_{j=1}^{H+1} \mathbf{v}_\mathsf{f}^{(n)}[j]\,\Delta$, for each $n \in [N]$.

Next, using $J_\mathrm{FFT} > H + 1$ points (for efficient implementation J_FFT has to be a power of 2) the fast Fourier transform (FFT) of PDF $\mathbf{v}_\mathsf{f}^{(n)}$ is evaluated, which is the characteristic function of RV $x^{(n)}$. The vector of characteristic function of RV $x^{(n)}$ is given by

$$\boldsymbol{\phi}^{(n)} = \mathsf{FFT}\left(\widetilde{\mathbf{v}}_\mathsf{f}^{(n)}\,\Delta\right) \in \mathbb{C}^{J_\mathrm{FFT}} \tag{2.50}$$

where $(\widetilde{\mathbf{v}}_\mathsf{f}^{(n)})^\top = \left[(\mathbf{v}_\mathsf{f}^{(n)})^\top \ \mathbf{0}_{J_\mathrm{FFT}-(H+1)}^\top\right]^\top$ is the zero-padded version of $\mathbf{v}_\mathsf{f}^{(n)}$, appending extra $J_\mathrm{FFT} - (H + 1)$ zeros at the end $\mathbf{v}_\mathsf{f}^{(n)}$. Using the following facts: (a) the sum of independent random variables is the convolution of their associated PDFs and (b) the equivalence among convolution operation and the inverse Fourier transform of the product of Fourier transforms, the final PDF of x is obtained as

$$\mathbf{v}_{\mathsf{f}_x} = \mathsf{IFFT}\left(\boldsymbol{\phi}^{(1)} \odot \boldsymbol{\phi}^{(2)} \odot \ldots \odot \boldsymbol{\phi}^{(N)}\right)[1 : H + 1] \tag{2.51}$$

where vector $\mathbf{v}_{\mathsf{f}_x}$ consists of the first $H + 1$ elements of vector $\mathsf{IFFT}(\boldsymbol{\phi}^{(1)} \odot \boldsymbol{\phi}^{(2)} \odot \ldots \odot \boldsymbol{\phi}^{(N)})$ and is an approximation of the PDF of RV x. The CDF vector for RV x can be evaluated as

$$\mathbf{v}_{\mathsf{F}_x}[j] = \sum_{i=1}^{j} \mathbf{v}_{\mathsf{f}_x}[i]\,\Delta, \ j \in [H + 1]. \tag{2.52}$$

Note with the above methodology the evaluation of $\mathbf{v}_{\mathsf{f}_x}$ requires only $\mathcal{O}(N\, J_{\mathrm{FFT}}\, \log J_{\mathrm{FFT}})$ arithmetic operations due to the properties of FFT [65].

To evaluate Eq. (2.28) for a given threshold θ, the PDF of RV $u = \sum_{n=1}^{N-1} x^{(n)}$, $\mathbf{v}_{\mathsf{f}_u}$, is first calculated using Eq. (2.51) with $N-1$. Then, the index associated with largest element of $\mathcal{H}_\Delta$ that is smaller than θ is found, i.e., if $\theta^* = \arg\max\{y \in \mathcal{H}_\Delta : y \le \theta\}$ the optimal index j_θ satisfies $\theta^* = \mathcal{H}_\Delta[j_\theta]$, and then we calculate

$$\mathbf{v}_{\mathsf{F}_u}[j_\theta] - \sum_{i=1}^{j_\theta} \mathbf{v}_{\mathsf{F}_u}[j_\theta - i + 1]\, \mathbf{v}_{\mathsf{f}}^{(N)}[i]\, \Delta. \tag{2.53}$$

The overall complexity to calculate $\overline{N}^\star$ for the proposed model is dominated by the calculation of $\mathbf{v}_{\mathsf{f}_u}$ which is $\mathcal{O}(N\, J_{\mathrm{FFT}}\, \log J_{\mathrm{FFT}})$.

Proof of Proposition 2.3

Consider two continuous monotone (invertible) functions $\mathsf{h}_1 : \mathcal{X}_1 \longrightarrow \mathcal{X}_2$, $\mathsf{h}_2 : \mathcal{X}_2 \longrightarrow \mathcal{X}_3$ with $\mathcal{X}_1$, $\mathcal{X}_2$, $\mathcal{X}_3$ subsets of $\mathbb{R}$. The proof relies on the following facts from calculus:

- If $\mathsf{h}_1 : \mathcal{X}_1 \longrightarrow: \mathcal{X}_2$ is monotone increasing (decreasing) then $\mathsf{h}_1^{-1} : \mathcal{X}_2 \longrightarrow: \mathcal{X}_1$ is monotone increasing (decreasing) too.

- Function $\mathsf{h} \triangleq \mathsf{h}_2 \circ \mathsf{h}_1 : \mathcal{X}_1 \longrightarrow \mathcal{X}_3$, i.e., $\mathsf{h}_2(\mathsf{h}_1(\cdot))$, is also monotone and invertible with inverse $\mathsf{h}^{-1} = \mathsf{h}_1^{-1} \circ \mathsf{h}_2^{-1} : \mathcal{X}_3 \longrightarrow \mathcal{X}_1$.

- If h_1 is monotone decreasing and h_2 monotone increasing then $\mathsf{h} = \mathsf{h}_2 \circ \mathsf{h}_1$ is monotone decreasing. In addition, h^{-1} is monotone decreasing as well.

Using the above we now prove the proposition.

Let $x \mapsto \mathsf{h}_1(x) \triangleq \mathsf{Q}(x)$, with $\mathcal{X}_1 = [0, \infty)$ and $\mathcal{X}_2 = [0, 0.5]$, and $x \mapsto \mathsf{h}_2(x) \triangleq 2\, x\, (1-x)$, with $\mathcal{X}_2 = [0, 0.5]$ and $\mathcal{X}_3 = [0, 0.5]$. Note that $\mathsf{h}_1(x) = \mathsf{Q}(x)$ is monotone decreasing in $[0, \infty)$, while $\mathsf{h}_2(x) = 2\, x\, (1-x)$ is monotone increasing in $[0, 0.5]$, thus due to bullet 3 above, both $\mathsf{R}(\cdot)$ and $\mathsf{R}^{-1}(\cdot)$, given in Eq. (2.33) and (2.34), respectively, are monotone decreasing. Finally, the formula for $\mathsf{R}^{-1}(\cdot)$ is shown. Note that for $y \in [0, 0.5]$ the following quadratic equation

$$2x - 2x^2 = y \tag{2.54}$$

has roots

$$x = \frac{2 \mp \sqrt{4 - 8y}}{4}. \tag{2.55}$$

Function $h_2(\cdot)$ is monotone increasing, thus, according to bullet 1, $h_2^{-1}(\cdot)$ has to be monotone increasing too. The first root $\frac{2-\sqrt{4-8y}}{4}$ offers increasing inverse for $y \in [0, 0.5]$, thus $h_2^{-1}(y) = \frac{2-\sqrt{4-8y}}{4}$. Using the rule for the inverse of composition discussed in bullet 2, the following is obtained

$$R^{-1}(y) = (h_1^{-1} \circ h_2^{-1})(y) = Q^{-1}\left(\frac{2-\sqrt{4-8y}}{4}\right). \tag{2.56}$$

Proof of Proposition 2.4

The proof is provided for the proposed model, as the rest baseline models are special cases. The proof for the baseline models can be obtained trivially using similar reasoning. First note that since image points are selected as $0 < v_1 < v_2 < \ldots < v_M$, the slopes satisfy $l_1 < l_2 < \ldots < l_M$, thus piecewise-linear function $\widetilde{p}(\cdot)$ is monotone increasing in $[b_0, b_M]$ (and thus invertible in $[0, v_M]$).

Firstly, consider the case $0 < P_c < v_M$, implying that $b_0 < \widetilde{p}^{-1}(P_c) < b_M$. Using similar reasoning with Eq. (2.36), the probability of successful reception at interrogator for the proposed model can be expressed as

$$\mathbb{P}(\widetilde{S}) \triangleq \mathbb{P}\left(P_R > \frac{\sqrt{P_T}\, R^{-1}(\beta)\sigma_u}{\sqrt{\rho_u}} \cap \widetilde{P}_{har}(\zeta_{har}P_R) > P_c\right)$$

$$\overset{(a)}{=} \mathbb{P}\left(P_R > \theta_A \cap P_R > \frac{\widetilde{p}^{-1}(P_c)}{\zeta_{har}}\right)$$

$$\overset{(b)}{=} \mathbb{P}\left(P_R > \widetilde{\theta}_{max}\right) = 1 - F_{P_R}(\widetilde{\theta}_{max}), \tag{2.57}$$

where (a) stems from the definition of θ_A as well as the fact that $0 < P_c < v_M$, while (b) relies on the definition of $\widetilde{\theta}_{max}$. The result follows by plugging the CDF of P_R for Nakagami fading.

For $P_c \geq v_M$, the following hold

$$\widetilde{S} \subseteq \{P_R \in \mathbb{R}_+ : \widetilde{P}_{har}(\zeta_{har}P_R) > P_c\} \overset{(a)}{\subseteq} \{P_R \in \mathbb{R}_+ : \widetilde{P}_{har}(P_R) > v_M\}, \tag{2.58}$$

where (a) results from the following facts: (i) $P_c \geq v_M$ and (ii) $\widetilde{p}(\zeta_{har}P_R) \leq \widetilde{p}(P_R)$, since $\zeta_{har} \in (0, 1)$ and function $\widetilde{p}(\cdot)$ is non-decreasing. Thus, by the monotonicity of probability measure [61], Eq. (2.58) implies that $\mathbb{P}(\widetilde{S}) \leq \mathbb{P}\left(\widetilde{P}_{har}(P_R) > v_M\right) = 1 - F_{\widetilde{P}_{har}}(v_M) = 0$, due to the definition of CDF in Eq. (2.18). Hence, for $P_c \geq v_M$, $\mathbb{P}(\widetilde{S}) = 0$.

Chapter 3

Backscatter Radios: Fundamentals, Detection, and Channel Coding

This chapter offers the basic communication principles and physical layer receiver designs for scatter radio point-to-point systems. A detailed exposition of a scatter radio signal model is provided, incorporating all microwave, tag-related, and wireless channel parameters. The chapter in the sequel presents coherent and noncoherent detection and decoding reception schemes tailored to the scatter radio frequency shift-keying (FSK) signal model. FSK modulation is employed as it is an ideal option for the power-limited regime. Specific small block-length channel codes are harnessed at both ends of scatter radio link to reduce the resulting bit error rate (BER) at the reader. The proposed reception algorithms are ideal for short packet communication. The latter offers reduced processing delay at the reader within practically meaningful limits and allows for large-scale multi-tag processing. Detailed simulation study demonstrates that the BER performance gap between coherent and noncoherent reception depends on whether channel codes are employed, on the fading conditions (e.g., Rayleigh vs Rician vs no fading), as well as on the utilized coding interleaving depth; the choice of one coding scheme over the other depends on the wireless fading parameters and the design choice for extra diversity vs extra power gain. Finally, experimental outdoor results at 13 dBm transmission power corroborate the practicality of the proposed detection and decoding techniques for scatter radio systems. The material of this chapter facilitates the adoption of intelligent, low-power scatter radio devices in the sensing regime of several tens of meters, ideal for ultra-low-power Internet-of-Things applications.

Related Work

The basic ingredients of current scatter radio technology include the illuminating radio frequency (RF) emitter towards the *tags*, the reflecting tags (scatter radio nodes), that may be passive (i.e., powered by the illuminating RF field) or semi-passive (i.e., power by an ambient source or an external battery) and the receiving device of the backscattered (from the tags) signals, also known as the *reader*. In contrast to Marconi radios that consist of signal conditioning RF components, such as amplifiers, mixers or active filters, in scatter radios, the communication is accomplished by means of reflection; scattering can be achieved with a single RF transistor at each tag, significantly reducing the energy consumption and monetary cost compared to Marconi radios.

Backscatter radios are embedded in a plethora of commercial devices [66] and various interfaces [67, 68]. The most prominent use of scatter radio is in radio frequency identification (RFID) systems, principally utilized for inventorying, electronic tickets and people identification [66, 69]. RFID is also expected to play a key role in the evolution of Internet-of-things (IoT) and related applications [70]. Typical scatter radio RFID systems are *monostatic*, i.e., the illuminating transmitter and the receiver are part of the same device. RFID systems suffer from limited communication range, in the order of a few meters, due to the following reasons: (a) the illuminating signal from the interrogator is used for both powering and communication of the tag, (b) the tag's circuit has limited sensitivity and RF harvesting efficiency, and (c) there are high bitrates, reducing the received energy per bit.

Semi-passive tags, i.e., tags powered by external power sources, are more suitable for increased scatter radio communication ranges [13]. As the modulation at the tags requires only the termination of the tag/sensor antenna at different loads, ultra-low-power is required for communication purposes. Such small amount of power can be available from a battery or an ambient source, such as solar, RF or their combination [23], enabling perpetual sensing [71] even at small levels of ambient power [28]. Another option to further increase communication ranges is to employ scatter radio modulations suitable for power-limited regime, such as minimum-shift keying (MSK) or frequency-shift keying (FSK). The latter can be implemented with rather simple hardware logic at the tag and allows frequency-division multiplexing (FDM), i.e., each tag backscatters over a unique portion of the spectrum and the reader can decode concurrently the superposition of FSK-modulated backscattered signals of multiple tags.

Low bitrate symbol-by-symbol noncoherent reception of MSK for monostatic scatter radio is studied in [13]. The authors in [24] studied fading and correlation of the two-way (from illuminating antennas to the tags and from the tags back to the reader) backscatter

radio channel, with emphasis on multi-antenna systems. Work in [32,72], offered a detailed link budget analysis for backscatter systems incorporating microwave and tag-related parameters. Single-antenna detectors for two-collided scatter radio tags are proposed in [73], exploiting the inherent memory of FM0 line codes, used in commercial RFID. Recent work in [63] examined the protocol utilized at Gen2 RFID tags and re-designed signal processing reception algorithms (e.g., for symbol level synchronization, channel estimation, bit duration estimation) for coherent maximum-likelihood (ML) detection at a commodity, monostatic software-defined radio (SDR) reader.

Bistatic scatter radio was first experimentally demonstrated in [11, 12, 33]. In bistatic scatter radio the illuminating emitter and the receiver of the backscattered signals are dislocated, i.e., they are two separate devices. Signal processing reception algorithms for tags employing scatter radio on-off keying [11] or FSK [12] and SDR symbol-by-symbol noncoherent detector are offered in [33], also highlighting the additional difficulties due to the bistatic nature, e.g., carrier frequency offset (CFO) between the illuminating emitter and the receiver. Ranges one order of magnitude larger than conventional RFID were demonstrated. Small block-length error-correction channel codes for inherently resource-constrained tags are proposed in [74] designing heuristic soft-decision metrics for noncoherent decoding with FSK and bistatic principles; compared to the uncoded case experimental communication range increase was shown. Subsequent work in [37] proposed coherent detection and decoding with small block-length cyclic channel codes for the bistatic scatter radio architecture with FSK modulation. The compound channel vector incorporated all wireless channel and microwave, tag-related parameters and was estimated through a least-squares (LS) technique, exploiting a short training packet preamble (known at the receiver). Work in [75] offered generalized-likelihood ratio testing (GLRT)-optimal noncoherent sequence detection of uncoded orthogonal signaling, also showing its relation with commercial Gen2 RFID protocols.

Scatter radio testbeds in [76] and [38] demonstrated reception of bistatic scatter radio FSK with an embedded receiver for Bluetooth and UHF frequencies, respectively. The system in [38] achieved tag-to-reader range of 250 meters. The authors in [77] generated Wi-Fi transmissions using bistatic scatter radio principles, offering 3 orders of magnitude lower power than existing Wi-Fi chipsets and the achieved tag-to-reader ranges were up to 30 meters. Another example of Wi-Fi backscatter can be found in [78], where the tags translate the original transmitted 802.11b codeword to another valid 802.11b codeword that can be decoded by the Wi-Fi receiver. The system offers up to 54 meters communication ranges with a 200 kbps throughput.

Contributions

The contributions of this chapter can be summarized as:

- It is proved that the square-law symbol-by-symbol detector for uncoded scatter radio FSK, is an instance of a composite hypothesis test (CHT), and more specifically, of a hybrid CHT (HCHT).

- Noncoherent symbol-by-symbol and sequence detectors for uncoded scatter radio FSK are designed based on GLRT.

- A noncoherent HCHT decoding rule is designed for coded scatter radio FSK signals, ideal for small packet and small block-length channel codes.

- It is found that a fully interleaved system under coherent ML decoding for backscatter FSK, offers probability of bit error (BER) that decays with the minimum distance of the utilized code. This is the same diversity order as the text-book coherent ML decoders.

- An extensive BER performance evaluation of the proposed scatter radio receivers is offered under Rician, Rayleigh or no fading, assuming *fixed* energy per packet. It is found that for the uncoded case, noncoherent reception may outperform coherent reception under fixed energy per packet, accounting in the coherent case the energy spent at the preamble bits for channel estimation. For the coded case, the performance gap between coherent and noncoherent decoding depends on the fading conditions (e.g., Rayleigh vs Rician vs no fading), the depth of utilized interleaver, that determines the diversity gain.

- Experimental outdoor measurements (with scatter radio testbed) corroborate the practicality of the proposed detection and decoding techniques for scatter radio.

Organization and Notation

The rest of this chapter is organized as follows: Section 3.1 presents the system model, showing how the bistatic signal model can also describe the monostatic, and describes the utilized modulation scheme. Section 3.2 designs noncoherent receivers for scatter radio FSK incorporated in the bistatic setup. Section 3.3 reviews the channel estimation procedure in scatter radio and offer the maximum-likelihood (ML) coherent detectors and decoders. Simulation and experimental results are offered in Section 3.4 and 3.5, respectively.

Symbols $(\cdot)^\top$, $(\cdot)^{\mathsf{H}}$, $(\cdot)^*$ will denote the transpose, Hermitian, and complex conjugate, respectively, of a vector or matrix. Real-part and imaginary-part operations are denoted by $\Re\{\cdot\}$ and $\Im\{\cdot\}$, respectively. The phase of a complex number z is denoted as $\angle z$. The distribution of a proper complex Gaussian $N \times 1$ vector $\mathbf{x}$ with mean $\boldsymbol{\mu}$ and covariance matrix $\boldsymbol{\Sigma}$ is denoted by $\mathcal{CN}(\boldsymbol{\mu}, \boldsymbol{\Sigma}) \triangleq \frac{1}{\pi^N \det(\boldsymbol{\Sigma})} \mathrm{e}^{-(\mathbf{x}-\boldsymbol{\mu})^{\mathsf{H}} \boldsymbol{\Sigma}^{-1}(\mathbf{x}-\boldsymbol{\mu})}$. $\mathcal{U}[a, b)$ and $\mathcal{N}(\mu, \sigma^2)$ denote, respectively, the uniform distribution in $[a, b)$ and the Gaussian distribution with mean μ and variance σ^2. Notation $\mathsf{f}_{\mathbf{x}|\boldsymbol{\theta}}(\cdot|\cdot)$ stands for the conditional probability density function (PDF) of random vector $\mathbf{x}$ parameterized by a random or deterministic vector $\boldsymbol{\theta}$. The expectation operator associated with conditional PDF $\mathsf{f}_{\mathbf{x}|\boldsymbol{\theta}}(\cdot|\cdot)$ of any function $\mathsf{g}(\mathbf{x}, \boldsymbol{\theta})$ is denoted as $\underset{\mathbf{x}|\boldsymbol{\theta}}{\mathbb{E}}[\mathsf{g}(\mathbf{x}, \boldsymbol{\theta})] \triangleq \int_{\mathbf{x}} \mathsf{g}(\mathbf{x}, \boldsymbol{\theta}) \mathsf{f}_{\mathbf{x}|\boldsymbol{\theta}}(\mathbf{x}|\boldsymbol{\theta}) \mathrm{d}\mathbf{x}$.

3.1 Scatter Radio Signal Model

Bistatic scatter radio consists of a carrier emitter (CE), a RF tag, and a software-defined radio (SDR) reader (a graphical illustration is provided in Fig. 3.1). Due to relatively small bitrate (in the order of kilo-bits per second), or equivalently large nominal bit period T, along with the small channel delay spread, frequency non-selective (flat) fading channel [79] is assumed, with complex baseband response given by:

$$h_{\mathrm{m}}(t) = h_{\mathrm{m}} = a_{\mathrm{m}}\, \mathrm{e}^{-\mathrm{j}\phi_{\mathrm{m}}},\ \mathrm{m} \in \{\mathrm{CR}, \mathrm{CT}, \mathrm{TR}\}, \tag{3.1}$$

where $a_{\mathrm{CR}}, a_{\mathrm{CT}}, a_{\mathrm{TR}} \in \mathbb{R}_+$ denote the channel attenuation parameters of the corresponding links and $\phi_{\mathrm{CR}}, \phi_{\mathrm{CT}}, \phi_{\mathrm{TR}} \in [0, 2\pi)$ the respective phases. Due to the bistatic setup in Fig. 3.1, the distance between the antennas of different devices is several wavelengths apart and thus, the channel response parameters are considered statistically independent of each other; channel parameters change independently every T_{coh} seconds, where T_{coh} is the coherence time.

For outdoor environments, there exists strong line-of-sight (LOS) signal for each individual link, and thus, channel parameters are assumed Rician random variables (RVs) [27], i.e., for $\mathrm{m} \in \{\mathrm{CR}, \mathrm{CT}, \mathrm{TR}\}$,

$$h_{\mathrm{m}} \sim \mathcal{CN}\left(\sqrt{\frac{\kappa_{\mathrm{m}}}{\kappa_{\mathrm{m}}+1}} \sigma_{\mathrm{m}}, \frac{\sigma_{\mathrm{m}}^2}{\kappa_{\mathrm{m}}+1}\right). \tag{3.2}$$

Rician parameter κ_{m} stands for the ratio between the power in the direct path and the power in the scattered paths of link $\mathrm{m} \in \{\mathrm{CR}, \mathrm{CT}, \mathrm{TR}\}$. The distribution of channel
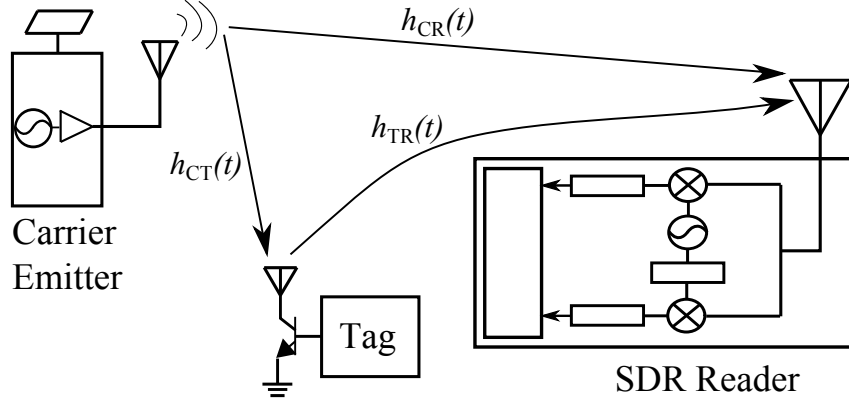
Figure 3.1: Bistatic architecture: carrier emitter (CE) is located away from software-defined radio (SDR) reader; RF tag modulates and backscatters the incident RF signal from CE towards the SDR reader.

amplitude a_m for link $m \in \{CR, CT, TR\}$ is Rice, given by:

$$\mathsf{f}_{a_m}(x) = 2\frac{\kappa_m + 1}{\sigma_m^2} x\, \mathsf{e}^{-\left(\kappa_m + \frac{(\kappa_m+1)x^2}{\sigma_m^2}\right)} \mathsf{I}_0\left(\frac{2\,x}{\sigma_m}\sqrt{\kappa_m(\kappa_m + 1)}\right), \ x \geq 0, \tag{3.3}$$

where $\mathsf{I}_0(\cdot)$ is the modified Bessel of the first kind and order zero [80, p. 47]. It is noted that for $\kappa_m = 0$, Rayleigh fading is obtained, while for $\kappa_m = \infty$, Gaussian channel is obtained with the parameter a_m being deterministic constant, i.e., $a_m = \sigma_m$, $m \in \{CR, CT, TR\}$. It is noted that the channel power of link m, given by $\mathbb{E}\left[|h_m|^2\right] = \sigma_m^2$, is independent of κ_m. For exposition purposes and without loss of generality, $\sigma_m^2 = 1$, $m \in \{CR, CT, TR\}$, is assumed hereafter.

CE transmits a continuous sinusoid wave at carrier frequency F_{car} whose complex baseband representation is

$$\mathsf{c}(t) = \sqrt{2P_C}\, \mathsf{e}^{-\mathsf{j}(2\pi\Delta F t + \Delta\phi)}, \tag{3.4}$$

where P_C is the carrier transmission power at passband, ΔF and $\Delta\phi$ model the carrier frequency and carrier phase offset between CE and SDR reader, respectively. $\Delta\phi$ is modeled as a uniform RV in $[0, 2\pi)$.

The carrier wave $\mathsf{c}(t)$, propagated through wireless channel h_{CT}, illuminates the antenna of the tag. The incident signal at tag is attenuated and rotated due to the channel gain $a_{CT}\, \mathsf{e}^{-\mathsf{j}\phi_{CT}}$. Portion of the incident signal is reflected back; the specific attenuation is related to the tag's scattering efficiency. Let s be denoting the scattering efficiency attenuation, which is considered constant for a duration of a packet. For two distinct tag load values (i.e., binary modulation at the tag), the baseband scattered waveform from

tag is [33]:

$$\mathsf{u}_i(t) = \mathsf{s}\left(\left(\mathtt{A}_s - \frac{\Gamma_0 + \Gamma_1}{2}\right) + \frac{\Gamma_0 - \Gamma_1}{2}\,\mathsf{b}_i(t)\right)a_{\mathrm{CT}}\,\mathsf{e}^{-\mathsf{j}\phi_{\mathrm{CT}}}\mathsf{c}(t),\ \ i \in \mathbb{B},\qquad(3.5)$$

where $\mathsf{b}_i(t)$ corresponds to the complex baseband waveform for bit $i \in \mathbb{B} \triangleq \{0,1\}$. The term $\mathsf{v}_0 \triangleq \mathtt{A}_s - \frac{\Gamma_0 + \Gamma_1}{2}$ is a DC constant depending on the (load-independent) tag antenna structural mode $\mathtt{A}_s$ [81] and the (tag load-dependent) tag reflection coefficients Γ_0 and Γ_1. As the scatter radio modulator at each tag does not include any type of signal conditioning units (e.g., amplifiers, filters or mixers) there is no noise term in Eq. (3.5). The absence of signal conditioning at each tag offers low-power consumption and is the main advantage of scatter radio.

In this work FSK modulation is employed at tags, thus, for FSK modulation, waveform $\mathsf{b}_i(t)$ represents the fundamental frequency component of a 50% duty cycle square waveform[1] of period $1/F_i$ and random initial phase Φ_i:

$$\mathsf{b}_i(t) = \frac{4}{\pi}\cos(2\pi F_i t + \Phi_i)\,\Pi_T(t),\ \ i \in \mathbb{B},\qquad(3.6)$$

where $\Pi_T(t)$ is the rectangular pulse of bit duration T, given by:

$$\Pi_T(t) \triangleq \begin{cases} 1, & 0 \leq t < T, \\ 0, & \text{otherwise.} \end{cases}\qquad(3.7)$$

$\Phi_i \sim \mathcal{U}[0, 2\pi)$ models the phase mismatch between tag and SDR reader when bit $i \in \mathbb{B}$ is transmitted, assumed constant for a duration of a packet. RVs Φ_0 and Φ_1 are assumed independent of each other. In addition, vector $\boldsymbol{\Phi} \triangleq [\Phi_0\ \Phi_1]^\top$ is also defined.

For the duration of single bit, T, the received demodulated complex baseband signal at the SDR reader is given by the superposition of the CE sinusoid and the backscattered

---

[1]It can be shown that the fundamental frequency component holds $\approx 80\%$ of the total power of the 50% duty cycle square pulse [13].

tag signal propagated through wireless channels h_{CR} and h_{TR}, respectively, i.e.,

$$
\begin{aligned}
\mathsf{y}(t) &= a_{\mathrm{CR}}\,\mathsf{e}^{-\mathsf{j}\phi_{\mathrm{CR}}}\,\mathsf{c}(t) + a_{\mathrm{TR}}\,\mathsf{e}^{-\mathsf{j}\phi_{\mathrm{TR}}}\,\mathsf{u}_i(t) + \mathsf{n}(t) \\[2mm]
&= \Bigg(\underbrace{\sqrt{2P_c}\,\mathsf{e}^{-\mathsf{j}\Delta\phi}\bigg(a_{\mathrm{CR}}\,\mathsf{e}^{-\mathsf{j}\phi_{\mathrm{CR}}} + \mathsf{s}\,\mathsf{v_0}\,a_{\mathrm{CT}}\,a_{\mathrm{TR}}\,\mathsf{e}^{-\mathsf{j}(\phi_{\mathrm{CT}}+\phi_{\mathrm{TR}})}\bigg)}_{\text{DC term}} \\[2mm]
&\quad + \sqrt{2P_c}\,\frac{2\,|\Gamma_0 - \Gamma_1|\,\mathsf{s}\,a_{\mathrm{CT}}\,a_{\mathrm{TR}}}{\pi}\,\mathsf{e}^{-\mathsf{j}\big(\phi_{\mathrm{CT}}+\phi_{\mathrm{TR}}+\Delta\phi+\underline{/\Gamma_0 - \Gamma_1}\big)}\,\cos\left(2\pi F_i t + \Phi_i\right)\Pi_T(t) \Bigg) \\[2mm]
&\quad \cdot\,\mathsf{e}^{-\mathsf{j}2\pi\Delta F t} + \mathsf{n}(t),
\end{aligned}
\tag{3.8}
$$

where $\mathsf{n}(t)$ is a complex, circularly symmetric, additive Gaussian noise process with power spectral density given by:

$$
\mathsf{S_n}(F) = \begin{cases} N_0, & |F| \le W_{\mathrm{SDR}} \\ 0, & \text{otherwise,} \end{cases}
\tag{3.9}
$$

where W_{SDR} denotes the SDR receiver bandwidth and $N_0 = \mathsf{k_b}\mathsf{T}_\theta$, where $\mathsf{k_b}$ and T_θ are the Boltzmann constant and receiver temperature, respectively.

The signal in Eq. (3.8) contains carrier frequency offset (CFO) ΔF, which can be directly estimated using periodogram-based techniques, and subsequently, compensated. It is apparent in Eq. (3.8) that CFO depends on all terms, including the DC terms. Therefore, tag-dependent parameters such as A_s, typically overlooked in the literature, do play important role in the CFO estimation step. SDR reader applies CFO compensation, and then eliminates the DC terms of the signal in (3.8) by estimation and removal of the received signal's time average [33]. Assuming perfect synchronization and CFO estimation, the DC-blocked received signal of Eq. (3.8) over a bit period T, can be simplified to:

$$
\widetilde{\mathsf{y}}(t) = \mu\,a\,\mathsf{e}^{-\mathsf{j}\phi}\,\cos\left(2\pi F_i t + \Phi_i\right)\Pi_T(t) + \mathsf{n}(t),
\tag{3.10}
$$

where the following abbreviations are utilized:

$$
a \triangleq a_{\mathrm{CT}}\,a_{\mathrm{TR}}, \quad \phi \triangleq \phi_{\mathrm{CT}} + \phi_{\mathrm{TR}} + \Delta\phi + \underline{/\Gamma_0 - \Gamma_1},
\tag{3.11}
$$

$$
\mu \triangleq \sqrt{2P_{\mathrm{C}}}\,\frac{|\Gamma_0 - \Gamma_1|}{2}\,\frac{4}{\pi}\,\mathsf{s} = \sqrt{2P_{\mathrm{C}}}\,|\Gamma_0 - \Gamma_1|\,\frac{2}{\pi}\,\mathsf{s}.
\tag{3.12}
$$

Expanding the cosine term in (3.10) it follows that:

$$\tilde{y}(t) = \frac{\mu\,h}{2}\left(e^{j(2\pi F_i t + \Phi_i)} + e^{-j(2\pi F_i t + \Phi_i)}\right)\Pi_T(t) + n(t), \tag{3.13}$$

with scalar

$$h \triangleq a\,e^{-j\phi} \tag{3.14}$$

be denoting the compound channel parameter including some phase and wireless channel fading parameters.

For $F_i \gg \frac{1}{T}$, $i \in \mathbb{B}$, the instantaneous received energy per bit is defined as:

$$E(a) \triangleq \int_0^T \left|\mu\,a\,e^{-j\phi}\cos(2\pi F_i t + \Phi_i)\right|^2 dt \approx \frac{T\mu^2 a^2}{2}, \tag{3.15}$$

where $\int_0^T \cos^2(2\pi F_i t + \Phi_i)dt \approx \frac{T}{2}$ is exploited, due to $F_i \gg \frac{1}{T}$. The average received energy per bit and the average received SNR are defined as:

$$E = \mathbb{E}_a[E(a)] = \frac{T\mu^2}{2} = \frac{4\,T\,P_C\,|\Gamma_0 - \Gamma_1|^2\,s^2}{\pi^2}, \tag{3.16}$$

$$SNR \triangleq \frac{E}{N_0} = \frac{T\,\mu^2}{2N_0} = \frac{4\,T\,P_C\,|\Gamma_0 - \Gamma_1|^2\,s^2}{N_0\,\pi^2}. \tag{3.17}$$

For each bit $i \in \mathbb{B}$, the received signal in (3.13) contains two exponential frequencies $\pm F_i$ and not one; thus, a classic FSK demodulator for conventional (Marconi) radio loses half of the signal and results in a 3-dB BER performance loss for bistatic FSK [33]. It is not difficult to see that for $|F_1 - F_0| = \frac{k}{T}$, $k \in \mathbb{N}$, along with $F_i \gg \frac{1}{T}$, $i \in \mathbb{B}$ (that implies that $F_i + F_0 \gg \frac{1}{T}$ or $F_i + F_1 \gg \frac{1}{T}$), the set $\left\{\frac{1}{\sqrt{T}}e^{\pm j2\pi F_i t}\Pi_T(t)\right\}_{i \in \mathbb{B}}$ constitutes a 4-dimensional orthonormal basis, that can be used for expansion of the received signal in (3.13). The next theorem exploits the above 4-dimensional basis and offers the discrete baseband equivalent scatter radio FSK signal model.

Theorem 3.1. For $F_i + \frac{20}{T} \ll W_{\mathrm{SDR}}$, the baseband equivalent signal over a bit duration T is given by the following 4-dimensional complex vector

$$\mathbf{r} = \begin{bmatrix} r_0^+ \\ r_0^- \\ r_1^+ \\ r_1^- \end{bmatrix} = h\sqrt{\frac{E}{2}}\begin{bmatrix} e^{+j\Phi_0} \\ e^{-j\Phi_0} \\ e^{+j\Phi_1} \\ e^{-j\Phi_1} \end{bmatrix} \odot \mathbf{s}_i + \begin{bmatrix} n_0^+ \\ n_0^- \\ n_1^+ \\ n_1^- \end{bmatrix}, \tag{3.18}$$

where vector $\mathbf{s}_i = [(1-i)\ (1-i)\ i\ i]^\top$ corresponds to bit $i \in \mathbb{B}$. Symbol $\odot$ denotes the component-wise (Hadamard) product and 4-dimensional complex, circularly symmetric

Gaussian noise vector $\mathbf{n}$ is distributed according to:

$$\mathbf{n} \triangleq [n_0^+ \ n_0^- \ n_1^+ \ n_1^-]^\top \sim \mathcal{CN}\left(\mathbf{0}_4, N_0 \mathbf{I}_4\right). \tag{3.19}$$

Proof. The proof is given in Appendix 3.6. $\square$

It is noted that the system model above has been verified experimentally [11, 12, 17, 33, 82, 83]. It is also noted that it is general enough to describe monostatic scatter radio (where illuminating carrier emitter and receiver belong to the same reader unit) as a special case, with h_{CR} (and appropriate $\kappa_{\mathrm{CR}}, \sigma_{\mathrm{CR}}$) modeling the leakage from the transmit to the receive RF chain of the reader.

3.2   Noncoherent Scatter Radio Reception

3.2.1   Uncoded Symbol-By-Symbol Detection

The optimal noncoherent symbol-by-symbol detector in terms of bit error rate (BER), is the maximum-likelihood (ML) detector, expressed as:

$$\mathsf{f}_{\mathbf{r}|i}(\mathbf{r}|0) \underset{i=1}{\overset{i=0}{\gtrless}} \mathsf{f}_{\mathbf{r}|i}(\mathbf{r}|1) \iff \underset{h,\boldsymbol{\Phi}}{\mathbb{E}}\left[\mathsf{f}_{\mathbf{r}|i,h,\Phi_0}(\mathbf{r}|0, h, \Phi_0)\right] \underset{i=1}{\overset{i=0}{\gtrless}} \underset{h,\boldsymbol{\Phi}}{\mathbb{E}}\left[\mathsf{f}_{\mathbf{r}|i,h,\Phi_1}(\mathbf{r}|1, h, \Phi_1)\right]. \tag{3.20}$$

Note that due to Eqs. (3.18) and (3.19),

$$\mathsf{f}_{\mathbf{r}|i,h,\boldsymbol{\Phi}}(\mathbf{r}|i, h, \boldsymbol{\Phi}) \equiv \mathcal{CN}\left(h\,\mathbf{x}_i(\boldsymbol{\Phi}), N_0 \mathbf{I}_4\right), \tag{3.21}$$

with $\mathbf{x}_i(\boldsymbol{\Phi}) = \sqrt{\frac{\mathsf{E}}{2}}\left[\mathsf{e}^{+\mathsf{j}\Phi_0}, \mathsf{e}^{-\mathsf{j}\Phi_0}, \mathsf{e}^{+\mathsf{j}\Phi_1}, \mathsf{e}^{-\mathsf{j}\Phi_1}\right]^\top \odot \mathbf{s}_i$. For the bistatic scatter radio signal model, the ML rule in (3.20) does not admit closed-form expression for Rician parameters $\kappa_{\mathrm{CT}}, \kappa_{\mathrm{TR}} \in [0, +\infty)$, and thus, alternative noncoherent detection rules should be designed.

Noncoherent Hybrid Composite Hypothesis-Testing (NC-HCHT) Symbol-By-Symbol FSK Detection

The first proposed noncoherent symbol-by-symbol detection rule is the NC-HCHT detector that treats the unknowns Φ_0 and Φ_1 as random parameters, while h is viewed as a nonrandom parameter; thus, NC-HCHT detector is given by:

$$\arg\max_{i\in\mathbb{B}}\left\{\underset{\boldsymbol{\Phi}}{\mathbb{E}}\left[\max_{h\in\mathbb{C}} \ln\left[\mathsf{f}_{\mathbf{r}|i,h,\boldsymbol{\Phi}}(\mathbf{r}|i, h, \boldsymbol{\Phi})\right]\right]\right\}. \tag{3.22}$$

Lemma 3.1. The noncoherent detector of Eq. (3.22) is channel-agnostic and is equivalent to:

$$|r_0^+|^2 + |r_0^-|^2 \underset{i=1}{\overset{i=0}{\gtrless}} |r_1^+|^2 + |r_1^-|^2, \tag{3.23}$$

i.e., the detector in (3.22) is the square-law detector.

Proof. For hypothesis $i = 0$, $\mathbf{x}_0(\mathbf{\Phi})$ depends solely on Φ_0, i.e., $\mathbf{x}_0(\Phi_0)$, and for the innermost maximization in (3.22) deterministic parameter h is eliminated as:

$$\arg \max_{h \in \mathbb{C}} \ln\left[\mathsf{f}_{\mathbf{r}|i,h,\Phi_0}(\mathbf{r}|0, h, \Phi_0)\right]$$

$$= \arg \min_{h \in \mathbb{C}} \|\mathbf{r} - h\mathbf{x}_0(\Phi_0)\|_2^2 \implies h_{\text{opt}} = \frac{(\mathbf{x}_0(\Phi_0))^{\mathsf{H}} \mathbf{r}}{\|\mathbf{x}_0(\Phi_0)\|_2^2}. \tag{3.24}$$

As a result, plugging the optimal h back:

$$\max_{h \in \mathbb{C}} \ln\left[\mathsf{f}_{\mathbf{r}|i,h,\Phi_0}(\mathbf{r}|0, h, \Phi_0)\right] = \ln\left[\mathsf{f}_{\mathbf{r}|i,h,\Phi_0}(\mathbf{r}|0, h_{\text{opt}}, \Phi_0)\right]$$

$$= 4\ln\left(\frac{1}{\pi N_0}\right) - \frac{1}{N_0}\left(\|\mathbf{r}\|_2^2 - \frac{|\mathbf{r}^{\mathsf{H}}\mathbf{x}_0(\Phi_0)|^2}{\|\mathbf{x}_0(\Phi_0)\|_2^2}\right)$$

$$= 4\ln\left(\frac{1}{\pi N_0}\right) - \frac{1}{N_0}\left(\|\mathbf{r}\|_2^2 - \frac{1}{2}\left|(r_0^+)^*\mathsf{e}^{\mathsf{j}\Phi_0} + (r_0^-)^*\mathsf{e}^{-\mathsf{j}\Phi_0}\right|^2\right)$$

$$= 4\ln\left(\frac{1}{\pi N_0}\right) - \frac{1}{N_0}\|\mathbf{r}\|_2^2 + \frac{1}{2N_0}\left(|r_0^+|^2 + |r_0^-|^2\right) + \frac{1}{N_0}\Re\left\{(r_0^+)^*(r_0^-)\mathsf{e}^{2\mathsf{j}\Phi_0}\right\}. \tag{3.25}$$

Only the last term in (3.25) depends on Φ_0, and thus, applying expectation with respect to $\mathbf{\Phi}$ in the last term in (3.25) offers

$$\mathbb{E}_{\mathbf{\Phi}}\left[\Re\left\{(r_0^+)^*(r_0^-)\mathsf{e}^{2\mathsf{j}\Phi_0}\right\}\right] = \mathbb{E}_{\Phi_0}\left[\Re\left\{(r_0^+)^*(r_0^-)\mathsf{e}^{2\mathsf{j}\Phi_0}\right\}\right] = 0, \tag{3.26}$$

where Eq. (3.26) relies on the fact that $\Phi_0 \sim \mathcal{U}[0, 2\pi)$. Therefore, applying expectation with respect to $\mathbf{\Phi}$ in (3.25) the last term is eliminated. Since $\Phi_1 \sim \mathcal{U}[0, 2\pi)$, applying similar reasoning for hypothesis $i = 1$, the detection rule of Eq. (3.23) is obtained after some elementary algebra. $\qquad \square$

Interestingly, the above square-law detector has been also proposed in [33] as a heuristic noncoherent detection rule.

Proposition 3.1. For Rayleigh fading, i.e., $\kappa_{\text{CT}} = \kappa_{\text{TR}} = 0$, the detector in (3.23) offers BER given by:

$$\Pr(e) = \frac{\mathsf{e}^{\frac{2}{\text{SNR}}}\left(5\text{SNR} + 2\right)\mathsf{E}_1\left(\frac{2}{\text{SNR}}\right) - \text{SNR}}{4\text{SNR}^2}, \tag{3.27}$$

where function $\mathsf{E}_1(x) = \int_x^\infty \frac{\mathsf{e}^{-t}}{t} \mathsf{d}t$ for $x > 0$ [84, p. 150].

Proof. In Appendix 3.6. $\qquad\qquad\qquad\qquad\qquad\qquad\qquad\qquad\qquad\qquad\quad$ □

Noncoherent Generalized Likelihood-Ratio Test (NC-GLRT) Symbol-By-Symbol FSK Detection

The NC-GLRT symbol-by-symbol detection rule treats the unknowns Φ_0, Φ_1 and h as deterministic parameters and can be expressed as:

$$\arg\max_{i\in\mathbb{B}} \left\{ \max_{\boldsymbol{\Phi}\in[0,2\pi)^2} \max_{h\in\mathbb{C}} \ln\Big[\mathsf{f}_{\mathbf{r}|i,h,\boldsymbol{\Phi}}(\mathbf{r}|i,h,\boldsymbol{\Phi}) \Big] \right\}. \tag{3.28}$$

Theorem 3.2. The detector of Eq. (3.28) is channel-agnostic and is equivalent to:

$$|r_0^+| + |r_0^-| \underset{i=1}{\overset{i=0}{\gtrless}} |r_1^+| + |r_1^-|. \tag{3.29}$$

Proof. The proof relies on fact that for any complex number α,

$$|\alpha| = \max_{v\in\mathbb{C}:|v|=1} \Re\{\alpha v^*\} = \max_{\varphi\in[0,2\pi)} \Re\Big\{ \alpha\mathsf{e}^{-\mathsf{j}\varphi} \Big\}. \tag{3.30}$$

Using Lemma 3.1, for $i = 0$, the innermost maximization in (3.28) is simplified to Eq. (3.25), depending solely on Φ_0. Applying maximization with respect to vector $\boldsymbol{\Phi} \in [0, 2\pi)^2$ in (3.25) affects only the last term Eq. (3.25); thus, in view of (3.30), the following holds:

$$\max_{\Phi_1\in[0,2\pi)} \max_{\Phi_0\in[0,2\pi)} \Re\left\{ (r_0^+)^*(r_0^-)\mathsf{e}^{2\mathsf{j}\Phi_0} \right\} = |r_0^+||r_0^-|, \tag{3.31}$$

where we exploited that $\Re\left\{ (r_0^+)^*(r_0^-)\mathsf{e}^{2\mathsf{j}\Phi_0} \right\}$ is a periodic function of Φ_0 with period π. Hence,

$$\max_{\boldsymbol{\Phi}\in[0,2\pi)^2} \max_{h\in\mathbb{C}} \ln\Big[\mathsf{f}_{\mathbf{r}|i,h,\Phi_0}(\mathbf{r}|0,h,\Phi_0) \Big] = 4\ln\left(\frac{1}{\pi N_0} \right) - \frac{1}{N_0}\|\mathbf{r}\|_2^2 + \frac{1}{2N_0}\Big(|r_0^+| + |r_0^-| \Big)^2. \tag{3.32}$$

Working similarly for $i = 1$, the result in (3.29) follows after elementary algebra. $\qquad$ □

3.2.2 Uncoded Sequence Detection

It is a well-known fact that when bit period T is smaller than channel coherence time T_{coh} noncoherent symbol-by-symbol detection is not BER-optimal in flat fading and instead, noncoherent *sequence* detection must be employed (e.g., [85] and references therein). For

static (immobile) scatter radio sensor networks, the above scenario of $T_{\mathrm{coh}} \gg T$ is possible. However, classic noncoherent sequence detection based on exhaustive search may be prohibitive, due to its exponential (in the sequence length) complexity. In this section, recent results in noncoherent sequence detection with log-linear complexity for orthogonal modulations are revisited from [85], in order to to design a noncoherent GLRT sequence detection for backscatter FSK, denoted as NC-GLRT.

Let $T_{\mathrm{coh}} = N_{\mathrm{coh}} T$, where N_{coh} denotes the number of symbols affected by the same channel coefficient and let $N_{\mathrm{coh}} \in \mathbb{N}$, for simplicity. Transmission of a bit sequence consisting of N_{s} information bits is considered, denoted as $\mathbf{i} = [i_1 \ i_2 \ \ldots \ i_{N_{\mathrm{s}}}]^\top \in \mathbb{B}^{N_{\mathrm{s}}}$, assuming $N_{\mathrm{s}} \leq N_{\mathrm{coh}}$. The associated received sequence, over a duration of N_{s} bits consists of the concatenation of N_{s} received vectors $\mathbf{r}_1, \mathbf{r}_2, \ldots, \mathbf{r}_{N_{\mathrm{s}}}$; each of them can be further expanded as in (3.18):

$$
\mathbf{r}_{1:N_{\mathrm{s}}} =
\begin{bmatrix} \mathbf{r}_1 \\ \mathbf{r}_2 \\ \vdots \\ \mathbf{r}_{N_{\mathrm{s}}} \end{bmatrix}
= h
\begin{bmatrix} \mathbf{x}_{i_1}(\mathbf{\Phi}) \\ \mathbf{x}_{i_2}(\mathbf{\Phi}) \\ \vdots \\ \mathbf{x}_{i_{N_{\mathrm{s}}}}(\mathbf{\Phi}) \end{bmatrix}
+
\begin{bmatrix} \mathbf{n}_1 \\ \mathbf{n}_2 \\ \vdots \\ \mathbf{n}_{N_{\mathrm{s}}} \end{bmatrix},
\tag{3.33}
$$

where $\mathbf{r}_n = \begin{bmatrix} r_0^+(n) & r_0^-(n) & r_1^+(n) & r_1^-(n) \end{bmatrix}^\top$ stands for the 4-dimensional received vector for the nth time instant and

$$
\mathbf{x}_{i_n}(\mathbf{\Phi}) \triangleq \sqrt{\frac{\mathsf{E}}{2}} \begin{bmatrix} \mathrm{e}^{\mathrm{j}\Phi_0} & \mathrm{e}^{-\mathrm{j}\Phi_0} & \mathrm{e}^{\mathrm{j}\Phi_1} & \mathrm{e}^{-\mathrm{j}\Phi_1} \end{bmatrix}^\top \odot \mathbf{s}_{i_n},
\tag{3.34}
$$

with $\mathbf{s}_{i_n} = [1 - i_n \ 1 - i_n \ i_n \ i_n]^\top$, $i_n \in \mathbb{B}$, $n = 1, 2, ..., N_{\mathrm{s}}$. Using the same reasoning with (3.19), the noise statistics in Eq. (3.33) are $\begin{bmatrix} \mathbf{n}_1^\top \ \mathbf{n}_2^\top \ \ldots \ \mathbf{n}_{N_{\mathrm{s}}}^\top \end{bmatrix}^\top \sim \mathcal{CN}\left(\mathbf{0}_{4N_{\mathrm{s}}}, N_0 \mathbf{I}_{4N_{\mathrm{s}}}\right)$. Additionally, vector $\mathbf{x_i}(\mathbf{\Phi}) \triangleq \begin{bmatrix} \mathbf{x}_{i_1}^\top(\mathbf{\Phi}) \ \mathbf{x}_{i_2}^\top(\mathbf{\Phi}) \ \ldots \ \mathbf{x}_{i_{N_{\mathrm{s}}}}^\top(\mathbf{\Phi}) \end{bmatrix}^\top$ is also defined. From (3.33) and the noise statistics above, the following is obtained,

$$
\mathsf{f}_{\mathbf{r}_{1:N_{\mathrm{s}}}|\mathbf{i},h,\mathbf{\Phi}}\left(\mathbf{r}_{1:N_{\mathrm{s}}}|\mathbf{i},h,\mathbf{\Phi}\right) \equiv \mathcal{CN}\left(h\,\mathbf{x_i}(\mathbf{\Phi}), N_0 \mathbf{I}_{4N_{\mathrm{s}}}\right),
\tag{3.35}
$$

implying that $\mathbf{r}_1, \mathbf{r}_2, .., \mathbf{r}_{N_{\mathrm{s}}}$ are conditionally independent of each other given parameters $h, \mathbf{\Phi}$, and any transmitted sequence $\mathbf{i}$. As in Section 3.2.1, the NC-GLRT detection metric

over the sequence $\mathbf{i}$ can be expressed as:

$$\max_{\mathbf{i}\in\mathbb{B}^{N_\mathrm{s}}} \max_{\mathbf{\Phi}\in[0,2\pi)^2} \max_{h\in\mathbb{C}} \ln\left[f_{\mathbf{r}_{1:N_\mathrm{s}}|\mathbf{i},h,\mathbf{\Phi}}\left(\mathbf{r}_{1:N_\mathrm{s}}|\mathbf{i},h,\mathbf{\Phi}\right)\right]$$
$$= \max_{\mathbf{\Phi}\in[0,2\pi)^2} \max_{\mathbf{i}\in\mathbb{B}^{N_\mathrm{s}}} \max_{h\in\mathbb{C}} \ln\left[f_{\mathbf{r}_{1:N_\mathrm{s}}|\mathbf{i},h,\mathbf{\Phi}}\left(\mathbf{r}_{1:N_\mathrm{s}}|\mathbf{i},h,\mathbf{\Phi}\right)\right]. \tag{3.36}$$

For fixed $\mathbf{\Phi}\in[0,2\pi)^2$ in (3.36), in accordance with the derivation of (3.25) in Lemma 3.1,

$$\arg\max_{\mathbf{i}\in\mathbb{B}^{N_\mathrm{s}}} \max_{h\in\mathbb{C}} \ln\left[f_{\mathbf{r}_{1:N_\mathrm{s}}|\mathbf{i},h,\mathbf{\Phi}}\left(\mathbf{r}_{1:N_\mathrm{s}}|\mathbf{i},h,\mathbf{\Phi}\right)\right] = \arg\max_{\mathbf{i}\in\mathbb{B}^{N_\mathrm{s}}} \left|(\mathbf{r}_{1:N_\mathrm{s}})^{\mathsf{H}}\mathbf{x}_\mathbf{i}(\mathbf{\Phi})\right|, \tag{3.37}$$

where Eq. (3.37) was obtained by plugging in the optimal h, $h_{\mathrm{opt}} = \frac{(\mathbf{x}_\mathbf{i}(\mathbf{\Phi}))^{\mathsf{H}}\mathbf{r}_{1:N_\mathrm{s}}}{\|\mathbf{x}_\mathbf{i}(\mathbf{\Phi})\|_2^2}$ and dropping out terms that do not affect the optimization problem. Thus, using Eq. (3.37) in conjunction with the identity in (3.30) for $\alpha = (\mathbf{r}_{1:N_\mathrm{s}})^{\mathsf{H}}\mathbf{x}_\mathbf{i}(\mathbf{\Phi})$, the NC-GLRT optimization problem in Eq. (3.36) can be equivalently expressed as follows:

$$\max_{\mathbf{\Phi}\in[0,2\pi)^2} \max_{\mathbf{i}\in\mathbb{B}^{N_\mathrm{s}}} \left|(\mathbf{r}_{1:N})^{\mathsf{H}}\mathbf{x}_\mathbf{i}(\mathbf{\Phi})\right| = \max_{\mathbf{\Phi}\in[0,2\pi)^2} \max_{\mathbf{i}\in\mathbb{B}^{N_\mathrm{s}}} \max_{\varphi\in[0,2\pi)} \Re\left\{\left((\mathbf{r}_{1:N})^{\mathsf{H}}\mathbf{x}_\mathbf{i}(\mathbf{\Phi})\right)\mathsf{e}^{-\mathsf{j}\varphi}\right\} \tag{3.38}$$

$$= \max_{\mathbf{\Phi}\in[0,2\pi)^2} \max_{\varphi\in[0,2\pi)} \max_{\mathbf{i}\in\mathbb{B}^{N_\mathrm{s}}} \sum_{n=1}^{N_\mathrm{s}} \Re\left\{(\mathbf{r}_n)^{\mathsf{H}}\mathbf{x}_{i_n}(\mathbf{\Phi})\mathsf{e}^{-\mathsf{j}\varphi}\right\} \tag{3.39}$$

$$= \max_{\mathbf{\Phi}\in[0,2\pi)^2} \max_{\varphi\in[0,2\pi)} \sum_{n=1}^{N_\mathrm{s}} \max_{i_n\in\mathbb{B}} \left\{\Re\left\{(\mathbf{r}_n)^{\mathsf{H}}\mathbf{x}_{i_n}(\mathbf{\Phi})\mathsf{e}^{-\mathsf{j}\varphi}\right\}\right\}. \tag{3.40}$$

From (3.40) we note that for fixed $\mathbf{\Phi}\in[0,2\pi)^2$ and $\varphi\in[0,2\pi)$, the innermost maximization in Eq. (3.39) splits into independent maximizations for any $n=1,2,\ldots,N_\mathrm{s}$, of the following form:

$$\widehat{i_n}(\mathbf{\Phi},\varphi) = \arg\max_{i\in\mathbb{B}} \Re\left\{(\mathbf{r}_n)^{\mathsf{H}}\mathbf{x}_i(\mathbf{\Phi})\mathsf{e}^{-\mathsf{j}\varphi}\right\}$$

$$\Longleftrightarrow \Re\left\{(\mathbf{r}_n)^{\mathsf{H}}\left(\mathbf{x}_0(\Phi_0) - \mathbf{x}_1(\Phi_1)\right)\mathsf{e}^{-\mathsf{j}\varphi}\right\} \overset{\widehat{i_n}(\mathbf{\Phi},\varphi)=0}{\underset{\widehat{i_n}(\mathbf{\Phi},\varphi)=1}{\gtrless}} 0$$

$$\Longleftrightarrow \cos\left(\angle(\mathbf{r}_n)^{\mathsf{H}}\left(\mathbf{x}_0(\Phi_0) - \mathbf{x}_1(\Phi_1)\right) - \varphi\right) \overset{\widehat{i_n}(\mathbf{\Phi},\varphi)=0}{\underset{\widehat{i_n}(\mathbf{\Phi},\varphi)=1}{\gtrless}} 0. \tag{3.41}$$

For fixed $\mathbf{\Phi} \in [0, 2\pi)^2$, as φ scans $[0, 2\pi)$, the decision $\widehat{i}_n(\mathbf{\Phi}, \varphi)$ changes, according to Eq. (3.41), only when:

$$\cos\left(\angle (\mathbf{r}_n)^\mathsf{H} (\mathbf{x}_0(\Phi_0) - \mathbf{x}_1(\Phi_1)) - \varphi\right) = 0 \tag{3.42}$$

$$\Longleftrightarrow \varphi = \underbrace{\pm\frac{\pi}{2} + \angle (\mathbf{r}_n)^\mathsf{H} (\mathbf{x}_0(\Phi_0) - \mathbf{x}_1(\Phi_1)) \pmod{2\pi}}_{\varphi_n^{(1)}, \varphi_n^{(2)}}.$$

Hence, the decision sequence $\widehat{\mathbf{i}}(\mathbf{\Phi}, \varphi) = \left[\widehat{i}_1(\mathbf{\Phi}, \varphi)\ \widehat{i}_2(\mathbf{\Phi}, \varphi)\ \ldots\ \widehat{i}_{N_\mathrm{s}}(\mathbf{\Phi}, \varphi)\right]^\top$ changes only at

$$\varphi_1^{(1)}, \varphi_1^{(2)}, \varphi_2^{(1)}, \varphi_2^{(2)}, \ldots, \varphi_{N_\mathrm{s}}^{(1)}, \varphi_{N_\mathrm{s}}^{(2)}, \tag{3.43}$$

where $0 < \varphi_n^{(l)} < 2\pi$, for any $n = 1, 2, \ldots, N_\mathrm{s}$, $l \in \{1, 2\}$. Since the $2N_\mathrm{s}$ points are distinct with probability one, only an element of decision $\widehat{\mathbf{i}}(\mathbf{\Phi}, \varphi)$ changes at each such point [85]. By sorting the above points in ascending order, i.e.,

$$(\theta_1, \theta_2, \ldots, \theta_{2N_\mathrm{s}}) = \mathsf{sort}\left(\varphi_1^{(1)}, \varphi_1^{(2)}, \varphi_2^{(1)}, \ldots, \varphi_{N_\mathrm{s}}^{(1)}, \varphi_{N_\mathrm{s}}^{(2)}\right), \tag{3.44}$$

the decision $\widehat{\mathbf{i}}(\mathbf{\Phi}, \varphi)$ remains constant in each one of the following $2N_\mathrm{s}$ intervals:

$$\mathcal{J}_0 = [\theta_0, \theta_1),\ \mathcal{J}_1 = [\theta_1, \theta_2), \ldots, \mathcal{J}_{2N_\mathrm{s}-1} = [\theta_{2N_\mathrm{s}-1}, \theta_{2N_\mathrm{s}}), \tag{3.45}$$

with $\theta_0 = 0$. It is noted that the interval $[\theta_{2N_\mathrm{s}}, 2\pi)$ is ignored because it corresponds to the same sequence $\widehat{\mathbf{i}}(\mathbf{\Phi}, \varphi)$ with $\mathcal{J}_0$. Thus, for fixed $\mathbf{\Phi} \in [0, 2\pi)^2$, our objective is the identification of the $2N_\mathrm{s}$ sequences $\widehat{\mathbf{i}}(\mathbf{\Phi}, 0), \widehat{\mathbf{i}}(\mathbf{\Phi}, \theta_1), \ldots, \widehat{\mathbf{i}}(\mathbf{\Phi}, \theta_{2N_\mathrm{s}-1})$, one of which offers the largest metric of interest, i.e., the left-hand side of Eq. (3.38). The procedure of finding the best sequence $\widehat{\mathbf{i}}^\star(\mathbf{\Phi}) \triangleq \widehat{\mathbf{i}}(\mathbf{\Phi}, \theta_{\mathrm{opt}})$ is given in Algorithm 1. For given $\mathbf{\Phi} \in [0, 2\pi)^2$, the algorithm offers the GLRT-optimal sequence following the same principles with sequence detection algorithm developed in [85], with complexity $\mathcal{O}(N_\mathrm{s}\log N_\mathrm{s})$.

After obtaining the sequence $\widehat{\mathbf{i}}^\star(\mathbf{\Phi})$ the optimal phase pair $\mathbf{\Phi}^\star$ is given by:

$$\mathbf{\Phi}^\star = \arg \max_{\mathbf{\Phi} \in [0, 2\pi)^2} \left|(\mathbf{r}_{1:N_\mathrm{s}})^\mathsf{H} \mathbf{x}_{\widehat{\mathbf{i}}^\star(\mathbf{\Phi})}(\mathbf{\Phi})\right|. \tag{3.46}$$

and satisfies the following:

$$\widehat{\mathbf{i}}^\star(\mathbf{\Phi}^\star) = \widehat{\mathbf{i}}_{\mathrm{GLRT}}. \tag{3.47}$$

There is no readily available closed-form solution of problem in Eq. (3.46), thus, the following approach is instead utilized.

Algorithm 1 GLRT_Sequence_Detection_Given_$\boldsymbol{\Phi}$

Input: $\mathbf{r}_{1:N_s} = \begin{bmatrix} \mathbf{r}_1^\top & \mathbf{r}_2^\top & \ldots & \mathbf{r}_{N_s}^\top \end{bmatrix}^\top, \boldsymbol{\Phi} = [\Phi_0 \ \Phi_1]^\top$

1: **for** $n = 1 : N_s$ **do**

2: $\quad \varphi_n^{(1)} := +\frac{\pi}{2} + \underline{/(\mathbf{r}_n)^{\mathsf{H}} (\mathbf{x}_0(\Phi_0) - \mathbf{x}_1(\Phi_1))} \pmod{2\pi}$

3: $\quad \varphi_n^{(2)} := -\frac{\pi}{2} + \underline{/(\mathbf{r}_n)^{\mathsf{H}} (\mathbf{x}_0(\Phi_0) - \mathbf{x}_1(\Phi_1))} \pmod{2\pi}$

4: **end for**

5: $(\theta_1, \theta_2, \ldots, \theta_{2N}) := \mathsf{sort}\left(\varphi_1^{(1)}, \varphi_1^{(2)}, \varphi_2^{(1)}, \ldots, \varphi_N^{(1)}, \varphi_N^{(2)}\right)$

6: **for** $n = 1 : N_s$ **do**

7: $\quad \widehat{i}_n(\boldsymbol{\Phi}, 0) \equiv \gamma_n := \arg \max_{i \in \{0,1\}} \Re\left\{(\mathbf{r}_n)^{\mathsf{H}} \mathbf{x}_i(\boldsymbol{\Phi})\right\}$

8: **end for**

9: $m_{\text{cur}} := \sum_{n=1}^{N_s} (\mathbf{r}_n)^{\mathsf{H}} \mathbf{x}_{\gamma_n}(\boldsymbol{\Phi})$

10: $v_{\text{best}} := |m_{\text{cur}}|$

11: $\widehat{\mathbf{i}}^\star(\boldsymbol{\Phi}) := [\gamma_1 \ \gamma_2 \ \ldots \ \gamma_{N_s}]^\top$

12: **for** $j = 1 : 2N_s - 1$ **do**

13: $\quad$ let n be the index: $\theta_j = \varphi_n^{(l)}$ for some $l \in \{1, 2\}$

14: $\quad \gamma := \widehat{i}_n(\boldsymbol{\Phi}, \theta_{j-1})$

15: $\quad \zeta := 1 - \gamma$

16: $\quad m_{\text{cur}} := m_{\text{cur}} + (\mathbf{r}_n)^{\mathsf{H}} (\mathbf{x}_\zeta(\boldsymbol{\Phi}) - \mathbf{x}_\gamma(\boldsymbol{\Phi}))$

17: $\quad \widehat{i}_n(\boldsymbol{\Phi}, \theta_j) := \zeta$

18: $\quad v_{\text{cur}} := |m_{\text{cur}}|$

19: $\quad$ **if** $v_{\text{cur}} > v_{\text{best}}$ **then**

20: $\quad\quad v_{\text{best}} := v_{\text{cur}}$

21: $\quad\quad \widehat{\mathbf{i}}^\star(\boldsymbol{\Phi}) := \widehat{\mathbf{i}}(\boldsymbol{\Phi}, \theta_j)$

22: $\quad$ **end if**

23: **end for**

Output: $\widehat{\mathbf{i}}^\star(\boldsymbol{\Phi})$

Algorithm 2

Input: $\mathbf{r}_{1:N_s} = \begin{bmatrix} \mathbf{r}_1^\top & \mathbf{r}_2^\top & \ldots & \mathbf{r}_{N_s}^\top \end{bmatrix}^\top, M$

1: $j := 1$

2: **for** $\boldsymbol{\Phi} \in \mathcal{W}_M \times \mathcal{W}_M$ **do**

3: $\quad \widehat{\mathbf{i}}_j^\star = \text{GLRT\_Sequence\_Detection\_Given\_}\boldsymbol{\Phi}(\mathbf{r}_{1:N_s}, \boldsymbol{\Phi})$

4: $\quad v_j := \left| (\mathbf{r}_{1:N_s})^{\mathsf{H}} \mathbf{x}_{\widehat{\mathbf{i}}_j^\star}(\boldsymbol{\Phi}) \right|$

5: $\quad j := j + 1$

6: **end for**

7: $j^\star := \arg \max_{j \in \{1, 2, \ldots, M^2\}} v_j$

Output: $\widehat{\mathbf{i}}_{j^\star}^\star$

As a practical intuitive alternative, a natural number $M \in \mathbb{N}$ is chosen and the following set is formed:

$$\mathcal{W}_M \triangleq \left\{ 0, \frac{2\pi}{M}, \frac{4\pi}{M}, \ldots, \frac{(M-1)2\pi}{M} \right\} \subset [0, 2\pi), \tag{3.48}$$

and instead of solving the problem in Eq. (3.46), the following optimization problem is formed:

$$\widetilde{\boldsymbol{\Phi}}_M^\star = \arg \max_{\boldsymbol{\Phi} \in (\mathcal{W}_M)^2} \left| (\mathbf{r}_{1:N})^\mathsf{H} \, \mathbf{x}_{\widehat{\mathbf{i}}^\star(\boldsymbol{\Phi})}(\boldsymbol{\Phi}) \right|. \tag{3.49}$$

The optimal phase pair for the above problem, $\widetilde{\boldsymbol{\Phi}}_M^\star$, offers sequence decision $\widehat{\mathbf{i}}^\star\left(\widetilde{\boldsymbol{\Phi}}_M^\star\right)$, which converges to $\widehat{\mathbf{i}}_{\mathrm{GLRT}}$ as $M \longrightarrow \infty$. Appropriate finite values of M are examined numerically. The above procedure is illustrated in Algorithm 2 and enjoys complexity of $\mathcal{O}(M^2 N_\mathrm{s} \log N_\mathrm{s})$, since there are M^2 Φ-pairs and for each pair, a sequence is found with $\mathcal{O}(N_\mathrm{s} \log N_\mathrm{s})$, while the quality metric for each sequence (in order to find the "best") is computed with linear in N_s complexity.

3.2.3 Noncoherent Coded Reception/Decoding

It is very challenging to apply error-correction channel coding in scatter radios due to the following reasons:

- scatter radio tags are inherently resource-constrained, and thus, encoding at each tag/sensor must be computationally affordable, and

- SDR reader must also employ low-complexity detection and decoding, in order to concurrently serve as many as possible frequency-modulated tags in a given spectrum band.

Encoding

The transmitter encodes a sequence of K information bits to a sequence of $N_\mathrm{c} \geq K$ coded bits through a linear function over the binary field. Specifically, a linear block code $\mathcal{C}$ over the field $\mathbb{B}$ is a K-dimensional subspace of $\mathbb{B}^{N_\mathrm{c}}$. A binary N_c-tuple is a codeword of $\mathcal{C}$ if and only if there exists a binary K-tuple that can generate this N_c-tuple from $\mathbf{G}$, i.e.,[2]

$$\mathbf{c} \in \mathcal{C} \iff \exists \, \mathbf{b} \in \mathbb{B}^K : \mathbf{c} = \mathbf{b}\mathbf{G}. \tag{3.50}$$

---

[2]All channel coding-related vectors are considered as row vectors, hereafter.

The ratio $R^{\mathcal{C}} \triangleq \frac{K}{N_c}$ defines the rate of the code $\mathcal{C}$, while the minimum distance $d^{\mathcal{C}}_{\min}$ of $\mathcal{C}$ is the smallest Hamming weight w_H (i.e., the number of non-zero components) of any non-zero codeword in $\mathcal{C}$, i.e., $d^{\mathcal{C}}_{\min} = \min_{\mathbf{c} \in \mathcal{C} \backslash \{\mathbf{0}\}} w_H(\mathbf{c})$. Hereafter, a code will be abbreviated by the triplet $(N_c, K, d^{\mathcal{C}}_{\min})$.

Soft-Decision Noncoherent Hybrid Composite Hypothesis-Testing (NC-HCHT) Decoding

As already mentioned, the inherently resource-constrained tags render the utilization of small block-length channel codes mandatory. However, a major obstacle for small block-length channel codes over wireless environments is the fact that errors usually occur in long bursts when the channel is in deep fade [79].[3] When wireless channel fading affects a sheer amount of bits, the use of channel codes with small block-length is not appropriate, due to their small error-correction capability. The interleaving technique in conjunction with linear block codes (of relatively small length, i.e., short packet) overcomes this difficulty [80].

The transmitter stores a block of D codewords in a $D \times N_c$ matrix and transmits the information column-wise (where D is the interleaving depth of the interleaver), i.e., it transmits the first coded bit of each of the D codewords and then the second bit of each of the D codewords and so forth, until the N_c-th coded bit. The receiver stores DN_c received symbols and performs decoding row-wise, i.e., it decodes symbol sequences corresponding to actual codewords. In that way, long errors in consecutive coded bits are avoided due to the fact that burst errors are now affecting coded bits from different codewords [79]. It can be shown that a fully interleaved coded system (i.e., $DT \geq T_{coh}$), with classic FSK and Rayleigh fading, achieves diversity order $d^{\mathcal{C}}_{\min}$ under ML noncoherent decoding [80].

For the scatter radio case, each tag backscatters a packet of DN_c coded bits. After DC-blocking, CFO estimation/compensation and symbol synchronization, SDR reader processes DN_c received symbols. Let $\mathbf{c} = [c_1 \ c_2 \ \ldots \ c_{N_c}] \in \mathcal{C}$ be a codeword corresponding to a specific row of the interleaving matrix; according to (3.18), the discrete baseband signal, associated with that row of interleaving matrix, is given by:

$$\mathbf{r}_{1:N_c} = \begin{bmatrix} \mathbf{r}_1 \\ \mathbf{r}_2 \\ \vdots \\ \mathbf{r}_{N_c} \end{bmatrix} = \begin{bmatrix} h_1 \mathbf{x}_{c_1}(\mathbf{\Phi}) \\ h_2 \mathbf{x}_{c_2}(\mathbf{\Phi}) \\ \vdots \\ h_{N_c} \mathbf{x}_{c_{N_c}}(\mathbf{\Phi}) \end{bmatrix} + \begin{bmatrix} \mathbf{n}_1 \\ \mathbf{n}_2 \\ \vdots \\ \mathbf{n}_{N_c} \end{bmatrix}, \tag{3.51}$$

---

[3]As discussed in [86], in bistatic scatter radio, deep fading events are even more frequent due to the product of channel gain terms a_{CT}, a_{TR}.

where $\mathbf{r}_n$ and $\mathbf{x}_{c_n}(\boldsymbol{\Phi})$ are defined as in Section 3.2.2, $c_n \in \mathbb{B}$, $n = 1, 2, \ldots, N_\mathrm{c}$ and $\{h_n\}_{n=1}^{N_\mathrm{c}}$ are the channel coefficients associated with coded bits $\{c_n\}_{n=1}^{N_\mathrm{c}}$. The noise statistics are given as in Section 3.2.2. In sharp contrast to Eq. (3.33), it is remarked that in Eq. (3.51): (a) the transmitted sequence $\mathbf{c}$ belongs to a linear subspace of $\mathbb{B}^{N_\mathrm{c}}$ and (b) some of $\{h_n\}_{n=1}^{N_\mathrm{c}}$ may be independent of each other, and their correlation depends on the (a) sequence length, (b) interleaving depth, and (c) channel coherence time. For the particular case of a fully interleaved system, i.e., $DT \geq T_\mathrm{coh}$, $\{h_n\}_{n=1}^{N_\mathrm{c}}$ are independent of each other and diversity gain can be obtained.

As in the uncoded case, the ML decoding rule does not amenable to a closed-form expression and thus, an alternative decoding rule is devised. Applying the notion of NC-HCHT decoding and treating Φ_0 and Φ_1 as uniform random variables in $[0, 2\pi)$ and $\{h_n\}_{n=1}^{N_\mathrm{c}}$ as unknown nonrandom parameters, the following decoding rule is proposed:

$$\arg \max_{\mathbf{c} \in \mathcal{C}} \left\{ \mathbb{E}_{\boldsymbol{\Phi}} \left[\max_{\mathbf{h} \in \mathbb{C}^{N_\mathrm{c}}} \ln \left[\mathsf{f}_{\mathbf{r}_{1:N_\mathrm{c}}|\mathbf{c},\mathbf{h},\boldsymbol{\Phi}}(\mathbf{r}_{1:N_\mathrm{c}}|\mathbf{c}, \mathbf{h}, \boldsymbol{\Phi}) \right] \right] \right\}, \tag{3.52}$$

where the vector $\mathbf{h} = [h_1 \ h_2 \ \ldots \ h_{N_\mathrm{c}}]^\top$ consists of all deterministic compound channel coefficients.

Theorem 3.3. For $DT \geq T_\mathrm{coh}$, the decoding rule in Eq. (3.52) is simplified to the following soft-decision, channel-agnostic rule:

$$\widehat{\mathbf{c}} = \arg \max_{\mathbf{c} \in \mathcal{C}} \sum_{n=1}^{N_\mathrm{c}} w_n c_n, \tag{3.53}$$

where $w_n \triangleq |r_1^+(n)|^2 + |r_1^-(n)|^2 - \left(|r_0^+(n)|^2 + |r_0^-(n)|^2 \right)$, $n = 1, 2, \ldots, N_\mathrm{c}$ are the soft-decision variables.

Proof. The proof can be found in Appendix 3.6. □

The receiver forms the vector $\mathbf{w} = \{w_n\}_{n=1}^{N_\mathrm{c}}$ of "soft decisions" for each row of inter-leaving matrix and applies the rule in (3.53) D times. In practice we apply the rule of Eq. (3.53) for any value of D (even when $DT < T_\mathrm{coh}$) due to its inherent simplicity. Soft-decision decoding offers smaller BER performance compared to hard-decision decoding, where the receiver applies first detection on a symbol-by-symbol basis and then applies decoding on the bit sequence. The optimization problem in (3.53) requires $\mathcal{O}(2^K N_\mathrm{c})$ arith-metic operations, which is exponential complexity on the number of information bits, K. However, such computational cost is not very high for SDR reader if relatively small block-length N_c (and thus small K) is utilized. For simulation results, small block-length,

cyclic Bose-Chaudhuri-Hocquenghem (BCH), as well as Reed-Muller (RM) channel codes are studied [87].

3.3   Coherent Scatter Radio Reception

For coherent reception let us define

$$
\mathbf{g} \triangleq h\sqrt{\frac{\mathrm{E}}{2}}\begin{bmatrix} \mathrm{e}^{+\mathrm{j}\Phi_0} \\ \mathrm{e}^{-\mathrm{j}\Phi_0} \\ \mathrm{e}^{+\mathrm{j}\Phi_1} \\ \mathrm{e}^{-\mathrm{j}\Phi_1} \end{bmatrix}, \tag{3.54}
$$

the compound channel vector that squeezes all unknown random parameters h, Φ_0, and Φ_1. Substituting (3.54) in (3.18) the baseband signal over a bit duration T can be written as:

$$
\mathbf{r} = \mathbf{g} \odot \mathbf{s}_i + \mathbf{n}. \tag{3.55}
$$

3.3.1   Channel Estimation of Compound Scatter Radio Wireless Channel

To coherently detect the received signal by Eq. (3.55), both the compound channel h as well as the random phases Φ_i, $i \in \{0,1\}$ need to be estimated. Following a training based technique, an priori known at the transmitter/receiver training signal is periodically backscattered from the tag and the SDR reader then applies least-squares (LS) estimation to obtain an estimate for compound vector channel $\mathbf{g}$. Such pilot signal could be the preamble, typically used for packet and/or symbol synchronization.

More specifically, once during the channel coherence time T_{coh}, N_{tr} training bits $\{b_{i_{\mathrm{tr}}}\}$, $i_{\mathrm{tr}} = 1, \ldots, N_{\mathrm{tr}}$, are transmitted by the tag. After CFO estimation, DC blocking, synchronization, and demodulation the vector representation of the received training signal over one bit period T can be written equivalently as

$$
\mathbf{r}_{i_{\mathrm{tr}}} = \mathbf{T}_{b_{i_{\mathrm{tr}}}}\mathbf{g} + \mathbf{n}_{i_{\mathrm{tr}}}, \tag{3.56}
$$

with

$$
\mathbf{T}_{b_{i_{\mathrm{tr}}}} = \begin{bmatrix} (1 - b_{i_{\mathrm{tr}}})\mathbf{e}_1 & (1 - b_{i_{\mathrm{tr}}})\mathbf{e}_2 & b_{i_{\mathrm{tr}}}\mathbf{e}_3 & b_{i_{\mathrm{tr}}}\mathbf{e}_4 \end{bmatrix} \in \mathbb{C}^{4\times4}, \tag{3.57}
$$

where $\mathbf{e}_k$, $k = 1, \ldots, 4$, denotes the k-th column of the $\mathbf{I}_4$ identity matrix.

Thus, for the duration of N_{tr} training symbols, the receiver applies column-wise concatenation of the vector representations of the N_{tr} bits in the training sequence and forms vector $\mathbf{y} \in \mathbb{C}^{4N_{\mathrm{tr}}}$:

$$\mathbf{r}_{\mathrm{tr}} = \begin{bmatrix} \mathbf{r}_1 \\ \mathbf{r}_2 \\ \vdots \\ \mathbf{r}_{N_{\mathrm{tr}}} \end{bmatrix} = \begin{bmatrix} \mathbf{T}_{b_1} \\ \mathbf{T}_{b_2} \\ \vdots \\ \mathbf{T}_{b_{N_{\mathrm{tr}}}} \end{bmatrix} \mathbf{g} + \begin{bmatrix} \mathbf{n}_1 \\ \mathbf{n}_2 \\ \vdots \\ \mathbf{n}_{N_{\mathrm{tr}}} \end{bmatrix} = \mathbf{T}_{\mathrm{tr}}\, \mathbf{g} + \mathbf{n}_{\mathrm{tr}}. \tag{3.58}$$

To jointly estimate the compound channel h and phases $\Phi_i, i \in \{0,1\}$, the receiver obtains the LS estimate of vector $\mathbf{g}$:

$$\widehat{\mathbf{g}} = \arg\min_{\mathbf{g} \in \mathbb{C}^4} \|\mathbf{r}_{\mathrm{tr}} - \mathbf{T}_{\mathrm{tr}}\, \mathbf{g}\|_2^2 \iff \widehat{\mathbf{g}} = \left(\mathbf{T}_{\mathrm{tr}}^{\mathsf{H}}\, \mathbf{T}_{\mathrm{tr}}\right)^{-1} \mathbf{T}_{\mathrm{tr}}^{\mathsf{H}}\, \mathbf{r}_{\mathrm{tr}}. \tag{3.59}$$

Although the LS estimate $\widehat{\mathbf{g}}$ is ignoring the dependencies in vector $\mathbf{g}$, it adheres to a simple closed-form expression.

3.3.2 Maximum-Likelihood Detection and Decoding

For the baseband signal in (3.55) the reader treats channel estimate $\widehat{\mathbf{g}}$ as the true channel vector and applies coherent ML detection:

$$\widehat{i}_{\mathrm{ML}} = \arg\max_{i \in \mathbb{B}} f_{\mathbf{r}|i,\mathbf{g}}(\mathbf{r}|i, \widehat{\mathbf{g}}) \stackrel{(a)}{=} \arg\max_{i \in \mathbb{B}} \Re\left\{\mathbf{r}^{\mathsf{H}}\, (\widehat{\mathbf{g}} \odot \mathbf{s}_i)\right\}, \tag{3.60}$$

where in (a) we exploited the fact that $f_{\mathbf{r}|i,\mathbf{g}}(\mathbf{r}|i, \widehat{\mathbf{g}}) \equiv \mathcal{CN}(\widehat{\mathbf{g}} \odot \mathbf{s}_i, N_0\, \mathbf{I}_4)$.

For decoding without interleaving technique utilized, i.e. $D = 1$, suppose that a codeword $\mathbf{c} = [c_1\ c_2\ \ldots c_{N_c}] \in \mathcal{C}$ (where $\mathcal{C}$ is a linear block code) is backscattered from the tag towards the SDR reader. The baseband signal associated with the sequence of bits in the codeword is given in (3.33). For a given the channel estimate $\widehat{\mathbf{g}}$, the ML decoder can be simplified to

$$\widehat{\mathbf{c}}_{\mathrm{ML}} = \arg\max_{\mathbf{c} \in \mathcal{C}} f_{\mathbf{r}|\mathbf{c},\mathbf{g}}(\mathbf{r}|\mathbf{c}, \widehat{\mathbf{g}}) \stackrel{(a)}{=} \arg\max_{\mathbf{c} \in \mathcal{C}} \left\{\sum_{i=1}^{N} \Re\left\{\mathbf{r}_i^{\mathsf{H}}\, (\widehat{\mathbf{g}} \odot \mathbf{s}_{c_i})\right\}\right\}, \tag{3.61}$$

where (a) exploits that

$$f_{\mathbf{r}|\mathbf{c},\mathbf{g}}(\mathbf{r}|\mathbf{c}, \widehat{\mathbf{g}}) \equiv \mathcal{CN}\left(\left[(\widehat{\mathbf{g}} \odot \mathbf{s}_{c_1})^{\top}\ (\widehat{\mathbf{g}} \odot \mathbf{s}_{c_2})^{\top}\ \ldots\ (\widehat{\mathbf{g}} \odot \mathbf{s}_{c_{N_c}})^{\top}\right]^{\top}, N_0\, \mathbf{I}_{4N_c}\right). \tag{3.62}$$

The complexity to find the optimal codeword $\widehat{\mathbf{c}}_{\mathrm{ML}}$ is $\mathcal{O}(2^K N_c)$, which is exponential on the number of information bits. However, for relatively small codeword lengths N_c, such complexity is affordable to SDR reader.

The final result in coherent receiver pertains to the diversity order achieved by coherent ML decoding in a fully interleaved system.

Theorem 3.4. Under Rayleigh fading scenario, i.e., $\kappa_{\mathrm{CT}} = \kappa_{\mathrm{TR}} = 0$, bistatic scatter radio system with coherent ML decoding with full interleaving, i.e., $T_{\mathrm{coh}} = (D + N_{\mathrm{tr}})T$, achieves diversity order $d_{\mathrm{min}}^{\mathcal{C}}$.

Proof. In Appendix 3.6.   □

However, the interleaving technique introduces delay and requires additional memory, since both the scatter radio tag/sensor, as well as the receiver process a block of D codewords upon transmission and reception, respectively. Since the tag is equipped with limited memory, the interleaving technique as presented for both coherent and noncoherent coded reception schemes may be a practical option only for relatively small values of D.

3.4   Simulation Results

Simulations for the bistatic scatter radio system model assume backscatter binary FSK transmissions with $T = 1$ msec bit duration, over quasi-static flat fading channel with coherence time $T_{\mathrm{coh}} = 100$ msec; Rayleigh fading ($\kappa_{\mathrm{CT}} = \kappa_{\mathrm{TR}} = 0$), Rician fading with $\kappa_{\mathrm{CT}} = 20, \kappa_{\mathrm{TR}} = 10$ and no fading, i.e., Gaussian channel ($\kappa_{\mathrm{CT}} = \kappa_{\mathrm{TR}} \longrightarrow \infty$) are studied.[4] In all simulated cases, perfect symbol synchronization and CFO estimation/compensation are also assumed. For comparison purposes, coherent detection and decoding schemes are also included with $N_{\mathrm{tr}} = 30$ training bits for channel estimation. In all cases, the average received SNR per information bit is given by Eq. (3.17), while packet length and energy consumption per transmitted packet are both fixed for comparison fairness. Hence, noncoherent receivers (without using a dedicated sequence of training bits in the packet for channel estimation) offer for equal packet lengths higher energy per information bit than their coherent counterparts.
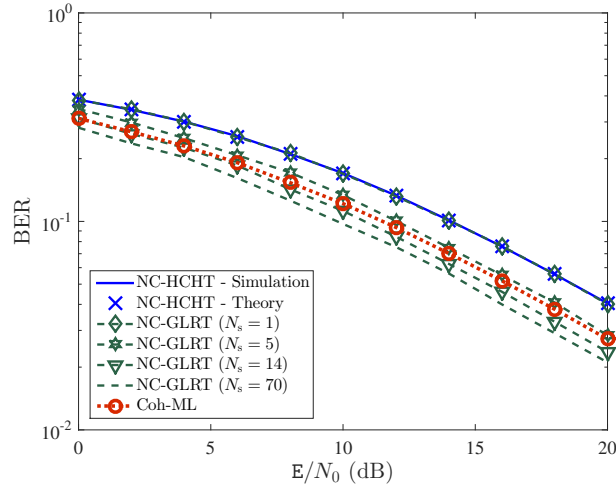
Figure 3.2: BER vs average received SNR for Rayleigh fading with no channel coding of the various noncoherent detectors. Comparison to the coherent case is conducted for fixed energy per packet, including energy spent for channel estimation.

3.4.1 Uncoded BER Performance

For uncoded bistatic scatter radio system, the noncoherent symbol-by-symbol and sequence detectors of Sections 3.2.1 and 3.2.2 are compared with the ML coherent detector given in (3.61) with least-squares (LS) channel estimation (abbreviated as Coh-ML), assuming packets with 70 information bits for all setups. Thus, the total energy per packet is $70\mathtt{E}$ and $(30+70)\mathtt{E}$ for noncoherent and coherent setup, respectively, taking into account the $N_{\mathrm{tr}} = 30$ training bits for channel estimation in the coherent case. For fixed energy per packet, the total energy per bit for noncoherent and coherent setup is $\mathtt{E}$ and $\frac{7}{10}\mathtt{E}$ Joules, respectively. Furthermore, $M = 6$ is employed for NC-GLRT sequence detection (for sequence length $N_{\mathrm{s}} \geq 2$).

Fig. 3.2 depicts for Rayleigh fading the BER of noncoherent symbol-by-symbol HCHT and GLRT detectors, GLRT sequence detector (for various sequence lengths N_{s}), and Coh-ML detector. It is remarked that for symbol-by-symbol NC-HCHT detection, simulation results and analytical expression in Eq. (3.27) coincide. Coh-ML detector outperforms symbol-by-symbol noncoherent detectors by 2-3dB. Increasing the sequence length N_{s} of NC-GLRT sequence detector improves the BER performance, exhibiting 1-2dB performance gain compared to Coh-ML detector. It can be seen that under a constant energy consumption per packet, the energy per information bit in the coherent case is 30% smaller compared to the noncoherent case, due to the overhead spent on training bits (in the co-

---

[4]Such coherence time and fading parameter values have been experimentally verified for immobile outdoor setups, CE close to tag and tag-to-reader distance more than 100 meters [33,37].
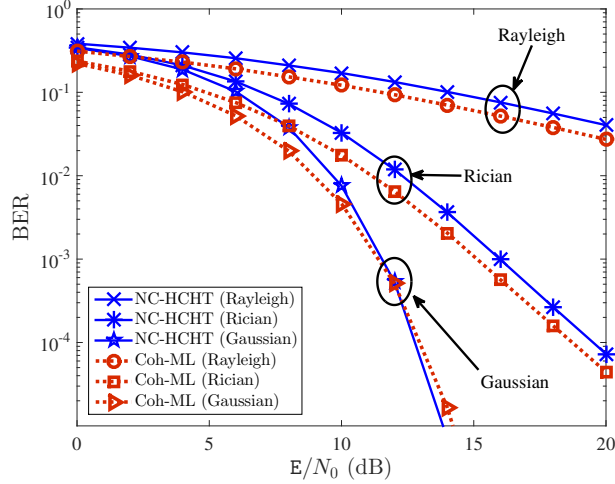
Figure 3.3: BER vs average received SNR of NC-HCHT and Coh-ML detection for different fading scenarios. Comparison to the coherent case is conducted for fixed energy per packet, including energy spent for channel estimation.

herent case) for channel estimation. The NC-GLRT sequence detector capitalizes upon that, exploiting correlation (due to the unknown channel) between consecutive symbols and offers blind detection, i.e., no requirement for overhead (training) channel estimation bits. It is also noted that increasing parameter M beyond 6, offers negligible extra performance gain for the NC-GLRT sequence detector.

Fig. 3.3 compares the BER performance of NC-HCHT and Coh-ML detectors for different types of fading as a function of average received SNR. As the SNR defined in (3.17) is the same for any type of fading and does not depend on Rician parameters, such comparison makes a lot of sense. It can be seen that as parameters κ_{CT} and κ_{TR} increase, i.e., the channel becomes more deterministic, the BER gap between the two detection schemes is reduced with increasing SNR. It is observed that as the fading becomes more deterministic, the power gain dominates the BER performance in moderate and high SNR regime. Interestingly, for the Gaussian channel case (no fading, deterministic channel), NC-HCHT detector outperforms Coh-ML detector for SNR values greater than 12. As discussed above, this stems from the fact that noncoherent schemes have a higher power gain (E vs $\frac{7}{10}$E Joules per bit) compared to coherent one. This is highly important in typical scatter radio scenarios, with strong line-of-sight (LOS).

Fig. 3.4 studies the sequence length of NC-GLRT in various fading scenarios; as fading becomes more deterministic, the performance gap between NC-GLRT sequence detector and Coh-ML detector slightly increases, showing that the proposed log-linear complexity sequence detector is a promising option for power-limited scatter radio networks. It is emphasized again that the BER performance gain of noncoherent receivers also exploits
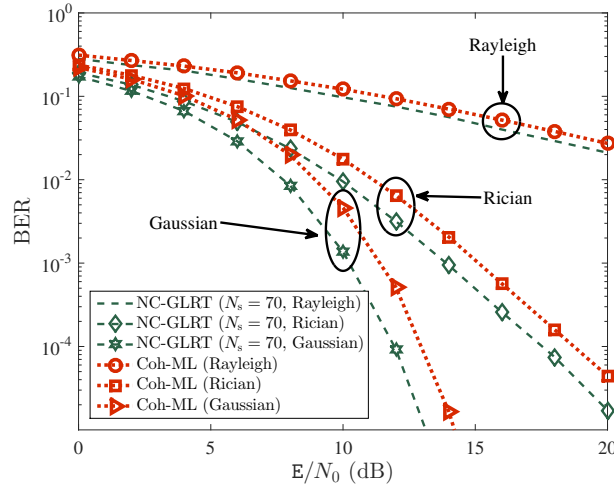
Figure 3.4: Performance of GLRT sequence detection with $N_{\mathrm{s}} = 70$ and Coh-ML detection for different fading scenarios and no channel coding. Comparison to the coherent case is conducted for fixed energy per packet, including energy spent for channel estimation.
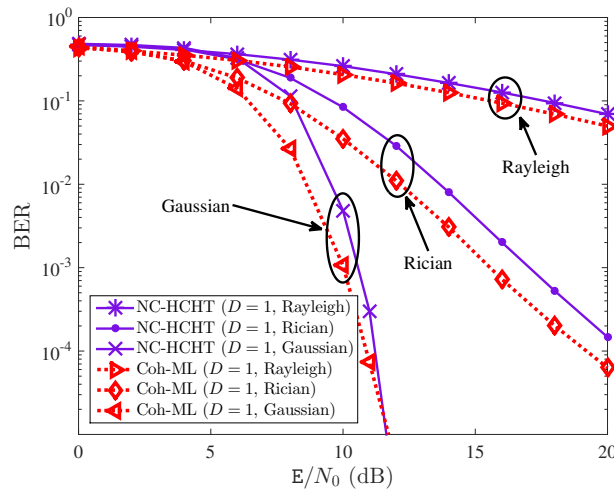
Figure 3.5: Impact of fading in BER performance for HCHT and Coh-ML decoders. Both setups utilize the cyclic $(31, 11, 11)$ BCH code and $D = 1$. Comparison to the coherent case is conducted for fixed energy per packet, including energy spent for channel estimation.

the higher energy per information bit, compared to the coherent receiver, due to fixed energy per packet and no need for training/overhead bits for channel estimation. Both Fig. 3.3 and Fig. 3.4 above clearly indicate that the choice of preferable noncoherent detection scheme depends on the specifics of the wireless fading channel and the SNR operating value.

Figure 3.6: Impact of interleaving depth D for NC-HCHT and Coh-ML decoders with cyclic $(31, 11, 11)$ BCH code over Rician fading. Comparison to the coherent case is conducted for fixed energy per packet, including energy spent for channel estimation.

3.4.2 Coded BER Performance

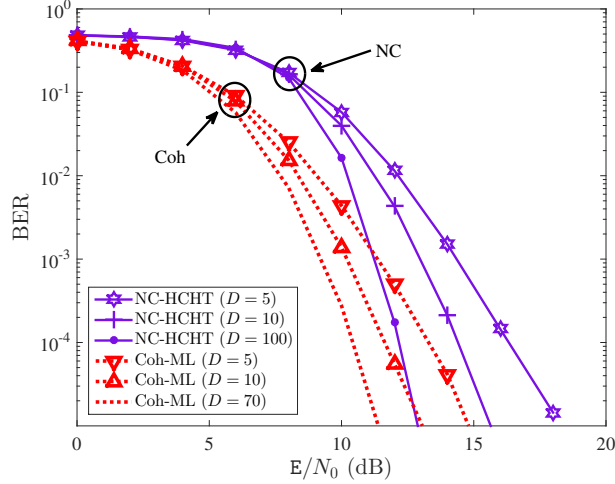Using code $\mathcal{C}(N_c, K, d_{\min}^{\mathcal{C}})$ along with interleaving, the proposed NC-HCHT decoder of Eq. (3.53) and the ML coherent decoder in Eq. (3.61) with LS channel estimation (Coh-ML) are compared in terms of BER. Two small block-length channel codes are studied: the cyclic $(31, 11, 11)$ BCH code $\mathcal{C}_{\text{BCH}}$ and the $(32, 16, 8)$ RM channel code $\mathcal{C}_{\text{RM}}$; the first has smaller rate but higher error-correction capability than the second. As in the uncoded case, a total energy budget constraint per packet is considered assuming packets of DN_c coded bits (i.e., $(K/N_c)DN_c$ information bits). Thus, for noncoherent coded setups the total energy per packet is $DN_c x$, where x is the energy cost per bit, while for coherent coded setups the total energy per packet is $[DN_c + L_{\text{coh}}N_{\text{tr}}]\, x$, where integer $L_{\text{coh}} \triangleq \left\lceil \dfrac{DN_c T}{T_{\text{coh}}} \right\rceil$ indicates how many times the channel needs to be estimated (utilizing N_{tr} training bits each time). Thus, for fixed energy per packet, i.e., $DN_c x = (K/N_c)DN_c \mathsf{E}$ or $[DN_c + L_{\text{coh}}N_{\text{tr}}]\, x = (K/N_c)DN_c \mathsf{E}$, the total energy per bit x for noncoherent and coherent coded setup is $\frac{K}{N_c}\mathsf{E}$ and $\dfrac{KD}{DN_c + L_{\text{coh}}N_{\text{tr}}}\mathsf{E}$ Joules, respectively.

Fig. 3.5 considers the use of $(31, 11, 11)$ BCH channel code with $D = 1$, i.e., no interleaving and studies the impact of fading in NC-HCHT and Coh-ML decoders. It can be seen that as fading parameters $\kappa_{\text{CT}}, \kappa_{\text{TR}}$ decrease, the BER for both decoding schemes increases. That is due to the higher randomness of fading for smaller values of κ_{CT} and κ_{TR} and the limited error-correction capability due to the small block-length of the utilized codes. It is also noted that as $\kappa_{\text{CT}}, \kappa_{\text{TR}}$, and SNR increase, the performance of noncoherent coded system approaches the performance of coherent one.
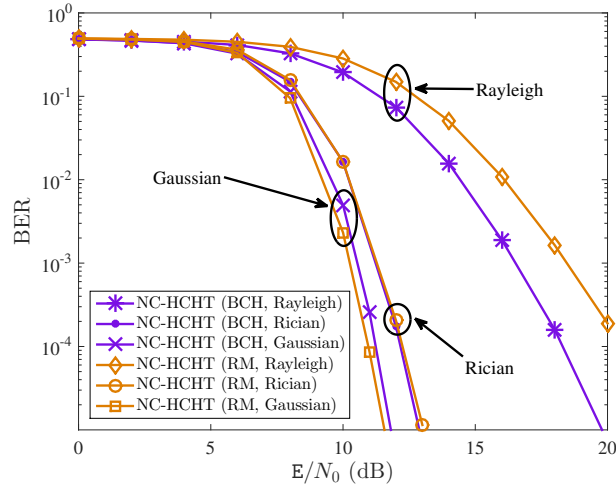
Figure 3.7: Impact of fading for NC-HCHT decoder with cyclic $(31, 11, 11)$ BCH or $(32, 16, 8)$ RM channel code and full interleaving.

Fig. 3.6 studies the impact of interleaving depth D in BCH NC-HCHT and Coh-ML decoders over Rician fading; as expected, the BER of both schemes is reduced with increasing D, due to the diversity gain introduced by interleaving. It is noted that for $D = 5$, Coh-ML decoder offers approximately 3 dB performance gain compared to NC-HCHT decoder. However, as D increases, their BER performance gap becomes smaller.

Finally, Fig. 3.7 compares the $(31, 11, 11)$ BCH cyclic and the $(32, 16, 8)$ RM channel codes for different fading scenarios, with NC-HCHT decoding and full interleaving. An interesting observation emerges: while for Rayleigh fading BCH-coded outperforms RM-coded system, for Rician fading they offer similar BER performance, whereas for no fading RM offers slightly smaller BER compared to BCH. This means that when κ_{CT} and κ_{TR} are small, i.e., in highly random fading scenarios, diversity gain (that depends on $d_{\min}^{\mathcal{C}}$) plays more important role in BER performance than energy gain (that depends on $R^{\mathcal{C}}$), while the opposite holds in more deterministic fading scenarios.

3.5 Experimental Results

Outdoors measurements were conducted with the experimental setup depicted in Fig. 3.8. An embedded carrier emitter (CE) was employed transmitting at frequency of 868 MHz with transmit power 13 dBm. A custom 8-bit microcontroller-based, scatter radio tag was utilized at 1 kbps with binary FSK and switching (subcarrier) frequencies of $F_0 = 125$ kHz and $F_1 = 250$ kHz. A commodity (USRP2) SDR with Flex-900 front-end radio card was utilized as the receiver, connected to a laptop running the noncoherent and
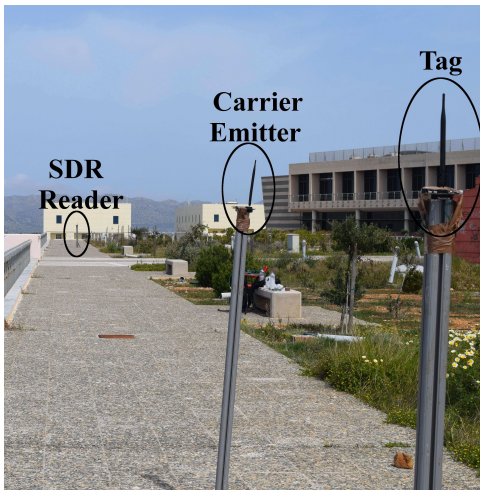
Figure 3.8: Experimental outdoor topology: depicted carrier emitter-to-tag distance d_{CT} was 8 meters.

coherent detection/decoding algorithms. All radio modules were equipped with omni-directional antennas, at height of 1.70 meters. Channel coherence time of 50 to 100 msec was observed during the experimental results, due to immobility. For the considered experimental scenario, CE was placed between tag and SDR reader, co-linearly (Fig. 3.8).

A packet of 47 bits was utilized for both coherent and noncoherent setups. Periodogram-based CFO estimation was applied using the whole received signal,[5] and energy-based symbol and packet synchronization was also employed. The (last) 31 bits constitute a BCH codeword (i.e., $N_{\mathrm{c}} = 31$), utilized at both coherent and noncoherent setups for detection and decoding, while the remaining 16 bits were exploited only at the coherent case, for LS channel estimation. The following schemes were compared in terms of BER:

- uncoded NC-HCHT symbol-by-symbol detector,

- uncoded GLRT symbol-by-symbol detector,

- uncoded GLRT sequence detector with $N_{\mathrm{s}} = 31$ and $M = 6$,

- uncoded Coh-ML detector,

- coded NC-HCHT decoder, and

- coded Coh-ML decoder.

---

[5] The periodogram is the maximum-likelihood estimate (MLE) of ΔF, whose mean-squared error (MSE) decays asymptotically with the cubic power of the number of utilized samples [88].
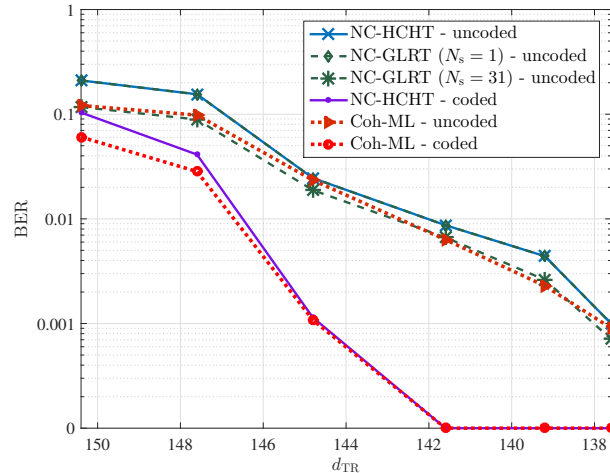
Figure 3.9: Experimental BER comparison of all scatter radio receivers as a function of tag-to-SDR reader distance d_{TR} (m).

$D = 1$ was utilized, i.e., coding schemes did not utilize interleaving. In addition, the energy per bit was held fixed, i.e., total energy per packet was not fixed among the different schemes (favoring coded vs uncoded or coherent vs noncoherent reception).

Fig. 3.9 offers the experimental BER of the above schemes as a function of the tag-to-reader distance. It can be seen that both coherent and noncoherent uncoded receivers achieve ranges in the order of 145m with BER $\leq$ 3%, while coded receivers achieve ranges of 148 and 141 meters approximately, at BER $\leq$ 4% and 0, respectively. It is observed that uncoded coh-ML detector offers similar BER with uncoded (noncoherent) GLRT sequence detector and both of them outperform by approximately one meter the symbol-by-symbol noncoherent detectors (under unequal total energy cost per packet). Interestingly, it can be shown that the proposed noncoherent coded receiver achieves comparable BER performance with the coded coherent one, even though the latter spends extra bits (and energy) for channel estimation; thus, potential energy gains are available for the noncoherent setup. It is worth emphasizing that the reported BER, in the order of 1%–5%, is acceptable for low bitrate sensing applications.

3.6   Appendix: Proofs of Chapter 3

Proof of Theorem 3.1

Under the orthogonality criterion for noncoherent FSK: $|F_1 - F_0| = \frac{k}{T}$, $k \in \mathbb{N}$, and for $F_i \gg \frac{1}{T}$, any two exponentials of frequencies F_0, F_1 will be orthogonal:

$$\int_T e^{j2\pi F_i t} \left(e^{j2\pi F_k t} \right)^* dt \approx \begin{cases} T, & F_i = F_k, \\ 0, & F_i \neq F_k, \end{cases} \quad k, i \in \mathbb{B}, \tag{3.63}$$

where the integration is performed over one bit period T. Thus, the set $\left\{ \frac{1}{\sqrt{T}} e^{\pm j2\pi F_i t} \Pi_T(t) \right\}_{i \in \mathbb{B}}$ constitutes a 4-dimensional orthonormal basis, that can be used for expansion of the received signal in Eq. (13) in the manuscript. Specifically, for bit duration T, a bank of correlators processes the received signal $\widetilde{y}(t)$ as

$$\begin{aligned} r_0^+ &= \int_{-\infty}^{+\infty} \widetilde{y}(t) \left(\frac{1}{\sqrt{T}} \Pi_T(t) e^{+j2\pi F_0 t} \right)^* dt \\ &= \int_0^T \frac{\mu h}{2\sqrt{T}} \left(e^{j(2\pi F_i t + \Phi_i)} + e^{-j(2\pi F_i t + \Phi_i)} \right) \left(e^{-j2\pi F_0 t} \right) dt + \int_0^T n(t) \left(\frac{e^{-j2\pi F_0 t}}{\sqrt{T}} \right) dt \\ &\overset{(a)}{=} \int_0^T \frac{\mu h}{2\sqrt{T}} e^{j(2\pi(F_i - F_0)t + \Phi_i)} dt \;+\; 0 +\; n_0^+ \overset{(3.63)}{=} h e^{+j\Phi_0} \frac{\sqrt{T}\mu}{2} (1 - i) + n_0^+ \\ &\overset{(b)}{=} h e^{+j\Phi_0} \sqrt{\frac{E}{2}} (1 - i) + n_0^+, \end{aligned} \tag{3.64a}$$

where (a) follows from the fact that the integral of the "fast" exponential with frequency $F_i + F_0$ is approximated by zero since $F_i \gg \frac{1}{T}$, $i \in \mathbb{B}$, and (b) follows from the definition of E in Eq. (15) of the manuscript. Similarly,

$$r_0^- = \int_{-\infty}^{+\infty} \widetilde{y}(t) \left(\frac{1}{\sqrt{T}} \Pi_T(t) e^{-j2\pi F_0 t} \right)^* dt = h e^{-j\Phi_0} \sqrt{\frac{E}{2}} (1 - i) + n_0^-, \tag{3.64b}$$

$$r_1^+ = \int_{-\infty}^{+\infty} \widetilde{y}(t) \left(\frac{1}{\sqrt{T}} \Pi_T(t) e^{+j2\pi F_1 t} \right)^* dt = h e^{+j\Phi_1} \sqrt{\frac{E}{2}} i + n_1^+, \tag{3.64c}$$

$$r_1^- = \int_{-\infty}^{+\infty} \widetilde{y}(t) \left(\frac{1}{\sqrt{T}} \Pi_T(t) e^{-j2\pi F_1 t} \right)^* dt = h e^{-j\Phi_1} \sqrt{\frac{E}{2}} i + n_1^-. \tag{3.64d}$$

The complex exponentials are time-limited in $[0, T)$, and thus, for $F_i + \frac{20}{T} \ll W_{\text{SDR}}$, the orthonormal basis $\left\{ \frac{1}{\sqrt{T}} e^{\pm j2\pi F_i t} \Pi_T(t) \right\}_{i \in \mathbb{B}}$ can be considered band-limited in $[-W_{\text{SDR}}, W_{\text{SDR}}]$. Since $n(t)$ is a circularly symmetric complex baseband Gaussian random process with power spectral density N_0 in $[-W_{\text{SDR}}, W_{\text{SDR}}]$ (cf. Eq. (3.9) in the manuscript), its projec-

tions on an orthonormal basis with bandwidth limited basis functions in $[-W_{\text{SDR}}, W_{\text{SDR}}]$, offer independent and identically distributed circularly symmetric complex Gaussian components with variance N_0 [80], i.e., $\mathbf{n} = [n_0^+ \ n_0^- \ n_1^+ \ n_1^-]^\top \sim \mathcal{CN}\left(\mathbf{0}_4, N_0 \mathbf{I}_4\right)$.

Proof of Proposition 3.1

Given hypothesis $i = 0$ and h, Φ_0, Φ_1, random variable (RV) $z_1 \triangleq |r_1^+|^2 + |r_1^-|^2$ is the sum of 4 independent, squared, zero-mean Gaussians, each of variance $\sigma^2 \triangleq N_0/2$ and thus, z_1 follows a Chi-squared distribution with 4 degrees of freedom and probability density function (PDF) given by [80, p. 45]: $\mathsf{f}_{z_1|i}(x|0) = \frac{x}{4\sigma^4}\mathsf{e}^{-\frac{x}{2\sigma^2}}$, $x \geq 0$, and corresponding cumulative distribution function (CDF) given by:

$$\mathsf{F}_{z_1|i}(x|0) = 1 - \mathsf{e}^{-\frac{x}{2\sigma^2}}\left(1 + \frac{x}{2\sigma^2}\right), \ x \geq 0. \tag{3.65}$$

Similarly, given hypothesis $i = 0$ and h, Φ_0, Φ_1, random variable $z_0 \triangleq |r_0^+|^2 + |r_0^-|^2$ is the sum of 4 independent squared non-zero-mean Gaussian RVs, each of variance σ^2 and thus, z_0 follows noncentral Chi-squared with 4 degrees of freedom with noncentrality parameter $\mathsf{E}\,|h|^2 = \mathsf{E}\,a^2$ that do not depend on RV Φ_0. The conditional PDF of z_0 is given by [80, p. 46]:

$$\mathsf{f}_{z_0|i,a}(x|0,a) = \frac{\sqrt{x}}{2\sigma^2\sqrt{\mathsf{E}}\,a}\mathsf{e}^{-\frac{x+\mathsf{E}\,a^2}{2\sigma^2}}\mathsf{I}_1\left(a\frac{\sqrt{x\,\mathsf{E}}}{\sigma^2}\right), x \geq 0, \tag{3.66}$$

where $\mathsf{I}_1(\cdot)$ is the modified Bessel of the first kind and order one [80, p. 47].

Under hypothesis $i = 0$, error occurs if $z_0 < z_1$. Applying the law of iterated expectation [89], the probability of that event can be calculated as follows:

$$\Pr(e|i=0) = \Pr(z_1 > z_0|i=0) = \mathop{\mathbb{E}}_{a}\left[\mathop{\mathbb{E}}_{z_0|a,i=0}\left[1 - \mathsf{F}_{z_1|i}(z_0|0)\right]\right]. \tag{3.67}$$

In view of Eq. (3.65), the inner expectation in Eq. (3.67) is given by:

$$\begin{aligned}
\mathop{\mathbb{E}}_{z_0|a,i=0}\left[1 - \mathsf{F}_{z_1|i}(z_0|0)\right] &= \int_0^{+\infty}\left(1 - \mathsf{F}_{z_1|i}(x|0)\right)\mathsf{f}_{z_0|i,a}(x|0,a)\mathsf{d}x \\
&= \int_0^{+\infty}\frac{\left(1 + \frac{x}{2\sigma^2}\right)\sqrt{x}}{2\sigma^2\sqrt{\mathsf{E}}\,a}\mathsf{e}^{-\frac{2x+\mathsf{E}\,a^2}{2\sigma^2}}\mathsf{I}_1\left(\frac{a\sqrt{\mathsf{E}\,x}}{\sigma^2}\right)\mathsf{d}x \overset{(a)}{=} \frac{\mathsf{e}^{-\frac{\mathsf{E}\,a^2}{4\sigma^2}}\left(\mathsf{E}\,a^2 + 16\sigma^2\right)}{32\sigma^2},
\end{aligned} \tag{3.68}$$

where in (a), we used [62, Eq. (6.643.2)] and [84, Eqs. (13.15.1), (13.18.3)].

Substituting $\texttt{SNR} = \texttt{E}/(2\sigma^2)$ in Eq. (3.68) , and applying expectation with respect to $a = a_\text{CT}a_\text{TR}$ under independent Rayleigh fading, offers the following:

$$
\mathbb{E}_a\left[\frac{e^{-\frac{\texttt{E}\ a^2}{4\sigma^2}}\left(\texttt{E}\ a^2 + 16\sigma^2\right)}{32\sigma^2}\right] = \mathbb{E}_a\left[e^{-\frac{\texttt{SNR}\ a^2}{2}}\left(\frac{\texttt{SNR}\ a^2}{16} + \frac{1}{2}\right)\right]
$$

$$
= \mathbb{E}_{a_\text{CT}}\left[\mathbb{E}_{a_\text{TR}}\left[e^{-\frac{(a_\text{CT}a_\text{TR})^2\ \texttt{SNR}}{2}}\left(\frac{(a_\text{CT}a_\text{TR})^2\ \texttt{SNR}}{16} + \frac{1}{2}\right)\right]\right]
$$

$$
= \int_0^\infty\int_0^\infty 4\ x\ y\ e^{-x^2-y^2-\frac{(xy)^2\ \texttt{SNR}}{2}}\left(\frac{(xy)^2\ \texttt{SNR}}{16} + \frac{1}{2}\right)\mathrm{d}x\mathrm{d}y
$$

$$
\overset{(a)}{=} \int_0^\infty y\,e^{-y^2}\frac{8 + 5y^2\texttt{SNR}}{2\left(y^2\texttt{SNR} + 2\right)^2}\mathrm{d}y
$$

$$
\overset{(b)}{=} \frac{e^{\frac{2}{\texttt{SNR}}}}{4\texttt{SNR}^2}\int_{\frac{2}{\texttt{SNR}}}^\infty e^{-y}\frac{-2 + 5y\texttt{SNR}}{y^2}\mathrm{d}y
$$

$$
\overset{(c)}{=} \frac{e^{\frac{2}{\texttt{SNR}}}\left(5\texttt{SNR} + 2\right)\mathsf{E}_1\left(\frac{2}{\texttt{SNR}}\right)}{4\texttt{SNR}^2} - \frac{1}{4\texttt{SNR}},
\tag{3.69}
$$

where in (a), [62, Eq. (3.461.3)] was exploited, in (b) we applied change of variables, while in (c), we used [62, Eq. (3.351.4)] and [84, Eq. (6.2.6)]. Due to symmetry, $\Pr(e|i = 0) = \Pr(e|i = 1) = \Pr(e)$ and the proof is completed.

Proof of Theorem 3.3

Due to the conditional independence of each $\mathbf{r}_n$ given the transmitted codeword $\mathbf{c}$ and the parameters $\mathbf{h}, \Phi_0, \Phi_1$, the log-likelihood PDF can be factorized as

$$
\ln\left(\mathsf{f}_{\mathbf{r}_{1:N}|\mathbf{c},\mathbf{h},\Phi_0,\Phi_1}(\mathbf{r}_{1:N_\text{c}}|\mathbf{c}, \mathbf{h}, \Phi_0, \Phi_1)\right) = \sum_{n=1}^{N_\text{c}} \ln\left[\mathsf{f}_{\mathbf{r}_n|c_n,h_n,\mathbf{\Phi}}(\mathbf{r}_n|c_n, h_n, \mathbf{\Phi})\right].
\tag{3.70}
$$

Hence, the log-likelihood PDF is a separable function of $\{h_n\}_{n=1}^{N_\text{c}}$. Given that the channel coefficients $\{h_n\}_{n=1}^{N_\text{c}}$ are statistically independent and distinct (due to $DT \geq T_\text{coh}$), the innermost maximization in (3.52) can be expressed as the sum of independent maximizations:

$$
\max_{\mathbf{h}\in\mathbb{C}^{N_\text{c}}} \ln\left[\mathsf{f}_{\mathbf{r}_{1:N_\text{c}}|\mathbf{c},\mathbf{h},\mathbf{\Phi}}(\mathbf{r}_{1:N_\text{c}}|\mathbf{c}, \mathbf{h}, \mathbf{\Phi})\right] = \sum_{n=1}^{N_\text{c}} \max_{h_n\in\mathbb{C}} \ln\left[\mathsf{f}_{\mathbf{r}_n|c_n,h_n,\mathbf{\Phi}}(\mathbf{r}_n|c_n, h_n, \mathbf{\Phi})\right].
\tag{3.71}
$$

Each individual maximization can be calculated as in Lemma 3.1 through Eq. (3.25). Applying expectation with respect to Φ_0 and Φ_1 in (3.71), the following is obtained:

$$\mathbb{E}_{\boldsymbol{\Phi}}\left[\sum_{n=1}^{N_c}\left[Q^{(n)}+A_{c_n}^{(n)}\right]\right]=\sum_{n=1}^{N_c}\mathbb{E}_{\boldsymbol{\Phi}}\left[Q^{(n)}+A_{c_n}^{(n)}\right]=\sum_{n=1}^{N_c}\left(Q^{(n)}+(1-c_n)\mathbb{E}_{\boldsymbol{\Phi}}\left[A_0^{(n)}\right]+c_n\mathbb{E}_{\boldsymbol{\Phi}}\left[A_1^{(n)}\right]\right)$$

$$=\sum_{n=1}^{N_c}\left(Q^{(n)}+\mathbb{E}_{\boldsymbol{\Phi}}\left[A_0^{(n)}\right]+c_n\left(\mathbb{E}_{\boldsymbol{\Phi}}\left[A_1^{(n)}\right]-\mathbb{E}_{\boldsymbol{\Phi}}\left[A_0^{(n)}\right]\right)\right), \tag{3.72}$$

where

$$A_{c_n}^{(n)}=\frac{1}{2N_0}\left(|r_{c_n}^+(n)|^2+|r_{c_n}^-(n)|^2\right)+\frac{1}{N_0}\Re\left\{(r_{c_n}^+(n))^*(r_{c_n}^-(n))e^{2j\Phi_{c_n}}\right\}, \tag{3.73}$$

$$Q^{(n)}=4\ln\left(\frac{1}{\pi N_0}\right)-\frac{1}{N_0}\|\mathbf{r}_n\|_2^2. \tag{3.74}$$

According to Eq. (3.26), for any $n=1,2,\ldots,N_c$, $\mathbb{E}_{\boldsymbol{\Phi}}\left[A_{c_n}^{(n)}\right]=\frac{1}{2N_0}\left(|r_{c_n}^+(n)|^2+|r_{c_n}^-(n)|^2\right)$.

Ignoring the terms in Eq. (3.72) that do not affect the outer maximization, the rule in Eq. (3.52) is simplified to:

$$\widehat{\mathbf{c}}=\arg\max_{\mathbf{c}\in\mathcal{C}}\left\{\sum_{n=1}^{N_c}c_n\left(\mathbb{E}_{\boldsymbol{\Phi}}\left[A_1^{(n)}\right]-\mathbb{E}_{\boldsymbol{\Phi}}\left[A_0^{(n)}\right]\right)\right\}, \tag{3.75}$$

completing the proof.

Proof of Theorem 3.4

To achieve a fully interleaved system for the coherent case the value of depth D is set

$$(D+N_{\mathrm{tr}})T=T_{\mathrm{coh}}. \tag{3.76}$$

The transmitter stores D codewords belonging to a linear block code $\mathcal{C}$ in a $D\times N_c$ matrix and transmits the information column-wise. For each D bits (each column of interleaving matrix), N_{tr} training bits are utilized for channel estimation. Thus, the transmitter sends at total $N_c(D+N_{\mathrm{tr}})$ bits.

The receiver has $N_c(D+N_{\mathrm{tr}})$ received symbols; $N_c N_{\mathrm{tr}}$ of them correspond to training bits to estimate the random channel vectors associated with each column of interleaving matrix. Let $\mathbf{g}_1,\mathbf{g}_2,\ldots,\mathbf{g}_{N_c}$ be the actual compound channel vectors associated with the symbols of the 1st, 2nd, ..., N_c-th column of interleaving matrix, respectively. Due to Eq. (3.76) the compound channel vectors are independent of each other (and identically distributed).

We conclude that in fully interleaved system the receiver decodes symbol sequences that correspond to codewords with coded bits experiencing independent fading. Accordingly with Eq. (3.51), the received signal for a single row of interleaving matrix can be expressed as

$$\mathbf{r}_i = \mathbf{g}_i \odot \mathbf{s}_{c_i} + \mathbf{n}_i, \quad i = 1, 2, \ldots, N_c, \tag{3.77}$$

with $\mathbf{c} = [c_1 \; c_2 \; \ldots \; c_{N_c}] \in \mathcal{C}$ denoting the transmitted codeword associated with the specific row of interleaving matrix and $\mathbf{s}_{c_i} = \begin{bmatrix} 1 - c_i & 1 - c_i & c_i & c_i \end{bmatrix}^\top$, $i = 1, \ldots, N_c$.

Assuming perfect knowledge of $\mathbf{g}_1, \ldots, \mathbf{g}_{N_c}$, and exploiting their independence, the average probability of decoding error is given by

$$\Pr(e) = \mathbb{E}_{\mathbf{g}_1, \ldots, \mathbf{g}_{N_c}} \left[\Pr(e|\mathbf{g}_1, \ldots, \mathbf{g}_{N_c}) \right]. \tag{3.78}$$

Let $\mathbf{g}_{1:N_c} = [\mathbf{g}_1^\top \; \mathbf{g}_2^\top \; \ldots \; \mathbf{g}_{N_c}^\top]^\top$ for simplicity. For each $i = 1, \ldots, N_c$, the log-likelihood ratio associated with vector $\mathbf{r}_i$ (which is a proper complex Gaussian given $c_i, \mathbf{g}_i$) can be written as

$$l_i = \ln\left(\frac{\mathsf{f}_{\mathbf{r}_i|c_i,\mathbf{g}_i}(\mathbf{r}_i|0,\mathbf{g}_i)}{\mathsf{f}_{\mathbf{r}_i|c_i,\mathbf{g}_i}(\mathbf{r}_i|1,\mathbf{g}_i)} \right) = \frac{2}{N_0} \Re\left\{ \left(\mathbf{g}_i \odot \left(\mathbf{s}_0 - \mathbf{s}_1 \right) \right)^H \mathbf{r}_i \right\}. \tag{3.79}$$

After some algebra and using Eqs (3.11) and (3.17), the conditional PDF of l_i can be expressed as

$$\mathsf{f}_{l_i|c_i,\mathbf{g}_i}(l_i|0, \mathbf{g}_i) \equiv \mathcal{N}\left(\mathsf{SNR}\, a_{\mathrm{CT},i}^2\, a_{\mathrm{TR},i}^2, 2\,\mathsf{SNR}\, a_{\mathrm{CT},i}^2\, a_{\mathrm{TR},i}^2 \right), \tag{3.80}$$

$$\mathsf{f}_{l_i|c_i,\mathbf{g}_i}(l_i|1, \mathbf{g}_i) \equiv \mathcal{N}\left(-\mathsf{SNR}\, a_{\mathrm{CT},i}^2\, a_{\mathrm{TR},i}^2, 2\,\mathsf{SNR}\, a_{\mathrm{CT},i}^2\, a_{\mathrm{TR},i}^2 \right), \tag{3.81}$$

where the parameters $a_{\mathrm{CT},i}, a_{\mathrm{TR},i}$ are associated with compound channel $\mathbf{g}_i$, $i = 1, 2, \ldots, N_c$. Thus, for the channel described by (3.77), the following is satisfied:

$$\mathsf{f}_{l_i|c_i,\mathbf{g}_i}(l_i|0, \mathbf{g}_i) = \mathsf{f}_{-l_i|c_i,\mathbf{g}_i}(-l_i|1, \mathbf{g}_i), \quad i = 1, 2, \ldots, N_c, \tag{3.82}$$

and the channel is memoryless given $\mathbf{g}_{1:N_c}$; thus, it can be considered as a binary-input symmetric-output channel [90].

Under equiprobable signaling, due to the linearity of block code $\mathcal{C}$ and the memoryless structure of channel given $\mathbf{g}_{1:N_c}$, the conditional probability of decoding error is upper bounded by [91, Eqs. (2)–(4)]

$$\Pr(e|\mathbf{g}_1, \ldots, \mathbf{g}_{N_c}) \le \sum_{d=d_{\min}^{\mathcal{C}}}^{N_c} N_d(\mathcal{C}) \Pr\left(\left(\sum_{i=1}^{d} l_i \right) < 0 \,\middle|\, \mathbf{c} = \mathbf{0}, \mathbf{g}_{1:N_c} \right), \tag{3.83}$$

where $N_d(\mathcal{C})$ is the number of codewords in $\mathcal{C}$ that have Hamming weight d, i.e.,

$$N_d(\mathcal{C}) = \Big| \{\mathbf{c} \in \mathcal{C} : w_{\mathrm{H}}(\mathbf{c}) = d\} \Big|. \tag{3.84}$$

The symmetry of channel (Eq. (3.82)) ensures that no loss of optimality is incurred by considering the all-zeros codeword in the pairwise error probability at the right-hand side of (3.83).

Under the assumption of all-zeros codeword and for given $\mathbf{g}_{1:N_c}$ the PDF of RV $l \triangleq \sum_{i=1}^{d} l_i$ is

$$f_{l|\mathbf{c},\mathbf{g}_{1:N_c}}(l|\mathbf{0}, \mathbf{g}_{1:N_c}) \equiv \mathcal{N}\left(\mathsf{SNR} \sum_{i=1}^{d} a_{\mathrm{CT},i}^2 \, a_{\mathrm{TR},i}^2, 2\,\mathsf{SNR} \sum_{i=1}^{d} a_{\mathrm{CT},i}^2 \, a_{\mathrm{TR},i}^2 \right), \tag{3.85}$$

where RVs $a_{\mathrm{CT},i}$ and $a_{\mathrm{TR},i}$ are independent and follow Rayleigh distribution with unit power, due to the assumption that $\kappa_{\mathrm{CT}} = \kappa_{\mathrm{TR}} = 0$.

In view of Eqs. (3.83) and (3.85) the conditional probability of decoding error satisfies

$$\Pr(e|\mathbf{g}_1, \ldots, \mathbf{g}_{N_c}) \leq \sum_{d=d_{\min}^{\mathcal{C}}}^{N_c} N_d(\mathcal{C})\, \mathsf{Q}\left(\sqrt{\mathsf{SNR} \sum_{i=1}^{d} a_{\mathrm{CT},i}^2 \, a_{\mathrm{TR},i}^2} \right)$$

$$\leq \frac{1}{2} \sum_{d=d_{\min}^{\mathcal{C}}}^{N_c} N_d(\mathcal{C})\, \mathsf{e}^{-\frac{1}{2}\mathsf{SNR} \sum_{i=1}^{d} a_{\mathrm{CT},i}^2 \, a_{\mathrm{TR},i}^2}. \tag{3.86}$$

Eq. (3.86) stems from the identity $X \sim \mathcal{N}(\mu, \sigma^2) \implies \Pr(X < 0) = \mathsf{Q}\left(\frac{\mu}{\sigma}\right)$, where $\mathsf{Q}(x) \triangleq \frac{1}{2\pi} \int_x^\infty \mathsf{e}^{-\frac{t^2}{2}} \mathsf{d}t$, and from the Chernoff bound for the Q function, $\mathsf{Q}(x) \leq \frac{1}{2}\mathsf{e}^{-\frac{1}{2}x^2}$. It is noted that the upper bound depends solely on the random amplitudes $a_{\mathrm{CT},i}, a_{\mathrm{TR},i}$, $\forall i$, which must be eliminated through expectation to obtain the upper bound on the probability of decoding error. In view of Eqs. (3.86) and (3.78), $\Pr(e)$ is upper bounded by

$$\Pr(e) \leq \mathop{\mathbb{E}}_{\mathbf{g}_{1:N_c}} \left[\frac{1}{2} \sum_{d=d_{\min}^{\mathcal{C}}}^{N_c} N_d(\mathcal{C})\, \mathsf{e}^{-\frac{1}{2}\mathsf{SNR} \sum_{i=1}^{d} a_{\mathrm{CT},i}^2 \, a_{\mathrm{TR},i}^2} \right]$$

$$= \frac{1}{2} \sum_{d=d_{\min}^{\mathcal{C}}}^{N_c} N_d(\mathcal{C}) \mathop{\mathbb{E}}_{\mathbf{g}_{1:N_c}} \left[\mathsf{e}^{-\frac{1}{2}\mathsf{SNR} \sum_{i=1}^{d} a_{\mathrm{CT},i}^2 \, a_{\mathrm{TR},i}^2} \right]$$

$$= \frac{1}{2} \sum_{d=d_{\min}^{\mathcal{C}}}^{N_c} N_d(\mathcal{C}) \prod_{i=1}^{d} \mathop{\mathbb{E}}_{a_{\mathrm{CT},i},a_{\mathrm{TR},i}} \left[\mathsf{e}^{-\frac{1}{2}\mathsf{SNR}\, a_{\mathrm{CT},i}^2 \, a_{\mathrm{TR},i}^2} \right]. \tag{3.87}$$

Each quantity $\underset{a_{\text{CT},i},a_{\text{TR},i}}{\mathbb{E}}\left[e^{-\frac{1}{2}\text{SNR}\,a_{\text{CT},i}^2\,a_{\text{TR},i}^2}\right]$ is calculated as

$$\underset{a_{\text{CT},i},a_{\text{TR},i}}{\mathbb{E}}\left[e^{-\frac{1}{2}\text{SNR}\,a_{\text{CT},i}^2\,a_{\text{TR},i}^2}\right] = \int_0^\infty \int_0^\infty e^{-\frac{1}{2}(\text{SNR}\,x^2\,y^2)}4\,x\,y\,e^{-x^2-y^2}\mathrm{d}x\mathrm{d}y$$

$$= \int_0^\infty 4\,\frac{y\,e^{-y^2}}{2+y^2\text{SNR}}\mathrm{d}y = \int_0^\infty 2\,\frac{e^{-y}}{2+y\text{SNR}}\mathrm{d}y \qquad (3.88)$$

$$= \left(\frac{2}{\text{SNR}}\right)e^{\frac{2}{\text{SNR}}}\Gamma\left(0,\frac{2}{\text{SNR}}\right). \qquad (3.89)$$

The result in [62, Eqs. (3.461.3) and (3.383.10)] is utilized to obtain Eqs. (3.88) and (3.89). $\Gamma(s,x) = \int_x^\infty t^{s-1}e^{-t}\mathrm{d}t$ is the upper incomplete gamma function. Substituting (3.89) in (3.87), the final upper bound of $\Pr(e)$ is expressed as

$$\Pr(e) \le \frac{1}{2}\sum_{d=d_{\text{min}}^{\mathcal{C}}}^{N_{\text{c}}} N_d(\mathcal{C}\left(\left(\frac{2}{\text{SNR}}\right)e^{\frac{2}{\text{SNR}}}\Gamma\left(0,\frac{2}{\text{SNR}}\right)\right)^d. \qquad (3.90)$$

To prove the diversity order argument, the definition of diversity order in [92, Eq. 3] will be utilized. Specifically, the quantity

$$\lim_{\text{SNR}\to\infty} \frac{\log\left(\left(\frac{2}{\text{SNR}}\right)e^{\frac{2}{\text{SNR}}}\Gamma\left(0,\frac{2}{\text{SNR}}\right)\right)}{\log(\text{SNR})}$$

$$= \lim_{\text{SNR}\to\infty}\left\{\frac{\log\left(\frac{2}{\text{SNR}}\right)}{\log(\text{SNR})} + \frac{\frac{2}{\text{SNR}}}{\log(\text{SNR})} + \frac{\log\left(\Gamma\left(0,\frac{2}{\text{SNR}}\right)\right)}{\log(\text{SNR})}\right\} \qquad (3.91)$$

equals -1, because the first term of the right-hand side of (3.91) offers -1, the second offers 0, and the third offers 0 if we use L'Hôpital's rule and [84, Eq. (8.8.13)]. Therefore,

$$\lim_{\text{SNR}\to\infty} \frac{\log\left(\left(\frac{2}{\text{SNR}}\right)e^{\frac{2}{\text{SNR}}}\Gamma\left(0,\frac{2}{\text{SNR}}\right)\right)^d}{\log(\text{SNR})} = -d. \qquad (3.92)$$

Using [84, Eqs. (8.4.4) and (6.8.2)] we conclude that $\left(\frac{2}{\text{SNR}}\right)e^{\frac{2}{\text{SNR}}}\Gamma\left(0,\frac{2}{\text{SNR}}\right) \le 1$ for every (non-negative) value of SNR. Hence, function

$$\left(\left(\frac{2}{\text{SNR}}\right)e^{\frac{2}{\text{SNR}}}\Gamma\left(0,\frac{2}{\text{SNR}}\right)\right)^d \qquad (3.93)$$

is a non-increasing function of d. Combining the above with Eqs. (3.90) and (3.92) the proof is completed.

Chapter 4

Extended Scatter Radio Coverage for Low-Power Internet-of-Things

Building upon the results presented in chapter 3, this chapter explores scatter radio from a networking point of view, trying to evaluate and contrast, in terms of several multi-tag performance metrics, the most prominent scatter radio network architectures, i.e., the monostatic and the multi-bistatic (multistatic) architectures. In monostatic architecture, the reader consists of both the illuminating transmitter and the receiver of signals scattered back from the tags/sensors. The multistatic architecture includes several ultra-low-cost illuminating carrier emitters and a single reader. The chapter analyses performance metrics such as, maximum-likelihood coherent and noncoherent bit error rate (BER), diversity order, average information and energy outage probability, under dyadic Nakagami fading. The latter is the most realistic small-scale fading wireless channel model for backscatter communications. The theoretical and simulation results revealed the following: (i) multistatic architecture outperforms monostatic one in terms of diversity order and BER performance, (ii) for passive tags with radio frequency (RF) energy harvesting, energy outage events are more infrequent in multistatic than monostatic architecture, and (iii) multistatic coverage is higher than monostatic. The chapter is closed with some experimental results attributed to [40]. A proof-of-concept digital multistatic backscatter sensor network (BSN) was demonstrated with a single receiver, four low-cost emitters and multiple ambiently-powered, low bitrate tags. The outcome of this research can be applied in the industries of wireless sensor networks (WSNs) and emerging Internet-of-things (IoT) applications.

Related Work

In environmental monitoring and precision agriculture, as well as in many other Internet-of-Things (IoT) applications from healthcare domain and smart homes (with many examples found in [1] and references therein), the reader (receiver) must be able to decode multiple sensors' signals for ranges that may be larger than conventional ranges in radio frequency identification (RFID) systems. In such situations one potential solution would be the adoption of conventional (Marconi) radios for multi-sensor communication. However, radio frequency (RF) front-ends in Marconi radios typically require signal conditioning units, such as mixers, active filters, and amplifiers, increasing complexity, power consumption, and monetary cost per IoT device. On the contrary, backscattering, i.e., communication by means of reflection, can be realized with a single RF transistor at each scatter radio node, and thus, power consumption and monetary cost per IoT device can be maintained at ultra-low levels.

There are two different architectures for scatter radio networks, namely the monostatic and the multi-bistatic (multistatic) architectures, depicted in Fig 4.1. In monostatic architecture [93], the reader consists of both the illuminating transmitter and the receiver of signals reflected back from the tags. In the bistatic architecture [33], the illuminating carrier emitter (CE) and the receiver of the reflected (backscattered) signals are distinct units, located at different positions, offering flexible network topologies. In the multistatic architecture, several low-cost CEs are available, two orders of magnitude cheaper than the reader. The latter can be a low-cost, commodity software-defined radio (SDR). Before presenting any theoretical or simulation result, simple intuition indicates that due to the morphology of the multistatic architecture, each tag can be close to a CE with high probability, offering two desired implications: (a) the tag-to-reader coverage is increased with high probability and (b) using passive tags that harvest RF energy from the illuminating emitters, the probability of energy outage during the energy harvesting phase can be decreased.

Proof-of-concept multistatic backscatter sensor network (BSN) examples with analog FM principles can be found in [17] and [19], for environmental humidity and soil moisture, respectively, while work in [18] used bistatic scatter radio to convey the electric potential of several plants and each BSN terminal was powered by the plant itself, capitalizing upon the ultra-low power requirements of scatter radio.

This first concrete step towards increased range digital scatter radio systems operating with multiple tags was done in [13], where frequency-based modulations were advocated for frequency-based multiple access and a monostatic reader was built to decode noncoherently minimum-shift keying (MSK)-modulated backscattered, low bitrate sig-

nals. Subsequent work in [94] conducted coverage analysis assuming tags backscattering frequency-modulated signals over orthogonal subcarriers. The required number of RF sources to obtain interference-free communication connectivity for wireless sensor networks consisting of passive devices was studied in [95]. The authors in [96] propose a network architecture that enables device-to-device (D2D) communication between passive nodes by simultaneously integrating backscatter communication along with wireless power transfer.

Contributions

The contributions of this chapter are summarized as follows:

- A multi-tag signal model based on joint time- and frequency-division multiplexing (joint TDM-FDM) for both multistatic and monostatic systems is proposed, exploiting existing results on scatter radio prior art. The signal model accounts for (large-scale) path-loss and small-scale fading, based on, realistic for scatter radio signal model, dyadic Nakagami fading.

- Upper bounds on BER performance of point-to-point backscatter systems under coherent maximum-likelihood (ML) detection for dyadic Nakagami fading are derived. These bounds coincide with the exact BER performance of noncoherent envelope detection. The derived BER expressions depend on the topology of the tags and can
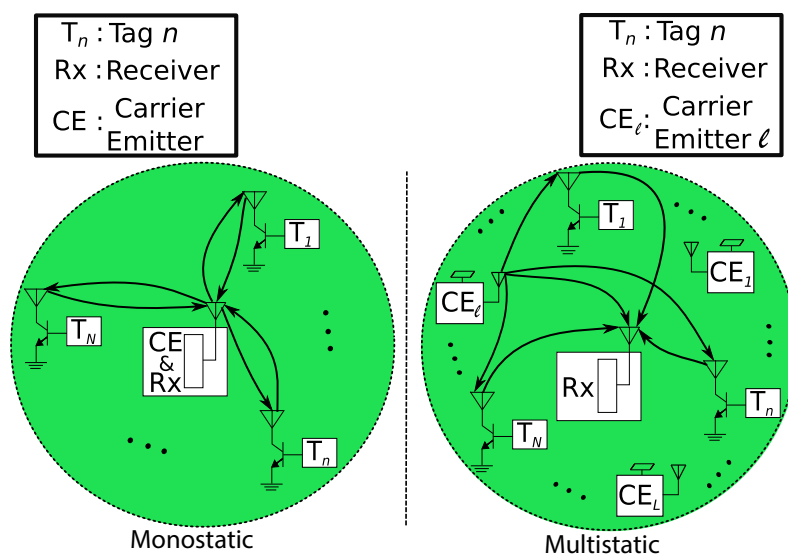

Figure 4.1: Monostatic (Left) and Multistatic (Right) backscatter sensor network (BSN) architecture with N tags, $n = 1 \ldots N$, and L illuminating carrier emitters (CEs), $l = 1 \ldots L$.

be exploited to a network level analysis. It is found that the bistatic architecture has higher diversity order than the monostatic architecture. Additionally, it is found that the multistatic analysis covers asymmetric cases, where the fading statistics of links emitter-to-tag and tag-to-reader are different.

- Information outage probability and tight Jensen-based upper bounds are provided for Rayleigh fading. In addition, for the case of passive tags, closed-form expressions for energy outage are derived for Nakagami fading.

- Numerical results demonstrate that multistatic architecture outperforms the monostatic one for every studied metric. Topology-free information and energy outage expressions are evaluated over the class of square grid topologies (related to the spatial distribution of the tags).

- A digital, multistatic BSN is experimentally demonstrated and contrasted to a monostatic counterpart, corroborating the theoretical findings and offering a concrete proof-of-concept. These experimental results are contributed from [40] and are presented in this thesis to offer a complete comparison between the two studied scatter radio architectures.

Organization and Notation

The rest of this document is organized as follows: Section 4.1 presents the model of the monostatic and multistatic architectures. Section 4.2 presents the single user (i.e., tag) error probability analysis and Section 4.3 offers the outage probability analysis for multiple tags and presents how to model the spatial distribution of tags. Next, Section 4.4 offers energy outage analytical results. Numerical and experimental (outdoor) results are presented in Sections 4.5 and 4.6, respectively.

Notation: Symbols $\mathbb{B}$, $\mathbb{N}$, $\mathbb{R}$, and $\mathbb{C}$ denote the set of binary, natural, real, and complex numbers, respectively. $\mathbf{0}_N$ and $\mathbf{I}_N$, denote, respectively, the all-zeros vector and identity matrix of size N. The phase of a complex number z is denoted as $\angle z$. The distribution of a proper complex Gaussian $N \times 1$ vector $\mathbf{x}$ with mean $\boldsymbol{\mu}$ and covariance matrix $\boldsymbol{\Sigma}$ is denoted by $\mathcal{CN}(\boldsymbol{\mu}, \boldsymbol{\Sigma}) \triangleq \frac{1}{\pi^N \det(\boldsymbol{\Sigma})} e^{-(\mathbf{x}-\boldsymbol{\mu})^{\mathsf{H}} \boldsymbol{\Sigma}^{-1}(\mathbf{x}-\boldsymbol{\mu})}$. $\mathcal{U}[a, b]$ denotes the uniform distribution in $[a, b]$. Expectation of function $\mathsf{g}(\cdot)$ of random variable x with probability density function (PDF) $\mathsf{f}_x(\cdot)$ is denoted as $\mathbb{E}[\mathsf{g}(x)] \triangleq \int_x \mathsf{g}(x)\mathsf{f}_x(x)\mathsf{d}x$. The probability of event $\mathcal{A}$ is denoted as $\mathbb{P}(\mathcal{A})$.

4.1 System Model

4.1.1 Network Architecture

We consider a backscatter sensor network (BSN) consisting of N static sensors (tags) at distinct positions that backscatter their measured data to a single-antenna software-defined radio (SDR) reader; let $\mathcal{N} \triangleq \{1, 2, \ldots, N\}$ be denoting the set of tags. Tags are considered semi-passive, i.e., they utilize scatter radio for communication and are powered by any type of energy source, either ambient (solar, thermoelectric, chemical) or dedicated (e.g., battery).

In multistatic BSN architecture a set of RF illuminators or carrier emitters (CE) is assumed, denoted as $\mathcal{L} \triangleq \{1, 2, \ldots, L\}$. The CEs are distinct units from the SDR receiver and transmit a continuous carrier wave (CW) with time-division multiple access (TDMA) or frequency-division multiple access (FDMA) (see Fig. 4.1-Right and Fig. 4.2). For TDMA operation, the l-th CE transmits at the l-th time slot using a common carrier frequency, whereas for FDMA operation, the l-th CE transmits at the l-th frequency slot, i.e., carrier frequency centered at a frequency band orthogonal to the bands of the other simultaneously (in-time) transmitting CEs. The wireless channel is assumed quasi-static, changing independently across different (time or frequency) slots. For the l-th (time or frequency) slot, $2N+1$ unidirectional links exist (N CE-to-tag links, N tag-to-SDR reader links and the CE-to-SDR reader link). The distance between the l-th CE and the n-th tag is denoted by $\mathsf{d}_{\mathrm{C}_l \mathrm{T}_n}$, the distance between the n-th tag and the reader is denoted as $\mathsf{d}_{\mathrm{T}_n \mathrm{R}}$ with $n \in \mathcal{N}$ and the distance between the l-th CE and the SDR reader is denoted as $\mathsf{d}_{\mathrm{C}_l \mathrm{R}}$ (Fig. 4.2). Under the assumptions of this work, it will be shown that TDMA and FDMA operations for CEs offer equivalent signal representations.

In the monostatic BSN architecture the single-antenna reader operates as both the receiver and the CW emitter, in full-duplex mode. Specifically, the tags are illuminated by the illuminating CE emitted from the SDR reader. The incident CE signal is modulated and backscattered towards the SDR reader. For fair comparison to the multistatic system, transmission across L time slots will be also assumed, with wireless channel changing independently between time or frequency slots. In this architecture N bidirectional links exist between the reader and the N tags (Fig. 4.1-Left). The distance between the reader and the n-th tag is denoted by d_{k}, where $\mathrm{k} \in \{\mathrm{T}_n \mathrm{R}, \mathrm{RT}_n\}$ denotes the unidirectional tag-to-reader, reader-to-tag link, respectively.

The positions of n-th tag, l-th CE, and SDR reader are denoted $\mathbf{u}_{\mathrm{T}_n}$, $n \in \mathcal{N}$, $\mathbf{u}_{\mathrm{C}_l}$, $l \in \mathcal{L}$, and $\mathbf{u}_{\mathrm{R}}$, respectively.
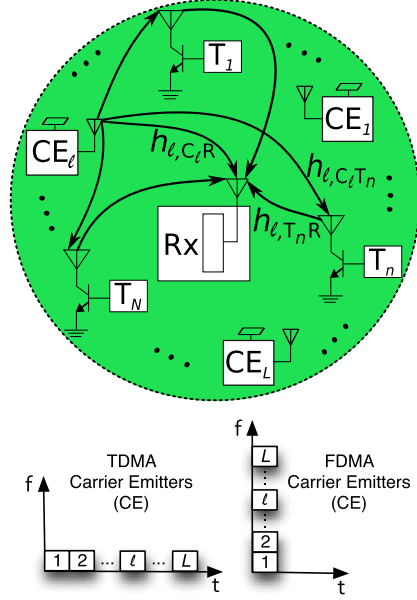
Figure 4.2: Multistatic BSN transmission model over the l-th time slot.

4.1.2   Channel Model

The adopted path-loss model is [27]:

$$\mathsf{L}_{\mathrm{k}} = \left(\frac{\lambda}{4\pi d_0}\right)^2 \left(\frac{d_0}{\mathsf{d}_{\mathrm{k}}}\right)^{\nu_{\mathrm{k}}}, \tag{4.1}$$

where $\mathrm{k} \in \{\mathrm{C}_l\mathrm{R}, \mathrm{C}_l\mathrm{T}_n, \mathrm{T}_n\mathrm{R}\}$ for multistatic and $\mathrm{k} \in \{\mathrm{T}_n\mathrm{R}, \mathrm{RT}_n\}$ for monostatic archi-tecture, d_0 is a reference distance (assumed unit thereinafter), λ is the carrier emission wavelength and ν_{k} is the path-loss exponent for link k.

Tag communication bandwidth and channel delay spread are assumed relatively small and thus, frequency non-selective (flat) fading is assumed. The complex channel gain for the l-th (time or frequency) slot is denoted as $h_{l,\mathrm{k}} = a_{l,\mathrm{k}}\, \mathsf{e}^{-\mathsf{j}\phi_{l,\mathrm{k}}}$, where $a_{l,\mathrm{k}} \in \mathbb{R}_+$, $\phi_{l,\mathrm{k}} \in [0, 2\pi)$, $\mathrm{k} \in \{\mathrm{C}_l\mathrm{R}, \mathrm{C}_l\mathrm{T}_n, \mathrm{T}_n\mathrm{R}\}$ and $\mathrm{k} \in \{\mathrm{T}_n\mathrm{R}, \mathrm{RT}_n\}$ for multistatic and monostatic architecture, respectively, with $\mathbb{E}[|h_{l,\mathrm{k}}|^2] \equiv \mathbb{E}\left[a_{l,\mathrm{k}}^2\right] = 1$. It is emphasized that for CEs in TDMA or FDMA mode, $h_{l_1,\mathrm{k}}$ is statistically independent to $h_{l_2,\mathrm{k}}$ for any $l_1 \neq l_2$. Moreover, at the monostatic architecture reciprocity implies $h_{l,\mathrm{T}_n\mathrm{R}} = h_{l,\mathrm{RT}_n}$, while at the multistatic architecture, $\{h_{l,\mathrm{k}}\}$ are independent (and not necessarily identically distributed) for dif-ferent $\mathrm{k} \in \{\mathrm{C}_l\mathrm{R}, \mathrm{C}_l\mathrm{T}_n, \mathrm{T}_n\mathrm{R}\}$.[1]

Due to potentially strong line-of-sight (LoS) signals in scatter radio environments, Nakagami small-scale fading is a valid assumption for small-scale fading at each scatter

---

[1]Results can be easily extended to the multi-antenna reader case.

radio link (with $\mathbb{E}\left[a_{l,\mathrm{k}}^2\right] = 1$) [27, p. 79]:

$$\mathsf{f}_{a_{l,\mathrm{k}}}(x) = 2\left(\mathsf{M}_\mathrm{k}\right)^{\mathsf{M}_\mathrm{k}} \frac{x^{2\mathsf{M}_\mathrm{k}-1}}{\Gamma(\mathsf{M}_\mathrm{k})}\, \mathsf{e}^{-\mathsf{M}_\mathrm{k} x^2}, \quad x \geq 0, \tag{4.2}$$

where $\mathsf{M}_\mathrm{k} \geq \frac{1}{2}$ is the Nakagami parameter and function $\Gamma(x) = \int_0^\infty t^{x-1}\mathsf{e}^{-t}\mathrm{d}t$ is the Gamma function. For the special cases of $\mathsf{M}_\mathrm{k} = 1$ and $\mathsf{M}_\mathrm{k} = \infty$, Rayleigh and no-fading (i.e., $a_{l,\mathrm{k}} = 1$) is obtained, respectively. For $\mathsf{M}_\mathrm{k} = \frac{(\kappa_\mathrm{k}+1)^2}{2\kappa_\mathrm{k}+1}$, the distribution in (4.2) approximates Rice with Rician parameter κ_k [27].

4.1.3 Signal Model

Multistatic

Following the scatter radio signal model in Section 3.1, the l-th CE transmits a CW at the l-th (time or frequency) slot, with complex baseband $\mathsf{c}_l^{[\mathrm{b}]}(t) = \sqrt{2P_{\mathrm{C}_l}}\, \mathsf{e}^{-\mathsf{j}(2\pi\Delta F_l t + \Delta\phi_l)}$, where P_{C_l} is the l-th CE transmission power, while ΔF_l and $\Delta\phi_l$ model the carrier frequency offset (CFO) and phase offset between the l-th CE and the SDR reader, respectively, due to the fact that CE and the SDR reader do not share the same oscillator.

Each tag $n \in \mathcal{N}$ is illuminated by the carrier wave $\mathsf{c}_l^{[\mathrm{b}]}(t)$. The tag's information is binary-modulated on the incident CW by switching the antenna load between two loads, associated with two distinct reflection coefficients: $\Gamma_{n,0}$ and $\Gamma_{n,1}$ for bit "0" and bit "1", respectively. Binary frequency-shift keying (FSK) modulation is employed, where each tag switches between the two loads using a 50% duty cycle square waveform of duration T per bit (nominal bit duration), fundamental frequency $F_{n,i}$, and random initial phase $\Phi_{n,i}$, for bit $i \in \mathbb{B} \triangleq \{0,1\}$ (cf. Eq. (3.6)); in other words, modulation occurs with different switching frequency between tag antenna loads, utilizing switching (also coined as subcarrier) frequency $F_{n,0}$ for bit "0" and $F_{n,1}$ for bit "1", without any type of signal conditioning, such as filtering, amplification or mixing [13].

Fig. 4.3 depicts the measured spectrum at a spectrum analyzer when a signal's generator's CW at $F_s = 868$ MHz illuminates tag n that utilizes binary FSK with $|F_{n,1} - F_{n,0}| = 122.5$ kHz. In contrast to conventional Marconi-radio FSK, frequencies $F_s - F_{n,0}$ and $F_s - F_{n,1}$ also contribute to the total received signal (in addition to $F_s + F_{n,0}$ and $F_s + F_{n,1}$), and thus, backscatter FSK modulation uses 4 frequencies, $\pm F_{n,i_n}, i_n \in \mathbb{B}$. Consequently, the optimal demodulator requires 4 matched filters and not 2, as in classic FSK demodulation.

A set of unique subcarrier frequencies $F_{n,i_n}, i_n \in \mathbb{B}$, are employed at tag n to scatter its data. At the network level, the $4N$ frequencies $\{\pm F_{n,i_n}\}, \forall (i_n, n) \in \mathbb{B} \times \mathcal{N}$ must satisfy
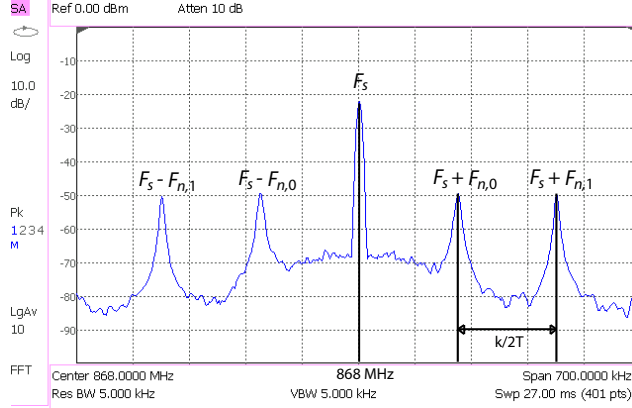
Figure 4.3: Measured backscatter radio FSK spectrum with two loads. Scattered signal appears in 4 frequencies, 2 left and 2 right of the illuminating carrier.

the orthogonality criterion, which for coherent FSK adheres to the following:[2]

$$|F_{n,i} - F_{j,m}| = \frac{k}{2T} \quad \text{and} \quad F_{n,i} \gg \frac{1}{2T}, \tag{4.3}$$

$\forall (i, n), (m, j) \in \mathbb{B} \times \mathcal{N} : m \neq i$, and $k \in \mathbb{N}$.

Under the above orthogonality criteria the system of N tags scattering simultaneously can be divided into N parallel orthogonal channels, where each can be received separately, without collision. Such single-tag processing techniques have been extensively covered in [13, 33, 37, 39, 97]. In view of Eq. (3.18), for the point-to-point backscatter system associated with the n-th tag during the l-th slot, the CFO-free, DC-blocked received baseband signal at the reader over a bit period T is given by

$$\mathbf{r}_{l,n}^{[\mathrm{b}]} = h_{l,n}^{[\mathrm{b}]} \sqrt{\mathrm{E}_{l,n}^{[\mathrm{b}]}} \, \mathbf{x}_n + \mathbf{w}_{l,n}, \quad n \in \mathcal{N}, \tag{4.4}$$

where the vector $\mathbf{x}_n$ is given by:

$$\mathbf{x}_n \triangleq \sqrt{\frac{1}{2}} \left[\mathsf{e}^{+\mathsf{j}\Phi_{n,0}} \; \mathsf{e}^{-\mathsf{j}\Phi_{n,0}} \; \mathsf{e}^{+\mathsf{j}\Phi_{n,1}} \; \mathsf{e}^{-\mathsf{j}\Phi_{n,1}} \right]^{\top} \odot \mathbf{s}_{i_n}, \quad n \in \mathcal{N}, \tag{4.5}$$

and $\mathbf{s}_{i_n} = \left[(1 - i_n) \; (1 - i_n) \; i_n \; i_n \right]^{\top}$ is the four-dimensional transmitted symbol of the n-th tag corresponding to transmitted bit $i_n \in \mathbb{B}$. $\Phi_{n,0}$ ($\Phi_{n,1}$) is implementation-specific phase mismatch between tag n and reader for bit 0 (bit 1), assumed constant for the L slots. Symbol $\odot$ denotes the component-wise (Hadamard) product. According to Theorem 3.1 for $F_{n,i_n} + \frac{20}{T} \ll W_{\mathrm{SDR}}$, where W_{SDR} is the SDR receiver baseband bandwidth,

---

[2]For noncoherent FSK, term $k/2T$ in Eq. (4.3) is replaced with k/T.

$\mathbf{w}_{l,n} \sim \mathcal{CN}\left(\mathbf{0}_4, N_0\mathbf{I}_4\right)$. Compound channel parameter $h_{l,n}^{[\mathrm{b}]}$ in Eq. (4.4) is given by:

$$h_{l,n}^{[\mathrm{b}]} \triangleq a_{l,n}^{[\mathrm{b}]}\, \mathsf{e}^{-\mathsf{j}\phi_{l,n}^{[\mathrm{b}]}}, \tag{4.6}$$

$$a_{l,n}^{[\mathrm{b}]} = a_{l,\mathrm{C}_l\mathrm{T}_n}\, a_{l,\mathrm{T}_n\mathrm{R}}, \tag{4.7}$$

$$\phi_{l,n}^{[\mathrm{b}]} = \phi_{l,\mathrm{C}_l\mathrm{T}_n} + \phi_{l,\mathrm{T}_n\mathrm{R}} + \Delta\phi_l + \underline{/\Gamma_{n,0} - \Gamma_{n,1}}. \tag{4.8}$$

Symbol $\mathsf{E}_{l,n}^{[\mathrm{b}]}$ denotes the average energy per bit for the n-th tag over the l-th slot and, accordingly with Eq. (3.16), is given by:

$$\mathsf{E}_{l,n}^{[\mathrm{b}]} = \frac{\mathbb{E}\left[\left(a_{l,n}^{[\mathrm{b}]}\,\mu_{l,n}^{[\mathrm{b}]}\right)^2 T\right]}{2} = \frac{\left(\mu_{l,n}^{[\mathrm{b}]}\right)^2 T}{2}, \tag{4.9}$$

taking into account that RVs $a_{l,\mathrm{C}_l\mathrm{T}_n}$ and $a_{l,\mathrm{T}_n\mathrm{R}}$ are independent with unit power. Parameter $\mu_{l,n}^{[\mathrm{b}]}$ above incorporates the compound scatter radio link path-losses and tag-related parameters, i.e.,

$$\mu_{l,n}^{[\mathrm{b}]} = \sqrt{2\,P_{\mathrm{C}_l}\,\mathsf{L}_{\mathrm{C}_l\mathrm{T}_n}\,\mathsf{L}_{\mathrm{T}_n\mathrm{R}}}\,\left|\Gamma_{n,0} - \Gamma_{n,1}\right|\,\frac{2}{\pi}\,\mathsf{s}_n, \tag{4.10}$$

with s_n modeling the n-th tag's (real) scattering efficiency, assumed constant over the L slots. The average received SNR of tag n at the l-th slot for multistatic system associated with the system in Eq. (4.4) is given by $\mathsf{SNR}_{l,n}^{[\mathrm{b}]} = \mathsf{E}_{l,n}^{[\mathrm{b}]}/N_0$.

As already mentioned, for CEs in TDMA or FDMA mode, $h_{l_1,\mathrm{k}}$ is statistically independent to $h_{l_2,\mathrm{k}}$ for any $l_1 \neq l_2$. Under this assumption, tools developed in this work can in principle accommodate both CE modes. For simpler presentation and concise comparison with the monostatic architecture, we will assume hereinafter CEs in TDMA mode.

Monostatic

In monostatic case CFO ΔF_l and phase offset $\Delta\phi_l$ are zero, due to the fact that the receiver and the emitter share the same oscillator. Using Eq. (4.4) and the reciprocity of the channel between the reader and each tag, the DC-blocked, demodulated received signal for tag n in the monostatic architecture at time slot l is given by:

$$\mathbf{r}_{l,n}^{[\mathrm{m}]} = h_{l,n}^{[\mathrm{m}]}\,\sqrt{\frac{\mathsf{M}_n}{\mathsf{M}_n + 1}\mathsf{E}_n^{[\mathrm{m}]}}\,\mathbf{x}_n + \mathbf{w}_{l,n}, \quad n \in \mathcal{N}, \tag{4.11}$$

under the same assumptions and definitions as in Eqs. (4.4), (4.5). In accordance with the multistatic case, $h_{l,n}^{[\mathrm{m}]}$ is given by:

$$h_{l,n}^{[\mathrm{m}]} \triangleq a_{l,n}^{[\mathrm{m}]} \, \mathrm{e}^{-\mathrm{j}\phi_{l,n}^{[\mathrm{m}]}}, \tag{4.12}$$

$$a_{l,n}^{[\mathrm{m}]} = (a_{l,\mathrm{T}_n\mathrm{R}})^2 , \quad \phi_{l,n}^{[\mathrm{m}]} = 2\phi_{l,\mathrm{T}_n\mathrm{R}} + \underline{/\Gamma_{n,0} - \Gamma_{n,1}}. \tag{4.13}$$

The average received energy per bit for monostatic system for the n-th tag over the l-th time slot, $\mathrm{E}_n^{[\mathrm{m}]}$, is expressed as:

$$\mathrm{E}_n^{[\mathrm{m}]} = \frac{\mathbb{E}\left[\left(a_{l,n}^{[\mathrm{m}]} \, \mu_{l,n}^{[\mathrm{m}]}\right)^2 T\right]}{2} = \frac{1 + \mathrm{M}_n}{2\,\mathrm{M}_n} \left(\mu_n^{[\mathrm{m}]}\right)^2 T, \tag{4.14}$$

since $\mathbb{E}\left[\left(a_{l,n}^{[\mathrm{m}]}\right)^2\right] = \mathbb{E}\left[(a_{l,\mathrm{T}_n\mathrm{R}})^4\right] = (\mathrm{M}_n + 1)/\mathrm{M}_n$ and $\mu_n^{[\mathrm{m}]}$ is simplified from Eq. (4.10) to:

$$\mu_n^{[\mathrm{m}]} = \sqrt{2P_\mathrm{R}} \, \mathsf{L}_{\mathrm{T}_n\mathrm{R}} \, |\Gamma_{n,0} - \Gamma_{n,1}| \, \frac{2}{\pi} \, \mathsf{s}_n. \tag{4.15}$$

The average received SNR of tag n at the l-th time slot for monostatic system is given by[3] $\mathrm{SNR}_n^{[\mathrm{m}]} = \mathrm{E}_n^{[\mathrm{m}]}/N_0$.

In the monostatic case above, quantities $\mathrm{E}_n^{[\mathrm{m}]}$ and $\mathrm{SNR}_n^{[\mathrm{m}]}$ do not depend on time index l, because they are functions of path loss $\mathsf{L}_{\mathrm{T}_n\mathrm{R}}$; the latter is constant during the L slots. On the contrary, $\mathrm{E}_{l,n}^{[\mathrm{b}]}$ and $\mathrm{SNR}_{l,n}^{[\mathrm{b}]}$ in the multistatic case, are both functions of path loss $\mathsf{L}_{\mathrm{C}_l\mathrm{T}_n}$, which depends on the slot index l, since different CE corresponds to each slot.

In addition, it is noted that due to the nature of FSK modulation, the discrete baseband signal expressions in Eqs. (4.4) and (4.11) depend solely on links $\mathrm{C}_l\mathrm{T}_n$ and $\mathrm{T}_n\mathrm{R}$ due to DC-blocking operation, and thus, the analysis is continued with link $\mathrm{T}_n\mathrm{R}$ for monostatic and links $\mathrm{C}_l\mathrm{T}_n$ and $\mathrm{T}_n\mathrm{R}$ for bistatic (one CE) or multistatic (multiple CEs) architecture, $\forall (l, n) \in \mathcal{L} \times \mathcal{N}$.

4.1.4   Distribution of Fading Amplitudes

It can be observed that RVs $(a_{l,\mathrm{C}_l\mathrm{T}_n})^2$ and $(a_{l,\mathrm{T}_n\mathrm{R}})^2$ are independent following Gamma distribution with parameters $\left(\mathrm{M}_{\mathrm{C}_l\mathrm{T}_n}, \frac{1}{\mathrm{M}_{\mathrm{C}_l\mathrm{T}_n}}\right)$ and $\left(\mathrm{M}_{\mathrm{T}_n\mathrm{R}}, \frac{1}{\mathrm{M}_{\mathrm{T}_n\mathrm{R}}}\right)$, respectively [60, p. 242], i.e., the probability density function (PDF) of RVs $(a_{l,\mathrm{k}})^2$ is given by:

$$\mathsf{f}_{a_{l,\mathrm{k}}^2}(x) = (\mathrm{M}_\mathrm{k})^{\mathrm{M}_\mathrm{k}} \frac{x^{\mathrm{M}_\mathrm{k}-1}}{\Gamma(\mathrm{M}_\mathrm{k})} \, \mathrm{e}^{-\mathrm{M}_\mathrm{k}x}, \quad x \geq 0, \quad \mathrm{k} \in \{\mathrm{C}_l\mathrm{T}_n, \mathrm{T}_n\mathrm{R}\}. \tag{4.16}$$

---

[3]From Eq. (4.11), notice that $\mathbb{E}\left[|h_{l,n}^{[\mathrm{m}]}|^2 \frac{\mathrm{M}_n}{\mathrm{M}_n+1} \mathrm{E}_n^{[\mathrm{m}]} ||\mathbf{x}_n||^2\right] = \mathrm{E}_n^{[\mathrm{m}]}$.

The above distribution reflects the power distribution of each small-scale fading scatter radio link for both monostatic and multistatic architectures and will be used as a building block to derive closed-form expressions for the metrics of interest.

For simplified notation, the following abbreviations are used: $\mathtt{M}_{\mathtt{C}_l\mathtt{T}_n} = \mathtt{M}_{ln}$ and $\mathtt{M}_{\mathtt{T}_n\mathtt{R}} = \mathtt{M}_n$.

4.2 BER Analysis with ML Detection

4.2.1 Coherent

Monostatic

According to Eq. (4.11), given channel realization $h_{l,n}^{[\mathrm{m}]}$ (with $\left|h_{l,n}^{[\mathrm{m}]}\right| = a_{l,n}^{[\mathrm{m}]}$) and phase parameters $\Phi_{n,0}, \Phi_{n,1}$, the conditional bit error rate (BER) for tag n over time slot l under ML coherent detection depends solely on amplitude $a_{l,n}^{[\mathrm{m}]}$ [37], and is given by [79, p. 508]:

$$\mathbb{P}\left(e_{l,n}^{[\mathrm{m}]} \mid a_{l,n}^{[\mathrm{m}]}\right) = \mathsf{Q}\left(\frac{a_{l,n}^{[\mathrm{m}]}\sqrt{\frac{\mathtt{M}_n}{\mathtt{M}_n+1}\mathtt{E}_n^{[\mathrm{m}]}}\,\|\mathbf{x}_0 - \mathbf{x}_1\|_2}{\sqrt{2\,N_0}}\right) = \mathsf{Q}\left(a_{l,n}^{[\mathrm{m}]}\sqrt{\frac{\mathtt{M}_n\mathsf{SNR}_n^{[\mathrm{m}]}}{\mathtt{M}_n + 1}}\right), \tag{4.17}$$

where function $\mathsf{Q}(x) = \frac{1}{2\pi}\int_x^\infty \mathsf{e}^{-\frac{t^2}{2}}\mathsf{dt}$ and $\|\mathbf{x}_0 - \mathbf{x}_1\|_2 = \sqrt{2}$ were utilized.

Using the Chernoff bound for $\mathsf{Q}(\cdot)$ function, Eq. (4.17) can be upper bounded as $\mathsf{Q}\left(a_{l,n}^{[\mathrm{m}]}\sqrt{\frac{\mathtt{M}_n\mathsf{SNR}_n^{[\mathrm{m}]}}{\mathtt{M}_n+1}}\right) \leq \frac{1}{2}\mathsf{e}^{-\frac{\left(a_{l,n}^{[\mathrm{m}]}\right)^2 \mathtt{M}_n\,\mathsf{SNR}_n^{[\mathrm{m}]}}{2\,(\mathtt{M}_n+1)}}$. Since RV $a_{l,n}^{[\mathrm{m}]} = (a_{l,\mathtt{T}_n\mathtt{R}})^2$ is Gamma distributed with parameter $\left(\mathtt{M}_n, \frac{1}{\mathtt{M}_n}\right)$, the unconditional BER can be bounded as:

$$\mathbb{P}\left(e_{l,n}^{[\mathrm{m}]}\right) = \underset{a_{l,n}^{[\mathrm{m}]}}{\mathbb{E}}\left[\mathbb{P}\left(e_{l,n}^{[\mathrm{m}]} \mid a_{l,n}^{[\mathrm{m}]}\right)\right] \overset{(a)}{\leq} \int_0^\infty \frac{1}{2}\mathsf{e}^{-\frac{x^2\,\mathtt{M}_n\,\mathsf{SNR}_n^{[\mathrm{m}]}}{2\,(\mathtt{M}_n+1)}}(\mathtt{M}_n)^{\mathtt{M}_n}\frac{x^{\mathtt{M}_n-1}}{\Gamma(\mathtt{M}_n)}\mathsf{e}^{-\mathtt{M}_n x}\mathsf{dx}$$

$$\overset{(b)}{=} \frac{1}{2}\left(\frac{\mathtt{M}_n + \mathtt{M}_n^2}{2\,\mathsf{SNR}_n^{[\mathrm{m}]}}\right)^{\frac{\mathtt{M}_n}{2}}\mathsf{U}\left(\frac{\mathtt{M}_n}{2}, \frac{1}{2}, \frac{\mathtt{M}_n + \mathtt{M}_n^2}{2\,\mathsf{SNR}_n^{[\mathrm{m}]}}\right), \tag{4.18}$$

where $\mathsf{U}(\cdot, \cdot, \cdot)$ is the confluent hypergeometric function [84, Eq. (13.4.4)]. In step (a) above, the Chernoff bound for Q function was exploited and in step (b), [62, Eqs. (3.462.1) and (9.240)] and then [84, Eq. (13.14.3)] were utilized to simplify the final formula.

Is is emphasized that BER in Eq. (4.18) depends on $\mathsf{SNR}_n^{[\mathrm{m}]}$ of tag n, which in turn, depends on Eq. (4.14); the latter is a function of tag's n location through Eq. (4.15). Thus, the above BER expression depends on the topology of the tags. The following proposition offers an important, topology-independent metric:

Proposition 4.1. Under Rayleigh fading, i.e., $M_n = 1$, mono-static architecture offers diversity order equal to $1/2$ for any $(l, n) \in \mathcal{L} \times \mathcal{N}$.

Proof. The proof is given in Appendix 4.7. □

The above result indicates that for any slot and Rayleigh fading, monostatic BER decays inversely proportional with square root of SNR at the high SNR regime. It is shown below that the decay is faster in the multistatic case.

Multistatic

Exploiting Eq. (4.7) along with the formula in [60, p. 302, Eq. 6.148], the PDF of the product $g_{l,n}^{[b]} \triangleq \left(a_{l,n}^{[b]} \right)^2 = (a_{l,C_l T_n})^2 \, (a_{l,T_n R})^2$ admits closed-form:

$$
\mathsf{f}_{g_{l,n}^{[b]}}(x) = \int_0^\infty \frac{1}{y} \, \mathsf{f}_{a_{l,C_l T_n}^2}(y) \, \mathsf{f}_{a_{l,T_n R}^2}\left(\frac{x}{y}\right) \mathsf{d}y = \frac{2(x \, M_{ln} \, M_n)^{\frac{M_{ln}+M_n}{2}} \, \mathsf{K}_{M_n - M_{ln}}\left(2\sqrt{M_{ln} \, M_n \, x}\right)}{x \, \Gamma(M_{ln}) \, \Gamma(M_n)}, \quad x \geq 0,
$$

(4.19)

where [62, Eq. (3.471.9)] was used to obtain the simplified form in Eq. (4.19). $\mathsf{K}_\nu(\cdot)$ is the ν-th order modified Bessel function of the second kind, satisfying $\mathsf{K}_\nu(\cdot) = \mathsf{K}_{-\nu}(\cdot)$ [84, Eq. (10.27.3)]. The above distribution is the power distribution of Nakagami dyadic backscatter channel. Similar expression with Eq. (4.19) can be found in [98], while a derivation of Eq. (4.19) in the special case of $M_{ln} = M_n$ is given in [99].

In the multistatic case, according to Eq. (4.4), the conditional BER for tag n over the l-th time slot is given by:

$$
\mathbb{P}\left(e_{l,n}^{[b]} \mid a_{l,n}^{[b]}\right) = \mathsf{Q}\left(a_{l,n}^{[b]} \sqrt{\mathsf{SNR}_{l,n}^{[b]}}\right),
$$

(4.20)

which with the use of Chernoff bound is upper bounded as $\mathsf{Q}\left(a_{l,n}^{[b]} \sqrt{\mathsf{SNR}_{l,n}^{[b]}}\right) \leq \frac{1}{2} \mathsf{e}^{-\frac{\left(a_{l,n}^{[b]}\right)^2 \mathsf{SNR}_{l,n}^{[b]}}{2}}$.

Hence, BER over the l-th slot for the n-th tag is upper bounded as follows:

$$
\mathbb{P}\left(e_{l,n}^{[b]}\right) = \mathop{\mathbb{E}}_{a_{l,n}^{[b]}}\left[\mathbb{P}\left(e_{l,n}^{[b]} \big| a_{l,n}^{[b]}\right)\right] \leq \int_0^\infty \mathsf{e}^{\left(-x\mathsf{SNR}_{l,n}^{[b]}/2\right)} \frac{(x \, M_{ln} \, M_n)^{\frac{M_{ln}+M_n}{2}} \, \mathsf{K}_{M_n - M_{ln}}\left(2\sqrt{M_{ln} \, M_n \, x}\right)}{x \, \Gamma(M_{ln}) \, \Gamma(M_n)} \mathsf{d}x
$$

$$
\stackrel{(a)}{=} \frac{1}{2} \left(\frac{2 \, M_{ln} M_n}{\mathsf{SNR}_{l,n}^{[b]}}\right)^{M_n} \mathsf{U}\left(M_n, 1 + M_n - M_{ln}, \frac{2 \, M_{ln} M_n}{\mathsf{SNR}_{l,n}^{[b]}}\right),
$$

(4.21)

where $\mathsf{U}(\cdot,\cdot,\cdot)$ is the confluent hypergeometric function [84, Eq. (13.4.4)]. In Step (a) above, change of variables $x = y^2$ is performed and the simplified final expression used [62, Eq. (6.631.3)] and [84, Eq. (13.14.3)].

BER of Eq. (4.21) also depends on the network topology, through the definition of $\mathrm{SNR}_{l,n}^{[\mathrm{b}]}$ and energy per bit per slot in Eqs. (4.9) and (4.10). The following proposition offers a topology-independent metric:

Proposition 4.2. Under Rayleigh fading, i.e., $\mathtt{M}_{ln} = \mathtt{M}_n = 1$, multistatic architecture offers diversity order *at least* 1 for any $(l, n) \in \mathcal{L} \times \mathcal{N}$.

Proof. The proof is immediate from the last proof in Appendix 3.6. $\qquad\qquad\square$

Thus, it is concluded that under Rayleigh fading, the multistatic BER drops faster compared to the monostatic, at the high SNR regime, even for a single, fixed slot.

4.2.2 Noncoherent

To better highlight the importance of the expressions derived in Eqs. (4.18) and (4.21), consider the n-th tag operating in noncoherent reception mode over the l-th slot. For fixed dyadic backscatter channel amplitudes $a_{l,n}^{[\mathrm{m}]}$ and $a_{l,n}^{[\mathrm{b}]}$, as well as phase offsets $\Phi_{n,0}$ and $\Phi_{n,1}$, and unknown dyadic backscatter channel angles $\phi_{l,n}^{[\mathrm{m}]}$ and $\phi_{l,n}^{[\mathrm{b}]}$, it can be shown that the ML reception rule for orthogonal signaling is based on envelope detection [80, Eq. 4.5-32] of the 4×1 complex received vector $\mathbf{r}_{l,n}$ which can be expressed as:

$$\left| \mathbf{r}_{l,n}^{[\mathrm{x}]}[1] + e^{2\mathsf{j}\Phi_{n,0}} \mathbf{r}_{l,n}^{[\mathrm{x}]}[2] \right| \underset{i_n=1}{\overset{i_n=0}{\gtrless}} \left| \mathbf{r}_{l,n}^{[\mathrm{x}]}[3] + e^{2\mathsf{j}\Phi_{n,1}} \mathbf{r}_{l,n}^{[\mathrm{x}]}[4] \right|, \qquad (4.22)$$

where x = m, x = b, for monostatic and multistatic system, respectively. Note that the above rule requires the received signal vector $\mathbf{r}_{l,n}^{[\mathrm{x}]}$ and the tag n implementation-specific phases $\Phi_{n,0}$ and $\Phi_{n,1}$, while it is different than the square-law detector: $|\mathbf{r}_{l,n}[1]|^2 + |\mathbf{r}_{l,n}[2]|^2 \underset{i_n=1}{\overset{i_n=0}{\gtrless}} |\mathbf{r}_{l,n}[3]|^2 + |\mathbf{r}_{l,n}[4]|^2$ in [33]. Following the same lines in [80, pp. 217–218], the corresponding conditional error probability of rule in Eq. (4.22) becomes $\frac{1}{2} e^{-\frac{\left(a_{l,n}^{[\mathrm{m}]}\right)^2 \mathtt{M}_n \, \mathrm{SNR}_n^{[\mathrm{m}]}}{2\,(\mathtt{M}_n+1)}}$ and $\frac{1}{2} e^{-\frac{\left(a_{l,n}^{[\mathrm{b}]}\right)^2 \mathrm{SNR}_n^{[\mathrm{b}]}}{2}}$ for monostatic and multistatic system, respectively. Note that the above expressions coincide with the upper bounds of conditional error probabilities given in Eq. (4.17) and (4.20). In other words, the expressions in (4.18) and (4.21) reflect

the exact BER performance under noncoherent envelope detection in monostatic and multistatic architecture, respectively.[4]

4.3   Information Outage Analysis

In Section 4.1 we assumed that all subcarrier frequencies used by the tags adhere to the orthogonality criterion provided in Eq. (4.3). In practice, this is not always the case, due to frequency generation constraints (e.g., clock drifts, lack of phase-locked loops). As a result, the allocated subcarrier frequencies at tags may cause adjacent channel interference. An adjacent in frequency tag j, i.e., tag with pair of subcarrier frequencies $(F_{j,0}, F_{j,1})$ relatively close to $(F_{n,0}, F_{n,1})$, may be received with significantly higher power than the tag of interest n; thus, any deviation from the orthogonality criterion may cause interference. Therefore, the relative spatial location of one tag versus the other, i.e., the network topology, as well as the subcarrier frequency allocation (denoted as $\mathcal{C}$) of N available pairs of subcarrier frequencies to N tags does affect overall performance in practice. Notice that there are $N!$ possible subcarrier frequency assignments to N tags. $\mathcal{A}(n)$ denotes the set of tags interfering the reception of tag n, while $g_{l,n}^{[\mathrm{m}]} = \left(a_{l,n}^{[\mathrm{m}]}\right)^2$ and $g_{l,n}^{[\mathrm{b}]} = \left(a_{l,n}^{[\mathrm{b}]}\right)^2$. For simplification purposes, we assume that dyadic channels $g_{l,n}$ and $g_{l,j}$ are statistically independent among different tags $(n \neq j)$ and any $l \in \mathcal{L}$.

4.3.1   Monostatic

For a given subcarrier frequency assignment $\mathcal{C}$, incorporating imperfections mentioned above, the instantaneous signal-to-interference-plus-noise ratio (SINR) of tag n at the l-th time slot is defined as by:

$$\mathrm{SINR}_{l,n}^{[\mathrm{m]}}(\mathcal{C}) \triangleq \frac{g_{l,n}^{[\mathrm{m}]} \frac{\mathtt{M}_n}{\mathtt{M}_n+1} \mathrm{E}_n^{[\mathrm{m}]}}{\sum_{j\in\mathcal{A}(n)} \rho_{nj}(\mathcal{C})\, g_{l,j}^{[\mathrm{m}]} \frac{\mathtt{M}_j}{\mathtt{M}_j+1} \mathrm{E}_j^{[\mathrm{m}]} + N_0}, \tag{4.23}$$

where parameter $\rho_{nj}(\mathcal{C})$ is inversely proportional to the assigned subcarrier frequencies separation between tag n and tag $j \in \mathcal{A}(n)$ [13]. It depends on the spectral efficiency of the specific binary modulation implemented at each tag and the filtering functions at the reader:

$$\rho_{nj}(\mathcal{C}) = \max_{i_n, i_j \in \mathbb{B}} \left\{ \left[\varepsilon_{n,j} \left| F_{n,i_n}^{\mathcal{C}} - F_{j,i_j}^{\mathcal{C}} \right| \right]^{-2} \right\}, \; j \in \mathcal{A}(n), \tag{4.24}$$

---

[4]Results are connected with the signal model of Section II, which assumes perfect CFO estimation and correction (in the multistatic case) and perfect DC blocking at the baseband signal for both monostatic and multistatic cases.

where $F_{n,i_n}^{\mathcal{C}}$ is the subcarrier frequency allocated under assignment $\mathcal{C}$ at tag n for bit $i_n \in \mathbb{B}$; parameter $\varepsilon_{n,j}$ is a constant depending on the utilized modulation and pulse shaping, as well as the mismatch between the clocks of tag n and j. Subcarrier frequency difference raised at the second power, as opposed to the fourth power, is due to the power spectral density of FSK implemented at each tag, as opposed to (continuous phase) MSK [13].

The average received SINR for any $(l, n) \in \mathcal{L} \times \mathcal{N}$ can be expressed as:

$$\text{SINR}_n^{[\text{m}]}(\mathcal{C}) = \frac{\mathbb{E}\left[g_{l,n}^{[\text{m}]}\right] \frac{\text{M}_n}{\text{M}_n+1} \text{E}_n^{[\text{m}]}}{\sum_{j \in \mathcal{A}(n)} \rho_{nj}(\mathcal{C}) \, \mathbb{E}\left[g_{l,j}^{[\text{m}]}\right] \frac{\text{M}_j}{\text{M}_j+1} \text{E}_j^{[\text{m}]} + N_0} = \frac{\text{E}_n^{[\text{m}]}}{\sum_{j \in \mathcal{A}(n)} \rho_{nj}(\mathcal{C}) \, \text{E}_j^{[\text{m}]} + N_0}. \quad (4.25)$$

Proposition 4.3. Under Rayleigh fading, i.e., $\text{M}_n = 1$, for given subcarrier frequency assignment $\mathcal{C}$ and fixed monostatic topology, outage probability for specific tag n and given slot $l \in \mathcal{L}$, can be upper bounded as:

$$\mathbb{P}\left(\text{SINR}_{l,n}^{[\text{m}]}(\mathcal{C}) \leq \theta\right) \leq 1 - e^{-\sqrt{\frac{2\theta}{\text{SINR}_n^{[\text{m}]}(\mathcal{C})}}}. \quad (4.26)$$

Proof. See Appendix 4.7. $\qquad\qquad\qquad\qquad\qquad\qquad\qquad\qquad\qquad\qquad\qquad$ $\square$

It is worth emphasizing that the above outcome depends on both network topology (through $\text{E}_n^{[\text{m}]}$), as well as subcarrier frequency assignment $\mathcal{C}$ (through parameter $\rho(\mathcal{C})$ above).

As the dyadic fading channel parameters change independently among different slots, i.e., $g_{l,n}$ and $g_{l',n}$ are statistically independent for any $l \neq l' \in \mathcal{L}$, we can offer outage expressions for operation over the L slots. Specifically, for a fixed subcarrier frequency assignment $\mathcal{C}$, the monostatic information outage event for the n-th tag over L attempts (time slots) is the probability that n-th tag's SINR is below threshold θ over all L slots, i.e.,

$$\mathbb{P}\left(\bigcap_{l=1}^{L}\left\{\text{SINR}_{l,n}^{[\text{m}]}(\mathcal{C}) \leq \theta\right\}\right) \overset{(a)}{=} \left[\mathbb{P}\left(\text{SINR}_{l,n}^{[\text{m}]}(\mathcal{C}) \leq \theta\right)\right]^L \quad (4.27)$$

$$\overset{(b)}{\leq} \left(1 - e^{-\sqrt{\frac{2\theta}{\text{SINR}_n^{[\text{m}]}(\mathcal{C})}}}\right)^L, \quad (4.28)$$

where (a) is due to the fact that $\{g_{l,n}^{[\text{m}]}\}$ are IID for all $l \in \mathcal{L}$ and (b) holds only under Rayleigh fading due to Eq. (4.26).

4.3.2 Multistatic

For given subcarrier frequency channel assignment $\mathcal{C}$, the instantaneous SINR of tag n for the l-th time slot is

$$\text{SINR}_{l,n}^{[b]}(\mathcal{C}) \triangleq \frac{g_{l,n}^{[b]}\, \mathsf{E}_{l,n}^{[b]}}{\sum_{j \in \mathcal{A}(n)} \rho_{nj}(\mathcal{C})\, g_{l,j}^{[b]}\, \mathsf{E}_{l,j}^{[b]} + N_0}. \tag{4.29}$$

The average SINR for multistatic case for any $(l,n) \in \mathcal{L} \times \mathcal{N}$ is given by:

$$\overline{\text{SINR}}_{l,n}^{[b]}(\mathcal{C}) = \frac{\mathsf{E}_{l,n}^{[b]}}{\sum_{j \in \mathcal{A}(n)} \rho_{nj}(\mathcal{C})\, \mathsf{E}_{l,j}^{[b]} + N_0}. \tag{4.30}$$

Proposition 4.4. Under Rayleigh fading, i.e., $\mathsf{M}_{ln} = \mathsf{M}_n = 1$, for fixed multistatic topology and subcarrier frequency assignment $\mathcal{C}$, outage probability for tag n and slot $l \in \mathcal{L}$ is upper bounded as:

$$\mathbb{P}\Big(\text{SINR}_{l,n}^{[b]}(\mathcal{C}) \le \theta\Big) \le 1 - 2\sqrt{\frac{\theta}{\overline{\text{SINR}}_{l,n}^{[b]}(\mathcal{C})}}\, \mathsf{K}_1\left(2\sqrt{\frac{\theta}{\overline{\text{SINR}}_{l,n}^{[b]}(\mathcal{C})}}\right), \tag{4.31}$$

where $\mathsf{K}_1(\cdot)$ is the first order modified Bessel function of the second kind [84, Eq. (10.27.3)].

Proof. The proof is provided in Appendix 4.7. □

It is noted again that the above bound depends on tag location and network topology (through $\mathsf{E}_{l,n}^{[b]}$), subcarrier frequency assignment $\mathcal{C}$ (through parameter $\rho(\mathcal{C})$ above) and slot l (in contrast to the monostatic case), since at each slot different CE emits.

Accordingly with the monostatic case, for fixed subcarrier frequency assignment $\mathcal{C}$ and given threshold θ, the multistatic information outage probability of tag n operating over L time slots becomes:

$$\mathbb{P}\left(\bigcap_{l=1}^{L}\big\{\text{SINR}_{l,n}^{[b]}(\mathcal{C}) \le \theta\big\}\right) \overset{(a)}{=} \prod_{l=1}^{L} \mathbb{P}\Big(\text{SINR}_{l,n}^{[b]}(\mathcal{C}) \le \theta\Big) \tag{4.32}$$

$$\overset{(b)}{\le} \prod_{l=1}^{L}\left(1 - 2\sqrt{\frac{\theta}{\overline{\text{SINR}}_{l,n}^{[b]}(\mathcal{C})}}\, \mathsf{K}_1\left(2\sqrt{\frac{\theta}{\overline{\text{SINR}}_{l,n}^{[b]}(\mathcal{C})}}\right)\right), \tag{4.33}$$

where (a) exploited the independence of $\big\{\text{SINR}_{l,n}^{[b]}(\mathcal{C})\big\}_{l \in \mathcal{L}}$ and (b) holds only in a Rayleigh fading scenario due to Eq. (4.31).

4.3.3 Average Probability over Random Square Grids

In order to obtain topology-independent outage probabilities, expressions that average over possible topologies have to be obtained. Since, there are infinite classes of topologies to choose from, attention is restricted to the class of square $M \times M$ grid network topologies used in practice. For simplicity, it is assumed that grid resolution Δ divides M, i.e., $M/\Delta = K \in \mathbb{N}$ and the set of 2-dimensional (2D) square grid points is denoted as follows:

$$\mathcal{G}_{M,\Delta} = \left\{ [k_1\Delta \ \ k_2\Delta]^\top : (k_1, k_2) \in \{0, 1, \ldots, K\}^2 \right\}. \tag{4.34}$$

Set $\mathcal{G}_{M,\Delta}$ has $(K+1)^2$ elements (2D grid points) and M, Δ are chosen such that $(K+1)^2 \geq N + L + 1$, i.e., possible tag locations are more than the total number of tags, emitters and reader.

For a monostatic architecture with fixed SDR reader's position $\mathbf{u}_R \in \mathcal{G}_{M,\Delta}$, there are $\mathsf{J}_{K,N}^{[m]} \triangleq \binom{(K+1)^2-1}{N}$ ways to place N tags in $\mathcal{G}_{M,\Delta} \backslash \{\mathbf{u}_R\}$.[5] This is the ensemble of admissible square grid monostatic topologies. The calculation of a topology-independent average outage probabilities requires averaging over all $\mathsf{J}_{K,N}^{[m]}$ possible topologies. Because $\mathsf{J}_{K,N}^{[m]}$ is practically enormous, especially for large K, the averaging in this work is applied through Monte-Carlo, i.e., for a relatively large number of times, the following experiment is repeated: uniformly and random select a topology $\mathcal{T}_L^{[m]}$ from the ensemble of monostatic grid topologies (i.e., each of them has probability $1/\mathsf{J}_{K,N}^{[m]}$) and estimate the outage probability for the sampled topology. Finally, averaging is applied over the sampled topologies. The same methodology is applied to a multistatic architecture with L CEs and a single SDR reader, where $\mathsf{J}_{K,L,N}^{[b]} \triangleq \binom{(K+1)^2-1-L}{N} = \binom{K^2+2K-L}{N}$ topologies exist, under the same assumption.

4.4 Energy Outage Analysis for Passive Tags with RF Harvesting

In contrast to the semi-passive tags assumed so-far, passive tags do not have a dedicated (ambient or not) energy source. Instead, passive tags harvest RF energy from the illuminating carrier(s).

---

[5]If the ordering of how they are placed is not considered and the reader location is fixed.

For fixed CE, tag n, and SDR reader positions at the l-th time slot, the input power at the RF harvesting circuit of tag n is given by:

$$P_{\mathrm{h},l,n}^{[\mathrm{m}]} = P_{\mathrm{R}}\, \mathsf{L}_{\mathrm{T}_n \mathrm{R}}\, (a_{l,\mathrm{T}_n \mathrm{R}})^2, \tag{4.35}$$

$$P_{\mathrm{h},l,n}^{[\mathrm{b}]} = P_{\mathrm{C}_l}\, \mathsf{L}_{\mathrm{C}_l \mathrm{T}_n}\, (a_{l,\mathrm{C}_l \mathrm{T}_n})^2, \tag{4.36}$$

for monostatic and multistatic architecture, respectively. Energy outage (EO) event at tag n occurs when for all L time slots the received input power at tag n RF circuitry is below a threshold θ_{h}, which models the sensitivity of the RF harvesting circuit, i.e., the input power threshold below which RF harvester offers zero power.[6] Mathematically, the EO event is defined as:

$$\mathbb{P}\Big(\mathrm{EO}_{L,n}^{[\mathrm{m}]} \,\big|\, \theta_{\mathrm{h}}\Big) \triangleq \mathbb{P}\bigg(\bigcap_{l=1}^{L}\Big\{P_{\mathrm{h},l,n}^{[\mathrm{m}]} \le \theta_{\mathrm{h}}\Big\}\bigg), \tag{4.37}$$

$$\mathbb{P}\Big(\mathrm{EO}_{L,n}^{[\mathrm{b}]} \,\big|\, \theta_{\mathrm{h}}\Big) \triangleq \mathbb{P}\bigg(\bigcap_{l=1}^{L}\Big\{P_{\mathrm{h},l,n}^{[\mathrm{b}]} \le \theta_{\mathrm{h}}\Big\}\bigg), \tag{4.38}$$

for monostatic and multistatic architecture, respectively. The impact of network topology in the energy outage probability expressions for multistatic and monostatic systems is due to the path-loss gains $\{\mathsf{L}_{\mathrm{C}_l \mathrm{T}_n}\}_{l \in \mathcal{L}}$ and $\mathsf{L}_{\mathrm{T}_n \mathrm{R}}$.

For the monostatic architecture, RVs $\{P_{\mathrm{h},l,n}^{[\mathrm{m}]}\}_{l \in \mathcal{L}}$ are IID and each $P_{\mathrm{h},l,n}^{[\mathrm{m}]}$ is Gamma RV with parameters $\big(\mathsf{M}_n, \frac{P_{\mathrm{R}}\mathsf{L}_{\mathrm{T}_n \mathrm{R}}}{\mathsf{M}_n}\big)$ and cumulative distribution function (CDF) given in [100, Table I]. Thus, energy outage event in (4.37) is given by:

$$\mathbb{P}\Big(\mathrm{EO}_{L,n}^{[\mathrm{m}]} \,\big|\, \theta_{\mathrm{h}}\Big) = \left(\frac{\gamma\Big(\mathsf{M}_n, \frac{\mathsf{M}_n \theta_{\mathrm{h}}}{P_{\mathrm{R}}\mathsf{L}_{\mathrm{T}_n \mathrm{R}}}\Big)}{\Gamma(\mathsf{M}_n)}\right)^{L}, \tag{4.39}$$

where $\gamma(a,x) = \int_0^x t^{a-1}\mathsf{e}^{-t}\mathsf{d}t$ is the lower incomplete gamma function.

For the multistatic architecture, $P_{\mathrm{h},l,n}^{[\mathrm{b}]}$ is a Gamma RV with parameters $\big(\mathsf{M}_{ln}, \frac{P_{\mathrm{C}_l}\mathsf{L}_{\mathrm{C}_l \mathrm{T}_n}}{\mathsf{M}_{ln}}\big)$ and RVs $\{P_{\mathrm{h},l,n}^{[\mathrm{b}]}\}_{l \in \mathcal{L}}$ are independent; as a result, the energy outage event in (4.38) can be simplified to:

$$\mathbb{P}\Big(\mathrm{EO}_{L,n}^{[\mathrm{b}]} \,\big|\, \theta_{\mathrm{h}}\Big) = \prod_{l=1}^{L} \frac{\gamma\Big(\mathsf{M}_{ln}, \frac{\mathsf{M}_{ln} \theta_{\mathrm{h}}}{P_{\mathrm{C}_l}\mathsf{L}_{\mathrm{C}_l \mathrm{T}_n}}\Big)}{\Gamma(\mathsf{M}_{ln})}. \tag{4.40}$$

---

[6]State-of-the-art passive RFID tags exhibit $\theta_{\mathrm{h}} = -22$ dBm [28].

The average across all tags energy outage event is by taking the average of Eqs. (4.37) and (4.38) across all tags, i.e.,

$$\frac{1}{N}\sum_{n=1}^{N}\mathbb{P}\left(\text{EO}_{L,n}^{[\text{m}]}\Big|\theta_{\text{h}}\right),\ \ \frac{1}{N}\sum_{n=1}^{N}\mathbb{P}\left(\text{EO}_{L,n}^{[\text{b}]}\Big|\theta_{\text{h}}\right).\tag{4.41}$$

Another important metric that measures the worst-case energy outage is the maximum energy outage across all tags, i.e.,

$$\max_{n\in\mathcal{N}}\left\{\mathbb{P}\left(\text{EO}_{L,n}^{[\text{m}]}\Big|\theta_{\text{h}}\right)\right\},\ \ \max_{n\in\mathcal{N}}\left\{\mathbb{P}\left(\text{EO}_{L,n}^{[\text{b}]}\Big|\theta_{\text{h}}\right)\right\}.\tag{4.42}$$

It is emphasized again that the above outage probabilities depend on a specific multi-static or monostatic topology. Energy outage expressions that are topology-independent can be offered using averaging over the ensemble of square grid topologies as in Section 4.3.3.

4.5 Simulation Results

First the BER performance of monostatic and bistatic systems is examined for $L = 1$ slot and $N = 1$ tag. Rician fading parameters $\kappa_n = 10$ and $\kappa_{ln} = 9$ are used, setting $\mathtt{M}_n = \frac{(\kappa_n+1)^2}{2\kappa_n+1} = 5.7619$ and $\mathtt{M}_{ln} = \frac{(\kappa_{ln}+1)^2}{2\kappa_{ln}+1} = 5.2632$. Fig. 4.4-Left illustrates the exact BER performance under coherent and noncoherent reception for the two scatter radio architectures. Common $\mathtt{SNR} = \mathtt{SNR}_{l,n}^{[\text{b}]} = \mathtt{SNR}_n^{[\text{m}]}$ is assumed, resulting to monostatic reader transmission power P_{R} and bistatic carrier emitter power P_{C_l} related according to Eqs. (4.9), (4.14) $\left(P_{\text{R}} = \frac{\mathtt{L}_{\text{C}_l,\text{T}_n}}{\mathtt{L}_{\text{T}_n,\text{R}}}\frac{\mathtt{M}_n P_{\text{C}_l}}{\mathtt{M}_n+1}\right)$. Any monostatic or bistatic topology offering the specific SNR is applicable to this plot. Upper bounds derived in Eq. (4.18) and Eq. (4.21) are also plotted. It can be seen that the bistatic architecture outperforms the monostatic and high-SNR slope is clearly different among the two architectures, as expected. Also, the derived upper bounds for coherent ML detection schemes coincide with the curves of noncoherent detection.

Fig. 4.4-Right studies the BER performance as a function of SNR for a scenario where the tag is far-away from CE (possibly a few kilometers) but the tag-to-reader distance is relatively small (a few feet). This is a Rayleigh-Nakagami (Rice) scenario, that could be the case when the tag is illuminated by broadcasting stations and the receiver is close to the tag. In such scenario, the monostatic architecture is not applicable. Due to the large CE-to-tag distance, the link from CE-to-tag is assumed NLoS, i.e., $\kappa_{ln} = 0$ and thus $\mathtt{M}_{ln} = \frac{(\kappa_{ln}+1)^2}{2\kappa_{ln}+1} = 1$, while tag-to-reader link has strong LoS, thus, $\kappa_n = 10$ with
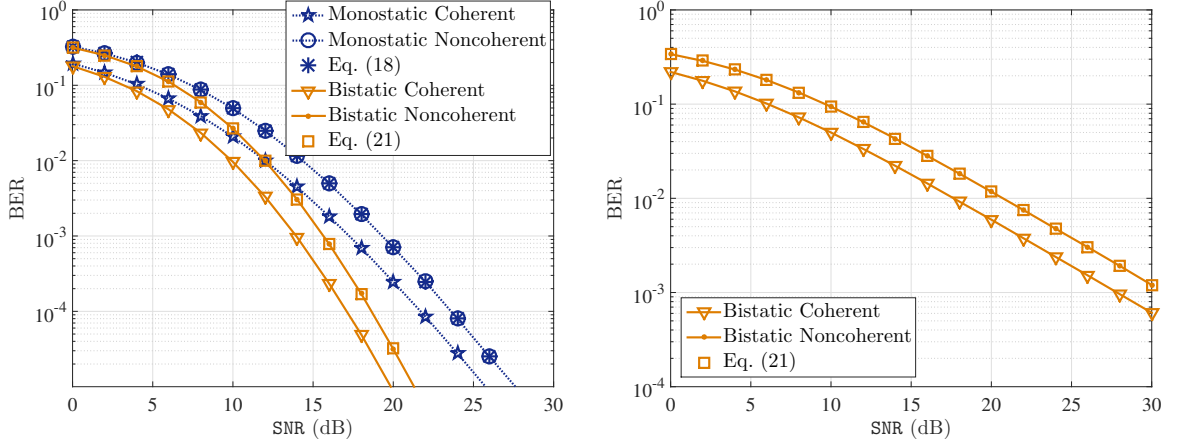
Figure 4.4: Left (Right): Monostatic vs bistatic BER versus SNR for ML coherent and noncoherent detection and Nakagami fading with parameters $\mathtt{M}_n = 5.7619$, $\mathtt{M}_{ln} = 5.2632$ $(\mathtt{M}_{ln} = 1, \mathtt{M}_n = 5.7619$, assuming a NLoS CE-to-tag scenario$)$.
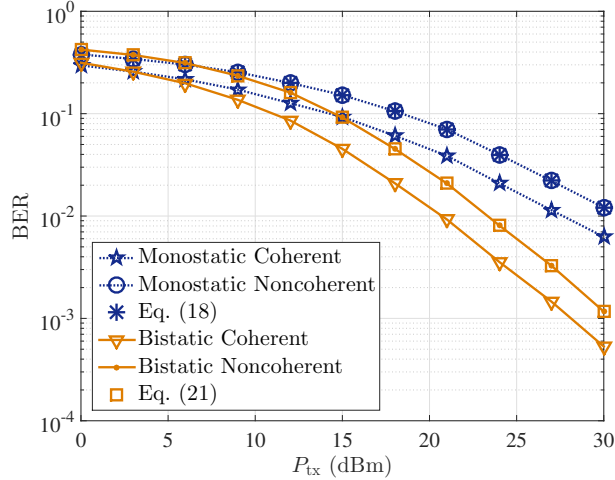

Figure 4.5: Monostatic vs bistatic BER performance versus P_{tx} in a 40×40 topology for ML coherent and noncoherent detection averaged over random tag locations.

Table 4.1: Noise and Tag Parameters

| $N_0 = -169$ dBm/Hz | $F_{\mathrm{c}} = 868$ MHz | $\lambda = \frac{3 \cdot 10^8}{F_{\mathrm{c}}}$ m | $\lvert \Gamma_{n,0} - \Gamma_{n,1} \rvert = 2, \forall n$ | $\mathtt{s}_n = 0.1, \forall n$ |

$\mathtt{M}_n = \frac{(\kappa_n + 1)^2}{2\kappa_n + 1} = 5.7619$. In such extreme case, where the monostatic architecture cannot be defined, the bistatic BER is less than 1% for received SNR values less than 17 dB (20 dB) under coherent (noncoherent) detection. The above demonstrate the potential benefits and flexibility of multistatic architecture in cases where CE is far away from tag.

Fig. 4.5 studies the impact of transmit power on BER for random tag locations. An SDR reader and a CE are placed in positions $[0\ 0]^\top$ and $[40\ 40]^\top$, respectively, while the position of tag follows uniform distribution over a 40×40 m^2 topology. Common
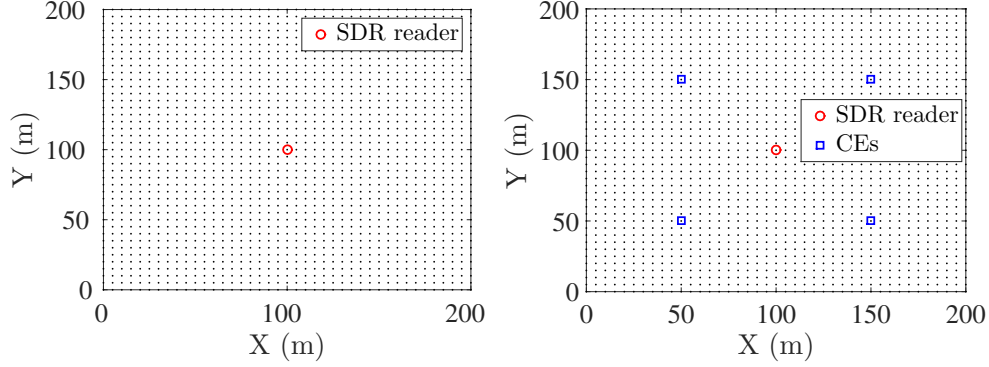
Figure 4.6: Network setup: monostatic (left) and multistatic with 4 carrier emitters (CEs) (right). Grid points (dots) are possible tag locations.

transmit power is used for fair comparison for monostatic and bistatic architectures, i.e., $P_{\text{tx}} = P_{\text{R}} = P_{\text{C}_l}$. For each sampled tag location the small-scale fading parameters change as $\kappa_n \sim \mathcal{U}[0, 20]$ and $\kappa_{ln} \sim \mathcal{U}[0, 20]$, setting $\mathtt{M}_n = \frac{(\kappa_n+1)^2}{2\kappa_n+1}$ and $\mathtt{M}_{ln} = \frac{(\kappa_{ln}+1)^2}{2\kappa_{ln}+1}$. In addition, the path-loss exponents (PLEs) from CE-to-tag and SDR reader-to-tag are $\mathcal{U}[2, 2.5]$. The noise- and tag-related parameters are shown in Table 4.1. It can be seen that the average BER performance of a randomly placed tag (evaluated over several possible tag locations) is smaller in the bistatic architecture. It is also observed that the BER decay is faster in the bistatic compared to the monostatic architecture, corroborating the diversity gains offered by the bistatic system.

For grid WSN topologies of size $M \times M$ m^2 and grid resolution Δ m, energy and information outage are studied, using $M = 2.5$, $\Delta = 0.125$ and $M = 200$, $\Delta = 5$, respectively. For information (energy) outage simulations, random tag topologies are generated from $\mathcal{G}_{200,5}$ ($\mathcal{G}_{2.5,0.125}$) consisting of N tags, $L = 4$ CEs placed at $\{\mathbf{u}_{\text{C}_l}\}_{l=1}^4 = \left\{ [\frac{M}{4}\ \frac{M}{4}]^\top, [\frac{3M}{4}\ \frac{M}{4}]^\top, [\frac{3M}{4}\ \frac{3M}{4}]^\top, [\frac{M}{4}\ \frac{3M}{4}]^\top \right\}$ for multistatic system, and an SDR reader placed at the middle of the topology (i.e., position $[\frac{M}{2}\ \frac{M}{2}]$), in order to maximize the coverage. The grid topology utilized in information outage simulations is depicted in Fig. 4.6-Left (-Right) for the monostatic (multistatic) architecture. Similar with the previous paragraph noise/tag-related parameters are considered (Table 4.1). After sampling the grid topology, random PLEs $\nu_{ln} \sim \mathcal{U}[2, 2.5]$ and $\nu_n \sim \mathcal{U}[2, 2.5]$ are generated for link from l-th CE to n-th tag and link from n-th tag to SDR reader, respectively. In addition, to offer robustness against channel fading, after sampling the topology in the Nakagami fading scenarios, Nakagami parameters are randomly generated as follows: $\mathtt{M}_{ln} \sim \mathcal{U}[1, 5]$ and $\mathtt{M}_n \sim \mathcal{U}[1, 5]$, for link from l-th CE to n-th tag and link from n-th tag to SDR reader, respectively. For a fair comparison, equal transmission power for monostatic and multistatic architecture is utilized, setting $P_{\text{tx}} = P_{\text{R}} = P_{\text{C}_l}, \forall l \in \mathcal{L}$.
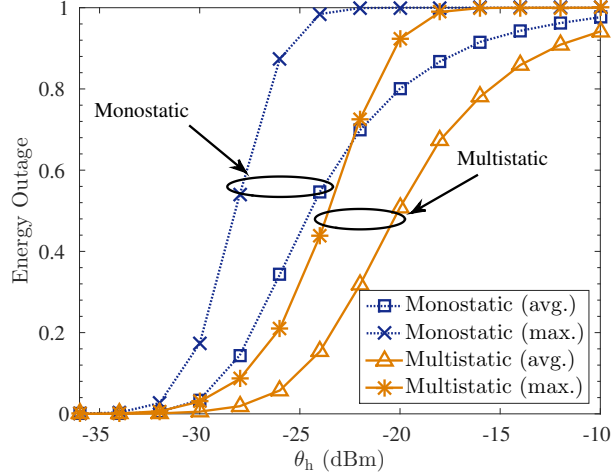
Figure 4.7: Topology-independent average and maximum energy outage performance versus threshold θ_h for monostatic and multistatic network of Fig. 4.6 using $\mathcal{G}_{2.5, 0.125}$.

Considering a passive-tag BSN scenario, the topology-independent average and maximum energy outage probability is plotted in Fig. 4.7 (by averaging Eqs. (4.41) and (4.42) over several sampled grid topologies) as a function of harvesting threshold θ_h under Nakagami fading, with $P_\mathrm{tx} = 35$ dBm and $N = 8$ tags. It is noted that the probability for a tag to be placed near a CE is higher in the multistatic architecture and thus, energy outage events are more frequent in the monostatic architecture. Energy outage is a performance bound for networks consisting of passive tags, since harvesting adequate energy is necessary for the tag to operate. It is worth noting that for energy outage probability of 10%, the multistatic architecture outperforms the monostatic by 4.5 dB for average and maximum outage performance.

Finally, information outage is evaluated for a network of semi-passive tags. Since expressions in Eqs. (4.27) and (4.32) do not admit a closed-form, an extra Monte Carlo step is conducted after sampling the grid tag topology. Specifically, in the extra Monte Carlo phase, Rayleigh ($\mathtt{M}_n = \mathtt{M}_{ln} = 1$) and Nakagami small-scale fading coefficients are generated, as well as a random subcarrier assignment to the tags. For an allocation $\mathcal{C}$, the c-th frequency pair is assigned to tag n if $c = \mathsf{p}_\mathcal{C}(n) \in \mathcal{N}$, where $\mathsf{p}_\mathcal{C}$ denotes the permutation associated with assignment $\mathcal{C}$. The following parameters are utilized: $T = 1$ msec (i.e., 1 Kbps bitrate), $\varepsilon_{n,j} = 2\pi T$ for all $n, j \in \mathcal{N}$ with $n \neq j$, and the subcarrier frequency pair for the n-th tag, $\left\{ F_{n,0}^\mathcal{C}, F_{n,1}^\mathcal{C} \right\}$, is given by $F_{n,0}^\mathcal{C} = (0.1 + c\,F_\mathrm{sp})$ MHz and $F_{n,1}^\mathcal{C} = (0.1 + c\,F_\mathrm{sp} + F_\mathrm{sp}/5)$ MHz with $F_\mathrm{sp} = 0.01$ MHz, $c = 1, 2, \ldots, N$. Hence, for a given channel assignment $\mathcal{C}$, the coefficients in Eq. (4.24) for any pair of tags $(n, j) \in \mathcal{N} \times \mathcal{N}$, with $n \neq j$, can be expressed as $\rho_{nj}(\mathcal{C}) = \rho_{jn}(\mathcal{C}) = \frac{25}{\left[2\pi T \left(5|\mathsf{p}_\mathcal{C}(n) - \mathsf{p}_\mathcal{C}(j)| - 1 \right) F_\mathrm{sp} \right]^2}$.
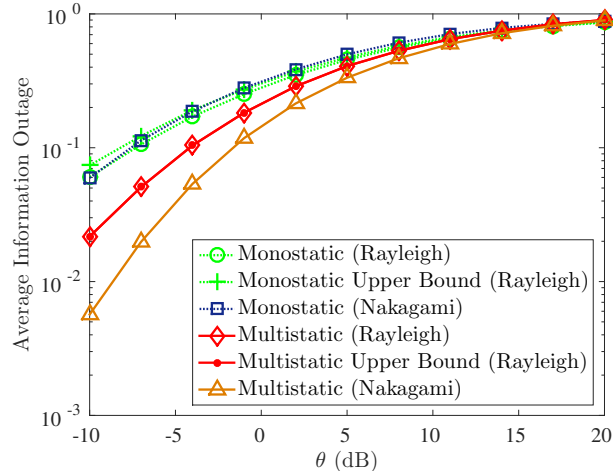
Figure 4.8: Tag location-independent, average information outage probability versus threshold θ for monostatic and multistatic architecture of Fig. 4.6.

Fig. 4.8 illustrates the topology-independent average outage probability (as well as the corresponding upper bounds for Rayleigh fading) for monostatic and multistatic architectures, as a function of threshold θ, for $N = 100$ tags and $P_{\text{tx}} = 28$ dBm. It is noted that the specific monostatic network setup (Fig. 4.6-Left) is the most appropriate among all possible choices of $\mathcal{G}_{200,5}$ in terms of coverage, since the SDR reader is located in the middle of the grid. Fig. 4.8 shows that for information outage 10% multistatic system outperforms monostatic by 3 dB in Rayleigh fading scenario, while for Nakagami fading the gap approaches 8 dB. The performance gap increases as threshold θ decreases. It can be also seen that the proposed bounds after averaging over all sampled tag locations are tight, especially for the multistatic architecture. It is clear again that the multistatic architecture offers higher reliability, as well as better coverage for scatter radio WSNs.

4.6 Experimental Results

Capitalizing upon the above promising results, a digital *multistatic* BSN is constructed, targeting on environmental and agriculture applications for ultra low-cost, microclimate monitoring around each plant [40]. The measured environmental quantities were: air-humidity, soil moisture, and temperature; all of them vary slowly as a function of time and thus, low bitrate (1 Kbps) per sensor was adequate. The communication among the tags and the reader was through subcarrier (switching) frequency division multiplexing (FDM), as explained in Section II; the CEs emitted a CW sinusoid in time division multiplexing (TDM) basis with transmission power 13 dBm over 868 MHz carrier frequency band.
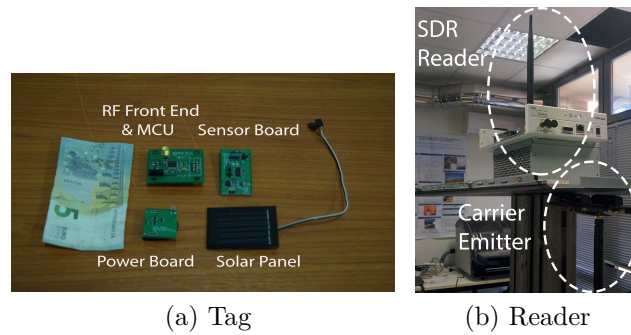
(a) Tag   (b) Reader

Figure 4.9: A prototype scatter radio tag (left) and a custom reader (right); the receiver antenna is on the top side of a metal box, while the carrier emitter (CE) is on the bottom side.

Each prototype tag consisted of two distinct boards, the communication and the power board (Fig. 4.9a). The communication board was applying the communication and sensing operations, including a 8-bit mixed-signal micro-controller unit (MCU) with analog-to-digital converter, an RF transistor and input/output (I/O) pins for sensors' inputs. Binary scatter radio FSK modulation was implemented at the tags; 30 distinct orthogonal subcarrier frequency pairs could be produced. In order to increase the total number of tags while sustaining low-power operation, a "sleep" mode was implemented in all tags, with random "wake up". Thus, multiple tags could share the same pair of subcarrier frequencies with very small collision probability, increasing the total number of tags in the network, exploiting the utilized "sleep-scatter" duty cycle. In addition, a rate 1/2 Reed-Muller encoder was implemented at each MCU [74]. The tag was able to operate with a small solar panel during the daytime and a small coin cell battery during the night. The battery can be easily replaced by a super-capacitor at the power board [17], [101], [19].

Furthermore, in order to emulate a monostatic reader, the SDR reader and the CE were placed on the opposite sides of a metallic box. This structure provided good isolation between the transmit and the receive antennas, without using a circulator. The monostatic setup is depicted in Fig. 4.9b.

The outdoor measurement campaign consisted of two campaigns. In the first one, the maximum ranges of the tag-to-SDR links were found. The maximum range was determined when the BER was up to 5%. The multistatic architecture achieved tag-to-SDR reader ranges over 140 m, with CE-to-tag range in the order of 10 m. The maximum tag-to-SDR range for the monostatic system was in the order of 15 m, one order of magnitude smaller than the multistatic.

In the second campaign, coverage was examined in a field of 3500 m² area. For the multistatic architecture, two network topologies were deployed, one with three and one
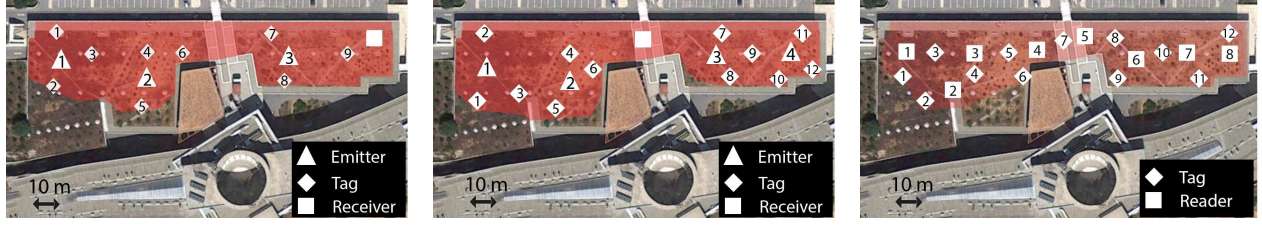
(a) Multistatic setup, receiver at the corner, 3 CEs.

(b) Multistatic setup, receiver at the center, 4 CEs.

(c) Monostatic setup, 8 readers.

Figure 4.10: Multistatic and monostatic setup for measurement campaigns.

with four CEs. In the first topology (shown in Fig. 4.10a), the SDR reader was placed at the right field corner, maximizing the tag-to-SDR reader distance, while the three CEs were placed around the field. In the second topology the reader was placed at the field center and the four CEs located as shown in Fig. 4.10b. For the monostatic architecture, multiple readers/CEs were deployed. Since the monostatic architecture's ranges were shorter, a total of eight readers were utilized, as shown in Fig. 4.10c. It should be remarked that using only four monostatic SDR readers at the same locations, at the same location where CEs were placed in the multistatic case, would offer a smaller monostatic coverage of $4 \cdot \pi \cdot 15^2 = 2827$ m^2.

From the second campaign we deduce that both architectures can cover similar areas provided that the monostatic architecture utilizes additional readers, incurring higher monetary cost. In sharp contrast, the multistatic architecture is more flexible and can offer greater ranges, even with one SDR reader and multiple low-cost CEs. Equivalently, with only one reader, the monostatic architecture would offer much smaller field coverage, compared to the multistatic, as clearly shown in Fig. 4.10a, Fig. 4.10b and Fig. 4.10c.

4.7   Appendix: Proofs of Chapter 4

Proof of Proposition 4.1

For Rayleigh fading, i.e., $\mathtt{M}_n = 1$, RV $a_{l,n}^{[\mathrm{m}]} = (a_{l,\mathrm{T}_n \mathrm{R}})^2$ follows exponential distribution. Using Eq. (4.17), the unconditional probability of error over the l-th slot for the n-th tag is given by:

$$\mathrm{Pr}\left(e_{l,n}^{[\mathrm{m}]}\right) = \underset{a_{l,n}^{[\mathrm{m}]}}{\mathbb{E}} \left[\mathrm{Pr}\left(e_{l,n}^{[\mathrm{m}]} \mid a_{l,n}^{[\mathrm{m}]}\right)\right] = \int_0^\infty \mathsf{Q}\left(x\sqrt{\frac{\mathsf{SNR}_n^{[\mathrm{m}]}}{2}}\right) \mathsf{e}^{-x}\mathsf{d}x = \frac{1}{2} - \mathsf{e}^{\frac{1}{\mathsf{SNR}_n^{[\mathrm{m}]}}}\mathsf{Q}\left(\sqrt{\frac{2}{\mathsf{SNR}_n^{[\mathrm{m}]}}}\right), \quad (4.43)$$

where [84, Eqs. (7.14.2), (7.2.1), (7.2.2)] are utilized. The diversity order for the probability of error in (4.43) is given by [92]:

$$\lim_{\mathrm{SNR}_n^{[m]} \to \infty} \frac{\log\left(\Pr\left(e_{l,n}^{[m]}\right)\right)}{\log\left(\mathrm{SNR}_n^{[m]}\right)} = \lim_{x \to 0} \frac{\log\left(\frac{1}{2} - \mathsf{e}^x \, \mathsf{Q}\left(\sqrt{2x}\right)\right)}{\log\left(\frac{1}{x}\right)}.$$

By applying the rule of L'Hospital:

$$\lim_{x \to 0} \frac{-\mathsf{e}^x \mathsf{Q}\left(\sqrt{2\,x}\right) + \frac{1}{2\sqrt{\pi\, x}}}{-\frac{1}{x}\left[\frac{1}{2} - \mathsf{e}^x\,\mathsf{Q}\left(\sqrt{2\,x}\right)\right]} = \lim_{x \to 0} \frac{x\,\mathsf{Q}\left(\sqrt{2\,x}\right) - \frac{\mathsf{e}^{-x}\sqrt{x}}{2\sqrt{\pi}}}{\frac{\mathsf{e}^{-x}}{2} - \mathsf{Q}\left(\sqrt{2\,x}\right)}. \tag{4.44}$$

Applying again the rule of L'Hospital:

$$\lim_{x \to 0} \frac{\mathsf{Q}\left(\sqrt{2\,x}\right) - \frac{\mathsf{e}^{-x}}{4\sqrt{\pi x}}}{-\frac{\mathsf{e}^{-x}}{2} + \frac{\mathsf{e}^{-x}}{2\sqrt{\pi x}}} = \lim_{x \to 0} \frac{\mathsf{e}^x \sqrt{x}\,\mathsf{Q}\left(\sqrt{2\,x}\right) - \frac{1}{4\sqrt{\pi}}}{-\frac{\sqrt{x}}{2} + \frac{1}{2\sqrt{\pi}}} = -\frac{1}{2}. \tag{4.45}$$

Proof of Proposition 4.3

The PDF of RV $g_{l,n}^{[m]} \triangleq \left(a_{l,n}^{[m]}\right)^2 = (a_{l,\mathrm{T}_n\mathrm{R}})^4$ can be determined through RV $a_{l,n}^{[m]} = (a_{l,\mathrm{T}_n\mathrm{R}})^2$, which follows Gamma distribution with PDF given in Eq. (4.16). Using the formula in [60, p. 199], the required PDF for $x \geq 0$ is

$$\mathsf{f}_{g_{l,n}^{[m]}}(x) = \frac{1}{2\sqrt{x}} \mathsf{f}_{a_{l,n}^{[m]}}\left(\sqrt{x}\right) = (\mathsf{M}_n)^{\mathsf{M}_n} \frac{x^{\frac{\mathsf{M}_n}{2}-1}}{2\,\Gamma(\mathsf{M}_n)}\, \mathsf{e}^{-\mathsf{M}_n \sqrt{x}}. \tag{4.46}$$

For Rayleigh fading, i.e., $\mathsf{M}_n = 1$ in Eq. (4.46), the PDF of RV $g_{l,n}^{[m]}$ is simplified to $\mathsf{f}_{g_{l,n}^{[m]}}(x) = \frac{1}{2\sqrt{x}} \mathsf{e}^{-\sqrt{x}}$, $x \geq 0$. The corresponding cumulative distribution function (CDF) is given by

$$\mathsf{F}_{g_{l,n}^{[m]}}(x) = \int_0^x \mathsf{f}_{g_{l,n}^{[m]}}(y)\, \mathsf{d}y = 1 - \mathsf{e}^{-\sqrt{x}}, \quad x \geq 0. \tag{4.47}$$

The monostatic outage probability for $\mathsf{M}_n = 1$ follows:

$$\mathbb{P}\left(\mathrm{SINR}_{l,n}^{[m]}(\mathcal{C}) \leq \theta\right) \overset{(a)}{=} \mathbb{P}\left(g_{l,n}^{[m]} \leq \frac{2\,\theta\,N_0}{\mathsf{E}_n^{[m]}} + \frac{\theta\,\mathrm{I}_{l,n}^{[m]}(\mathcal{C})}{\mathsf{E}_n^{[m]}}\right)$$

$$\overset{(b1)}{=} \underset{\mathrm{I}_{l,n}^{[m]}(\mathcal{C})}{\mathbb{E}}\left[\mathsf{F}_{g_{l,n}^{[m]}|\mathrm{I}_{l,n}^{[m]}(\mathcal{C})}\left(\frac{2\,\theta\,N_0}{\mathsf{E}_n^{[m]}} + \frac{\theta\,\mathrm{I}_{l,n}^{[m]}(\mathcal{C})}{\mathsf{E}_n^{[m]}}\right)\right] \overset{(b2)}{=} \underset{\mathrm{I}_{l,n}^{[m]}(\mathcal{C})}{\mathbb{E}}\left[\mathsf{F}_{g_{l,n}^{[m]}}\left(\frac{2\,\theta\,N_0}{\mathsf{E}_n^{[m]}} + \frac{\theta\,\mathrm{I}_{l,n}^{[m]}(\mathcal{C})}{\mathsf{E}_n^{[m]}}\right)\right] \tag{4.48}$$

$$\overset{(c)}{\leq} \mathsf{F}_{g_{l,n}^{[m]}}\left(\frac{2\,\theta\,N_0}{\mathsf{E}_n^{[m]}} + \frac{\theta\,\mathbb{E}\left[\mathrm{I}_{l,n}^{[m]}(\mathcal{C})\right]}{\mathsf{E}_n^{[m]}}\right) \overset{(d)}{=} \mathsf{F}_{g_{l,n}^{[m]}}\left(\frac{2\,\theta}{\mathrm{SINR}_n^{[m]}(\mathcal{C})}\right) = 1 - \mathsf{e}^{-\sqrt{\frac{2\theta}{\mathrm{SINR}_n^{[m]}(\mathcal{C})}}}. \tag{4.49}$$

In (a), total interference at tag n for the monostatic system at the l-th time slot was defined as $\mathsf{I}_{l,n}^{[\mathrm{m}]}(\mathcal{C}) \triangleq \sum_{j \in \mathcal{A}(n)} \rho_{nj}(\mathcal{C}) \, g_{l,j}^{[\mathrm{m}]} \, \mathsf{E}_j^{[\mathrm{m}]}$; step $(b1)$ exploited the law of iterated expectation [89]; step $(b2)$ exploited the assumed statistical independence between $g_{l,n}^{[\mathrm{m}]}$ and $g_{l,j}^{[\mathrm{m}]}$ for any $j \neq n$; step (c) utilized Jensen's inequality, taking into account the concavity of CDF in Eq. (4.47); (d) exploited the linearity of expectation, the SINR definition in Eq. (4.25), and $\mathsf{M}_n = 1$.

Proof of Proposition 4.4

Proof of Eq. (4.31) is along the same lines with proof in Proposition 4.3. The CDF of $g_{l,n}^{[\mathrm{b}]}$ for Rayleigh fading is needed, as well as proof of its concavity. Using $\mathsf{M}_{ln} = \mathsf{M}_n = 1$ in Eq. (4.19), the PDF is simplified to $\mathsf{f}_{g_{l,n}^{[\mathrm{b}]}}(x) = 2 \, \mathsf{K}_0(2\sqrt{x})$, $x \geq 0$. The corresponding CDF can be calculated as follows:

$$
\begin{aligned}
\mathsf{F}_{g_{l,n}^{[\mathrm{b}]}}(x) &= \int_0^x \mathsf{f}_{g_{l,n}^{[\mathrm{b}]}}(y)\mathsf{d}y = \int_0^x 2 \, \mathsf{K}_0(2\sqrt{y}) \, \mathsf{d}y \\
&\overset{(a)}{=} \int_0^{2\sqrt{x}} z \, \mathsf{K}_0(z) \, \mathsf{d}z \overset{(b)}{=} 4x \int_0^1 y \, \mathsf{K}_0\left(2\sqrt{x}\, y\right) \mathsf{d}y \overset{(c)}{=} 1 - 2\sqrt{x} \, \mathsf{K}_1(2\sqrt{x}), \; x \geq 0, \quad (4.50)
\end{aligned}
$$

where step (a) used $2\sqrt{y} = z$, (b) $\frac{z}{2\sqrt{x}} = y$, and (c) used [62, Eq. (6.561.8)]. Concavity of $\mathsf{F}_{g_{l,n}^{[\mathrm{b}]}}$ is shown by differentiating twice the CDF $\mathsf{F}_{g_{l,n}^{[\mathrm{b}]}}(x)$ and utilizing [84, Eq. (10.29.3)]:

$$
\frac{\mathsf{d}^2}{\mathsf{d}x^2} \mathsf{F}_{g_{l,n}^{[\mathrm{b}]}}(x) = \frac{\mathsf{d}}{\mathsf{d}x} \mathsf{f}_{g_{l,n}^{[\mathrm{b}]}}(x) = \frac{\mathsf{d}}{\mathsf{d}x} 2 \, \mathsf{K}_0\left(2\sqrt{x}\right) = -\frac{2 \, \mathsf{K}_1(2\sqrt{x})}{\sqrt{x}} < 0, \quad (4.51)
$$

since $\mathsf{K}_1(x) > 0, \forall x > 0$. Thus, $\mathsf{F}_{g_{l,n}^{[\mathrm{b}]}}$ is concave and Eq. (4.31) follows using the same reasoning as in Proposition 4.3.

Chapter 5

Resource Allocation in Multi-Cell Backscatter Sensor Networks

The topic of this chapter is devoted on alternative ultra-low-power, large-scale wireless sensor networks (WSNs) relying on scatter radio principles. The notion of multi-cell backscatter sensor networks (BSNs) is proposed: a few interrogators (or cores) that act as fusion centers and tags/sensors that are responsible for measuring environmental quantities, and transmitting the sensed information towards the cores constitute a multi-cell BSN. Cores use the conventional Marconi radio technology with front-ends consisting of active filters, mixers, and amplifiers, whereas tags/sensors use scatter principle to convey wirelessly the sensed information. To realize extended coverage with prolonged network sensor batteries lifetime, the ultimate goal in this chapter is to build multi-cell BSNs where the tag-to-core achievable range is maximized. First, a complete baseband multi-cell signal model is presented incorporating all scatter radio wireless channel parameters over dyadic Rician fading channel. A multi-tag channel estimation closed-form solution is proposed based on linear minimum mean-squared error (LMMSE) estimator. The average signal-to-interference-plus-noise ratio (SINR) of maximum-ratio combining (MRC) and zero-forcing (ZF) linear detectors is found and harnessed for frequency sub-channel allocation at tags. The proposed resource allocation algorithm, called Max-Sum algorithm, adheres to simple message-passing update rules and is executed over a factor graph at each core independently. The algorithm is very lightweight and converges to the optimal solution within very few iteration steps. Judicious simulation study reveals that ZF detector is more suitable for large-scale BSNs, capable to cancel out the intra-cell interference. The proposed sub-channel–tag allocation algorithm offers remarkable convergence-complexity trade-off. The outcome of this research can be used for practical receiver design and resource allocation in ultra-low-power, large-scale WSNs.

Related Work

Over the recent years, wireless communications and signal processing research on scatter radios has focused on point-to-point scenarios, where the reader decodes backscattered signals from a single tag. Very few works have offered concrete solutions on multi-tag scenarios, where the reader has to decode signals from multiple tags backscattering concurrently. To the best of our knowledge, no work has offered reception algorithms for multi-cell scatter radio network architectures, where multiple readers (or cores) aggregate sensed information from multiple tags in their vicinity. The last problem becomes even more complicated if one accounts the scatter radio aspect of the sensors/tags. Each tag in the field is illuminated by the superposition of cores' emitted carrier waves and backscattered to the nearby cores. The interference experienced at each core after the reception of multiple backscattered signals is from the tags within the cell formed by the core (i.e., *intra-cell interference*) as well as from the tags from other cells (i.e., *inter-cell interference*). To mitigate the resulting interference and efficiently assign frequency/time resources to receiver-less tags, sophisticated resource allocation algorithms accounting for the idiosyncrasies of scatter radio need to be designed at the cores.

Multi-tag reception algorithms found in scatter radio prior art are primarily designed for passive radio frequency (RF) tags and focus on single cell reception with a single receiver, e.g., radio frequency identification (RFID) systems, where an interrogator reads/decodes backscattered signals from tags in its vicinity. The first example of reliable backscatter communication with cell-like flavor is found in [17,83]. Work in [102] studied joint decoding algorithms for multi-tag reception based on clustering and expectation-maximization framework. Work in [103] designed reception algorithms for channel estimation and detection from multi-tag RFID signals exploiting multiple receive antennas at interrogator. Subsequent work [104] proposed multi-packet RFID reception algorithms for estimating the difference in delay and the tags frequency dispersion and then multi-tag detection was applied. Multi-tag decoding algorithms based on compressive sensing are designed in [105] exploiting several collisions at the receiver side.

Backscatter sensor networks (BSNs) are extremely power-limited due to the round-trip nature of backscatter communication; even for free-space propagation loss, received power decays with the forth-power as a function of core-to-tag distance [32]. Especially, for passive tags the maximum achieved ranges is on the order of two to five meters—far from standards of large-scale, low-cost, ubiquitous sensing applications. As a result, increasing the coverage, or equivalently, increasing core-to-tag communication range, is of principle importance in low-cost, low-power BSNs. The authors in [94] offered coverage analysis for high-density, multi-cell BSNs and discovered that high coverage is feasible

only if frequency-oriented modulation is harnessed at the tags. Coverage and capacity analysis for multi-cell BSNs using random Poisson cluster point processes is offered in [96].

Contributions

This chapter proposes a multi-cell BSN architecture with joint time-frequency multiple-access following the guidelines from [13] and exploiting the know-how and the experimental experience of our group [11, 12, 17, 33, 37, 39, 82, 83, 86, 106]. Several multi-antenna cores emit continuous sinusoid waves illuminating the tags in the field. A set of available orthogonal frequency sub-bands (also called sub-frequencies) is assumed available and each tag backscatters a packet of training (for channel estimation and synchronization) and data symbols modulated over a specific frequency sub-band. The packet is received and decoded at the closest core. To alleviate intra-cell interference during the training phase, the training sequences are orthogonal of each other and the tags using the same training sequence are configured to backscatter over different frequency sub-bands. A measurement phase is also considered where cores conduct signal-to-interference-plus-noise ratio (SINR) measurements with the tags in their cell. The frequency sub-channel allocation at tags changes during the measurement phase and the goal at each core is to assess the average SINR for each pair of neighboring tag–frequency sub-band. Subsequently, resource allocation based on a specific metric involving a function of estimated average SINR is applied to find the optimal assignment.

Using the above multi-cell BSN framework, the contributions of this chapter can be summarized as:

- For the first time in the scatter radio literature a realistic and complete baseband signal model for multiple-access in multi-cell BSNs is derived. The signal model incorporates: (a) microwave- and tag-related parameters obtained from real experimental testbeds, (b) path-loss and dyadic Rician small-scale fading in wireless channel modeling, and (c) multiple transmit and receive antennas at the cores.

- Based on the multi-cell BSN model, a novel linear minimum mean-squared error (LMMSE) channel estimator is employed at the cores to estimate the compound uplink wireless round-trip channels of the tags within the cell. The proposed estimator takes into account the idiosyncrasies of scatter radio wireless signal model. Using the estimated channel, two multi-tag linear detectors are proposed: maximum-ratio combining (MRC) and zero-forcing (ZF).

- Using the average received SINR measurements associated with both linear detection techniques a generic formulation for resource allocation in BSNs is proposed. The formulated problem is attacked with a message-passing inference algorithm with simple update rules and convergence to the desired solution within very few steps. The proposed algorithm is an instance of the Max-Sum algorithm.

- Judicious simulation study reveals that ZF generally outperforms MRC in terms of both bit error rate (BER) and outage probability. It is found that orthogonal training transmissions are mandatory to maintain good channel estimation accuracy. The proposed Max-Sum algorithm [107] offers the same optimal performance with classic convex optimization methods with reduced computational cost, measured in terms of execution time in large-scale BSNs.

Organization and Notation

The rest of this work is organized as follows. Section 5.1 presents the adopted wireless scatter radio channel model, Section 5.2 offers the multi-tag baseband signal model, while the proposed channel estimation closed-form solution along with the average SINR calculation for MRC and ZF linear detectors is provided in Section 5.3. Section 5.4 formulates the resource allocation optimization problem and designs the simple Max-Sum algorithm associated with the problem. Finally, simulation results are presented in Section 5.5.

The set of real, complex, natural, and binary numbers is denoted $\mathbb{R}$, $\mathbb{C}$, $\mathbb{N}$, and $\mathbb{B}$, respectively. Italic letters (e.g., x), simple bold letters (e.g., $\mathbf{x}$), and capital bold letters (e.g., $\mathbf{X}$) represent scalars, vectors, and matrices, respectively. Operators $(\cdot)^*$, $\Re\{\cdot\}$, $(\cdot)^\top$, $(\cdot)^\mathsf{H}$, $(\cdot)^{-1}$, $(\cdot)^\dagger$ take the conjugate, real part, transpose, conjugate transpose, inverse, and pseudo-inverse of a matrix, respectively. $\mathbf{I}_N$ and $\mathbf{0}_N$ ($\mathbf{1}_N$) represent the $N \times N$ identity matrix and the all-zeros (all-ones) vector of size N, respectively. For a vector $\mathbf{x}$, vector $\mathbf{x}_{i:j}$ is the subvector of $\mathbf{x}$ comprising of the i-th up to j-th element. For a matrix $\mathbf{A}$, $[\mathbf{A}]_{i,:}$ denotes the vector formed by $\mathbf{A}$'s i-th row. For two functions $\mathsf{f}_1 : \mathbb{R} \longrightarrow \mathbb{C}$ and $\mathsf{f}_2 : \mathbb{R} \longrightarrow \mathbb{C}$ the inner product is defined as $\langle \mathsf{f}_1, \mathsf{f}_2 \rangle \triangleq \int_{\mathbb{R}} \mathsf{f}_1(t)\mathsf{f}_2^*(t)\mathsf{d}t$. Moreover, if either f_1 or f_2 are matrix functions, the inner product is applied component-wise. $\mathcal{CN}(\boldsymbol{\mu}, \boldsymbol{\Sigma})$ denotes the proper complex Gaussian distribution with mean $\boldsymbol{\mu}$ and covariance matrix $\boldsymbol{\Sigma}$, while $\mathcal{U}[a, b]$ is the uniform distribution over interval $[a, b]$. $\mathbb{P}(\cdot)$, $\mathbb{E}[\cdot]$, and $\mathsf{var}[\cdot]$, denote the probability, expectation, and variance operator, respectively. Finally, $\sum_{\substack{i \in \mathcal{I} \\ j \in \mathcal{J}}}$ is equivalent with $\sum_{i \in \mathcal{I}} \sum_{j \in \mathcal{J}}$.
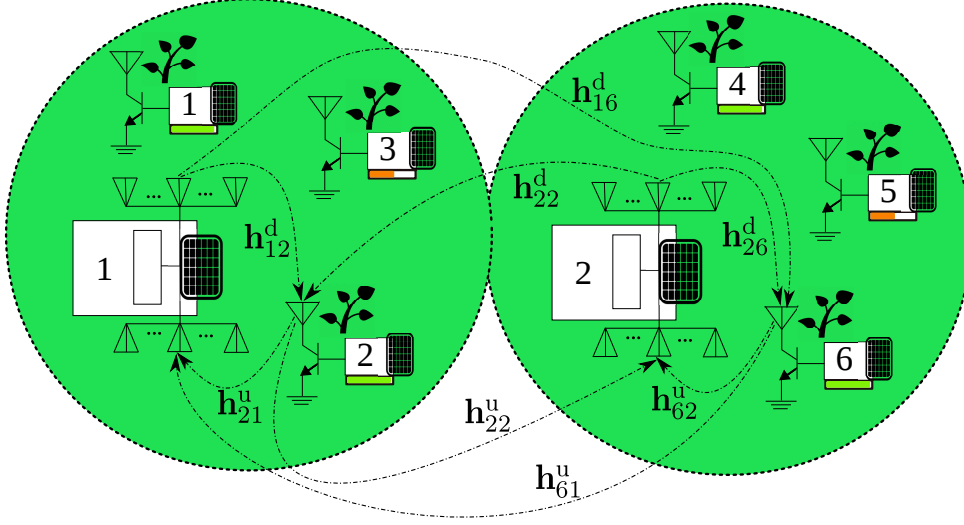
Figure 5.1: A multi-cell BSN with $B = 2$ cores and $K = 6$ tags.

5.1 Wireless Scatter Radio System Model

We consider a static multi-cell backscatter sensor network (BSN) consisting of B cores and K sensors/tags, an example is given in Fig. 5.1. Each core is a Marconi radio with separate transmit and receive antennas, e.g., a software define radio (SDR) reader. It is assumed that each core has N_{T} transmit and N_{R} receive antennas. Note that for simplification purposes monostatic architecture (with different transmit and receive antennas) is employed at each cell. Although, the proposed reception techniques can be also applied to the case of multistatic multi-cell architecture.

The sets of all cores and tags are given by the sets $\mathcal{B} \triangleq \{1, 2, \ldots, B\}$ and $\mathcal{K} \triangleq \{1, 2, \ldots, K\}$, respectively. There exist at total C orthogonal frequency sub-bands $\left\{\mathtt{f}^{(1)}, \mathtt{f}^{(2)}, \ldots, \mathtt{f}^{(C)}\right\}$, given in an ascending order, indexed by set $\mathcal{C} \triangleq \{1, 2, \ldots, C\}$.

Due to relatively small delay spread, frequency non-selective (flat) fading channel [27] is assumed across all links (b, k) and (k, b), $b \in \mathcal{B}$, $k \in \mathcal{K}$. Moreover, for outdoor environments, common in wireless sensor network applications, there exist possible strong line-of-sight propagation paths. Hence, incorporating all the above in wireless channel model, the baseband complex channel response for links (b, k) and (k, b) is given by

$$\mathbf{h}_{bk}^{\mathrm{d}} \sim \mathcal{CN}\left(\sqrt{\frac{\kappa_{bk}^{\mathrm{d}}}{\kappa_{bk}^{\mathrm{d}} + 1}}\sigma_{bk}\mathbf{e}_{bk}^{\mathrm{d}}, \frac{\sigma_{bk}^2}{\kappa_{bk}^{\mathrm{d}} + 1}\mathbf{I}_{N_{\mathrm{T}}}\right), \tag{5.1}$$

$$\mathbf{h}_{kb}^{\mathrm{u}} \sim \mathcal{CN}\left(\sqrt{\frac{\kappa_{kb}^{\mathrm{u}}}{\kappa_{kb}^{\mathrm{u}} + 1}}\sigma_{kb}\mathbf{e}_{kb}^{\mathrm{u}}, \frac{\sigma_{kb}^2}{\kappa_{kb}^{\mathrm{u}} + 1}\mathbf{I}_{N_{\mathrm{R}}}\right), \tag{5.2}$$

where κ_{bk}^{d} and κ_{kb}^{u} denote the ratio between the power in the direct path and the power in the scattered paths of core-to-tag link (b,k) and tag-to-core link (k,b), respectively, $\mathbf{e}_{bk}^{\text{d}}$ and $\mathbf{e}_{bk}^{\text{u}}$ are the antenna steering vectors at core b for the transmit and received antennas, respectively, depending on antenna array geometry with $\|\mathbf{e}_{bk}^{\text{d}}\|_2^2 = N_{\text{T}}$ and $\|\mathbf{e}_{kb}^{\text{u}}\|_2^2 = N_{\text{R}}$. $\frac{1}{N_{\text{T}}}\mathbb{E}[\|\mathbf{h}_{bk}^{\text{d}}\|_2^2] = \sigma_{bk}^2$ and $\frac{1}{N_{\text{R}}}\mathbb{E}[\|\mathbf{h}_{kb}^{\text{u}}\|_2^2] = \sigma_{kb}^2$ denote the normalized channel powers of core-to-tag link (b,k) and tag-to-core link (k,b), respectively. Both downlink $\{\mathbf{h}_{bk}^{\text{d}}\}_{(b,k)\in\mathcal{B}\times\mathcal{K}}$ and uplink $\{\mathbf{h}_{kb}^{\text{u}}\}_{(b,k)\in\mathcal{B}\times\mathcal{K}}$ channels are assumed uncorrelated of each other and change independently every T_{coh} seconds, where T_{coh} is the channel coherence time.

When uniform linear arrays (ULAs) are employed at both ends of core b, transmit and receive antenna steering vectors can be, respectively, written as

$$\mathbf{e}_{bk}^{\text{d}} = \left[1 \;\; e^{\frac{j\,2\,\pi\,\sin(\varphi_{bk}^{\text{d}})\,D_y}{\lambda}} \;\; \ldots \;\; e^{\frac{j\,2\,\pi\,\sin(\varphi_{bk}^{\text{d}})\,(N_{\text{T}}-1)\,D_y}{\lambda}}\right]^{\top}, \tag{5.3}$$

$$\mathbf{e}_{kb}^{\text{u}} = \left[1 \;\; e^{\frac{j\,2\,\pi\,\sin(\varphi_{kb}^{\text{u}})\,D_y}{\lambda}} \;\; \ldots \;\; e^{\frac{j\,2\,\pi\,\sin(\varphi_{kb}^{\text{u}})\,(N_{\text{R}}-1)\,D_y}{\lambda}}\right]^{\top}, \tag{5.4}$$

where φ_{bk}^{d} and φ_{kb}^{u} denote the angle-of-departure (AoD) for link (b,k) and angle-of-arrival (AoA) for link (k,b), respectively, λ denotes the propagation wavelength, and D_y is the antenna spacing (usually $D_y = \frac{\lambda}{2}$). The normalized channel powers σ_{kb}^2 and σ_{kb}^2 depend on large-scale path-gain (inverse of path-loss) which, due to reciprocity theorem, is the same for links (b,k) and (k,b), i.e., $\sigma_{bk} = \sigma_{kb}$.

When a tag $k \in \mathcal{K}$ reflects information, it backscatters a packet of M symbols, where each symbol within packet takes values $\{\pm 1\}$. A fraction τ_{tr} of total packet duration is dedicated for channel estimation while the rest $1 - \tau_{\text{tr}}$ is used for data transmission, i.e., the total number of training symbols is $M_{\text{tr}} = \tau_{\text{tr}} M \in \mathbb{N}$, while the rest $M_{\text{d}} = M - M_{\text{tr}}$ are data symbols and depend on the sensed information. There is a set of available pilot sequences $\mathcal{X}_{\text{tr}} = \left\{\mathbf{x}^{(1)}, \mathbf{x}^{(2)}, \ldots, \mathbf{x}^{(M_{\text{tr}})}\right\} \subset \{\pm 1\}^{M_{\text{tr}}}$, i.e., set $\mathcal{X}_{\text{tr}}$ contains M_{tr} sequences, each of dimension M_{tr}. The sequences in set $\mathcal{X}_{\text{tr}}$ are orthogonal, i.e.,

$$\left(\mathbf{x}^{(m)}\right)^{\top}\mathbf{x}^{(m')} = \begin{cases} M_{\text{tr}}, & \text{if } m = m', \\ 0, & \text{if } m \neq m'. \end{cases} \tag{5.5}$$

The sequence assigned to tag k has been decided a-priori and is assumed fixed. In a practical scenario, to reduce the interference, the same sequence has to be reused across tags that are far apart. Finally, sets $\mathcal{M}_{\text{tr}} \triangleq \{1, 2, \ldots, M_{\text{tr}}\}$ and $\mathcal{M}_{\text{d}} \triangleq \{M_{\text{tr}} + 1, M_{\text{tr}} + 2, \ldots, M\}$ are also defined.

To obtain accurate resource allocation exploiting long-term information, a periodic measurement process is conducted divided in several time frames; each frame has duration equal to the channel coherence time. During the measurement process each core conducts (independently from the rest ones) signal-to-interference-plus-noise ratio (SINR) measurements with tags in its vicinity. Frequency sub-band allocation changes from frame to frame while tag sequence assignment is assumed fixed across all frames for simplicity in implementation. Section 5.3.2 offers a detailed exposition on the proposed average SINR estimation procedure.

The following sets are defined

$$\mathcal{K}_{\mathcal{M}_{\mathrm{tr}}}(m) \triangleq \left\{ k \in \mathcal{K} : \text{tag } k \text{ uses training sequence } \mathbf{x}^{(m)} \right\}, \tag{5.6}$$

$$\mathcal{K}_{\mathcal{C}}(c) \triangleq \left\{ k \in \mathcal{K} : \text{tag } k \text{ uses frequency sub-band } \mathbf{f}^{(c)} \right\}, \tag{5.7}$$

$$\mathcal{K}_{\mathcal{B}}(b) \triangleq \left\{ k \in \mathcal{K} : \mathsf{d}_{bk} = \min_{b' \in \mathcal{B}} \mathsf{d}_{b'k} \right\}. \tag{5.8}$$

It is not difficult to see that set $\mathcal{K}$ can be partitioned as $\mathcal{K} = \bigcup_{b \in \mathcal{B}} \mathcal{K}_{\mathcal{B}}(b)$. Each set $\mathcal{K}_{\mathcal{B}}(b)$ can be further partitioned as $\mathcal{K}_{\mathcal{B}}(b) = \bigcup_{m \in \mathcal{M}_{\mathrm{tr}}} \mathcal{K}_{bm}$, where $\mathcal{K}_{bm} \triangleq \mathcal{K}_{\mathcal{B}}(b) \cap \mathcal{K}_{\mathcal{M}_{\mathrm{tr}}}(m)$. Each set $\mathcal{K}_{bm}$ can be expressed as $\mathcal{K}_{bm} = \bigcup_{c \in \mathcal{C}} \mathcal{K}_{bmc}$, where $\mathcal{K}_{bmc} = \mathcal{K}_{bm} \cap \mathcal{K}_{\mathcal{C}}(c)$. It is not difficult to see that for two triplets $(b, m, c), (b', m', c') \in \mathcal{B} \times \mathcal{M}_{\mathrm{tr}} \times \mathcal{C}$, $\mathcal{K}_{bmc}$ and $\mathcal{K}_{b'm'c'}$ are disjoint if $b \neq b$ or $m \neq m'$ or $c \neq c'$. To minimize intra-cell interference, during the training phase for each frame of the measurements, we consider orthogonal training transmissions, i.e., tags sharing the same training sequence are configured to transmit at different frequency sub-bands. In other words, tags within the same cell are assigned to a unique pair $(m, c) \in \mathcal{M}_{\mathrm{tr}} \times \mathcal{C}$, i.e., $|\mathcal{K}_{bmc}| \leq 1$.

The goal at each core b is to estimate the average SINR for each pair $(k, c) \in \mathcal{K}_{\mathcal{B}}(b) \times \mathcal{C}$, by changing tag-channel allocation (i.e., set $\mathcal{K}_{\mathcal{C}}(c)$) across different frames.

5.2 Multi-Cell and Multi-tag Processing

Each core $b \in \mathcal{B}$ emits from each transmit antenna a continuous sinusoid wave with baseband representation $\sqrt{\frac{P_b}{N_{\mathrm{T}}}} \, \mathrm{e}^{\mathrm{j}\phi_b}$, where P_b is the total transmission power and ϕ_b is the phase mismatch between transmit and receive circuitry at core b and is assumed fixed and known. The superposition of cores' emitted signals, propagated across downlink channels $\{\mathbf{h}^{\mathrm{d}}_{bk}\}_{b \in \mathcal{B}}$, incidents at the antenna of tag k, i.e., tag k receives $\sum_{b'=1}^{B} \sqrt{\frac{P_{b'}}{N_{\mathrm{T}}}} \, \mathrm{e}^{\mathrm{j}\phi_{b'}} \left(\mathbf{h}^{\mathrm{d}}_{b'k} \right)^{\top} \mathbf{1}_{N_{\mathrm{T}}}$.

Using similar ideas developed in [12, 37, 39] each tag k employees joint frequency and amplitude modulation and backscatters towards core b

$$\mathsf{u}_{kb}(t) = \mathrm{DC}_k + \frac{\left(\sum_{b'=1}^{B} \sqrt{\frac{P_{b'}}{N_\mathrm{T}}}\, \mathsf{e}^{\mathsf{j}\phi_{b'}} \left(\mathbf{h}_{b'k}^\mathrm{d}\right)^\top \mathbf{1}_{N_\mathrm{T}}\right)\eta_k}{2}(\Gamma_{k,0} - \Gamma_{k,1}) \sum_{i=1}^{M} x_{k,i}\, \mathsf{v}_{kb}(t - (i-1)T),$$

(5.9)

where η_k is the scattering efficiency, remaining constant within packet duration, $\Gamma_{k,0}$ and $\Gamma_{k,1}$ are the (load-dependent) reflection coefficients, DC_k is a DC term depending on antenna structural mode as well as on reflection coefficients $\Gamma_{k,0}$ and $\Gamma_{k,1}$ and does not depend on time t, and $\mathsf{v}_{kb}(t)$ is the reflected waveform of tag k. Waveform $\mathsf{v}_{kb}(t)$ is the fundamental frequency component of a 50% duty cycle square waveform of period $1/f_k$, i.e.,

$$\mathsf{v}_{kb}(t) = \frac{4}{\pi}\mathsf{cos}(2\pi f_k t + \Phi_{kb})\,\Pi_T(t),$$

(5.10)

where $\Pi_T(t) \triangleq \mathbf{1}\{t \in [0, T)\}$, where

$$\mathbf{1}\{X\} \triangleq \begin{cases} 1, & X \text{ is true,} \\ 0, & X \text{ is false,} \end{cases}$$

(5.11)

is the sum-indicator function of statement X. f_k and Φ_{kb} in (5.10) are the generated frequency of tag k and the random phase mismatch between tag k and core b, respectively. Phases Φ_{kb} are modeled as uniform RVs in $[0, 2\pi)$, assumed independent and identically distributed (IID) across different k. If the m-th training sequence and the c-th frequency sub-channel are assigned to tag k, then $\{x_{k,i}\}_{i=1}^{M_\mathrm{tr}} = \mathbf{x}^{(m)} \in \mathcal{X}_\mathrm{tr}$ and $f_k = \mathsf{f}^{(c)}$. Tag frequency sub-channels satisfy the following

$$\mathsf{f}^{(c)} = \frac{l_c}{T}, \quad \forall c \in \mathcal{C},$$

(5.12)

for some $l_c \in \mathbb{N}$, implying that for $c \neq c'$, $c, c' \in \mathcal{C}$, $\left|\mathsf{f}^{(c)} - \mathsf{f}^{(c')}\right| = |l_c - l_{c'}|\frac{1}{T}$. Random phase mismatch, as well as the uplink and downlink channels are independent of each other. Moreover, all data symbols are independent across all tags and time instants and $\mathbb{P}(x_{k,i} = \pm 1) = \frac{1}{2}, \forall k \in \mathcal{K}, \forall i \in \mathcal{M}_\mathrm{d}$.

Core b receives the superposition of $\{\mathsf{u}_{kb}(t)\}_{k\in\mathcal{K}}$, propagated by uplink channels $\{\mathbf{h}_{kb}^\mathrm{u}\}_{k\in\mathcal{K}}$, i.e.,

$$\tilde{\mathbf{y}}_b(t) = \sum_{k\in\mathcal{K}} \mathbf{h}_{kb}^\mathrm{u}\, \mathsf{u}_{kb}(t) + \mathbf{w}_b(t),$$

(5.13)

where the components of $\mathbf{w}_b(t)$ are independent circularly symmetric, complex Gaussian noise processes with flat power spectral density (PSD) N_0 over $[-W_b, W_b]$ frequency band, and zero otherwise, i.e.,

$$\mathcal{F}\left\{\mathbb{E}\left[\mathbf{w}_b(t)\mathbf{w}_b(t+\tau)^{\mathsf{H}}\right]\right\} = N_0\,\mathbf{1}\{|F| \leq W_b\}\,\mathbf{I}_{N_{\mathrm{R}}}, \tag{5.14}$$

where $\mathcal{F}\{\cdot\}$ denote the Fourier transform, applied element-wise, and parameter W_b denotes the receiver bandwidth at core b.

Signal in (5.13) contains DC terms, thus, the time average is removed. After DC-blocking filtering, signal $\mathbf{y}_b(t) = \tilde{\mathbf{y}}_b(t) - \int_{\mathcal{T}_0} \tilde{\mathbf{y}}_b(t)\mathrm{d}t$ is formed, where $[0, MT) \subseteq \mathcal{T}_0$, and $\mathcal{T}_0$ is the time processing interval. Note that $\int_{\mathcal{T}_0} \tilde{\mathbf{y}}_b(t)\mathrm{d}t \approx \sum_{k\in\mathcal{K}} \mathbf{h}_{kb}^{\mathrm{u}}\,\mathrm{DC}_k$ holds true, due to (a) the linearity of integration, (b) $\int_a^{a+T} \cos(2\pi f_k t + \Phi_{kb})\,\mathrm{d}t = 0$ for every $a \in \mathbb{R}$ since $f_k = \frac{l}{T}$, for some $l \in \mathbb{N}$, and (c) the fact that the components of $\mathbf{w}_b^{[n]}(t)$ are zero-mean random processes. Hence, abbreviating $\forall k \in \mathcal{K}$

$$\mathbf{g}_{kb} \triangleq \frac{\left(\sum_{b'=1}^{B} \sqrt{\frac{P_{b'}}{N_{\mathrm{T}}}}\,\mathrm{e}^{\mathsf{j}\phi_{b'}}\left(\mathbf{h}_{b'k}^{\mathrm{d}}\right)^{\top}\mathbf{1}_{N_{\mathrm{T}}}\right)\eta_k(\Gamma_{k,0} - \Gamma_{k,1})\,\mathbf{h}_{kb}^{\mathrm{u}}}{\frac{\pi}{2}}, \tag{5.15}$$

and plugging Eq. (5.10) in (5.9) and then substituting in (5.13), the DC-blocked signal $\mathbf{y}_b(t)$ can be written as

$$\mathbf{y}_b(t) = \sum_{k\in\mathcal{K}} \mathbf{g}_{kb} \sum_{i=1}^{M} x_{k,i} \cos(2\pi f_k(t - (i-1)T) + \Phi_{kb})\,\Pi_T(t + (i-1)T) + \mathbf{w}_b(t). \tag{5.16}$$

Theorem 5.1. *For $W_b \gg \frac{1}{T}$, when multiple tags are backscattering, the baseband equivalent signal at core b, associated with c-th frequency sub-band, at the i-th time instant is given by*

$$\mathbf{r}_{b,i}^{(c)} = \sum_{k\in\mathcal{K}_{\mathcal{C}}(c)} \boldsymbol{\xi}_{kb}^{(c)}\,x_{k,i} + \mathbf{n}_{b,i}^{(c)}, \quad i = 1, 2, \ldots, M, \tag{5.17}$$

where $\boldsymbol{\xi}_{kb}^{(c)} \triangleq \mathbf{1}\{k \in \mathcal{K}_{\mathcal{C}}(c)\}\,\mathbf{g}_{kb}\sqrt{\frac{T}{2}}\cos(\Phi_{kb})$ is the compound (uplink) channel between tag $k \in \mathcal{K}$ and core b at the output of c-th frequency matched filter, incorporating microwave and wireless propagation parameters, while noise vector $\mathbf{n}_{b,i}^{(c)} \sim \mathcal{CN}(\mathbf{0}_{N_{\mathrm{R}}}, \sigma_b^2\,\mathbf{I}_{N_{\mathrm{R}}})$, with $\sigma_b^2 = N_0$.

Proof. The proof is provided in Appendix 5.6. $\square$

By the independence of small-scale fading coefficients and Φ_{kb} across all tags $k \in \mathcal{K}$, compound uplink channel vectors $\{\boldsymbol{\xi}_{kb}^{(c)}\}_{k\in\mathcal{K}}$ are independent of each other. In addition,

for a tag $k \in \mathcal{K}_{bmc}$ vector $\boldsymbol{\xi}_{kb}^{(c)}$ is trivially independent from the rest $\{\boldsymbol{\xi}_{kb}^{(c')}\}_{c' \neq c}$, because $\boldsymbol{\xi}_{kb}^{(c')} = \mathbf{0}_{N_R}, \forall c' \in \mathcal{C} \backslash c$.

5.3   Channel Estimation and SINR Calculation

Assuming that the first M_{tr} symbols correspond to the pilot sequence, the training signal associated with the c-th sub-band at core b can be expressed compactly as

$$\widetilde{\mathbf{R}}_{b,tr}^{(c)} = \sum_{k \in \mathcal{K}_\mathcal{C}(c)} \boldsymbol{\xi}_{kb}^{(c)} \mathbf{x}_{k,1:M_{tr}}^\top + \mathbf{N}_{b,tr}^{(c)}, \tag{5.18}$$

where $\widetilde{\mathbf{R}}_{b,tr}^{(c)} = [\mathbf{r}_{b,1}^{(c)} \ \mathbf{r}_{b,2}^{(c)} \ \ldots \ \mathbf{r}_{b,M_{tr}}^{(c)}] \in \mathbb{C}^{N_R \times M_{tr}}$, $\mathbf{x}_{k,1:M_{tr}}^\top = [x_{k,1} \ x_{k,2} \ \ldots \ x_{k,M_{tr}}]$, and $\mathbf{N}_{b,tr}^{(c)} = [\mathbf{n}_{b,1}^{(c)} \ \mathbf{n}_{b,2}^{(c)} \ \ldots \ \mathbf{n}_{b,M_{tr}}^{(c)}]$. Since for any tag $k \in \mathcal{K}_{\mathcal{M}_{tr}}(m)$, $\mathbf{x}_{k,1:M_{tr}} = \mathbf{x}^{(m)}$, to eliminate the intra-cell interference and estimate the uplink compound channel of tag $k \in \mathcal{K}_{bmc}$, the training signal in (5.18) is multiplied with a rescaled version of $\mathbf{x}^{(m)}$, i.e., $\widetilde{\mathbf{R}}_{b,tr}^{(c)} \frac{\mathbf{x}^{(m)}}{\|\mathbf{x}^{(m)}\|_2^2}$ [108]. Thus, due to the orthogonality of $\{\mathbf{x}^{(m)}\}_{m \in \mathcal{M}_{tr}}$, the training signal associated with tag $k \in \mathcal{K}_{bmc}$ at core b can be written as

$$\widetilde{\mathbf{R}}_{b,tr}^{(c)} \frac{\mathbf{x}^{(m)}}{\|\mathbf{x}^{(m)}\|_2^2} \triangleq \mathbf{r}_{b,tr}^{(c)} = \boldsymbol{\xi}_{kb}^{(c)} + \sum_{\substack{b' \neq b \\ k' \in \mathcal{K}_{b'mc}}} \boldsymbol{\xi}_{k'b}^{(c)} + \mathbf{v}_{b,tr}^{(c)}, \tag{5.19}$$

where $\mathbf{N}_{b,tr}^{(c)} \frac{\mathbf{x}^{(m)}}{\|\mathbf{x}^{(m)}\|_2^2} \triangleq \mathbf{v}_{b,tr}^{(c)} \sim \mathcal{CN}(\mathbf{0}_{N_R}, \frac{N_0}{M_{tr}}\mathbf{I}_{N_R})$. It is remarked that training signal $\mathbf{r}_{b,tr}^{(c)}$ associated with tag $k \in \mathcal{K}_{bmc}$ does not contain intra-cell interference terms, including only interference from tags of neighboring cells utilizing the same pair (m, c) with tag k.

Before proceeding to the proposed channel estimator the following proposition is needed.

Proposition 5.1. For vectors $\{\boldsymbol{\xi}_{kb}^{(c)}\}_{k \in \mathcal{K}_\mathcal{C}(c)}, \forall c \in \mathcal{C}, \forall b \in \mathcal{B}$, the expected value is given by $\mathbb{E}[\boldsymbol{\xi}_{kb}^{(c)}] = \mathbf{0}_{N_R}$, while the covariance $\mathbf{C}_{\boldsymbol{\xi}_{kb}^{(c)}} \triangleq \mathbb{E}[\boldsymbol{\xi}_{kb}^{(c)}(\boldsymbol{\xi}_{kb}^{(c)})^\mathsf{H}]$ is given by

$$\mathbf{C}_{\boldsymbol{\xi}_{kb}^{(c)}} = \frac{T \eta_k^2 |\Gamma_{k,0} - \Gamma_{k,1}|^2}{\pi^2} \left(\sum_{b'=1}^{B} \frac{P_{b'} \sigma_{b'k}^2}{\kappa_{b'k}^d + 1} + \left| \sum_{b'=1}^{B} \sqrt{\frac{P_{b'} \kappa_{b'k}^d \sigma_{b'k}^2}{N_T(\kappa_{b'k}^d + 1)}} e^{j\phi_{b'}} (\mathbf{e}_{b'k}^d)^\top \mathbf{1}_{N_T} \right|^2 \right) \cdot$$
$$\cdot \left(\frac{\sigma_{kb}^2}{\kappa_{kb}^u + 1} \left(\mathbf{I}_{N_R} + \kappa_{kb}^u \mathbf{e}_{kb}^u (\mathbf{e}_{kb}^u)^\mathsf{H} \right) \right) \tag{5.20}$$

Proof. The proof is provided in Appendix 5.6.   □

In this work the linear minimum mean-squared error (LMMSE) estimator for parameter vector $\boldsymbol{\xi}_{kb}^{(c)}$ is used.

Theorem 5.2. For a tag $k \in \mathcal{K}_{bmc}$ the LMMSE estimate of $\boldsymbol{\xi}_{kb}^{(c)}$ based on training signal $\mathbf{r}_{b,\text{tr}}^{(c)}$ is given by

$$\widehat{\boldsymbol{\xi}}_{kb}^{(c)} = \mathbf{C}_{\boldsymbol{\xi}_{kb}^{(c)}} \left(\sum_{\substack{b' \in \mathcal{B} \\ k' \in \mathcal{K}_{b'mc}}} \mathbf{C}_{\boldsymbol{\xi}_{k'b}^{(c)}} + \frac{N_0}{M_{\text{tr}}} \mathbf{I}_{N_{\text{R}}} \right)^{-1} \mathbf{r}_{b,\text{tr}}^{(c)}. \tag{5.21}$$

In addition, vector $\widehat{\boldsymbol{\xi}}_{kb}^{(c)}$ and error vector $\boldsymbol{\epsilon}_{kb}^{(c)} = \widehat{\boldsymbol{\xi}}_{kb}^{(c)} - \boldsymbol{\xi}_{kb}^{(c)}$ are uncorrelated. The mean and the covariance of vector $\boldsymbol{\epsilon}_{kb}^{(c)}$ are, respectively, $\mathbb{E}[\boldsymbol{\epsilon}_{kb}^{(c)}] = \mathbf{0}_{N_{\text{R}}}$ and

$$\mathbf{C}_{\boldsymbol{\epsilon}_{kb}^{(c)}} = \mathbf{C}_{\boldsymbol{\xi}_{kb}^{(c)}} \left(\mathbf{I}_{N_{\text{R}}} - \left(\sum_{\substack{b' \in \mathcal{B} \\ k' \in \mathcal{K}_{b'mc}}} \mathbf{C}_{\boldsymbol{\xi}_{k'b}^{(c)}} + \frac{N_0}{M_{\text{tr}}} \mathbf{I}_{N_{\text{R}}} \right)^{-1} \mathbf{C}_{\boldsymbol{\xi}_{kb}^{(c)}} \right). \tag{5.22}$$

Proof. The proof of this theorem relies on Bayesian Gauss-Markov theorem [88, Theorem 12.1], Proposition 5.1, and the independence of $\{\boldsymbol{\xi}_{kb}^{(c)}\}_{k \in \mathcal{K}}$. $\qquad\square$

Note that LMMSE estimator relies only on the first and second moments of parameter vectors $\{\boldsymbol{\xi}_{kb}^{(c)}\}$ involved in (5.21) and is suboptimal in terms of mean squared-error (MSE) as it imposes $\widehat{\boldsymbol{\xi}}_{kb}^{(c)}$ to be a linear function of the observation vector $\mathbf{r}_{b,\text{tr}}^{(c)}$, while $\mathbf{r}_{b,\text{tr}}^{(c)}$ and $\widehat{\boldsymbol{\xi}}_{kb}^{(c)}$ are not proper complex Gaussian vectors. However, amongst all linear estimators, LMMSE is the one that minimizes the MSE [88].

The received signal $\mathbf{r}_{b,i}^{(c)}$ in Eq. (5.17) for tag $k \in \mathcal{K}_{bmc}$ can be written as

$$\mathbf{r}_{b,i}^{(c)} = \sum_{\substack{m' \in \mathcal{M}_{\text{tr}} \\ k' \in \mathcal{K}_{bm'c}}} \left(\widehat{\boldsymbol{\xi}}_{k'b}^{(c)} - \boldsymbol{\epsilon}_{kb}^{(c)} \right) x_{k'i} + \sum_{\substack{b' \neq b \\ m' \in \mathcal{M}_{\text{tr}} \\ k' \in \mathcal{K}_{b'm'c}}} \boldsymbol{\xi}_{k'b}^{(c)} x_{k'i} + \mathbf{n}_{b,i}^{(c)}, \tag{5.23}$$

where the sum over the set $\mathcal{K}_{\mathcal{C}}(c)$ is decomposed across two terms, the first pertains to intra-cell interference, i.e., the tags in $\mathcal{K}_{\mathcal{C}}(c)$ within cell b (i.e., $k \in \mathcal{K}_{\mathcal{B}}(b) \cap \mathcal{K}_{\mathcal{C}}(c) = \bigcup_{m' \in \mathcal{M}_{\text{tr}}} \mathcal{K}_{bm'c}$), while the second one accounts for the inter-cell interference associated with tags in $\mathcal{K}_{\mathcal{C}}(c)$ that do not belong in cell b (i.e., $k \in \bigcup_{b' \neq b} \bigcup_{m' \in \mathcal{M}_{\text{tr}}} \mathcal{K}_{b'm'c}$). Note that core b can estimate the corresponding $\widehat{\boldsymbol{\xi}}_{kb}^{(c)}$ for all tags in its cell, i.e., $k \in \bigcup_{m' \in \mathcal{M}_{\text{tr}}} \mathcal{K}_{bm'c}$ and thus, by the properties of LMMSE estimator, the compound uplink channel can be written as $\boldsymbol{\xi}_{k'b}^{(c)} = \widehat{\boldsymbol{\xi}}_{k'b}^{(c)} - \boldsymbol{\epsilon}_{k'b}^{(c)}$, where $\widehat{\boldsymbol{\xi}}_{k'b}^{(c)}$ and $\boldsymbol{\epsilon}_{k'b}^{(c)}$ are uncorrelated.

5.3.1　Multi-Tag Linear Detection

Core b treats the channel estimate $\widehat{\boldsymbol{\xi}}_{kb}^{(c)}$ for user $k \in \mathcal{K}_{bmc}$ as the actual uplink compound channel and applies linear detection using $\widehat{\boldsymbol{\xi}}_{kb}^{(c)}$. For linear detection, a linear transformation is applied on received signal and the sign of the outcome is used as the estimated symbol. Applying linear transformation $\mathbf{a}_{kb}^{(c)}$ on received vector $\mathbf{r}_{b,i}^{(c)}$, we obtain $z_{k,i} = (\mathbf{a}_{kb}^{(c)})^{\mathsf{H}} \mathbf{r}_{b,i}^{(c)}$, i.e.,

$$
z_{k,i} = (\mathbf{a}_{kb}^{(c)})^{\mathsf{H}} \left(\widehat{\boldsymbol{\xi}}_{kb}^{(c)} x_{ki} + \sum_{\substack{m' \in \mathcal{M}_{\mathrm{tr}} \\ k' \in \mathcal{K}_{bm'c} \setminus k}} \widehat{\boldsymbol{\xi}}_{k'b}^{(c)} x_{k'i} - \sum_{\substack{m' \in \mathcal{M}_{\mathrm{tr}} \\ k' \in \mathcal{K}_{bm'c}}} \boldsymbol{\epsilon}_{k'b}^{(c)} x_{k'i} + \sum_{\substack{b' \neq b \\ m' \in \mathcal{M}_{\mathrm{tr}} \\ k' \in \mathcal{K}_{b'm'c}}} \boldsymbol{\xi}_{k'b}^{(c)} x_{k'i} + \mathbf{n}_{b,i}^{(c)} \right).
$$

$$(5.24)$$

For each $k \in \mathcal{K}_{\mathcal{B}}(b)$, the estimate of $x_{k,i}$ is given by

$$
\widehat{x}_{k,i} = \mathsf{sign}(\Re\{z_{k,i}\}), \quad i \in \mathcal{M}_{\mathrm{d}}. \tag{5.25}
$$

Two linear detection techniques are examined for symbol $x_{k,i}$, $i \in \mathcal{M}_{\mathrm{d}}$: maximum-ratio combining (MRC) and frequency zero-forcing (ZF) [109]. For MRC detection, vector $\mathbf{a}_{kb}^{(c)} = \widehat{\boldsymbol{\xi}}_{kb}^{(c)}$. On the other hand, for ZF detection, core b partitions the tags in the cell according the their utilized frequency sub-bands and for sub-band $\mathbf{f}^{(c)}$ the following matrix is formed $\mathbf{P}_b^{(c)} = \left[\widehat{\boldsymbol{\xi}}_{l_1 b}^{(c)} \ \widehat{\boldsymbol{\xi}}_{l_2 b}^{(c)} \ \dots \ \widehat{\boldsymbol{\xi}}_{l_{K_{bc}} b}^{(c)} \right]$, where $\mathcal{K}_{\mathcal{B}}(b) \cap \mathcal{K}_{\mathcal{C}}(c) = \{l_1, l_2, \dots l_{K_{bc}}\}$ and $K_{bc} = |\mathcal{K}_{\mathcal{B}}(b) \cap \mathcal{K}_{\mathcal{C}}(c)|$. The final ZF operator is given by $(\mathbf{a}_{kb}^{(c)})^{\mathsf{H}} = \left[(\mathbf{P}_b^{(c)})^{\dagger} \right]_{q,:}$, where the q-th element of set $\mathcal{K}_{\mathcal{B}}(b) \cap \mathcal{K}_{\mathcal{C}}(c)$ satisfies $l_q = k$. Note that ZF detector tries to mitigate the intra-cell interference coming from tags using the same sub-band with tag k since for $N_{\mathrm{R}} \geq K_{bc}$, $(\mathbf{a}_{kb}^{(c)})^{\mathsf{H}} \widehat{\boldsymbol{\xi}}_{k'b}^{(c)} = 0$ for $k' \in (\mathcal{K}_{\mathcal{B}}(b) \cap \mathcal{K}_{\mathcal{C}}(c)) \setminus k$.

Core b treats the channel estimate $\widehat{\boldsymbol{\xi}}_{kb}^{(c)}$ as the true channel, and the part including the last three terms inside parenthesis of (5.24) is considered as interference and noise. Thus, using the independence of zero-mean $\{\boldsymbol{\epsilon}_{kb}^{(c)}\}_{k \in \mathcal{K}_{\mathcal{B}}(b) \cap \mathcal{K}_{\mathcal{C}}(c)}$, $\{x_{k,i}\}_{k \in \mathcal{K}}$, and $\mathbf{n}_{b,i}^{(c)}$, the received signal-to-interference-plus-noise ratio (SINR) for tag $k \in \mathcal{K}_{bmc}$ is given by

$$
\mathrm{SINR}_{kb}^{(c)} = \frac{\left| (\mathbf{a}_{kb}^{(c)})^{\mathsf{H}} \widehat{\boldsymbol{\xi}}_{kb}^{(c)} \right|^2}{I_{kb}^{1(c)} + I_{kb}^{2(c)} + \sigma_b^2 \|\mathbf{a}_{kb}^{(c)}\|_2^2}, \tag{5.26}
$$

where intra-cell ($I_{k,b}^{1(c)}$) and inter-cell ($I_{k,b}^{2(c)}$) interference terms are given, respectively, by

$$I_{kb}^{1(c)} = \sum_{\substack{m' \in \mathcal{M}_{\mathrm{tr}} \\ k' \in \mathcal{K}_{bm'c} \setminus k}} \left| (\mathbf{a}_{kb}^{(c)})^{\mathsf{H}} \widehat{\boldsymbol{\xi}}_{k'b}^{(c)} \right| + \sum_{\substack{m' \in \mathcal{M}_{\mathrm{tr}} \\ k' \in \mathcal{K}_{bm'c}}} (\mathbf{a}_{kb}^{(c)})^{\mathsf{H}} \mathbf{C}_{\boldsymbol{\epsilon}_{k'b}^{(c)}} \mathbf{a}_{kb}^{(c)}, \qquad (5.27)$$

$$I_{kb}^{2(c)} = \sum_{\substack{b' \neq b \\ m' \in \mathcal{M}_{\mathrm{tr}} \\ k' \in \mathcal{K}_{b'm'c}}} (\mathbf{a}_{kb}^{(c)})^{\mathsf{H}} \mathbf{C}_{\boldsymbol{\xi}_{k'b}^{(c)}} \mathbf{a}_{kb}^{(c)}. \qquad (5.28)$$

Note that for $N_{\mathrm{R}} \geq K_{bc}$ and ZF detection the first term in Eq. (5.27) becomes zero. In addition, it is worth-noting that SINR in (5.26) depends on estimated $\widehat{\boldsymbol{\xi}}_{kb}^{(c)}$ as well as on quantities that are known to the core and change very slowly with the time due to the staticness of the cores and the tags.

5.3.2 Measuring the Long-Term SINR

The SINR in (5.26) depends on $\widehat{\boldsymbol{\xi}}_{kb}^{(c)}$ which in turn changes every coherence period. To apply robust frequency allocation an average SINR across many channel and frequency allocation realizations has to be calculated. To this end, a measurement procedure is employed by all cores and tags to obtain long-term SINR information for subsequent frequency allocation.

Each tag is assigned to a fixed preamble sequence across the whole measurement phase, while the channel allocation of each tag changes in a per frame basis. Each frame has time duration equal to the channel coherence time T_{coh}. Let us denote J the total number of frames for the measurement phase, while set $\mathcal{J} \triangleq \{1, 2, \ldots J\}$ denotes the set of all measurement frame indexes. For a core b and a tag $k \in \mathcal{K}_{\mathcal{B}}(b)$, let us denote $\mathcal{J}_{kb}^{(c)}$ the measurements indexes which tag k is assigned to sub-band $\mathbf{f}^{(c)}$. For each tag $k \in \mathcal{K}_{\mathcal{B}}(b)$ core b calculates the received SINR in (5.26) for the frames indexed by set $\mathcal{J}_{kb}^{(c)}$, denoted as $\mathrm{SINR}_{kb}^{(c)}[j]$, forming the set $\left\{ \mathrm{SINR}_{kb}^{(c)}[j] : j \in \mathcal{J}_{kb}^{(c)} \right\}$.

At the end, for each tag $k \in \mathcal{K}_{\mathcal{B}}(b)$, an estimate of average SINR at core b for the c-th sub-band is obtained as

$$\overline{\mathrm{SINR}}_{kb}^{(c)} = \frac{1}{\left| \mathcal{J}_{kb}^{(c)} \right|} \sum_{j \in \mathcal{J}_{kb}^{(c)}} \mathrm{SINR}_{kb}^{(c)}[j]. \qquad (5.29)$$

Note that due to the strong law of large numbers [110, Theorem 6.1], as the number of frames $\left| \mathcal{J}_{kb}^{(c)} \right|$ increases, $\overline{\mathrm{SINR}}_{kb}^{(c)}$ tends to the actual $\mathbb{E}\left[\mathrm{SINR}_{kb}^{(c)} \right]$ for tag $k \in \mathcal{K}_{\mathcal{B}}(b) \cap \mathcal{K}_{\mathcal{C}}(c)$.

5.4　Frequency Allocation Based On Max-Sum Message-Passing

5.4.1　Problem Formulation

After obtaining the average SINR estimates $\overline{\mathtt{SINR}}_{kb}^{(c)}$ for all tuples $\{(k, b, c) \in \mathcal{K} \times \mathcal{B} \times \mathcal{C} : k \in \mathcal{K}_\mathcal{B}(b)\}$ all cores try to obtain frequency sub-channel–tag assignment that maximizes a specific metric involving the estimated received SINRs. Using the average received SINR instead of instantaneous SINR, the impact of random intra- and inter- interference is averaged out, and thus, the optimization problem can be decoupled to B parallel sub-problems across all cores without significant performance loss.

The proposed formulation to obtain the optimal tag–frequency sub-channel association is expressed at each core individually through the following optimization problem

$$\text{maximize} \quad \sum_{k \in \mathcal{K}_\mathcal{B}(b)} \sum_{c \in \mathcal{C}} \mathtt{g}\left(\overline{\mathtt{SINR}}_{kb}^{(c)}\right) \cdot v_{kc} \tag{5.30a}$$

$$\text{subject to} \quad \sum_{k \in \mathcal{K}_{bm}} v_{kc} \leq 1, \ \forall (m, c) \in \mathcal{M}_{\mathrm{tr}} \times \mathcal{C}, \tag{5.30b}$$

$$\sum_{c \in \mathcal{C}} v_{kc} = 1, \ \forall k \in \mathcal{K}_\mathcal{B}(b), \tag{5.30c}$$

$$v_{kc} \in \mathbb{B}, \ \forall (k, c) \in \mathcal{K}_\mathcal{B}(b) \times \mathcal{C}, \tag{5.30d}$$

where $\mathtt{g} : \mathbb{R}^+ \longrightarrow \mathbb{R}$ is an arbitrary increasing function. Resource allocation variables v_{kc} indicate either if tag $k \in \mathcal{K}$ backscatters on the c-th frequency sub-band ($v_{kc} = 1$) or not ($v_{kc} = 0$). Constraint (5.30b) imposes that a frequency sub-band $\mathtt{f}^{(c)}$ can be assigned to at most one tag in $\mathcal{K}_{bm}$, $\forall m \in \mathcal{M}_{\mathrm{tr}}$, For constraint (5.30c), each tag has to be assigned to one frequency sub-channel. From a practical point of view, constraint (5.30b) offers intra-cell pilot interference cancellation by assigning all tags in cell b to a unique pair $(m, c) \in \mathcal{M}_{\mathrm{tr}} \times \mathcal{C}$ of sequence $\mathbf{x}^{(m)}$ and frequency sub-band $\mathtt{f}^{(c)}$, causing orthogonal training transmissions. In doing so, the channel estimate obtained for the tag $k \in \mathcal{K}_{bmc}$ is contaminated only by the tags from other cells that use the same frequency sub-band $\mathtt{f}^{(c)}$ along with the m-th training sequence (i.e., $k \in \bigcup_{b' \neq b} \mathcal{K}_{b'mc}$). It is noted that if $|\mathcal{K}_\mathcal{B}(b)| \leq M_{\mathrm{tr}} \cdot C$, problem (5.30) is feasible.

For set $\mathcal{K}_{\mathcal{B}}(b)$, the corresponding assignment matrix is defined $\mathbf{V}_b \triangleq \{v_{kc} : \forall (k,c) \in \mathcal{K}_{\mathcal{B}}(b) \times \mathcal{C}\}$. The following functions are also defined for all cores $b \in \mathcal{K}_{\mathcal{B}}(b)$:

$$\mathsf{G}(\mathbf{V}_b) \triangleq \sum_{k \in \mathcal{K}_{\mathcal{B}}(b)} \sum_{c \in \mathcal{C}} \mathsf{G}_{kc}(v_{kc}), \tag{5.31}$$

$$\mathsf{G}_{kc}(v_{kc}) \triangleq \mathsf{g}\left(\overline{\mathtt{SINR}}_{kb}^{(c)}\right) \cdot v_{kc}, \tag{5.32}$$

$$\mathsf{p}_{mc}(\{v_{kc}\}_{k \in \mathcal{K}_{bm}}) \triangleq \mathbb{I}\left\{\sum_{k \in \mathcal{K}_{bm}} v_{kc} \le 1\right\}, \; \forall (c,m) \in \mathcal{C} \times \mathcal{M}_{\mathrm{tr}}, \tag{5.33}$$

$$\mathsf{h}_k(\{v_{kc}\}_{c \in \mathcal{C}}) \triangleq \mathbb{I}\left\{\sum_{c \in \mathcal{C}} v_{kc} = 1\right\}, \; \forall k \in \mathcal{K}_{\mathcal{B}}(b), \tag{5.34}$$

where the last two functions (factors) are associated with constraints (5.30b) and (5.30c), respectively; for a statement X, function $\mathbb{I}\{X\}$ is the max-indicator function defined as

$$\mathbb{I}\{X\} \triangleq \begin{cases} 0, & X \text{ is true}, \\ -\infty, & X \text{ is false}. \end{cases} \tag{5.35}$$

The integer programming problem in (5.30) belongs to the class of maximum weighted matching problems [111, 112] that can be solved through Max-Sum algorithm. To this end, the optimization problem in Eq. (5.30) is equivalently expressed as

$$\max_{\mathbf{V}_b \in \mathbb{B}^{|\mathcal{K}_{\mathcal{B}}(b)| \times |\mathcal{C}|}} \left\{ \mathsf{G}(\mathbf{V}_b) + \sum_{\substack{m \in \mathcal{M}_{\mathrm{tr}} \\ c \in \mathcal{C}}} \mathsf{p}_{mc}(\{v_{kc}\}_{k \in \mathcal{K}_{bm}}) + \sum_{k \in \mathcal{K}_{\mathcal{B}}(b)} \mathsf{h}_k(\{v_{kc}\}_{c \in \mathcal{C}}) \right\}. \tag{5.36}$$

The above (unconstrained) maximization problem is equivalent to the constrained problem (5.30) because the constraints in (5.30b) and (5.30c) are imposed through indicator functions $\{\mathsf{p}_{mc}\}_{c \in \mathcal{C}, m \in \mathcal{M}_{\mathrm{tr}}}$ and $\{\mathsf{h}_k\}_{k \in \mathcal{K}_{\mathcal{B}}(b)}$. The problem in (5.36) can be easily transformed to an equivalent factor graph (FG) and can be solved through Max-Sum algorithm.

5.4.2 Factor Graph Construction

A FG expresses factorizations as the one in Eq. (5.36), consisting of factor nodes and variable nodes. Each factor node in the FG is connected through an edge to a variable node if the corresponding factor has input the specific variable. In the optimization problem (5.36) there exist 4 kind of factors:

- factors $\{\mathsf{G}_{kc} : \forall (k,c) \in \mathcal{K}_{\mathcal{B}}(b) \times \mathcal{C}\}$: each of them is connected to the corresponding variable v_{kc},
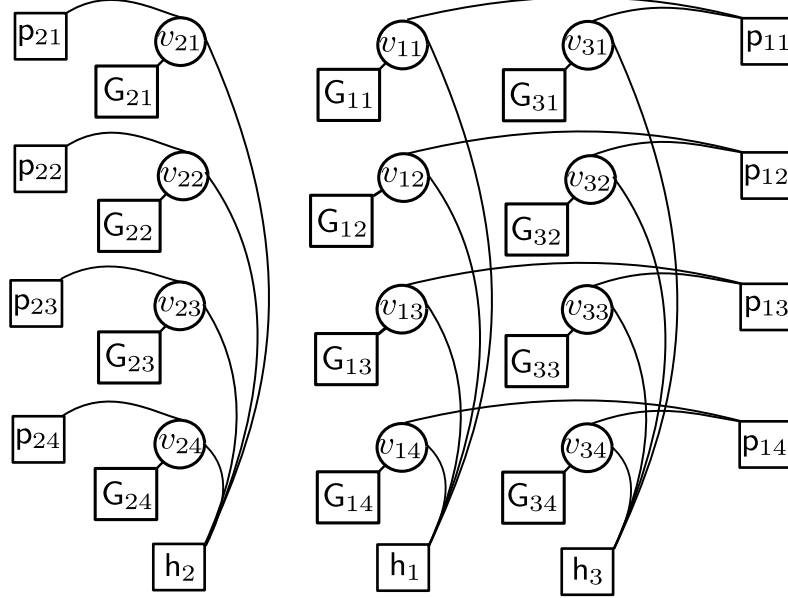
Figure 5.2: A FG instance associated with the first core (i.e., $b = 1$) for the multi-cell BSN of Fig. 5.1 assuming: (a) $C = 4$ frequency channels, (b) $M = 2$ orthogonal sequences of length 2, and (c) $\mathcal{K}_{11} = \{1, 3\}$ and $\mathcal{K}_{12} = \{2\}$, i.e., tags 1 and 3 are assigned to $m = 1$ and tag 2 to $m = 2$.

- factors $\{\mathsf{p}_{mc}\}_{c \in \mathcal{C}, m \in \mathcal{M}_{\mathrm{tr}}}$: each of them is connected to variables $\{v_{kc}\}_{k \in \mathcal{K}_{bm}}$,

- factors $\{\mathsf{h}_k\}_{k \in \mathcal{K}_{\mathcal{B}}(b)}$: each of them is connected to variables $\{v_{kc}\}_{c \in \mathcal{C}}$.

Given the definition of the above factors and the assignment variable matrix $\mathbf{V}_b$, a FG can be constructed for each core $b \in \mathcal{B}$. Each such FG corresponds to the max-sum factorization in (5.36). An example of a FG associated with the BSN of Fig. 5.1 is depicted in Fig. 5.2.

5.4.3   Proposed Algorithm

For a given FG, the standard Max-Sum message-passing rules can be derived to find the optimal configuration for tag–sub-channel association matrix $\mathbf{V}_b$ that maximizes the objective function in (5.30) and satisfies the constraints (5.30b)–(5.30d).

Theorem 5.3. The FG message-passing update rules can be simplified to the following single-variable update rules

$$\phi_{kc}^{(n)} = \max_{c' \in \mathcal{C} \backslash c} \left\{ -\rho_{kc'}^{(n-1)} + \mathsf{g}\left(\overline{\mathtt{SINR}}_{kb}^{(c')}\right) \right\}, \tag{5.37}$$

$$\rho_{kc}^{(n)} = \left[\max_{k' \in \mathcal{K}_{bm} \backslash k} \left\{ -\phi_{k'c}^{(n)} + \mathsf{g}\left(\overline{\mathtt{SINR}}_{k'b}^{(c)}\right) \right\} \right]^+, \quad k \in \mathcal{K}_{bm}, \tag{5.38}$$

where $[x]^+ \triangleq \max\{x, 0\}$. Moreover, to infer the value for variable $v_{kc} \in \mathbb{B}$ at the n-th iteration, the decision rule is

$$\widehat{v}_{kc}^{(n)} = \mathbf{1}\Big\{\phi_{kc}^{(n)} + \rho_{kc}^{(n)} \leq \mathbf{g}\Big(\overline{\mathtt{SINR}}_{kb}^{(c)}\Big)\Big\} = \mathbf{1}\Big\{\chi_{kc}^{(n)} \leq 0\Big\}, \tag{5.39}$$

where any $\chi_{kc}^{(n)} \triangleq \phi_{kc}^{(n)} + \rho_{kc}^{(n)} - \mathbf{g}\Big(\overline{\mathtt{SINR}}_{kb}^{(c)}\Big)$ is the soft-estimate for variable v_{kc} at iteration n.

Proof. The proof is provided in Appendix 5.6. □

Algorithm 3 Max-Sum Algorithm

Input: $\Big\{\overline{\mathtt{SINR}}_{kb}^{(c)} : k \in \mathcal{K}_{\mathcal{B}}(b), c \in \mathcal{C}\Big\}$

1: $n = 0$, $\phi_{kc}^{(0)} = \rho_{kc}^{(0)} = \zeta_{kc}^{(0)} = 0$, $\forall (k,c) \in \mathcal{K}_{\mathcal{B}}(b) \times \mathcal{C}$, $a \in [0,1)$
2: **while** termination criterion is **not** reached **do**
3:      $n := n + 1$
4:      **for** each $(k,c) \in \mathcal{K}_{\mathcal{B}}(b) \times \mathcal{C}$ **do**
5:          $\phi_{kc}^{(n)} = \max\limits_{c' \in \mathcal{C} \backslash c}\Big\{-\rho_{kc'}^{(n-1)} + \mathbf{g}\Big(\overline{\mathtt{SINR}}_{kb}^{(c')}\Big)\Big\}$
6:          $\phi_{kc}^{(n)} := a\phi_{kc}^{(n-1)} + (1-a)\phi_{kc}^{(n)}$
7:      **end for**
8:      **for** each $m \in \mathcal{M}_{\mathrm{tr}}$ and each $(k,c) \in \mathcal{K}_{bm} \times \mathcal{C}$ **do**
9:          $\rho_{kc}^{(n)} = \Big[\max\limits_{k' \in \mathcal{K}_{bm} \backslash k}\Big\{-\phi_{k'c}^{(n)} + \mathbf{g}\Big(\overline{\mathtt{SINR}}_{k'b}^{(c)}\Big)\Big\}\Big]^+$
10:         $\rho_{kc}^{(n)} := a\rho_{kc}^{(n-1)} + (1-a)\rho_{kc}^{(n)}$
11:     **end for**
12:     **for** each $(k,c) \in \mathcal{K}_{\mathcal{B}}(b) \times \mathcal{C}$ **do**
13:         $\chi_{kc}^{(n)} = \phi_{kc}^{(n)} + \rho_{kc}^{(n)} - \mathbf{g}\Big(\overline{\mathtt{SINR}}_{kb}^{(c)}\Big)$
14:         $\widehat{v}_{kc}^{(n)} = \mathbf{1}\Big\{\chi_{kc}^{(n)} \leq 0\Big\}$
15:     **end for**
16: **end while**

Output: $\widehat{\mathbf{V}}_b = \Big\{\widehat{v}_{kc}^{(n)} : \forall (k,c) \in \mathcal{K}_{\mathcal{B}}(b) \times \mathcal{C}\Big\}$

The overall procedure to solve the optimization problem in (5.30) is provided in Algorithm 3. The algorithm is executed for all cores $b \in \mathcal{B}$ in parallel. It can be observed that a damping technique with an extra one-iteration-memory step is employed at lines 6 and 10 of the algorithm. Damping technique is utilized to prevent pathological oscillations [113]. Algorithm 3 terminates either if a maximum number of iterations, $n_{\max}$, is reached, or if the normalized max-absolute error (NMAE) between two consecutive soft-estimates, $\frac{\max_{(k,c)\in\mathcal{K}_{\mathcal{B}}(b)\times\mathcal{C}}\left|\chi_{kc}^{(n)} - \chi_{kc}^{(n-1)}\right|}{\max_{(k,c)\in\mathcal{K}_{\mathcal{B}}(b)\times\mathcal{C}}\left|\chi_{kc}^{(n-1)}\right|}$, is below a prescribed precision ϵ.

5.4.4   Convergence and Complexity Analysis

Note that the underlying FG associated with Eq. (5.36) contains cycles and generally convergence cannot be guaranteed for the FGs with cycles. Fortunately, for the class of the FGs corresponding to weighed matching problems, Max-Sum algorithm always converges to a fixed point which is also the exact solution. Invoking the convergence results derived in [114] for general weighed b-matching problems, it follows that if the optimal solution of linear program (LP) associated with the relaxed version of problem (5.30) is integral (i.e., optimal solution belongs in $\mathbb{B}^{|\mathcal{K}_{\mathcal{B}}(b)| \times |\mathcal{C}|}$) and unique, then Max-Sum algorithm converges to the exact solution after $\mathcal{O}(C\,|\mathcal{K}_{\mathcal{B}}(b)|)$ iterations.

Regarding per iteration computational cost of the proposed algorithm, it is not difficult to see that lines (4)–(7), (8)–(11), and (12)–(15) require $\mathcal{O}(C^2|\mathcal{K}_{\mathcal{B}}(b)|)$, $\mathcal{O}(C\,|\mathcal{K}_{\mathcal{B}}(b)|^2)$, and $\mathcal{O}(C\,|\mathcal{K}_{\mathcal{B}}(b)|)$ arithmetic operations, respectively. Thus, the overall per iteration complexity is dominated by lines (4)-(11). The algorithm iterates at most $n_{\max}$ times, and thus, the overall computation cost of Algorithm 3 becomes $\mathcal{O}(n_{\max}\,(C\,|\mathcal{K}_{\mathcal{B}}(b)|^2 + C^2|\mathcal{K}_{\mathcal{B}}(b)|))$. From simulation results it is noticed that 5 to 10 iterations usually suffice for the algorithm to converge to the desired solution for all studied setups.

The problem in (5.30) can be transformed to a LP, where constraint (5.30d) is relaxed to $v_{kc} \in [0,1], \forall (k,c) \in \mathcal{K}_{\mathcal{B}}(b) \times \mathcal{C}$. The relaxed LP problem can be solved through standard convex optimization interior point methods [115]. However, we choose to solve (5.30) with Max-Sum message-passing framework due to its low per-iteration cost and its fast convergence rate, observed through simulations. Simulation results also demonstrated that the proposed Max-Sum algorithm could offer the same optimal solution with classic interior point solvers requiring smaller execution time.

5.5   Simulation Results

The multi-cell BSN topology of Fig. 5.3 is studied, consisting of $B = 21$ cores and $K = 500$ tags. Cores (blue squares) are placed in a cellular setting [27] and the distance of neighboring cores is $\sqrt{3}R_{\text{core}}$, where $R_{\text{core}} = 10$ meters. The height of all cores (i.e., their z coordinate) is 2 meters. Tags (yellow circles) are placed randomly in the vicinity of cores. Their height is a uniform random variable in $[0,1]$.

The adopted path-loss model is given by [27]

$$\sigma_{bk}^2 = \sigma_{kb}^2 = \left(\frac{d_0}{\mathsf{d}_{bk}}\right)^{\nu_{bk}} \left(\frac{\lambda}{4\pi d_0}\right)^2, \tag{5.40}$$
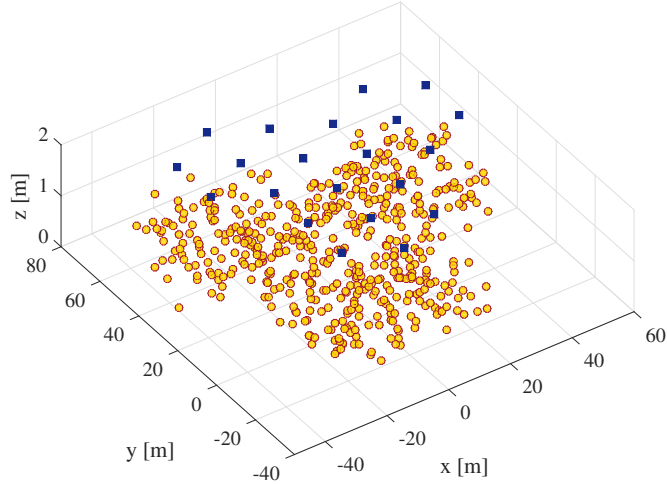
Figure 5.3: Studied multi-cell BSN with $B = 21$ cores and $K = 500$ tags.

Table 5.1: Wireless Channel parameters.

Parameters	Values
Carrier wavelength	$\lambda \approx 0.3456$ m
Noise figure	$\mathrm{NF}_b = 4$ dB, $\forall b \in \mathcal{B}$
Noise energy	$\sigma_b^2 = -174 + \mathrm{NF}_b$ dBm/Hz
Reference distance	$d_0 = 1$ m
Path-loss exponent	$\nu_{bk} = 2.1, \ \forall b \in \mathcal{B}, \ \forall k \in \mathcal{K}_\mathcal{B}(b)$
Rician parameters	$\kappa_{kb}^{\mathrm{u}} = \kappa_{bk}^{\mathrm{d}} = 10$ dB, $\forall b \in \mathcal{B}, \ \forall k \in \mathcal{K}_\mathcal{B}(b)$

where ν_{bk} is the path-loss exponent for link (b, k) (same for (k, b)), d_{bk} is the distance from core b to tag k, while d_0 is a reference distance. All considered wireless and noise parameters are shown in Table 5.1. For simplicity, common backscatter reflection coefficients are considered for all tags $k \in \mathcal{K}$, with $\Gamma_{k,0} = 0.92$ and $\Gamma_{k,1} = -0.91$. The tag scattering efficiency is assumed common for all tags, given by $\eta_k = 20\%$, $\forall k \in \mathcal{K}$. The random phase mismatch at each core $b \in \mathcal{B}$ is assumed zero, i.e., $\phi_b = 0$. The transmission power of each core is the same, i.e., $P_b = P_{\mathrm{tx}}$, $\forall b \in \mathcal{B}$. AoA $\varphi_{bk}^{\mathrm{d}}$ and AoD $\varphi_{kb}^{\mathrm{u}}$ are considered fixed and known for any pair $(k, b) \in \mathcal{K} \times \mathcal{B}$. The BSN has $C = 15$ available frequency sub-channels and $M = 8$ orthogonal training sequences. Each sub-channel is given by $\mathsf{f}^{(c)} = \frac{2c}{T}$, with $T = 0.1$ msec. Finally, set $\mathcal{X}_M$ comprises of the columns of the $M \times M$ Hadamard matrix [116].
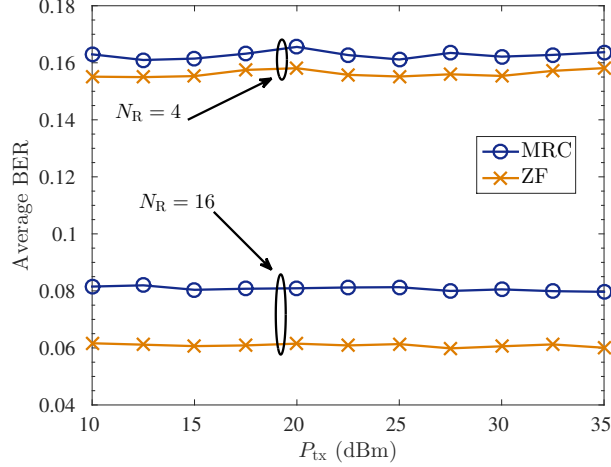
Figure 5.4: Average BER vs P_{tx} for different values of N_R for MRC and ZF linear detection.

5.5.1   Average BER

In the first scenario we compare ZF and MRC multi-tag linear detectors in terms of their bit error rate (BER). The corresponding average BER performance across all tags is

$$\frac{1}{K} \sum_{k \in \mathcal{K}} \mathbb{P}(\widehat{x}_{k,i} \neq x_{k,i}). \tag{5.41}$$

The average BER performance is tested as a function of both transmission power and the number of receive antennas, assuming $N_T = 1$ transmit antennas. For channel estimation phase, tags within the same cell employ unique pairs $(m, c) \in \mathcal{M}_{tr} \times \mathcal{C}$ (orthogonal transmissions).

Fig. 5.4 studies the average BER performance in Eq. (5.41) of MRC and ZF detectors as a function of transmission power P_{tx} under different receive antennas setups. It can be observed that increasing the transmission power does not reduce the average BER performance. This stems from the fact that both useful signal power as well as interference depend linearly on transmission power (cf. Eq. (5.26)) and thus there is a saturation effect on total received SINR.

Fig. 5.5 depicts the BER performance as a function of N_R for $P_{tx} = 15$ dBm. In contrast to transmission power, as can be seen in Fig. 5.5, the impact of receive antennas is significant in average BER performance for multi-tag system. It is observed that increasing the number of receive antennas offers diversity gains for both linear detectors, diminishing the average BER. The performance of ZF is slightly better compared to MRC because the former mitigates the interference coming from tags sharing the same frequency sub-band in the same cell, i.e., intra-cell interference.
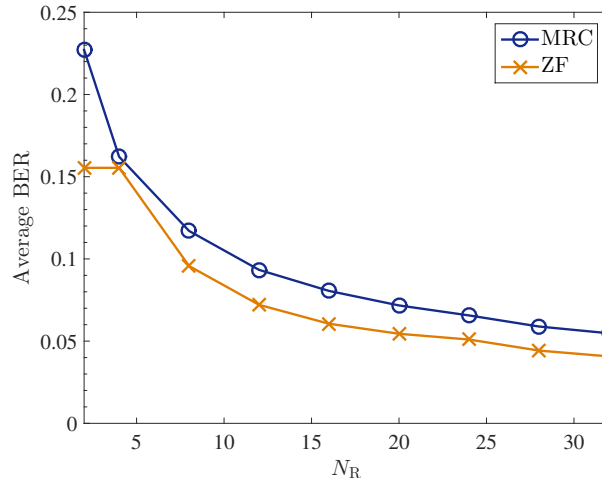
Figure 5.5: Average BER vs N_R for MRC and ZF linear detection.

5.5.2 Average Outage Probability

Next, we study the impact of orthogonal versus nonorthogonal pilot transmission on average outage performance. When a tag $k \in \mathcal{K}_\mathcal{B}(b)$ backscatters at frequency sub-band $\mathbf{f}^{(c)}$, an outage event occurs if $\mathbb{P}\big(\mathrm{SINR}_{kb}^{(c)} \leq \theta\big)$, with $\mathrm{SINR}_{kb}^{(c)}$ defined in Eq. (5.26) and θ an outage threshold. Assuming fixed training sequence assignment, we compare the average outage performance

$$\frac{1}{K} \sum_{b \in \mathcal{B}} \sum_{k \in \mathcal{K}_\mathcal{B}(b)} \sum_{c \in \mathcal{C}} v_{kc} \cdot \mathbb{P}\big(\mathrm{SINR}_{kb}^{(c)} \leq \theta\big) \tag{5.42}$$

of random training transmissions versus the proposed orthogonal transmissions. In the former each tag chooses completely random sub-channels. In (5.42), $\{v_{kc}\}_{(k,c) \in \mathcal{K} \times \mathcal{C}}$ are the tag–frequency sub-channel allocation variables.

Using $N_\mathrm{T} = 2$, $N_\mathrm{R} = 8$, and $P_\mathrm{tx} = 30$ dBm, Fig. 5.6 illustrates the average outage performance of (5.42) as a function of outage threshold θ comparing ZF vs MRC linear detection as well as random vs orthogonal training transmissions. It can be seen that outage events are more frequent for MRC detection, stemming directly from the fact that MRC allows intra-cell interference, while ZF eliminates it. Orthogonal training transmissions reduce the intra-cell interference on channel estimate and thus outperform nonorthogonal training transmissions.

5.5.3 Performance of Max-Sum Algorithm

Using the same parameters as in previous paragraph, $J = 5000$ SINR measurements are obtained to estimate the average (long-term) SINR according to Eq. (5.29). The proposed
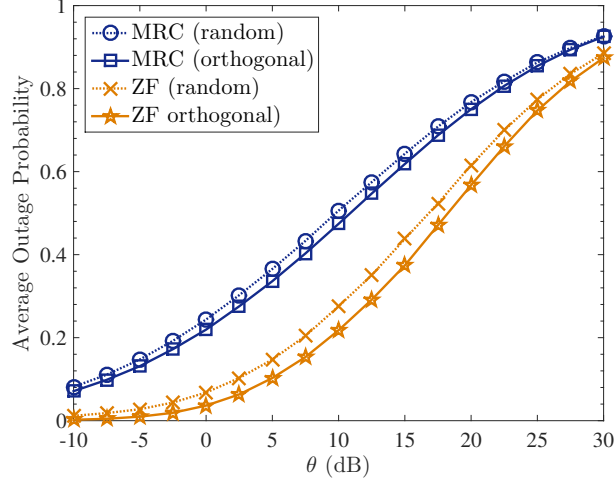
Figure 5.6: Average outage probability as a function of outage threshold θ for linear detection schemes using both nonorthogonal and orthogonal training transmissions.
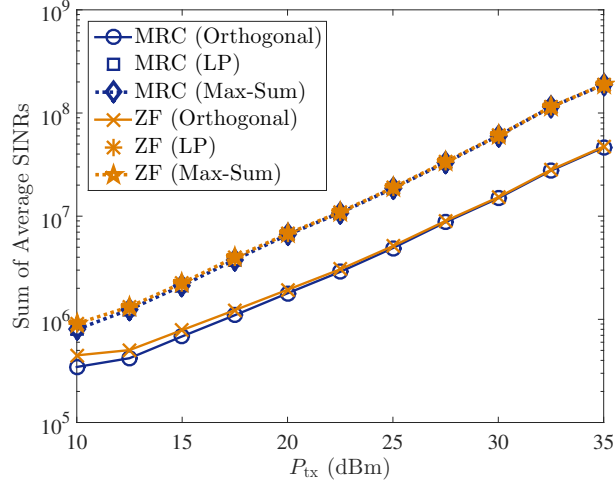

Figure 5.7: Sum of SINRs for the Max-Sum algorithm, LP, and orthogonal channel allocation.

algorithm is executed to obtain the optimal assignment of variables $\{v_{kc}\}_{(k,c)\in\mathcal{K}\times\mathcal{C}}$, using parameters $\mathsf{g}(x) = x$, $x \geq 0$, $n_{\max} = 50$, $\alpha = 0.1$, and $\epsilon = 10^{-4}$. The specific value for the objective tries to maximize the sum of average SINRs, although other metrics could be employed.

Fig. 5.7 compares the sum of average SINR performance across all tags as a function of transmission power. As expected, for both ZF and MRC, the proposed Max-Sum algorithm offers the same optimal performance with relaxed LP technique and both outperform orthogonal training transmissions for which tags of the same cell use unique pairs $(m, c) \in \mathcal{M}_{\mathrm{tr}} \times \mathcal{C}$, i.e., an orthogonal tag–sub-channel assignment is a feasible assignment in optimization problem (5.30). The results for orthogonal tag–sub-channel assignments
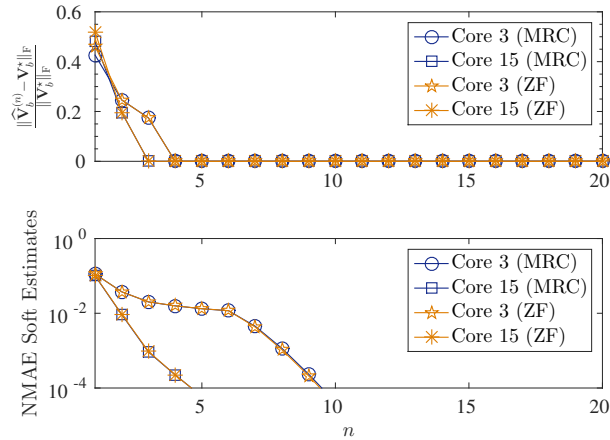
Figure 5.8: Convergence rate and NMAE of soft-estimates for the Max-Sum algorithm executed at cores 3 and 15.

Table 5.2: Average Execution Time in Seconds.

	MRC		ZF	
	Max-Sum	LP	Max-Sum	LP
$K = 500$	**0.0968**	0.6350	**0.0982**	0.6331
$K = 750$	**0.1304**	0.6934	**0.1357**	0.6945
$K = 1000$	**0.2175**	0.7445	**0.2215**	0.7266

have been averaged over 1000 Monte Carlo experiments. It can be remarked that the gap between ZF and MRC is negligible. This performance gap among the optimal assignment (Max-Sum and relaxed LP) and a feasible assignment (orthogonal transmissions) tends to slightly increase as the transmission power increases.

Fig. 5.8 shows how fast the proposed algorithm converges to the optimal $\mathbf{V}_b^\star$ and how many iterations are required until termination criterion is reached for cores 3 and 15. Only 3-4 iterations of the proposed algorithm are required for convergence to the optimal solution for both MRC and ZF linear detectors. For all cores the algorithm terminated after 10-15 iterations on the average, and for all cases the termination criterion of NMAE in soft estimates below ϵ was met. The above demonstrates the potential benefits of the proposed Max-Sum algorithm, since per iteration complexity is small and convergence is accomplished within few steps.

Finally, one important question would be why one should use the proposed algorithm instead of classic LP to solve the studied optimization problem in (5.30). To this end, the proposed algorithm was compared with CVX convex optimization solver [117] in terms of average execution time across all cores. For the simulations, MATLAB R2016a was used on a desktop computer with 32-bit operating system and Intel(R) Core(TM)2 Quad CPU

at 2.83 GHz. The proposed algorithm was implemented with a custom MATLAB script, while the solution of LP relaxed problem was obtained by CVX solver. Table 5.2 shows the execution time of the proposed Max-Sum algorithm and LP program solved with CVX solver under different number of tags scenarios. It is worth noting for $K = 1000$ tags the average execution time across all cores for the proposed algorithm is 0.2-0.22 secs, while for LP requires 0.7-0.75 secs.

5.6   Appendix: Proofs of Chapter 5

Proof of Theorem 5.1

The proof relies on the following trigonometric identities:

$$\cos(\alpha)\cos(\beta) = \frac{1}{2}\left(\cos(\alpha+\beta) + \cos(\alpha-\beta)\right) \tag{5.43}$$

$$\int_0^T \cos(2\pi x t + \gamma)\mathrm{d}t = \begin{cases} \cos(\gamma)\,T, & \text{if } x = 0, \\ 0, & \text{if } x = \frac{l}{T},\ l \in \mathbb{N}. \end{cases} \tag{5.44}$$

The signal in Eq. (5.16) consists of time delayed cosine terms which any of them is time limited in one of the following intervals: $[0,T)$, $[T, 2T)$, $\ldots$, $[(M-1)T, MT)$. For the i-th interval, $[(i-1)T, iT)$, we define C functions given by

$$\mathsf{s}_i^{(c)}(t) \triangleq \frac{\cos\left(2\pi\mathsf{f}^{(c)}\left(t - (i-1)T\right)\right)\Pi_T(t - (i-1)T)}{\sqrt{\frac{T}{2}}}, \tag{5.45}$$

for all $c \in \mathcal{C}$. Doing the same for all intervals $[(i-1)T, iT)$, $i = 1, 2, \ldots, M$, total $M \cdot C$ functions are obtained. The following set of functions $\mathcal{S}_{\mathcal{C}}(M) \triangleq \left\{\left\{\mathsf{s}_i^{(c)}(t)\right\}_{c\in\mathcal{C}}\right\}_{i=1}^{M}$ is formed. For any pair in $\mathcal{S}_{\mathcal{C}}(M)$ the following holds

$$\left\langle \mathsf{s}_i^{(c)}(t), \mathsf{s}_j^{(c')}(t) \right\rangle \overset{(a)}{=} \begin{cases} \frac{2}{T}\int_0^T \cos\left(2\pi\mathsf{f}^{(c)}t\right)\cos\left(2\pi\mathsf{f}^{(c')}t\right)\mathrm{d}t, & \text{if } i = j, \\ 0, & \text{if } i \neq j, \end{cases} \tag{5.46a}$$

$$\overset{(b)}{=} \begin{cases} 1 & \text{if } i = j \text{ and } c' = c, \\ 0, & \text{otherwise,} \end{cases} \tag{5.46b}$$

where in (a) the orthogonality of functions across disjoint time intervals $[(i-1)T, iT)$ and $[(j-1)T, jT)$ for $i \neq j$ is exploited and we used change of variables $t' = t - (i-1)T$ for $i = j$, while in (b), we used Eqs. (5.43) and (5.44) with $\alpha = 2\pi\mathsf{f}^{(c)}t$, $\beta = 2\pi\mathsf{f}^{(c')}t$,

and $\gamma = 0$ along with identity (5.44) using the assumption that each sub-band satisfies $\mathtt{f}^{(c)} = \frac{l_c}{T}$, for some $l_c \in \mathbb{N}$ (cf. Eq. (5.12)). Thus, set $\mathcal{S}_\mathcal{C}(M)$ constitutes an orthonormal basis for $M \cdot C$-dimensional subspace of time-limited functions within $[0, MT)$. That set can be used for expansion of the signal in Eq. (5.16), i.e., for each user k

$$\sqrt{\frac{2}{T}} \int_0^T \cos(2\pi f_k t + \Phi_{kb}) \cos\left(2\pi \mathtt{f}^{(c)} t\right) \mathrm{d}t \overset{(a)}{=} \begin{cases} \cos(\Phi_{kb}) \sqrt{\frac{T}{2}}, & \text{if } k \in \mathcal{K}_\mathcal{C}(c), \\ 0, & \text{if } k \notin \mathcal{K}_\mathcal{C}(c). \end{cases} \tag{5.47}$$

where in (a) we used: (i) Eq. (5.43) with $\alpha = 2\pi f_k t + \Phi_{kb}$, $\beta = 2\pi \mathtt{f}^{(c)} t$, and $\gamma = \Phi_{kb}$, and (ii) Eq. (5.44) combined with the facts: (b1) for any two $c, c' \in \mathcal{C}$, $\mathtt{f}^{(c')} + \mathtt{f}^{(c)} = \frac{l}{T}$, for some $l \in \mathbb{N}$, and (b2) $k \notin \mathcal{K}_\mathcal{C}(c) \implies f_k - \mathtt{f}^{(c)} = \frac{l}{T}$, for some $l \in \mathbb{N}$, whereas $k \in \mathcal{K}_\mathcal{C}(c) \implies f_k - \mathtt{f}^{(c)} = 0$.

For optimal demodulation, core b projects the DC-blocked received signal $\mathbf{y}_b(t)$ in Eq. (5.16) onto basis $\mathcal{S}_\mathcal{C}(M)$, offering vector coefficients

$$\mathbf{r}_{b,i}^{(c)} \triangleq \left\langle \mathbf{y}_b(t), \mathsf{s}_i^{(c)}(t) \right\rangle \overset{(a)}{=} \sum_{k \in \mathcal{K}_\mathcal{C}(c)} \mathbf{g}_{kb} \sqrt{\frac{T}{2}} \cos(\Phi_{kb}) \, x_{k,i} + \mathbf{n}_{b,i}^{(c)}, \tag{5.48}$$

where in (a), we used Eq. (5.47) and we abbreviated $\mathbf{n}_{b,i}^{(c)} = \left\langle \mathbf{w}_b(t), \mathsf{s}_i^{(c)}(t) \right\rangle$. The noise components $\mathbf{n}_{b,i}^{(c)}$ satisfy

$$\begin{aligned} \mathbb{E}\left[\mathbf{n}_{b,i}^{(c)} \, (\mathbf{n}_{b,j}^{(c')})^\mathsf{H}\right] &\overset{(a)}{=} \int_\mathbb{R} \int_\mathbb{R} \mathbb{E}\left[\mathbf{w}_b(t) \, \mathbf{w}_b(t')^\mathsf{H}\right] \mathsf{s}_i^{(c)}(t) \, \mathsf{s}_j^{(c')}(t') \, \mathrm{d}t \, \mathrm{d}t' \\ &\overset{(b)}{=} \int_\mathbb{R} \left(\int_\mathbb{R} \mathbf{C}_{\mathsf{w}_b}(t - t') \, \mathsf{s}_j^{(c')}(t') \, \mathrm{d}t'\right) \mathsf{s}_i^{(c)}(t) \, \mathrm{d}t \\ &\overset{(c)}{=} \int_\mathbb{R} \mathcal{F}^{-1}\left\{N_0 \, \mathbb{1}\{|F| \le W_b\} \, \mathbf{I}_{N_\mathrm{R}} \, \mathsf{S}_j^{(c')}(F)\right\} \mathsf{s}_i^{(c)}(t) \, \mathrm{d}t \\ &\overset{(d)}{\approx} N_0 \, \mathbf{I}_{N_\mathrm{R}} \int_\mathbb{R} \mathcal{F}^{-1}\left\{\mathsf{S}_j^{(c')}(F)\right\} \mathsf{s}_i^{(c)}(t) \, \mathrm{d}t \overset{(e)}{=} N_0 \, \mathbf{I}_{N_\mathrm{R}} \left\langle \mathsf{s}_i^{(c)}(t), \mathsf{s}_j^{(c')}(t) \right\rangle, \end{aligned} \tag{5.49}$$

where in (a), Fubini theorem [61] is employed along with the linearity of expectation. Equality (b) follows from the definition of the autocorrelation matrix function of complex white Gaussian noise process $\mathbf{w}_b(t)$, $\mathbf{C}_{\mathsf{w}_b}(t - t') = \mathbb{E}\left[\mathbf{w}_b(t) \, \mathbf{w}_b(t')^\mathsf{H}\right]$, which stems from the fact that the noise process is also wide-sense stationary [80, Chapter 2.7]. In (c), we use: (i) the definition of convolution operation given by the inverse Fourier transform (abbreviated $\mathcal{F}^{-1}\{\cdot\}$) of the product of the two functions involved in their Fourier domain, (ii) the definition of power spectral density of process $\mathbf{w}_b(t)$ in Eq. (5.14), and (iii) the Fourier transform of $\mathsf{s}_j^{(c')}(t')$, $\mathsf{S}_j^{(c')}(F) = \mathcal{F}\left\{\mathsf{s}_j^{(c')}(t')\right\}$. In (d), we use that $\mathsf{S}_j^{(c')}(F)$ can be approximated as a band-limited function in $[-W_b, W_b]$ frequency band, since we have

assumed that $W_b \gg \frac{1}{T}$, whereas, in (e), $\mathsf{s}_j^{(c')}(t) = \mathcal{F}^{-1}\{\mathsf{S}_j^{(c')}(F)\}$ is used. Thus, in view of (5.49), the projection of $\mathbf{w}_b(t)$ on basis $\mathcal{S}_\mathcal{C}(M)$ offers IID circularly symmetric Gaussian vectors $\left\{ \mathbf{n}_{b,i}^{(c)} \; : \; c \in \mathcal{C}, \; i = 1, 2, \ldots, M \right\}$ with covariance matrix $N_0 \, \mathbf{I}_{N_\mathrm{R}}$. Eqs (5.48) and (5.49) complete the proof.

Proof of Proposition 5.1

The proof for mean value is relying on the following identity

$$\mathbb{E}[\cos(a + \Phi_{kb})] = 0, \quad \forall a \in \mathbb{R}, \tag{5.50}$$

which in turn stems from the fact that $\Phi_{kb} \sim \mathcal{U}[0, 2\pi)$. Thus, $\mathbb{E}[\boldsymbol{\xi}_{kb}^{(c)}] = \sqrt{\frac{T}{2}} \, \mathbb{E}[\mathbf{g}_{kb}] \, \mathbb{E}[\cos(\Phi_{kb})] = \mathbf{0}_{N_\mathrm{R}}$.

For the calculation of the covariance, it is noted that RV $a_k = \sum_{b'=1}^B \sqrt{\frac{P_{b'}}{N_\mathrm{T}}} \, \mathsf{e}^{\mathsf{j}\phi_{b'}} \left(\mathbf{h}_{b'k}^\mathrm{d}\right)^\top \mathbf{1}_{N_\mathrm{T}}$ is a proper complex Gaussian RV with expected value

$$\mathbb{E}[a_k] = \sum_{b'=1}^B \sqrt{\frac{P_{b'} \, \kappa_{b'k}^\mathrm{d} \, \sigma_{b'k}^2}{N_\mathrm{T}(\kappa_{b'k}^\mathrm{d} + 1)}} \, \mathsf{e}^{\mathsf{j}\phi_{b'}} (\mathbf{e}_{b'k}^\mathrm{d})^\top \mathbf{1}_{N_\mathrm{T}} \tag{5.51}$$

and variance

$$\mathsf{var}[a_k] = \sum_{b'=1}^B \frac{P_{b'} \, \sigma_{b'k}^2}{\kappa_{b'k}^\mathrm{d} + 1}. \tag{5.52}$$

Thus, the power of RV a_k is $\mathbb{E}[|a_k|^2] = \mathsf{var}[a_k] + |\mathbb{E}[a_k]|^2$. With similar reasoning it follows that

$$\mathbb{E}\left[\mathbf{h}_{kb}^\mathrm{u}(\mathbf{h}_{kb}^\mathrm{u})^\mathsf{H}\right] = \frac{\sigma_{kb}^2}{\kappa_{kb}^\mathrm{u} + 1} \left(\mathbf{I}_{N_\mathrm{R}} + \kappa_{kb}^\mathrm{u} \, \mathbf{e}_{kb}^\mathrm{u}(\mathbf{e}_{kb}^\mathrm{u})^\mathsf{H}\right). \tag{5.53}$$

Finally, it is not difficult to see that

$$\mathbb{E}[\cos^2(\Phi_{kb})] = \frac{1 + \mathbb{E}[\cos(2\Phi_{kb})]}{2} \overset{(5.50)}{=} \frac{1}{2}. \tag{5.54}$$

Since $\boldsymbol{\xi}_{kb}^{(c)}$ is zero-mean vector, its covariance is given by

$$\mathbb{E}\left[\boldsymbol{\xi}_{kb}^{(c)}(\boldsymbol{\xi}_{kb}^{(c)})^\mathsf{H}\right] = \frac{T}{2} \, \mathbb{E}[\mathbf{g}_{kb}\mathbf{g}_{kb}^\mathsf{H}] \, \mathbb{E}[\cos^2(\Phi_{kb})], \tag{5.55}$$

thus, using the above equations in conjunction with Eq. (5.15), the result in Eq. (5.20) follows after elementary algebra.

Proof of Theorem 5.3

Applying the framework of [107, 118] for the proposed FG, we derive the Max-Sum message-passing update rules. Let us denote $\mathsf{m}^{(n)}_{mc\to kc}(v_{kc})$ and $\mathsf{m}^{(n)}_{k\to kc}(v_{kc})$ $(\mathsf{m}^{(n)}_{kc\to mc}(v_{kc})$ and $\mathsf{m}^{(n)}_{kc\to k}(v_{kc}))$ the messages from factors p_{mc} and h_k to variable v_{kc} at iteration n, respectively (and vice versa). The standard Max-Sum update rules are

$$\mathsf{m}^{(n)}_{k\to kc}(x) = \max_{\substack{\{v_{kc'}\}_{c'\in\mathcal{C}\backslash c}\\ v_{kc}=x}} \left\{\mathsf{h}_k(\{v_{kc'}\}_{c'\in\mathcal{C}}) + \sum_{c'\in\mathcal{C}\backslash c} \mathsf{m}^{(n-1)}_{kc'\to k}(v_{kc'})\right\}, \tag{5.56}$$

$$\mathsf{m}^{(n)}_{kc\to mc}(x) = \mathsf{G}_{kc}(x) + \mathsf{m}^{(n)}_{k\to kc}(x), \tag{5.57}$$

$$\mathsf{m}^{(n)}_{mc\to kc}(x) = \max_{\substack{\{v_{k'c}\}_{k'\in\mathcal{K}_{bm}\backslash k}\\ v_{kc}=x}} \left\{\mathsf{p}_c(\{v_{k'c}\}_{k'\in\mathcal{K}_{bm}}) + \sum_{k'\in\mathcal{K}_{bm}\backslash k} \mathsf{m}^{(n)}_{k'c\to mc}(v_{k'c})\right\}, \tag{5.58}$$

$$\mathsf{m}^{(n)}_{kc\to k}(x) = \mathsf{G}_{kc}(x) + \mathsf{m}^{(n)}_{mc\to kc}(x), \tag{5.59}$$

$\forall k \in \mathcal{K}_{bm}$, $\forall (m,c) \in \mathcal{M}_{\mathrm{tr}} \times \mathcal{C}$, and for any message, $x \in \mathbb{B}$. The optimal marginal rule [118] to obtain an estimate for variable v_{kc}, $k \in \mathcal{K}_{bm}$, at the n-th iteration is given by

$$\hat{v}^{(n)}_{kc} = \arg\max_{x\in\mathbb{B}}\left\{\mathsf{m}^{(n)}_{k\to kc}(x) + \mathsf{m}^{(n)}_{mc\to kc}(x) + \mathsf{G}_{kc}(x)\right\}, \tag{5.60}$$

$\forall k \in \mathcal{K}_{bm}$, $\forall (m,c) \in \mathcal{M}_{\mathrm{tr}} \times \mathcal{C}$.

Applying the definition of max-indicator factors h_k (p_{mc}), which impose that exactly (at most) one of their input variables should be 1 and the rest 0, the maximizations in Eqs. (5.56) and (5.58) are feasible only when exactly (at most) one input message is for decision "1" and the rest are for "0". In other words, the update rules for factor nodes in Eqs. (5.56) and (5.58) can be simplified as

$$\mathsf{m}^{(n)}_{k\to kc}(0) = \max_{c'\in\mathcal{C}\backslash c}\left\{\mathsf{m}^{(n-1)}_{kc'\to k}(1) + \sum_{c''\in\mathcal{C}\backslash\{c,c'\}} \mathsf{m}^{(n-1)}_{kc''\to k}(0)\right\}, \tag{5.61}$$

$$\mathsf{m}^{(n)}_{k\to kc}(1) = \sum_{c'\in\mathcal{C}\backslash c} \mathsf{m}^{(n-1)}_{kc'\to k}(0), \tag{5.62}$$

$$\mathsf{m}^{(n)}_{mc\to kc}(0) = \max\left\{\sum_{k'\in\mathcal{K}_{bm}\backslash k} \mathsf{m}^{(n)}_{k'c\to mc}(0), \max_{k'\in\mathcal{K}_{bm}\backslash k}\left\{\mathsf{m}^{(n)}_{k'c\to mc}(1) + \sum_{k''\in\mathcal{K}_{bm}\backslash\{k,k'\}} \mathsf{m}^{(n)}_{k''c\to mc}(0)\right\}\right\}, \tag{5.63}$$

$$\mathsf{m}^{(n)}_{mc\to kc}(1) = \sum_{k'\in\mathcal{K}_{bm}\backslash k} \mathsf{m}^{(n)}_{k'c\to mc}(0). \tag{5.64}$$

Since all FG messages take two values, they can be re-parameterized as a single message through

$$\phi_{kc}^{(n)} \triangleq \mathsf{m}_{k \to kc}^{(n)}(0) - \mathsf{m}_{k \to kc}^{(n)}(1), \tag{5.65}$$

$$\rho_{kc}^{(n)} \triangleq \mathsf{m}_{mc \to kc}^{(n)}(0) - \mathsf{m}_{mc \to kc}^{(n)}(1), \quad k \in \mathcal{K}_{bm}, \tag{5.66}$$

Plugging Eqs. (5.61) and (5.62) into (5.65), the common term $\sum_{c'' \in \mathcal{C} \backslash \{c,c'\}} \mathsf{m}_{kc'' \to k}^{(n-1)}(0)$ cancels out, and thus,

$$\phi_{kc}^{(n)} = \max_{c' \in \mathcal{C} \backslash c} \left\{ \mathsf{m}_{kc' \to k}^{(n-1)}(1) - \mathsf{m}_{kc' \to k}^{(n-1)}(0) \right\}$$

$$\stackrel{(5.59)}{=} \max_{c' \in \mathcal{C} \backslash c} \left\{ -\rho_{kc'}^{(n-1)} + \mathsf{g}\left(\overline{\mathtt{SINR}}_{kb}^{(c')} \right) \right\}, \tag{5.67}$$

Using similar reasoning as above and plugging Eqs. (5.63) and (5.64) in (5.66), it follows that for $k \in \mathcal{K}_{bm}$

$$\rho_{kc}^{(n)} = \max \left\{ \max_{k' \in \mathcal{K}_{bm} \backslash k} \left\{ \mathsf{m}_{k'c \to mc}^{(n)}(1) - \mathsf{m}_{k'c \to mc}^{(n)}(0) \right\}, 0 \right\}$$

$$\stackrel{(5.57)}{=} \left[\max_{k' \in \mathcal{K}_{bm} \backslash k} \left\{ -\phi_{k'c}^{(n)} + \mathsf{g}\left(\overline{\mathtt{SINR}}_{k'b}^{(c)} \right) \right\} \right]^+, \tag{5.68}$$

where $[x]^+ \triangleq \max\{x, 0\}$. Note that the variable decision rule in Eq. (5.60) for $k \in \mathcal{K}_{bm}$ can be written as

$$\widehat{v}_{kc}^{(n)} = \mathbf{1} \left\{ \mathsf{m}_{k \to kc}^{(n)}(1) + \mathsf{m}_{mc \to kc}^{(n)}(1) + \mathsf{g}\left(\overline{\mathtt{SINR}}_{kb}^{(c)} \right) \geq \mathsf{m}_{k \to kc}^{(n)}(0) + \mathsf{m}_{mc \to kc}^{(n)}(0) \right\}$$

$$\stackrel{(a)}{=} \mathbf{1} \{ \chi_{kb}^{(n)} \leq 0 \}, \tag{5.69}$$

where in (a), soft variable estimates $\chi_{kb}^{(n)} \triangleq \phi_{kc}^{(n)} + \rho_{kc}^{(n)} - \mathsf{g}\left(\overline{\mathtt{SINR}}_{kb}^{(c)} \right)$ are defined and Eqs. (5.65)–(5.66) are also exploited.

Chapter 6

Conclusion

Internet-of-Things (IoT) is expected to play a prominent role for ubiquitous sensing anywhere and anytime. Plethora of IoT applications at the near future will affect and interact with billions of humans offering significant socio-economical impact.

The outcomes of this dissertation constitute a significant step towards the improvement of ultra-low-power IoT from the points-of-view listed in detail below.

An in-depth analytical framework to deduce accurate fundamental performance bounds for nonlinear RF energy harvesting in ultra-low-power IoT is offered. Specifically, for the first time in the RF energy harvesting literature, realistic efficiency models are studied accounting for the sensitivity, nonlinearity, and saturation of the RF harvesting circuits. A piece-wise linear approximation model is proposed, offering closed-form expression and tuning-free modeling. Two real RF harvesting efficiency models from RF harvesting circuits prior art are evaluated and contrasted with the proposed analytical model and the RF harvesting models from prior art. It is demonstrated that the proposed approximation model is in complete agreement with reality and more importantly, the simple, linear RF harvesting modeling results deviate from reality.

An analytical point-to-point scatter radio signal model is presented accounting for tag-related, microwave, and realistic wireless channel parameters. Novel, low-complexity noncoherent and coherent detection and decoding reception algorithms are designed for frequency-shift keying (FSK) at tags taking into account the idiosyncrasies of scatter radio model. The proposed algorithms are ideal for short packet communication. A detailed simulation study comparing coherent and noncoherent reception schemes under energy budget constraints reveals that their performance depends on the type of fading conditions, the training symbols energy budget for coherent schemes, the size of interleaving depth for coded interleaved systems, as well as the type of utilized channel codes. Experimental results demonstrate an order of magnitude range increase compared to con-

ventional scatter radio technology verifying the efficacy of the proposed scatter radio reception schemes.

It was clearly shown that the multistatic scatter radio architecture offers more reliable reception as well as better field coverage, while demonstrating smaller sensitivity to the topology of the tags, compared to the monostatic architecture. It is demonstrated under realistic Nakagami small-scale fading scenarios and path-loss models that not only the BER decay is doubled in a multistatic architecture compared to a monostatic one, but also, energy and information outage events are less frequent in multistatic systems due to the flexible morphology of the multistatic WSN architecture. A concrete experimental proof-of-concept scenario for large-scale and reliable scatter radio networks is also offered.

For the first time in the scatter radio literature a complete signal model for multi-cell backscatter sensor networks (BSNs) is presented, incorporating the idiosyncrasies of scatter radio wireless models under realistic Rician small-scale fading and path-loss models. A new closed-form channel estimation procedure is designed to estimate the tag-to-reader compound uplink channels for every cell. The average SINR of two multi-tag linear detectors is found and harnessed for resource allocation. To allocate frequency sub-channels to the tags, a generic optimization problem is formulated. The proposed resource allocation algorithm has very simple update rules and attains the performance of classic convex optimization algorithms with very small computational cost. It was shown that convergence to the desired solution can be obtained within very few iteration steps.

The dissertation concludes with a discussion of some research directions that are a natural extension of the problems considered.

Accurate Resource Allocation with Nonlinear RF Harvesting

The status quo of resource allocation algorithms in the simultaneous wireless and information power transfer (SWIPT) literature neglects the three operation regimes of realistic RF harvesting circuits mentioned in Chapter 2. Resource allocation optimization problems can be redesigned by incorporating the proposed RF harvesting model in Chapter 2, reflecting more accurately the reality. In addition, the provided expressions for the probability density and cumulative distribution function for RF harvested power under general small-scale fading models can be exploited to offer accurate queueing delay and power allocation analysis using a realistic probabilistic model regarding RF energy arrival events.

Performance Bounds For Energy Harvesting IoT Applications

The provided generic probabilistic analysis under any fading model provided in Chapter 2 can aid to explore several communication-theoretic performance expressions for RF harvesting IoT devices. To be precise, with the provided analysis, RF energy harvesting IoT devices with given RF harvesting circuit specifications, one can find corresponding outage, spectral efficiency, bit error rate (BER) expressions, for given parameters of transmission RF power, transmitter-receiver distance, fading distribution parameters, path-loss exponent.

Multistatic Scatter Radio Cooperative Localization

Another promising future direction regarding multistatic scatter radio network architecture is the development of cooperative localization algorithms in order to deduce the position of randomly placed tags on the field. Specifically, multiple carrier emitters (CEs) can be harnessed to illuminate in a time- or frequency-division multiplexing basis a tag in the field, while the power of the backscattered signals at the reader can be employed to estimate the tag-to-reader distance. Using at least three CEs for every tag, the position of the tags could be estimated using standard state estimation algorithms, e.g., particle filtering, maximum-likelihood estimation, and many others.

Linear Detection Performance Analysis in Multi-Cell BSNs and Comparison With Existing Technology

Performance analysis of the developed linear detections schemes for multi-cell BSNs can be offered in order to calculate several relevant multi-tag performance metrics, such as average outage, BER, and sum spectral efficiency for a studied BSN topology. Comparison of the conventional low-power wireless sensor networks (WSNs) consisting of Marconi radio sensors with the proposed BSN architecture against the aforementioned performance metrics in an interesting research avenue that definitely deserves further investigation.

List of Abbreviations

ASK	Amplitude-shift keying
BCH	Bose-Chaudhuri-Hocquenghem
BER	Bit error rate
BSN	Backscatter sensor network
CDF	Cumulative distribution function
CE	Carrier emitter
CFO	Carrier frequency offset
CW	Carrier wave
FDM	Frequency-division multiplexing
FSK	Frequency-shift keying
GLRT	Generalized likelihood-ratio test
HCHT	Hybrid composite hypothesis test
IEH	Information and energy harvesting
IoT	Internet-of-things
LMMSE	Linear minimum mean-squared error
LoS	Line-of-sight
LS	Least-squares
ML	Maximum-likelihood
MRC	Maximum-ratio combining
MSK	Minimum-shift keying
NLoS	Non-line-of-sight
OFDM	Orthogonal frequency-division multiplexing
PDF	Probability density function
RF	Radio frequency
RFID	Radio frequency identification
RM	Reed-Muller
RV	Random variable

SDR	Software-defined radio
SINR	Signal-to-interference-plus-noise ratio
SNR	Signal-to-noise ratio
TDMA	Time-division multiple access
SWIPT	Simultaneous wireless information and power transfer
WSN	Wireless sensor network
ZF	Zero-forcing

Bibliography

[1] L. Atzori, A. Iera, and G. Morabito, "The internet of things: A survey," *Computer networks*, vol. 54, no. 15, pp. 2787–2805, 2010.

[2] L. Da Xu, W. He, and S. Li, "Internet of things in industries: A survey," *IEEE Trans. Ind. Informat.*, vol. 10, no. 4, pp. 2233–2243, 2014.

[3] A. Al-Fuqaha, M. Guizani, M. Mohammadi, M. Aledhari, and M. Ayyash, "Internet of things: A survey on enabling technologies, protocols, and applications," *IEEE Commun. Surveys Tuts.*, vol. 17, no. 4, pp. 2347–2376, Nov. 2015.

[4] J. Gantz and D. Reinsel, "The digital universe in 2020: Big data, bigger digital shadows, and biggest growth in the far east," *IDC iView: IDC Anal. Future*, vol. 2007, pp. 1–16, Dec. 2012.

[5] J. Manyika *et al.*, *Disruptive Technologies: Advances that Will Transform Life, Business, and the Global Economy.* San Francisco, CA: McKinsey Global Instit., 2013.

[6] H. Stockman, "Communication by means of reflected power," *Proc. IRE*, pp. 1196–1204, 1948.

[7] A. Bletsas, A. G. Dimitriou, and J. N. Sahalos, "Improving backscatter radio tag efficiency," *IEEE Trans. Microw. Theory Techn.*, vol. 58, no. 6, pp. 1502–1509, Jun. 2010.

[8] S. Thomas, E. Wheeler, J. Teizer, and M. Reynolds, "Quadrature amplitude modulated backscatter in passive and semipassive UHF RFID systems," *IEEE Trans. Microw. Theory Techn.*, vol. 60, no. 4, pp. 1175–1182, Apr. 2012.

[9] J. Kimionis and M. M. Tentzeris, "Pulse shaping for backscatter radio," in *Proc. IEEE Int. Microwave Symposium (IMS)*, San Francisco, CA, 2016, pp. 1–4.

[10] U. Karthaus and M. Fischer, "Fully integrated passive UHF RFID transponder IC with 16.7-μW minimum RF input power," *IEEE J. Solid-State Circuits*, vol. 38, no. 10, pp. 1602–1608, Oct. 2003.

[11] J. Kimionis, A. Bletsas, and J. N. Sahalos, "Bistatic backscatter radio for tag read-range extension," in *Proc. IEEE RFID Techn. and Applications (RFID-TA)*, Nice, France, 2012, pp. 356–361.

[12] ——, "Bistatic backscatter radio for power-limited sensor networks," in *Proc. IEEE Global Commun. Conf. (Globecom)*, Atlanta, GA, Dec. 2013, pp. 353–358.

[13] G. Vannucci, A. Bletsas, and D. Leigh, "A software-defined radio system for backscatter sensor networks," *IEEE Trans. Wireless Commun.*, vol. 7, no. 6, pp. 2170–2179, Jun. 2008.

[14] F. Fuschini, C. Piersanti, F. Paolazzi, and G. Falciasecca, "Analytical approach to the backscattering from UHF RFID transponder," *IEEE Antennas Wireless Propag. Lett.*, vol. 7, pp. 33–35, 2008.

[15] R. Chakraborty, S. Roy, and V. Jandhyala, "Revisiting RFID link budgets for technology scaling: Range maximization of RFID tags," vol. 59, no. 2, pp. 496–503, Feb. 2011.

[16] W. Liu, K. Huang, X. Zhou, and S. Durrani, "Backscatter communications for Internet-of-Things: Theory and applications," *arXiv preprint arXiv:1701.07588*, 2017.

[17] E. Kampianakis, J. Kimionis, K. Tountas, C. Konstantopoulos, E. Koutroulis, and A. Bletsas, "Wireless environmental sensor networking with analog scatter radio & timer principles," *IEEE Sensors J.*, vol. 14, no. 10, pp. 3365–3376, Oct. 2014.

[18] C. Konstantopoulos, E. Koutroulis, N. Mitianoudis, and A. Bletsas, "Converting a plant to a battery and wireless sensor with scatter radio and ultra-low cost," *IEEE Trans. Instrum. Meas.*, vol. 65, no. 2, pp. 388–398, Feb. 2016.

[19] S. N. Daskalakis, S. D. Assimonis, E. Kampianakis, and A. Bletsas, "Soil moisture scatter radio networking with low power," *IEEE Trans. Microw. Theory Techn.*, vol. 64, no. 7, pp. 2338–2346, Jul. 2016.

[20] S. Z. Biswas, "Backscatter protocols and energy-efficient computing for RF-power devices," Ph.D. dissertation, University of Washington, 2012.

[21] K. Penttila, L. Sydanheimo, and M. Kivikoski, "Performance development of a high-speed automatic object identification using passive RFID technology," in *Proc. IEEE Int. Conf. on Robotics and Automation (ICRA)*, vol. 5. IEEE, 2004, pp. 4864–4868.

[22] P. V. Nikitin and K. Rao, "Performance limitations of passive UHF RFID systems," in *Proc. IEEE Antennas and Propagat. Society Int. Symp.*, Albuquerque, NM, Jul. 2006, pp. 1011–1014.

[23] A. Collado and A. Georgiadis, "Conformal hybrid solar and electromagnetic (EM) energy harvesting rectenna," *IEEE Trans. Circuits Syst. I*, vol. 60, pp. 2225–2234, Aug. 2013.

[24] J. D. Griffin and G. D. Durgin, "Link envelope correlation in the backscatter channel," *IEEE Commun. Lett.*, vol. 11, no. 9, pp. 735–737, Sep. 2007.

[25] C. Boyer and S. Roy, "Space time coding for backscatter RFID," *IEEE Trans. Wireless Commun.*, vol. 12, no. 5, pp. 2272–2280, May 2013.

[26] ——, "Backscatter communication and RFID: Coding, energy, and MIMO analysis," *IEEE Trans. Commun.*, vol. 62, no. 3, pp. 770–785, Mar. 2014.

[27] A. Goldsmith, *Wireless Communications.* New York, NY, USA: Cambridge University Press, 2005.

[28] G. D. Durgin, "RF thermoelectric generation for passive RFID," in *Proc. IEEE RFID*, Orlando, FL, May 2016, pp. 1–8.

[29] Z. Popović, E. A. Falkenstein, D. Costinett, and R. Zane, "Low-power far-field wireless powering for wireless sensors," *Proc. IEEE*, vol. 101, no. 6, pp. 1397–1409, Jun. 2013.

[30] C. R. Valenta and G. D. Durgin, "Harvesting wireless power: Survey of energy-harvester conversion efficiency in far-field, wireless power transfer systems," *IEEE Microw. Mag*, vol. 15, no. 4, pp. 108–120, Jun. 2014.

[31] S. D. Assimonis, S.-N. Daskalakis, and A. Bletsas, "Sensitive and efficient RF harvesting supply for batteryless backscatter sensor networks," *IEEE Trans. Microw. Theory Techn.*, vol. 64, no. 4, pp. 1327–1338, Apr. 2016.

[32] J. D. Griffin and G. D. Durgin, "Complete link budgets for backscatter-radio and RFID systems," *IEEE Antennas Propag. Mag.*, vol. 51, no. 2, pp. 11–25, Apr. 2009.

[33] J. Kimionis, A. Bletsas, and J. N. Sahalos, "Increased range bistatic scatter radio," *IEEE Trans. Commun.*, vol. 62, no. 3, pp. 1091–1104, Mar. 2014.

[34] T. Le, K. Mayaram, and T. Fiez, "Efficient far-field radio frequency energy harvesting for passively powered sensor networks," *IEEE J. Solid-State Circuits*, vol. 43, no. 5, pp. 1287–1302, May 2008.

[35] C. M. Kruesi, R. Vyas, and M. Tetzeris, "Design and development of a novel 3D cubic antenna for wireless sensor networks (WSN) and RFID applications," *IEEE Trans. Antennas Propag.*, vol. 57, no. 10, pp. 3293–3299, Oct. 2009.

[36] V. Lakafosis, A. Rida, R. Vyas, L. Yang, S. Nikolaou, and M. M. Tentzeris, "Progress towards the first wireless sensor networks consisting of inkjet-printed, paper-based RFID-enabled sensor tags," *Proc. IEEE*, vol. 98, no. 9, pp. 1601–1609, Sep. 2010.

[37] N. Fasarakis-Hilliard, P. N. Alevizos, and A. Bletsas, "Coherent detection and channel coding for bistatic scatter radio sensor networking," *IEEE Trans. Commun.*, vol. 63, pp. 1798–1810, May 2015.

[38] G. Vougioukas, S. N. Daskalakis, and A. Bletsas, "Could battery-less scatter radio tags achieve 270-meter range?" Aveiro, Portugal, May 2016, pp. 1–3.

[39] P. N. Alevizos, A. Bletsas, and G. N. Karystinos, "Noncoherent short packet detection and decoding for scatter radio sensor networking," *IEEE Trans. Commun.*, vol. 65, no. 5, pp. 1–13, May 2017.

[40] K. Tountas, "Performance analysis, middleware & hardware for bistatic, ultra-low power scatter radio networks," Master's thesis, Technical University of Crete, Jul. 2016, supervisor A. Bletsas.

[41] A. A. Nasir, X. Zhou, S. Durrani, and R. A. Kennedy, "Relaying protocols for wireless energy harvesting and information processing," *IEEE Trans. Wireless Commun.*, vol. 12, no. 7, pp. 3622–3636, Jul. 2013.

[42] X. Zhou, R. Zhang, and C. K. Ho, "Wireless information and power transfer: Architecture design and rate-energy tradeoff," *IEEE Trans. Commun.*, vol. 61, no. 11, pp. 4754–4767, Nov. 2013.

[43] K. Huang and E. Larsson, "Simultaneous information and power transfer for broadband wireless systems," *IEEE Trans. Signal Process.*, vol. 61, no. 23, pp. 5972–5986, Dec. 2013.

[44] X. Zhou, R. Zhang, and C. K. Ho, "Wireless information and power transfer in multiuser OFDM systems," *IEEE Trans. Wireless Commun.*, vol. 13, no. 4, pp. 2282–2294, Apr. 2014.

[45] E. Boshkovska, D. W. K. Ng, N. Zlatanov, and R. Schober, "Practical non-linear energy harvesting model and resource allocation for SWIPT systems," *IEEE Commun. Lett.*, vol. 19, no. 12, pp. 2082–2085, Dec. 2015.

[46] S. Timotheou, I. Krikidis, G. Zheng, and B. Ottersten, "Beamforming for MISO interference channels with QoS and RF energy transfer," *IEEE Trans. Wireless Commun.*, vol. 13, no. 5, pp. 2646–2658, May 2014.

[47] S. Sudevalayam and P. Kulkarni, "Energy harvesting sensor nodes: Survey and implications," *IEEE Commun. Surv. Tuts*, vol. 13, no. 3, pp. 443–461, Third Quart. 2011.

[48] I. Krikidis, S. Timotheou, S. Nikolaou, G. Zheng, D. W. K. Ng, and R. Schober, "Simultaneous wireless information and power transfer in modern communication systems," *IEEE Commun. Mag.*, vol. 52, no. 11, pp. 104–110, Nov. 2014.

[49] S. Ulukus, A. Yener, E. Erkip, O. Simeone, M. Zorzi, P. Grover, and K. Huang, "Energy harvesting wireless communications: A review of recent advances," *IEEE J. Sel. Areas Commun.*, vol. 33, no. 3, pp. 360–381, Mar. 2015.

[50] M. M. Butt, I. Krikidis, A. Mohamed, and M. Guizani, "RF energy harvesting communications: Recent advances and research issues," in *Energy Management in Wireless Cellular and Ad-hoc Networks*. Springer, 2016, pp. 339–363.

[51] M. Ku, W. Li, Y. Chen, and K. J. R. Liu, "Advances in energy harvesting communications: Past, present, and future challenges," *IEEE Commun. Surv. Tuts*, vol. 18, no. 2, pp. 1384–1412, Second Quart. 2016.

[52] Texas Instruments Inc., "White paper RF harvesting," http://focus.ti.com/lit/wp/slyy018a/slyy018a.pdf, Apr. 2010.

[53] Part Code: SZGD5433, http://www.futurlec.com/Solar_Cell.shtml.

[54] J. A. Hagerty, F. B. Helmbrecht, W. H. McCalpin, R. Zane, and Z. B. Popovic, "Recycling ambient microwave energy with broad-band rectenna arrays," *IEEE Trans. Microw. Theory Techn.*, vol. 52, no. 3, pp. 1014–1024, Mar. 2004.

[55] Z. Zakaria, N. Zainuddin, M. A. Aziz, M. Husain, and M. Mutalib, "A parametric study on dual-band meander line monopole antenna for RF energy harvesting," in *Proc. IEEE RFID Techn. and Applications (RFID-TA)*, Johor Bahru, Malaysia, 2013, pp. 1–5.

[56] M. Roberg, T. Reveyrand, I. Ramos, E. A. Falkenstein, and Z. Popovic, "High-efficiency harmonically terminated diode and transistor rectifiers," *IEEE Trans. Microw. Theory Techn.*, vol. 60, no. 12, pp. 4043–4052, Dec. 2012.

[57] P. Nintanavongsa, U. Muncuk, D. R. Lewis, and K. R. Chowdhury, "Design optimization and implementation for RF energy harvesting circuits," *IEE Trans. Emerg. Sel. Topics Circuits Syst.*, vol. 2, no. 1, pp. 24–33, Mar. 2012.

[58] U. Olgun, C.-C. Chen, and J. L. Volakis, "Investigation of rectenna array configurations for enhanced RF power harvesting," *IEEE Antennas Wireless Propag. Lett.*, vol. 10, pp. 262–265, Apr. 2011.

[59] PowerCast Module, http://www.mouser.com/ds/2/329/P2110B-Datasheet-Rev-3-1091766.pdf.

[60] A. Pappoulis and S. U. Pillai, *Probability, Random Variables and Stochastic Processes*, 4th ed.   New York, NY: McGraw-Hill, 2002.

[61] G. B. Folland, *Real analysis: Modern techniques and their applications*, 2nd ed. John Wiley & Sons, Inc., New York, 1999.

[62] I. S. Gradshteyn and I. M. Ryzhik, *Table of Integrals, Series, and Products*, 7th ed. Elsevier/Academic Press, Amsterdam, 2007.

[63] N. Kargas, F. Mavromatis, and A. Bletsas, "Fully-coherent reader with commodity SDR for Gen2 FM0 and computational RFID," *IEEE Wireless Commun. Lett.*, vol. 4, no. 6, pp. 617–620, Dec. 2015.

[64] E. Süli and D. F. Mayers, *An Introduction to Numerical Analysis.*   Cambridge University Press, 2003.

[65] G. H. Golub and C. F. van Loan, *Matrix Computations*, 3rd ed.   The Johns Hopkins University Press, 1989.

[66] K. Finkenzeller, *RFID Handbook: Fundamentals and Applications in Contactless Smart Cards and Identification*, 2nd ed.   New York, NY, USA: John Wiley & Sons, Inc., 2003.

[67] J. Paradiso, K. Hsiao, and A. Benbasat, "Tangible music interfaces using passive magnetic tags," in *ACM Conf. Human Factors in Computing Systems: Special Workshop on New Interfaces for Musical Expression*, Chicago, IL, 2001.

[68] J. Paradiso, L. Pardue, K. Hsiao, and A. Benbasat, "Electromagnetic tagging for electronic music interfaces," in *Journal of New Music Research*, vol. 32, Dec. 2003, pp. 395–409.

[69] *EPC Radio-Frequency Identity Protocols, Class-1 Generation-2 UHF RFID Protocol for Communications at 860 MHZ-960 MHZ.* EPC Global, 2008, version 1.2.0.

[70] A. Al-Fuqaha, M. Guizani, M. Mohammadi, M. Aledhari, and M. Ayyash, "Internet of things: A survey on enabling technologies, protocols, and applications," *IEEE Commun. Surveys Tuts.*, vol. 17, no. 4, pp. 2347–2376, Nov. 2015.

[71] S. Kim, C. Mariotti, F. Alimenti, P. Mezzanotte, A. Georgiadis, A. Collado, L. Roselli, and M. Tentzeris, "No battery required: perpetual RFID-enabled wireless sensors for cognitive intelligence applications," *IEEE Microw. Mag.*, vol. 14, no. 5, pp. 66–77, Jul. 2013.

[72] J. D. Griffin and G. D. Durgin, "Gains for RF tags using multiple antennas," *IEEE Trans. Antennas Propag.*, vol. 56, no. 2, pp. 563–570, Feb. 2008.

[73] A. Bletsas, J. Kimionis, A. G. Dimitriou, and G. N. Karystinos, "Single-antenna coherent detection of collided FM0 RFID signals," *IEEE Trans. Commun.*, vol. 60, no. 3, pp. 756–766, 2012.

[74] P. N. Alevizos, N. Fasarakis-Hilliard, K. Tountas, N. Agadakos, N. Kargas, and A. Bletsas, "Channel coding for increased range bistatic backscatter radio: Experimental results," in *Proc. IEEE RFID Techn. and Applications (RFID-TA)*, Tampere, Finland, Sep. 2014, pp. 38–43.

[75] P. N. Alevizos, Y. Fountzoulas, G. N. Karystinos, and A. Bletsas, "Noncoherent sequence detection of orthogonally modulated signals in flat fading with log-linear complexity," in *Proc. IEEE Int. Conf. Acoustics, Speech, and Signal Processing (ICASSP)*, Brisbane, Australia, Apr. 2015, pp. 2974–2978.

[76] J. F. Ensworth and M. S. Reynolds, "Every smart phone is a backscatter reader: Modulated backscatter compatibility with bluetooth 4.0 low energy (BLE) devices," in *Proc. IEEE RFID*, San Diego, CA, Apr. 2015, pp. 78–85.

[77] B. Kellogg, V. Talla, J. R. Smith, and S. Gollakot, "PASSIVE WI-FI: Bringing low power to Wi-Fi transmissions," *GetMobile: Mobile Comp. and Comm.*, vol. 20, no. 3, pp. 38–41, Jan. 2017.

[78] P. Zhang, D. Bharadia, K. Joshi, and S. Katti, "Hitchhike: Practical backscatter using commodity wifi," in *Proc. ACM Conference on Embedded Network Sensor Systems CD-ROM (SenSys)*, 2016, pp. 259–271.

[79] D. Tse and P. Viswanath, *Fundamentals of Wireless Communication.* New York, NY: Cambridge University Press, 2005.

[80] J. G. Proakis and M. Salehi, *Digital Communications*, 5th ed. New York, NY: McGraw-Hill, 2007.

[81] A. Bletsas, A. G. Dimitriou, and J. Sahalos, "Improving backscatter radio tag efficiency," *IEEE Trans. Microw. Theory Techn.*, vol. 58, no. 6, pp. 1502 – 1509, Jun. 2010.

[82] J. Kimionis, "Bistatic scatter radio for increased-range environmental sensing," Master's thesis, Technical University of Crete, Aug. 2013, supervisor A. Bletsas.

[83] E. Kampianakis, "Scatter radio sensor network with analog frequency modulation principles," Master's thesis, Technical University of Crete, Jul. 2014, supervisor A. Bletsas.

[84] F. W. J. Olver, D. W. Lozier, R. F. Boisvert, and C. W. Clark, *NIST handbook of mathematical functions.* New York, NY: Cambridge Univ. Press, 2010.

[85] P. N. Alevizos, Y. Fountzoulas, G. N. Karystinos, and A. Bletsas, "Log-linear-complexity GLRT-optimal noncoherent sequence detection for orthogonal and RFID-oriented modulations," *IEEE Trans. Commun.*, vol. 64, no. 4, pp. 1600–1612, Apr. 2016.

[86] P. N. Alevizos, "Channel coding and detection for increased range bistatic scatter radio," Master's thesis, Technical University of Crete, Oct. 2014, supervisor A. Bletsas.

[87] D. J. Costello and G. D. Forney Jr., "Channel coding: The road to channel capacity," *Proc. IEEE*, vol. 95, no. 6, pp. 1150–1177, Jun. 2007.

[88] S. M. Kay, *Fundamentals of statistical signal processing. [Volume I]. , Estimation theory.* Upper Saddle River (N.J.): Prentice Hall, 1993.

[89] B. C. Levy, *Principles of Signal Detection and Parameter Estimation.* New York: Springer, 2008.

[90] T. Richardson and R. Urbanke, *Modern Coding Theory.* Cambridge University Press, 2008.

[91] A. Martinez, A. G. i. Fabregas, and G. Caire, "Error probability analysis of bit-interleaved coded modulation," *IEEE Trans. Inform. Theory*, vol. 52, no. 1, pp. 262–271, Jan. 2006.

[92] L. Zheng and D. N. C. Tse, "Diversity and multiplexing: A fundamental tradeoff in multiple antenna channels," *IEEE Trans. Inform. Theory*, vol. 49, no. 5, pp. 1073–1096, May 2003.

[93] C. Angerer, "Design and exploration of radio frequency identification systems by rapid prototyping," Ph.D. dissertation, Vienna University of Technology, 2010, supervisor M. Rupp.

[94] A. Bletsas, S. Siachalou, and J. N. Sahalos, "Anti-collision backscatter sensor networks," *IEEE Trans. Wireless Commun.*, vol. 8, no. 10, pp. 5018–5029, Oct. 2009.

[95] A. Bereketli and O. B. Akan, "Communication coverage in wireless passive sensor networks," *IEEE Commun. Lett.*, vol. 13, no. 2, pp. 133–135, Feb. 2009.

[96] K. Han and K. Huang, "Wirelessly powered backscatter communication networks: Modeling, coverage and capacity," *IEEE Trans. Wireless Commun.*, vol. 16, no. 4, pp. 2548–2561, Apr. 2017.

[97] P. N. Alevizos and A. Bletsas, "Noncoherent composite hypothesis testing receivers for extended range bistatic scatter radio WSNs," in *Proc. IEEE Int. Conf. on Commun.*, London, U.K., Jun. 2015.

[98] N. D. Chatzidiamantis, G. K. Karagiannidis, and D. S. Michalopoulos, "On the distribution of the sum of Gamma-Gamma variates and application in MIMO optical wireless systems," in *Proc. IEEE Global Commun. Conf. (Globecom)*, Hawaii, USA, 2009, pp. 1–6.

[99] P. S. Bithas, N. C. Sagias, T. A. Tsiftsis, and G. K. Karagiannidis, "Distributions involving correlated generalized Gamma variables," in *Proc. International Conference on Applied Stochastic Models and Data Analysis (ASMDA)*, Crete, Greece, 2007.

[100] J. M. Romero-Jerez and A. J. Goldsmith, "Receive antenna array strategies in fading and interference: an outage probability comparison," *IEEE Trans. Wireless Commun.*, vol. 7, no. 3, pp. 920–932, Mar. 2008.

[101] S. N. Daskalakis, S. D. Assimonis, E. Kampianakis, and A. Bletsas, "Soil moisture wireless sensing with analog scatter radio, low power, ultra-low cost and extended communication ranges," in *Proc. IEEE Sensors Conf. (Sensors)*, Valencia, Spain, Nov. 2014, pp. 122–125.

[102] D. Shen, G. Woo, D. P. Reed, A. B. Lippman, and J. Wang, "Separation of multiple passive RFID signals using software defined radio," in *Proc. IEEE Int. Conf. on RFID*, Orlando, FL, 2009, pp. 139–146.

[103] C. Angerer, R. Langwieser, and M. Rupp, "RFID reader receivers for physical layer collision recovery," *IEEE Trans. Commun.*, vol. 58, no. 12, pp. 3526–3537, Dec. 2010.

[104] K. Fyhn, R. M. Jacobsen, P. Popovski, A. Scaglione, and T. Larsen, "Multipacket reception of passive UHF RFID tags: a communication theoretic approach," *IEEE Trans. Signal Process.*, vol. 59, no. 9, pp. 4225–4237, Sep. 2011.

[105] J. Wang, H. Hassanieh, D. Katabi, and P. Indyk, "Efficient and reliable low-power backscatter networks," in *Proc. ACM SIGCOMM*, Helsinki, Finland, 2012, pp. 61–72.

[106] N. Fasarakis-Hilliard, "Coherent detection and channel coding for backscatter sensor networks," Master's thesis, Technical University of Crete, Aug. 2014, supervisor A. Bletsas.

[107] S. M. Aji and R. J. McEliece, "The generalized distributive law," *IEEE Trans. Inf. Theor.*, vol. 46, no. 2, pp. 325–343, Mar. 2000.

[108] J. Hoydis, S. ten Brink, and M. Debbah, "Massive MIMO in the UL/DL of cellular networks: How many antennas do we need?" *IEEE J. Sel. Areas Commun.*, vol. 31, no. 2, pp. 160–171, Feb. 2013.

[109] H. Q. Ngo, E. G. Larsson, and T. L. Marzetta, "Energy and spectral efficiency of very large multiuser MIMO systems," *IEEE Trans. Commun.*, vol. 61, no. 4, pp. 1436–1449, Apr. 2013.

[110] P. Billingsley, *Probability and Measure*, 2nd ed.   John Wiley and Sons, 1986.

[111] M. Bayati, D. Shah, and M. Sharma, "Max-product for maximum weight matching: Convergence, correctness, and LP duality," *IEEE Trans. Inf. Theory*, vol. 54, no. 3, pp. 1241–1251, Mar. 2008.

[112] M. Bayati, C. Borgs, J. Chayes, and R. Zecchina, "On the exactness of the cavity method for weighted *b*-matchings on arbitrary graphs and its relation to linear programs," *Journal of Statistical Mechanics: Theory and Experiment*, vol. 2008, no. 06, Jun. 2008.

[113] T. Heskes, "On the uniqueness of loopy belief propagation fixed points," *Neural Comput.*, vol. 16, no. 11, pp. 2379–2413, Nov. 2004.

[114] M. Bayati, C. Borgs, J. Chayes, and R. Zecchina, "Belief propagation for weighted *b*-matchings on arbitrary graphs and its relation to linear programs with integer solutions," *SIAM Journal on Discrete Mathematics*, vol. 25, no. 2, pp. 989–1011, Jul. 2011.

[115] S. Boyd and L. Vandenberghe, *Convex Optimization.* New York, NY, USA: Cambridge University Press, 2004.

[116] T. K. Moon, *Error Correction Coding, Mathematical Methods and Algorithms*, 1st ed. Hoboken, NJ: Wiley-Interscience, 2005.

[117] M. Grant and S. Boyd, "CVX: Matlab software for disciplined convex programming, version 2.1," http://cvxr.com/cvx, Mar. 2014.

[118] F. R. Kschischang, B. J. Frey, and H.-A. Loeliger, "Factor graphs and the sum-product algorithm," *IEEE Trans. Inf. Theor.*, vol. 47, pp. 498–519, Feb. 2001.